X-Ray Fluorescence Holography and Multiple Energy X-Ray Holography: A Comparative Study

Dissertation
zur Erlangung des Doktorgrades
des Fachbereichs Physik
der Universität Hamburg

vorgelegt von
Tina Corinna Hiort
aus Hamburg

Hamburg
2000

Gutachter der Dissertation:	Prof. Dr. G. Materlik Prof. Dr. D. Heitmann
Gutachter der Disputation:	Prof. Dr. G. Materlik Prof. Dr. R. Wiesendanger
Datum der Disputation:	28. Juni 2000
Dekan des Fachbereichs Physik und Vorsitzender des Promotionsausschusses:	Prof. Dr. F.-W. Büßer

X-Ray Fluorescence Holography and Multiple Energy X-Ray Holography: A Comparative Study

Abstract

X-ray fluorescence holography (XFH) and multiple energy x-ray holography (MEXH) are new methods for structure determination. They are based on measuring the interference of a known reference wave with an unknown object wave so that the phase information is not lost. Such interference intensities can be interpreted as holograms. In order to improve the understanding of these methods and to analyse their perspectives and limitations, they are investigated in this work theoretically and experimentally.

Three-dimensional spatial information of a structure is obtained by transforming XFH or MEXH holograms from $\mathbf{k}$ space into real space. The transformation is called reconstruction. Different reconstruction algorithms and their consequences for the images of the atomically resolved structures are analysed using analytical and numerical calculations. The influence of reference wave removal on the atomic images is investigated.

The experimental setups for XFH and MEXH and the data analysis are discussed. An optimized measurement procedure for XFH and MEXH was developed that allows a straightforward data evaluation and a quantitative analysis of atomic images. Estimates are derived for the necessary statistics to be recorded in a hologram and for the angular and energy ranges and step sizes in which holograms have to be measured. An electron yield detector was developed for MEXH experiments and used in a first experiment.

Experimental XFH and MEXH holograms and the corresponding reconstructed images are analysed and compared to results from calculated holograms. Reconstructions of holograms that are known on a full sphere have a nearly isotropic spatial resolution of about half the interference wavelength. XFH is limited to the (few) interference energies that are given by the x-ray emission lines of atoms incorporated in the structure under investigation. At a few energies, a structural refinement is usually necessary. This may be avoided at multiple energies in MEXH where the interference energy is the energy of the incident radiation and can be chosen freely above an electron binding energy of an atom incorporated in the structure.

The holographic signal is very weak in XFH and MEXH due to the weak elastic scattering cross section of x rays from atoms. Therefore the methods are limited to structures that provide a sufficiently strong signal. Present developments of new radiation sources and detectors will in the future allow the application of the methods to unknown, diluted structures.

Direkte und reziproke Röntgenholographie mit atomarer Auflösung: Ein Vergleich

Kurzfassung

Direkte (XFH) und reziproke Röntgenholographie (MEXH) sind neue Methoden zur Strukturbestimmung. In beiden wird die Interferenzintensität zwischen einer bekannten Referenzwelle mit der gesuchten Objektwelle gemessen, so daß die Phaseninformation erhalten bleibt. Solche Interferenzintensitäten können als Hologramme interpretiert werden. In dieser Arbeit werden XFH und MEXH theoretisch und experimentell untersucht, um zum verbesserten Verständnis der Methoden beizutragen und um ihre Perspektiven und Beschränkungen zu analysieren.

Man erhält dreidimensionale räumliche Informationen über eine Struktur, indem XFH oder MEXH Hologramme vom **k**-Raum in den Ortsraum transformiert werden. Die Transformation wird als Rekonstruktion bezeichnet. Verschiedene Rekonstruktionsalgorithmen und ihre Konsequenzen für die Bilder der atomar aufgelösten Strukturen werden anhand von analytischen und numerischen Berechnungen analysiert, und der Einfluß des Untergrundabzugs auf die atomar aufgelösten Bilder wird untersucht.

Der experimentelle Aufbau für XFH und MEXH und die Datenanalyse werden diskutiert. Für beide Methoden wurde die experimentelle Methodik optimiert, um eine einfache Datenbehandlung und eine quantitative Analyse der atomaren Bilder zu ermöglichen. Abschätzungen der für ein Hologramm erforderlichen Statistik und der benötigten Winkel- und Energiebereiche und -schrittweiten werden hergeleitet. Für MEXH Experimente wurde ein Elektronendetektor entwickelt und in einem ersten Experiment verwendet.

Gemessene XFH und MEXH Hologramme und die daraus rekonstruierten atomar aufgelösten Bilder werden analysiert und mit Ergebnissen aus berechneten Hologrammen verglichen. Hologramme, die im gesamten Winkelbereich bekannt sind, ermöglichen eine nahezu isotrope räumliche Auflösung von etwa der halben Interferenzwellenlänge. In XFH stehen als Interferenzenergien nur die Röntgenemissionslinien von Atomen der zu untersuchenden Struktur zur Verfügung. Bei wenigen Energien ist meist eine Strukturverfeinerung notwendig. Sie kann durch die Verwendung vieler Energien vermieden werden, die in MEXH möglich ist. In MEXH ist die Interferenzenergie durch die Energie der einfallenden Strahlung gegeben, die frei oberhalb einer Elektronenbindungsenergie von Atomen der Struktur gewählt werden kann.

Das holographische Signal ist in XFH und MEXH aufgrund des kleinen elastischen Streuquerschnitts von Röntgenstrahlen an Atomen sehr schwach. Die Methoden können daher nur auf solche Strukturen angewendet werden, die ein genügend starkes Signal liefern. Derzeitige Entwicklungen neuer Strahlungsquellen und Detektoren werden in der Zukunft die Anwendung der Methoden auf unbekannte, verdünnte Strukturen ermöglichen.

Contents

1 Introduction **1**

2 Atomic Resolution X-Ray Holography **5**
2.1 The Holographic Principle 6
2.1.1 Spatial Resolution 8
2.1.2 Coherence 8
2.2 Atomic Resolution Holography 10
2.3 Theory of Atomic Resolution X-Ray Holography 12
2.3.1 X-Ray Fluorescence Holography (XFH) 14
2.3.2 Multiple Energy X-Ray Holography (MEXH) 20
2.3.3 Comparison of XFH and MEXH 23
2.3.4 XFH and MEXH as Two Aspects of the Same Process 24
2.4 Inherent Background 26
2.4.1 Reference Wave and Absorption Effects 26
2.4.2 Mixed MEXH, Mixed XFH 29
2.5 Structural Aspects 32
2.5.1 Short-Range Order and Long-Range Rotational Order 32
2.5.2 Long-Range Translational Order 33
2.6 Reconstructing Atomic Images 36
2.6.1 Reconstruction Algorithms 36
2.6.2 Twin Images 39
2.6.3 Analytical Reconstructions of Simple Holograms 41

3 Reconstructions of Calculated Holograms **49**
3.1 Numerical Hologram Calculations 49
3.2 Numerical Reconstructions 51
3.2.1 Reconstructions at Two Energies 53
3.2.2 Reconstructions at Multiple Energies 59

4 Experiments **65**
4.1 Experimental Setup 65
4.1.1 Sample Alignment 66
4.1.2 Data Acquisition 68
4.2 Radiation Source 68
4.3 Detectors 70
4.3.1 Silicon Drift Detectors 70
4.3.2 An Electron Yield Detector 73

4.3.3 Future Detectors and Sources 76
4.4 Choice of Structure 77
4.4.1 bcc Fe 77
4.4.2 Cu_3Au 78
4.4.3 Cu_2O, Cu 80

5 Experimental Results: Parameters 81
5.1 Experimental Overview 81
5.2 Data Treatment 83
5.3 Mixed MEXH Experiments 83
5.3.1 Cu_3Au Data Recorded in August 1996 84
5.3.2 Cu_3Au, Cu, and Cu_2O Data Recorded in October and November 1996 84
5.3.3 Cu_2O Data Recorded in December 1996 88
5.3.4 Cu_3Au Data Recorded in April 1997 93
5.4 Pure Experiments 97
5.4.1 Cu_3Au XFH Data Recorded in May 1997, Cu_3Au MEXH Data Recorded in June 1997 97
5.4.2 bcc Fe XFH Data Recorded in October 1998 102
5.4.3 bcc Fe MEXH Data Recorded in July 1998 and in March 1999 104
5.5 Optimized Measurement Procedure 108

6 Experimental Results from bcc Fe 111
6.1 X-Ray Fluorescence Holography 111
6.1.1 Experimental Data 111
6.1.2 Reconstructions 114
6.2 Multiple Energy X-Ray Holography 127
6.2.1 Experimental Data 127
6.2.2 Reconstructions 130
6.3 Comparison of XFH and MEXH 141

7 Conclusion and Future Perspectives 144

A Calculation of XFH Intensity 148

B Reconstructions of Calculated Holograms 152

C Parameters of XFH and MEXH Experiments 161
C.1 bcc Fe XFH Experiment of October 1998 161
C.2 bcc Fe MEXH Experiments of July 1998 and March 1999 162

D Reconstructions of Experimental Holograms 164
D.1 Reconstructions of bcc Fe XFH Holograms 164
D.2 Reconstructions of bcc Fe MEXH Holograms 167

Bibliography 174

Danksagung 184

Chapter 1

Introduction

The physical properties of solids are directly related to the atomic structure so that the knowledge of a material's atomic structure can be used to explain and predict material properties. Structure determination is therefore an important tool for understanding the physical properties which are investigated not only in fundamental and applied physics but also in material sciences. An understanding of the properties is essential for applications and for designing new materials. A method for structure determination should ideally provide directly three-dimensional spatial information about a structure.

Solid structures can be roughly classified as crystals that possess long-range translational order and as solids without long-range order. Many real structures are not perfect single crystals but possess short-range order. As a response to this, different methods of structure determination are used and optimized for solving different types of structures. There are methods for local structure determination and others that integrate or average over a certain region of a structure. Several methods are surface sensitive while others provide information mainly on bulk structure. Surface-determination methods are discussed in [Lueth98]. There are scanning techniques that can be used for direct surface determination by measuring a certain physical quantity with spatial resolution [Lueth98] (p. 127ff). For example, a Scanning Tunneling Microscope (STM) is a special scanning device that provides information about a solid surface with atomic resolution [Lueth98] (p. 134ff).

Scattering methods for atomic structure determination use radiation of a wavelength that is comparable to the typical interatomic separation. Electrons, neutrons, and x rays are used as radiation. These methods are non-destructive at least for low radiation doses. A description of crystallographic diffraction geometries and a classification of experimental techniques are given in [IUC92] (p. 23 ff). Crystallographic methods require a structure to have long-range order. In these methods, the far-field intensity radiated by an object is measured. This provides information on amplitudes but not on phases so that the phase information is lost and cannot be directly regained, a fact that is known as the *phase problem* of crystallography. In order to determine a structure, measured intensities have to be compared to calculated intensities. For calculating intensities, a guess about the structure has to be made. An x-ray microscope was invented by W. L. Bragg. The principle is based on recording

diffraction intensities so that the phase information is lost. [Bragg42]. The dream to directly visualize the three-dimensional arrangement of atoms in solids has not been realized in this way.

Presently, many different methods of structure determination are known and applied. Structures are often solved by combining different methods, using their various advantages. Biological materials or new classes of structures such as doped semiconductors provide new challenges for structure determination. Therefore, from the point of view of structure determination, new methods provide new possiblities for solving structures and it is necessary to evaluate perspectives and limitations of new methods.

D. Gabor invented "a new microscopic principle" in 1948 [Gabor48] which is now known as holography. Holography uses the interference of a known reference wave with a secondary wave - called object wave - that is emitted elastically by the object under investigation. The interference pattern contains "amplitudes *and* phases in one diagram" called a hologram. The information about the object is regained by illuminating the hologram with the reference wave. This makes it possible to obtain spatial information *directly* without comparing experimental data with model calculations.

Holography was first demonstrated in an optical experiment [Gabor48] and was established at optical wavelengths which was made possible by the rapid development of lasers. Optical holograms are today known from daily life. They appear for example on bank notes and credit cards. They provide three-dimensional images of objects and are fascinating not only to physicists. An overview over optical holography is for example given in [Born97, Eichler93, Lauterborn93]. Holography with soft x rays at typical wavelengths of 10 Å to 50 Å made progress due to the development of undulator x-ray radiation from third-generation synchrotron radiation sources. [Howells90]. This kind of holography presently reaches about 400 Å spatial resolution [Howells87, Lindaas96].

D. Gabor's original goal was to achieve atomic resolution and to use the holographic principle for structure determination [Gabor48]. In order to realize holography with atomic resolution, A. Szöke proposed in 1986 to use the radiation of an atom incorporated in the structure as the holographic reference wave. It is scattered elastically from neighboring atoms, producing the object wave. The interference pattern of reference and object wave can be interpreted as a hologram [Szoeke86]. This kind of atomic resolution holography can be performed with different kinds of radiation, among them x rays. There are two promising holographic methods of structure determination that use x rays: x-ray fluorescence holography (XFH) [Tegze96] which follows directly A. Szöke's idea, and multiple energy x-ray holography (MEXH) [Gog96a]. XFH and MEXH were first realized in 1996 and are still at an early stage of development. In order to improve the understanding of these methods and to analyse their perspectives and limitations, they are investigated theoretically and experimentally. The advancement of XFH and MEXH is described and the methods are compared.

The holographic principle is described in chapter 2 and the hologram formation is investigated for both methods of x-ray holography using classical electrodynamics. This leads to estimates for the angular and energy ranges and step sizes in which holograms have to be measured. Origin and removal of backgrounds inherent to the methods are described. The methods are best suited for solving certain types of structure so that structural aspects are important to understand what place these new methods might take in the future. The retrieval of spatial information on an object from a hologram is discussed. The physical illumination of the hologram with the reference wave in optical holography is replaced in the atomic resolution holographies by a Fourier-like transformation of the hologram from $\mathbf{k}$ space into real space. The transformed hologram contains spatial information on the object and is called reconstruction. Analytical calculations allow the investigation of different influences on holograms and on reconstructions under simple assumptions.

In order to investigate the methods under more realistic assumptions, numerical calculations of holograms were made (chapter 3). These holograms were reconstructed numerically. The reconstructions are analysed to determine for an ideal theoretical case the influence of hologram energy and angular range and the influence of the data evaluation on the reconstructions.

The setups for XFH and MEXH experiments are described in chapter 4. The holographic signal in XFH and MEXH is very weak due to the small elastic scattering cross section of x rays from atoms. Present-day radiation sources and detectors limit XFH and MEXH to structures that provide a sufficiently high signal. In addition, present-day energy-dispersive fluorescence radiation detectors have a limited detection angle so that only a fraction of the sample radiation can be detected. In order to achieve a higher signal, an electron yield detector that allows electron detection in a large angular range was developed for MEXH experiments and used in an initial test.

The experimental development at the Hamburger Synchrotronstrahlungslabor HASYLAB at the Deutsches Elektronensynchrotron DESY is discussed in chapter 5. A very important aspect is the fact that most XFH and MEXH experiments were performed in a mixed setup which is easy to implement. This lead to a mixing of XFH contributions with MEXH contributions in the experimental intensities. Mixed XFH and MEXH signals must be separated in the data evaluation which is not always possible. Therefore it is important to measure in *pure* XFH or MEXH mode which was for the first time achieved in the frame of this work. The results of mixed MEXH and of first pure XFH and MEXH experiments are discussed and an optimized measurement procedure is described.

Holograms and reconstructions of optimized pure XFH and MEXH experiments are discussed in chapter 6. The effect of statistical noise is investigated and an estimate for the necessary number of recorded photons in a hologram is derived. A body-centered cubic (bcc) Fe single-crystal served as a sample structure in these experiments. The structure is very simple and the crystal provides a high holographic signal so that it is presently the best suitable structure for evaluating the

new methods XFH and MEXH. In order to understand the experimental results, they are compared with results of holograms that were numerically calculated for an Fe cluster. These results allow a first experimental comparison of XFH and MEXH. Since XFH can only be performed at the x-ray emission line energies of atoms incorporated in the structure under investigation and since the results at single or few energies can deviate systematically from the actual structure, a refinement of the results is usually necessary in XFH but can be avoided in MEXH at multiple energies. Conclusions and future perspectives are given in chapter 7.

Chapter 2

Atomic Resolution X-Ray Holography

Atomic resolution x-ray holography is a special kind of holography. This chapter treats its fundamental and theoretical aspects. In order to explain the method, the general holographic principle will be described in section 2.1. A way to realize holography with atomic resolution is explained in section 2.2. Atomic resolution holography can be performed with different kinds of radiation, among them x rays. Two methods of atomic resolution x-ray holography, XFH and MEXH, will be described and analysed theoretically in section 2.3. These methods are still under development and have not been used to solve unknown structures yet.

An important theoretical and practical aspect of the methods is their inherent background. Two kinds of background are analysed in section 2.4. One of them is due to the holographic reference wave and to absorption effects and the other is due to mixing of XFH and MEXH.

The holographic approach can be regarded as complementary to methods of *crystal* structure determination that determine long-range structural order: The goal of atomic resolution holography is to image the *local* environment of an atom incorporated in a structure. The method does not require the structure under investigation to be a crystal. On the contrary, the long-range translational order in crystals can lead to complications in the holographic methods as will become clear from section 2.5.

While the first sections emphasize the aspects of the hologram formation, section 2.6 explains how spatial information on the object is reconstructed from the holograms.

2.1 The Holographic Principle

Holography was invented by D. Gabor for determining structures with atomic resolution [Gabor48]. A primary wave called reference wave $\mathbf{R}(\mathbf{k})$ is scattered from the object under investigation. $\mathbf{k}$ is the wave vector. [1] The elastic part of the secondary wave emitted by the object is the holographic object wave $\mathbf{O}(\mathbf{k})$. The hologram formation and reconstruction in optical holography are schematically shown in figs. 2.1 (a) and (b), respectively. A hologram is formed by the interference of the known reference wave $\mathbf{R}(\mathbf{k})$ with $\mathbf{O}(\mathbf{k})$. The intensity observed in holography is given by

$$I(\mathbf{k}) = |\mathbf{R}(\mathbf{k}) + \mathbf{O}(\mathbf{k})|^2 = |\mathbf{R}(\mathbf{k})|^2 + \mathbf{R}^*(\mathbf{k})\mathbf{O}(\mathbf{k}) + \mathbf{R}(\mathbf{k})\mathbf{O}^*(\mathbf{k}) + |\mathbf{O}(\mathbf{k})|^2, \quad (2.1)$$

where $|\mathbf{R}|^2$ is the intensity of the reference wave. $|\mathbf{O}|^2$ is the intensity of the object wave. $|\mathbf{O}|^2$ is a speckle pattern in optical holograms. $\mathbf{R}^*\mathbf{O}$ and $\mathbf{R}\mathbf{O}^*$ are the interference terms containing the phase information. In holography, amplitudes *and* phases are recorded together. If the intensity of an unknown object wave is measured alone, then the phase information is lost. This fact is the origin of the *phase problem in crystallography.*

The image of the object is obtained by illuminating the hologram with the reference wave $\mathbf{R}$ (or its complex conjugate $\mathbf{R}^*$). Usually a constant reference wave $|\mathbf{R}| = const$ is used so that $|\mathbf{R}|^2\mathbf{R}$ is constant. $\mathbf{R}^*\mathbf{O}$ produces $|\mathbf{R}|^2\mathbf{O}$ which is proportional to the object wave. It gives rise to the direct image of the object and is called virtual image because it appears behind the holographic plate and cannot be visualized on a screen. $\mathbf{R}\mathbf{O}^*$ becomes $\mathbf{R}^2\mathbf{O}^*$ and gives rise to the conjugated image or twin image. The position and orientation of the twin image and the direct image are shown in fig. 2.1 (b). The twin image occurs because a hologram recorded in two dimensions does not allow the unambiguous retrieval of information in three dimensions: Two terms in the hologram, $\mathbf{R}^*\mathbf{O}$ and $\mathbf{R}\mathbf{O}^*$, contain phase information between the reference and object wave so that the reconstruction produces the direct image $|\mathbf{R}|^2\mathbf{O}$ of the object at the object position and with the object orientation, and another conjugated image $\mathbf{R}^2\mathbf{O}^*$. The conjugated image can be visualized in optical holography on a screen and is called real image. The term $|\mathbf{O}|^2\mathbf{R}$ can be neglected if $|\mathbf{O}| \ll |\mathbf{R}|$. A review of optical holography is for example given in [Born97, Lauterborn93].

[1] Vectors will be denoted by boldface letters, complex numbers by plain characters. The dot product of two vectors $\mathbf{a}$ and $\mathbf{b}$ will be denoted by $\mathbf{ab}$.

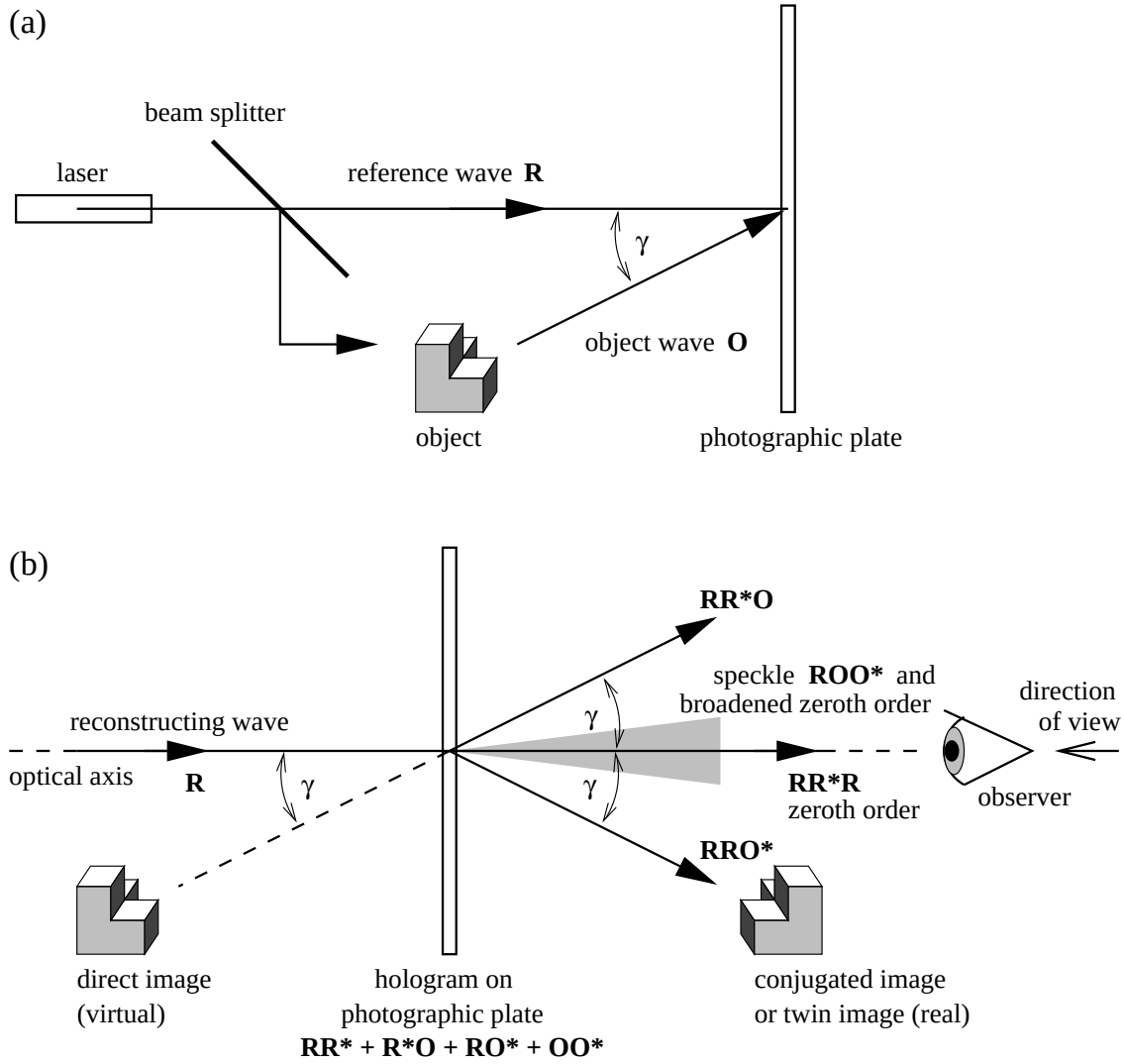

Figure 2.1: (a) Formation of an optical hologram. The direct beam from a laser serves as the holographic reference wave $\mathbf{R}$. It is scattered elastically from the object under investigation, forming the object wave $\mathbf{O}$. The interference intensity $I = |\mathbf{R} + \mathbf{O}|^2$ is recorded on a photographic plate. The incidence of the reference wave on the photographic plate is perpendicular for the case shown here. (b) Reconstruction of the object. The hologram is illuminated by $\mathbf{R}$ which now serves as the reconstructing wave. This produces images corresponding to the following four terms: $|\mathbf{R}|^2\mathbf{R}$ is proportional to the reference wave $\mathbf{R}$. $|\mathbf{O}|^2\mathbf{R}$ is due to the object wave $|\mathbf{O}|^2$. $|\mathbf{R}|^2\mathbf{O}$ is proportional to the object wave $\mathbf{O}$ and is called the direct image of the object. For an observer, the direct image appears behind the hologram so that it cannot be visualized on a screen and is a virtual image. $\mathbf{R}^2\mathbf{O}^*$ is proportional to the conjugated object wave $\mathbf{O}^*$ and is called the conjugated image or twin image. It is on the same side of the hologram as the observer so that it can be visualized on a screen and is a real image. Here, the incidence of the reconstructing beam on the hologram is perpendicular. [Lauterborn93]

2.1.1 Spatial Resolution

Gabor's goal was to obtain atomic resolution [Gabor48]. As an estimate of the resolution in holography, the resolution of a microscope may be used. The smallest distance d between two object points which a microscope of opening angle θ can just resolve is

$$d = \frac{b\lambda_0}{n \sin\theta}, \tag{2.2}$$

where n is the refractive index of the object, and λ_0 is the wavelength in vacuum. b is a factor that depends upon the coherence: $b = 0.61$ for incoherent radiation and a circular aperture [Born97] (chapter 8.6.3, p. 419, eq. (32)), and $b = 0.82$ for strictly coherent radiation and a rectangular aperture [Born97] (chapter 8.6.3, p. 424, eq. (55)). In order to obtain atomic resolution, that is, in order to resolve distances d on the order of ≈ 1Å, a wavelength $\lambda = \lambda_0/n$ on the order of $\lambda \approx 1$Å is necessary for $\sin\theta \approx 1$.

2.1.2 Coherence

Interference between reference wave and object wave can be observed if the waves $\mathbf{R}(\mathbf{k})$ and $\mathbf{O}(\mathbf{k})$ are *coherent*. Two waves are coherent if they have a fixed phase relation that is constant in time and space.

Spatial or Lateral Coherence

The light from a real source can be expressed as a sum of Fourier components with phases $(\omega t - \mathbf{kr})$ at a time t and at position $\mathbf{r}$ where $\omega = kc$ is the angular frequency, and $c = 3 \cdot 10^8$ m/s is the speed of light. *Spatial* or *lateral coherence* refers to the term $\mathbf{kr}$ that is connected to directions perpendicular to the propagation direction of the light. A phase difference can be caused by different propagation directions $\Delta\mathbf{k}$ of the Fourier components which are present in a divergent beam, or by an extended source with position differences $\Delta\mathbf{r}$. Consider two point sources S_1 and S_2, separated by a distance d, emitting radiation of equal wavelength λ, with electric fields

$$\mathbf{E}_1(\mathbf{r},t) = \mathbf{E}_1^0 \frac{e^{i(kr_1+\phi_1-\omega t)}}{r_1}, \quad \text{and} \quad \mathbf{E}_2(\mathbf{r},t) = \mathbf{E}_2^0 \frac{e^{i(kr_2+\phi_2-\omega t)}}{r_2}. \tag{2.3}$$

Here, $\mathbf{r}$ is the vector from the origin of a coordinate system to a point P in the far field on a screen, $\mathbf{r}_{1,2}$ are vectors from $S_{1,2}$ to the point P as shown in fig. 2.2, $r_{1,2} = |\mathbf{r}_{1,2}|$, and $\phi_{1,2}$ are the phases of the fields $\mathbf{E}_{1,2}(\mathbf{r}_{1,2} = 0, t = 0)$. The intensity I of the superposition $\mathbf{E} = \mathbf{E}_1 + \mathbf{E}_2$ of both waves is obtained by taking the time average over an interval large compared with the period $T = 2\pi/\omega$,

$$I(\mathbf{r}) \;=\; \langle|\mathbf{E}|^2\rangle = \left(\frac{|\mathbf{E}_1^0|^2}{r_1^2} + 2\frac{|\mathbf{E}_1^0||\mathbf{E}_2^0|}{r_1 r_2}\cos(kr_2 - kr_1 + \phi_2 - \phi_1) + \frac{|\mathbf{E}_2^0|^2}{r_2^2}\right). \tag{2.4}$$

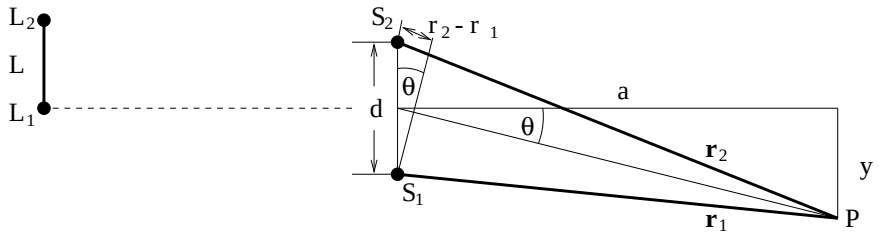

Figure 2.2: The light from two point sources S_1 and S_2 of equal wavelength λ, separated by a distance d, is superposed at a point P on a screen in the far field $a \gg \lambda \gg d$. The figure is not to scale. L is an extended light source, containing the points L_1 and L_2.

I can be interpreted as a holographic interference intensity and oscillates with the phase difference $\delta = k(r_2 - r_1) + \phi_2 - \phi_1$ of the two waves. If the screen is parallel to the line connecting S_1 and S_2 and has a distance $a \gg d$ from it, intensity maxima are obtained for $\delta = 2n\pi, n \in \mathbb{Z}$ and minima for $\delta = (2n+1)\pi, n \in \mathbb{Z}$. For small $\theta \ll \pi/2$, $r_2 - r_1 \approx yd/a \equiv d \tan\theta \approx d \sin\theta$. For $\phi_1 = \phi_2$ the central maximum is obtained for $r_1 = r_2$ and the first minimum for $\lambda/2 = r_2 - r_1$. Then, at the first minimum and for small θ

$$\sin\theta \approx \frac{\lambda}{2d} \qquad \leftrightarrow \qquad y \approx \frac{\lambda a}{2d}. \tag{2.5}$$

For a phase difference $\phi_2 - \phi_1$, the extrema will be shifted by $y_s \equiv \lambda a(\phi_1 - \phi_2)/(2\pi d)$ on the screen. The position shift is equal to $\lambda a/(2d)$ for $\phi_1 - \phi_2 = \pi$. Now consider the sources S_1 and S_2 to be slits, illuminated by an extended source L. S_1 and S_2 will emit waves with zero phase difference due to one point L_1 on L and also with a phase difference $\phi_1 - \phi_2$ due to a different point L_2 on L. In order to obtain an interference pattern of sufficient contrast on the screen, the resulting shift of the extrema should be less than the *lateral coherence length* $y \approx \lambda a/(2d)$. [Lauterborn93]

Temporal or Longitudinal Coherence

Temporal or *longitudinal coherence* refers to the term ωt in the wave phase that is connected to directions along the propagation direction $\mathbf{k}/k$. A phase difference between different Fourier components can be caused by differences in frequency ω or by differences in time t. Let Δt be the average duration of a light pulse $V(t)$. Δt is the *coherence time* of the light. If c is the speed of light and $\overline{\lambda_0}$ the mean wavelength then

$$\Delta l = c\Delta t \approx \frac{(\overline{\lambda_0})^2}{\Delta\lambda_0} \tag{2.6}$$

is the *longitudinal coherence length* [Born97] (chapter 7.5.8, p. 319f, eq. (107)). Consider the wave field from an extended quasi-monochromatic source in the far field of the source at two points $P1$ and $P2$. The fields at these points will be coherent if the path from any source point to $P1$ does not differ from the path from the same source point to $P2$ by more than Δl. This leads to the concept of a *region of coherence* around any point in a wave field. [Born97] (chapter 10.1, p. 491) For a typical

x-ray wavelength $\lambda = 1$Å and a typical $\lambda/\Delta\lambda = 10^4$, the longitudinal coherence length is $\Delta l = 10^4$ Å $= 1\mu$m. For a bcc Fe crystal of lattice constant $a_0 = 2.87$ Å [Wyckoff63], the coherence region will contain about $2\cdot(4\pi/3)\cdot(\Delta l/a_0)^3 \approx 3.5\times10^{11}$ atoms, showing that very many neighbors of an atom are illuminated coherently and that it is easy to fulfil the coherence requirement in a local neighborhood of an atom.

These equations can also be expressed in terms of the x-ray energy. For x rays of wavelength λ and wave vector $\mathbf{k}$, the energy is given by

$$E = \hbar\omega = \hbar kc = \frac{hc}{\lambda}; \qquad E(\text{keV}) = \frac{12.398}{\lambda(\text{Å})}, \tag{2.7}$$

where $h = 2\pi\hbar = 6.63\cdot10^{-34}$ Js.

Coherence and Holography

The reference wave in holography has to be coherent in order to create an interference pattern of sufficient contrast. D. Gabor's idea was to use a point focus of electrons to create the holographic reference wave [Gabor48]. Holography using a point focus has been performed using electrons by A. Tonomura [Tonomura90, Tonomura92] and synchrotron radiation by S. Aoki, Y. Ichihara and S. Kikuta [Aoki72]. These methods were limited by the coherence of available x-ray sources and by the resolution of the recording medium according to M. R. Howells and C. J. Jacobsen [Howells90]. Typical wavelengths in soft x-ray holography are 10 Å to 50 Å. Holograms of about 400 Å spatial resolution can be measured using an x-ray undulator source in an electron storage ring [Howells87, Lindaas96]. In [Howells90], an estimate of 100 Å to 300 Å is given for the spatial resolution that can be reached in the future. A review on soft x-ray holography can be found in [Howells90]. The coherence requirements for this kind of x-ray holography are discussed in [Lindaas96]. As an example, to obtain 400 Å spatial resolution for a typical sample-hologram spacing of 500μm at $\lambda = 18.9$ Å, spatial coherence over a transverse distance of $\gtrsim 15\mu$m and $\lambda/\Delta\lambda \gtrsim 80$ are required [Lindaas96].

2.2 Atomic Resolution Holography

In 1986, A. Szöke proposed a way to realize atomic resolution holography [Szoeke86]. The radiation of an atom *inside* the structure has a coherence volume large enough to contain the neighbors of the source atom in a cluster or a solid so that this radiation can be used as the holographic reference wave. It is elastically scattered from neighboring atoms producing the object wave. Reference and object wave interfere with each other. Their interference pattern $I(\mathbf{k})$ can be detected in the far field. The principle is illustrated for x rays in fig. 2.3. This kind of holography is called "inside-source" holography since the reference wave is produced by a source inside the sample. The coherence requirement can be satisfied much easier in inside-source holography than in soft x-ray holography: In atomic resolution holography, it is the goal to image the *local* environment of a fluorescence atom so that a coherence length of a few atomic distances is sufficient. Typical interatomic distances d in a

solid are on the order of a few Å. For $\lambda = 1$ Å, $d = 2.87$ Å, and detection of the interference pattern at a distance $a = 6$ cm from the atoms, the lateral coherence length is ≈ 1 cm (eq. 2.5). For a typical $\lambda = 1$ Å of fluorescence radiation or of monochromatic x rays from a storage ring, the longitudinal coherence length is on the order of 1μm (eq. 2.6). Under these conditions, x rays provide much larger coherence lengths than necessary for illuminating the local neighborhood of an atom coherently. A. Szöke proposed to use as radiation source photoelectrons, Auger electrons, Mössbauer γ rays or the characteristic fluorescence radiation of atoms.

Atomic resolution holography was first realized with electrons in 1990, using a diffuse low-energy electron diffraction (LEED) pattern [Saldin90] and Kikuchi electrons [Harp90], followed by Auger electrons [Saldin91], photoelectrons [Thevuthasan93, Terminello93], conventional LEED [Mendez92, Mendez93, Reuter97], x rays [Tegze96, Gog96a], Mössbauer γ rays [Korecki97, Korecki99], and recently Bremsstrahlung [Bompadre99]. Reviews on electron holography are for example given in [Fadley93, Saldin97, Len97c]. Theoretical investigations of electron holography can be found in [Thevuthasan91, Tonner91].

The holographic interference term is given by the second and third terms on the right side of eq. 2.1. If $|\mathbf{R}|^2$ is known and $|\mathbf{O}|^2$ can be neglected, then the normalized holographic interference term $\chi(\mathbf{k})$ can be extracted from the observed intensity via

$$\chi(\mathbf{k}) = \frac{\mathbf{R}(\mathbf{k})^*\mathbf{O}(\mathbf{k}) + \mathbf{R}(\mathbf{k})\mathbf{O}(\mathbf{k})^*}{|\mathbf{R}(\mathbf{k})|^2} \simeq \frac{I(\mathbf{k}) - |\mathbf{R}(\mathbf{k})|^2}{|\mathbf{R}(\mathbf{k})|^2}. \tag{2.8}$$

This normalization is used for example in [Tonner91, Saldin91, Tong91] and will be used in this text whereas

$$\chi'(\mathbf{k}) \simeq \frac{I(\mathbf{k}) - |\mathbf{R}(\mathbf{k})|^2}{|\mathbf{R}(\mathbf{k})|} \tag{2.9}$$

is used for example in [Barton88, Barton90, Thevuthasan91]. For $|\mathbf{R}| = const$, both normalizations are equivalent except for a constant factor. The image of the object can be obtained by a numerical reconstruction [2] of the hologram as discussed in section 2.6.

A. Szöke suggests a generalized interpretation of eq. 2.1. Everything that is known about a structure can be regarded as the part of the structure that produces the reference wave, while everything that is unknown produces the object wave. This leads to holography with a *complicated reference wave*. If nothing is known about the structure a priori, then only the intensity of the object wave is measured and the phase information is lost, which corresponds to the situation in crystallography. [Szoeke86, Szoeke93, Szoeke97a, Szoeke97b]

Crystallography and atomic resolution holography can be regarded as complementary in the following sense: Crystallography provides excellent methods for crystal

[2] In atomic resolution holography, the term "reconstruction", is used for obtaining real-space information on a structure from hologram intensities measured in **k**-space.

structure determination that are based on measuring the object wave intensity $|\mathbf{O}|^2$ without recording a reference wave simultaneously ($\mathbf{R} = 0$ in eq. 2.1), and the measured intensity is compared to theoretically calculated intensities in order to determine a structure. Atomic resolution holography uses a different approach. These new methods for structure determination obtain the spatial information directly by reconstructing holograms and a comparison with theoretically calculated intensities is in principle not necessary. [3] Therefore results obtained from atomic resolution holography can be used as a starting point for a conventional crystallographic structure analysis. The different methods can be combined. They can be used to investigate different classes of structures: Crystals provide high diffraction intensities in certain directions. Such an object wave of high intensity can be a disadvantage in atomic resolution holography since it cannot be neglected in eq. 2.8. In this sense crystals are not ideal structures for the holographic methods. Structural aspects in atomic resolution x-ray holography will be discussed in section 2.5.2. The special cases of atomic resolution holography where the interference is formed by x rays will be treated in the following section 2.3.

2.3 Theory of Atomic Resolution X-Ray Holography

As mentioned in chapter 1, XFH and MEXH are two methods of atomic resolution x-ray holography. They will be briefly described here and analysed in detail in sections 2.3.1 and 2.3.2, respectively. Recent reviews of atomic resolution x-ray holography are given in [Faigel99, Adams99, Adams00a].

XFH was first demonstrated on a strontium titanate single crystal providing images of the heavy strontium atoms [Tegze96]. XFH is the special case of inside source holography, where the radiation source is a fluorescing atom inside the sample. The situation is schematically illustrated in fig. 2.3. This reference wave is scattered from neighboring atoms. The scattered waves are the holographic object wave. An energy dispersive detector registers the interference intensity in the far field outside the sample. The detector of limited acceptance angle is rotated around the sample in order to measure the angular dependence of the holographic intensity. XFH will be discussed in section 2.3.1.

The restriction [4] of XFH to the few energies provided by the characteristic fluorescence lines of atoms in a sample was overcome in [Gog96a] by inventing MEXH as a special case of inside detector holography. Inside detector holography is atomic resolution holography where the incident beam is the holographic reference wave. It is scattered from atoms of the structure, forming the holographic object wave. The radiation of an atom incorporated in the structure serves as a detector of the local field

[3] At the present state of the new holographic methods, theoretical calculations are often used to study the methods (chapter 3) and to understand experimental results. Theoretical calculations can also be used for a structural refinement.

[4] A restriction to a few holographic interference energies is a disadvatage as will be discussed in section 2.6 and chapter 3.

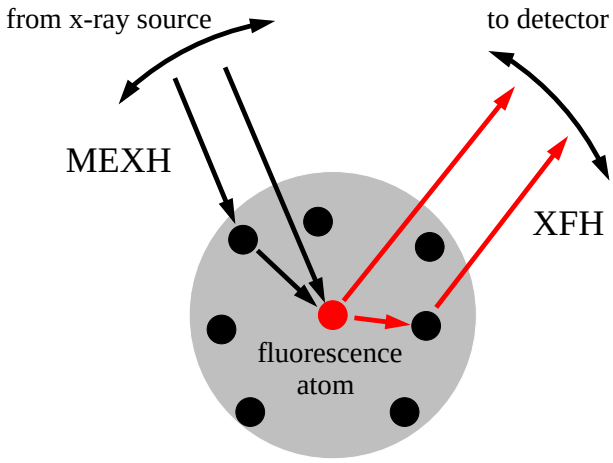

Figure 2.3: Illustration of the principles of atomic resolution x-ray holography. In XFH, the fluorescence radiation of an atom inside the structure is the holographic reference wave. This reference wave is scattered from neighboring atoms. An energy dispersive detector registers the intensity in the far field outside the sample. In XFH, the sample is kept stationary with respect to the incident radiation while the detector is rotated around the sample in order to measure the angular dependence of the holographic intensity. In MEXH, the monochromatic radiation from an external x-ray source serves as the holographic reference wave. It is scattered from atoms of the structure, forming the holographic object waves. The radiation of an atom inside the structure serves as a detector of the local field intensity. In MEXH, the radiation is detected by a detector that is kept stationary with respect to the sample and both are rotated with respect to the incident radiation direction. Additionally, the energy of the incident radiation can be changed.

intensity. The positions of source and detector in A. Szöke's inside source holography are interchanged in inside detector holography. XFH can be called the "direct" or "normal" [Tegze99] method of x-ray fluorescence holography and MEXH can be called "reciprocal", "time reversed" [Gog96a] or "inverse" [Tegze99] x-ray holography. In MEXH, an x-ray radiation source outside the sample emits a monochromatic plane wave that serves as the holographic reference wave. It is scattered from the atoms inside the sample producing the holographic object wave. The reference and the object wave interfere inside the sample. The local intensity of the resulting x-ray standing wave field (XSW) is registered through the fluorescence yield of an atom incorporated in the structure [Gog95] or through Auger or photoelectrons. The holographic interference pattern is obtained by rotating the sample relative to the incoming beam (fig. 2.3). A detector that is usually stationary (compare section 2.3.4) with respect to the sample registers the intensity of the radiation of the sample in the far field. In MEXH, the interference energy can be chosen by changing the energy of the incident x rays. MEXH will be discussed in section 2.3.2.

2.3.1 X-Ray Fluorescence Holography (XFH)

In XFH, the interference pattern is produced by the fluorescence radiation of the sample, which has the following consequences.

- The angular resolution of XFH is determined by the beam footprint size on the sample surface and the detector acceptance angle. They must be limited so that the angular dependence of the holographic signal can be detected.
- The possible interference energies in XFH are determined by the characteristic x-ray emission lines of the atoms in a structure. Therefore the method is usually restricted to a few energies.
- For a source of dimension $d \ll \lambda = 2\pi c/\omega = 2\pi/k$, there are three spatial regions defined: the near (static) zone $d \ll r \ll \lambda$, the intermediate (induction) zone $d \ll r \sim \lambda$, and the far (radiation) zone $d \ll \lambda \ll r$ [Jackson75]. In order to achieve atomic resolution, the wavelength λ must be comparable to or smaller than interatomic distances r. If this condition holds then the object is in the intermediate or far field of the source while the detector is in the far field of both the object and the source.
- The fluorescence of the structure can be excited not only with x rays but also with electrons. In the XFH experiments published so far [Tegze96, Tegze99, Hiort00], incident x rays were used to excite the fluorescence of the sample. In [Bompadre99], Bremsstrahlung holography was performed, demonstrating experimentally that Bremsstrahlung excited by electrons can be used to create a holographic interference pattern.

Formation of the Holographic Intensity

A rigorous quantum electrodynamical treatment of XFH is given in [Fonda97, Miller97, Nishino99]. The quantum electrodynamical results for XFH are consistent with the results from classical electrodynamics [Nishino99] and will not be treated here. A short description of the equations relevant for XFH is given in the following in the frame of classical electrodynamics [Jackson75, Adams98]. The full calculation can be found in appendix A. Consider a fluorescence atom at the origin $(0,0,0) = \mathbf{0}$ of a coordinate system, and another atom at position $\mathbf{r}_j$. The local intensity

$$I_i(\mathbf{0}) = \langle |\mathbf{E}_i(\mathbf{0},t)|^2 \rangle \tag{2.10}$$

excites the atom at the origin to fluorescence radiation if the energy of the incident wave is greater than an electron binding energy of the atom. Here, $\langle x \rangle$ denotes the time average of x over an interval large compared with the period $T = 2\pi/\omega_i$, and $\mathbf{E}_i$ is the electric field of the incident wave. A fraction $\sigma_p \cdot w_f$ of the incident intensity is converted to fluorescence radiation, where σ_p is the photoionisation cross section, and w_f is the probability that a core hole will be reoccupied in a radiative process, competing with nonradiative processes. For the K shell, only Auger processes compete with fluorescence. For K fluorescence, w_f can be approximated

by $w_f = 1/(1 + \alpha Z^{-m})$ where $\alpha = 7.92 \cdot 10^5$, $m = 3.94$, Z = atomic number [Zegenhagen93]. For Fe, $Z = 26$ and $w_f \approx 32\%$. w_f increases with increasing Z.

In the electric dipole approximation, the electric field of fluorescence radiation can be described by

$$\mathbf{E}_d(\mathbf{r},t) = -\frac{k^2}{r}\left[(\mathbf{u}(\mathbf{up}) - \mathbf{p}) - (3\mathbf{u}(\mathbf{up}) - \mathbf{p})\left(\frac{1}{k^2r^2} - \frac{i}{kr}\right)\right], \tag{2.11}$$

where $\mathbf{r}$ is the vector from the electric dipole $\mathbf{p}$ to the observation point, $\mathbf{u} = \mathbf{r}/r$, $k = |\mathbf{k}| = 2\pi/\lambda$, and $\mathbf{k} = \mathbf{k}_f$ is the wave vector of the fluorescence radiation. The wavelength of the fluorescence radiation is larger than the wavelength of the incident radiation, $\lambda_f > \lambda_i$. For sufficiently small wavelengths or large atomic distances r, the scattering atom is in the far field of the fluorescence atom. In the far field, the second term of eq. 2.11 may be neglected [Jackson75]. For a bcc Fe single crystal, the lattice constant is $a_0 = 2.87$Å so that the smallest interatomic distance is $a_0\sqrt{3}/2 = 2.49$Å. This distance can serve as a very rough estimate for a small distance to a scattering electron, keeping in mind that the electrons move around the nucleus of an atom. At the Fe K_α line, $E_f \approx 6.4$ keV and $\lambda_f \approx 1.9$ Å, so that $a_0\sqrt{3}/2 \approx \lambda_f$ corresponds to the intermediate field. The dipole moment of a fluorescence atom at the origin can be expressed as

$$\mathbf{p}_f(\mathbf{r},t) = \mathbf{p}_0 e^{i(k_f r - \omega_f t)}. \tag{2.12}$$

p_0^2 is proportional to $\langle|\mathbf{E}_i(\mathbf{0})|^2\rangle$, so that the fluorescence intensity is proportional to $I_i(\mathbf{0})$. At a distance $\mathbf{r}$ from the origin, the electric field is

$$\mathbf{E}_f(\mathbf{r},t) = \mathbf{E}_d(\mathbf{r},t) + \mathbf{E}_s(\mathbf{r},t), \tag{2.13}$$

where $\mathbf{E}_d(\mathbf{r},t)$ is the field radiated by the fluorescence atom (see appendix A),

$$\mathbf{E}_d(\mathbf{r},t) = -\frac{k_f^2}{r}e^{i(k_f r - \omega_f t)}\left[\frac{\mathbf{r}}{r}\left(\frac{\mathbf{r}}{r}\mathbf{p}_0\right) - \mathbf{p}_0\right] \qquad \text{if } r \gg \lambda_f. \tag{2.14}$$

$\mathbf{E}_s(\mathbf{r},t)$ is the same field scattered from the atom at $\mathbf{r}_j$ at the retarded time $\tau = t - |\mathbf{r} - \mathbf{r}_j|/c$. Let $\mathbf{r}'_j = \mathbf{r} - \mathbf{r}_j$. Far from any absorption edges of the scattering atom, $\mathbf{E}_s(\mathbf{r},t)$ may be described by the Thomson scattering amplitude,

$$\mathbf{E}_s(\mathbf{r},t) = -\frac{k_f^2}{r'_j}\left[\frac{\mathbf{r}}{r}\left(\frac{\mathbf{r}}{r}\mathbf{p}_d(\mathbf{r}_j,\tau)\right) - \mathbf{p}_d(\mathbf{r}_j,\tau)\right] \qquad \text{if } r'_j \approx r \gg \lambda_f. \tag{2.15}$$

The electric dipole moment $\mathbf{p}_d$ is induced at the position of the scattering atom $\mathbf{r}_j$ by the incident $\mathbf{E}_d(\mathbf{r}_j,\tau)$. For a point like atom with atomic form factor $f(\mathbf{r}_j,\mathbf{k}_f)$ for scattering from the direction $\mathbf{r}_j$ to $\mathbf{k}_f$, one obtains

$$\mathbf{p}_d(\mathbf{r},t) = -\frac{r_e f(\mathbf{r}_j,\mathbf{k}_f)}{k_f^2}\mathbf{E}_d(\mathbf{r},t). \tag{2.16}$$

The classical electron radius is $r_e = e^2/mc^2 = 2.818 \cdot 10^{-5}$Å. $\mathbf{p}_d$ is thus obtained from

$$\mathbf{p}_d(\mathbf{r}_j, \tau) = \frac{r_e f(\mathbf{r}_j, \mathbf{k}_f)}{r_j} e^{i(k_f r_j + k_f r'_j - \omega_f t)} \mathbf{p}_j \quad (2.17)$$

$$\mathbf{p}_j \equiv \frac{\mathbf{r}_j}{r_j}\left(\frac{\mathbf{r}_j}{r_j}\mathbf{p}_0\right) - \mathbf{p}_0 - \left(3\frac{\mathbf{r}_j}{r_j}\left(\frac{\mathbf{r}_j}{r_j}\mathbf{p}_0\right) - \mathbf{p}_0\right)\left(\frac{1}{k_f^2 r_j^2} - \frac{i}{k_f r_j}\right). \quad (2.18)$$

Now, inserting eqns. 2.14 to 2.17 into eq. 2.13 gives the electric field

$$\begin{aligned}\mathbf{E}_f(\mathbf{r}, t) = & -\frac{k_f^2}{r} e^{i(k_f r - \omega_f t)} \mathbf{p}_r \\ & -\frac{k_f^2}{r'_j} \frac{r_e f(\mathbf{r}_j, \mathbf{k}_f)}{r_j} e^{i(k_f r_j + k_f r'_j - \omega_f t)} \left[\frac{\mathbf{r}}{r}\left(\frac{\mathbf{r}}{r}\mathbf{p}_j\right) - \mathbf{p}_j\right]. \end{aligned} \quad (2.19)$$

The second term in eq. 2.19 is the scattering term corresponding to the holographic object wave. Compared with the first term which describes the reference wave, it is typically smaller than $r_e f(\mathbf{r}_j, \mathbf{k}_f)/r_j \approx 10^{-4}$. The interference intensity for XFH is given by

$$I_f(\mathbf{r}) = \langle |\mathbf{E}_f(\mathbf{r}, t)|^2 \rangle. \quad (2.20)$$

Summation over n scattering neighbors of the fluorescence atom yields

$$I_f(\mathbf{r}) = \left| -\frac{k_f^2}{r} e^{ik_f r} \mathbf{p}_r - \sum_{j=1}^{n} \frac{k_f^2}{r'_j} \frac{r_e f(\mathbf{r}_j, \mathbf{k}_f)}{r_j} e^{ik_f(r_j + r'_j)} \left[\frac{\mathbf{r}}{r}\left(\frac{\mathbf{r}}{r}\mathbf{p}_j\right) - \mathbf{p}_j\right] \right|^2. \quad (2.21)$$

For small clusters and far away from Bragg angles, multiple scattering may be neglected. Since scattering is much stronger for electrons than x rays, this assumption is more valid for x rays [Len94]. For spontaneous emission of fluorescence radiation, $\mathbf{E}_f(\mathbf{r}, t)$ has to be averaged over all directions of the polarization $\mathbf{p}_0$ (appendix A).

The vector $\mathbf{r}$ from the emitter to the detector is parallel to the wavevector $\mathbf{k}_f$ so that $\mathbf{k}_f = k_f \mathbf{r}/r$. If $\mathbf{r}'_j \approx \mathbf{r} \gg \mathbf{r}_j$, then $1/\mathbf{r}'_j \approx 1/r$ and $\exp(ik_f r'_j) \approx \exp(ik_f r - i\mathbf{k}_f \mathbf{r}_j)$. The XFH intensity is therefore given by

$$\begin{aligned} I_f(\mathbf{r}) = & \frac{2p_0^2 k_f^4}{3r^2} \left\{ 1 - r_e \mathrm{Re} \sum_{j=0}^{n} \frac{f(\mathbf{r}_j, \mathbf{k}_f)}{r_j} e^{i(k_f r_j - \mathbf{k}_f \mathbf{r}_j)} \right. \\ & \left. \times \left[1 + \frac{(\mathbf{r}\mathbf{r}_j)^2}{r^2 r_j^2} + \left(\frac{1}{k_f^2 r_j^2} - \frac{i}{k_f r_j}\right)\left(1 - \frac{3(\mathbf{r}\mathbf{r}_j)^2}{r^2 r_j^2}\right) \right] \right\} \end{aligned} \quad (2.22)$$

$$\equiv \frac{2p_0^2 k_f^4}{3r^2} \left\{ 1 - 2r_e \mathrm{Re} \sum_{j=0}^{n} \frac{f_S(\mathbf{r}_j, \mathbf{k}_f)}{r_j} e^{i(k_f r_j - \mathbf{k}_f \mathbf{r}_j)} \right\}. \quad (2.23)$$

Eq. 2.23 defines $f_S(\mathbf{r}_j, \mathbf{k}_f)$ as an effective scattering factor that includes polarization effects and near-field terms. In the far field approximation $r_j \gg \lambda_f$ and at a given observation point $\mathbf{r}$, the last term in eq. 2.22 will be maximal (= 2) for atoms at positions $\mathbf{r}_j \parallel \pm\mathbf{r}$ and minimal (= 1), if $\mathbf{r}_j \perp \mathbf{r}$.

Discussion of the Holographic Intensity

The holographic signal $\chi(\mathbf{k})$ is obtained from the interference intensity $I_f(\mathbf{k})$ of eq. 2.23 using the normalization of eq. 2.8. Under the assumptions leading to eq. 2.23 and for f_S being real, $\chi(\mathbf{k})$ is given by

$$\chi(\mathbf{k}) \quad = \quad -2r_e \sum_{j=0}^{n} \frac{f_S(\mathbf{r}_j, \mathbf{k})}{r_j} \cos(kr_j - \mathbf{k}\mathbf{r}_j) \tag{2.24}$$

where $f_S(\mathbf{r}_j, \mathbf{k}) = f(\mathbf{r}_j, \mathbf{k})[1 + (\mathbf{r}\mathbf{r}_j)^2/(rr_j)^2]$ in the far field approximation. $\chi(\mathbf{k})$ of eq. 2.24 will be analysed in this section for a simple case in order to understand its functional behavior. This way, a rough estimate can be found for the sampling rate at which $\chi(\mathbf{k})$ should be measured.

The vector $\mathbf{r}$ from the emitter to the detector is parallel to the wavevector $\mathbf{k}$ so that $\mathbf{k}/k = \mathbf{r}/r$ and $\mathbf{k}\mathbf{r}_j/(kr_j) = \mathbf{r}\mathbf{r}_j/(rr_j)$. For a single scatterer at position $\mathbf{r}_j$, for a real and constant $f = f^* = f_0$, and for $\mathbf{k}\mathbf{r}_j = kr_j \cos\alpha$, eq. 2.24 becomes

$$\chi(\mathbf{k}) \quad = \quad -\frac{2r_e f_0}{r_j} \left(1 + \cos^2\alpha\right) \cos(kr_j(1 - \cos\alpha)). \tag{2.25}$$

Neglecting polarization leads to

$$\chi(\mathbf{k}) \quad = \quad -\frac{2r_e f_0}{r_j} \cos(kr_j(1 - \cos\alpha)). \tag{2.26}$$

$\chi(\mathbf{k})$ of eq. 2.26 is a cosine function of amplitude $2r_e f_0/r_j$. This amplitude is typically on the order of 10^{-4}, for example, $2r_e f_0/r_j \approx 4 \times 10^{-4}$ if $f_0 = 26$ and $r_j = 4$ Å.

The factor $kr_j = 2\pi r_j/\lambda$ in the argument of the cosine function becomes small for small r_j/λ. The factor r_j/λ is small for small r_j or for large λ. An estimate for a small interatomic distance in a solid is given by $r_j \approx 2$ Å. In order to obtain atomic resolution, distances of this order of magnitude have to be separated. The highest possible spatial resolution is about $\lambda/2$ (section 2.6.3) so that a large wavelength is $\lambda = 4$ Å. An estimate of a small value of kr_j is therefore given by $kr_j = \pi$. For larger distances of interest and for smaller wavelengths, kr_j will have larger values, for example $kr_j = 5\pi$. The functions $\chi(\mathbf{k})r_j/(2r_e f_0)$ of eqns. 2.25, 2.26 are depicted in fig. 2.4 for $kr_j = \pi/2$ and in fig. 2.5 for $kr_j = 5\pi$.

In order to measure the full dependence of χ on $\mathbf{k}$, the full 2π range in α should be scanned. For an unknown structure, the direction of $\mathbf{r}_j$ is unknown so that as

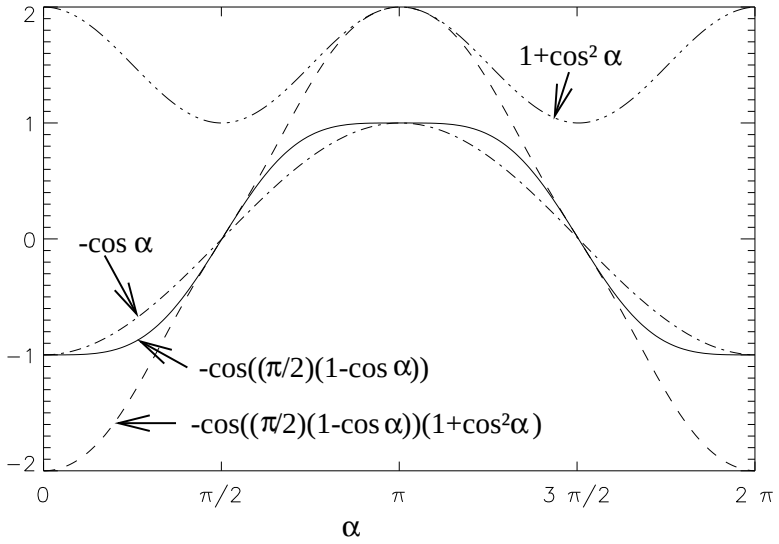

Figure 2.4: The dependence of $\chi(\mathbf{k})r_j/(2r_e f_0)$ in eqns. 2.25, 2.26 on α for $kr_j = \pi/2$. The function $-\cos((\pi/2)(1-\cos\alpha))(1+\cos^2\alpha)$ is displayed as a dashed line, $-\cos((\pi/2)(1-\cos\alpha))$ as a solid line, $-\cos\alpha$ is shown for comparison as a dash-dotted line, and the polarization factor $(1+\cos^2\alpha)$ as a dash-dot-dotted line.

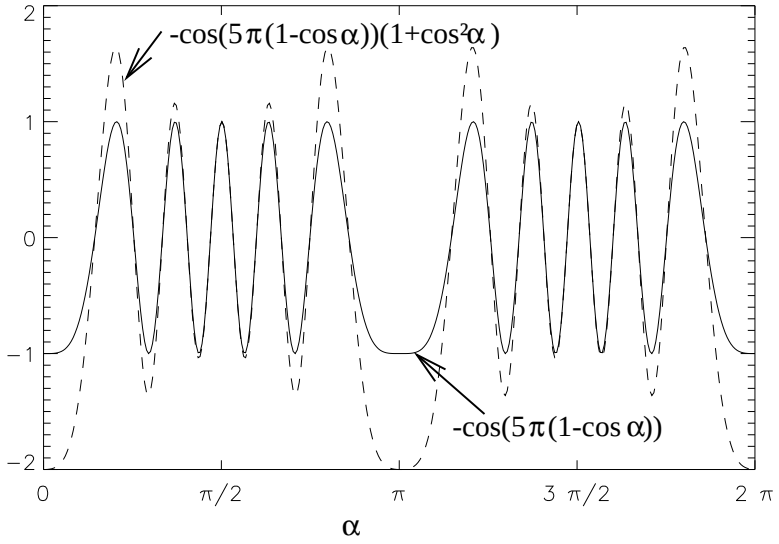

Figure 2.5: The dependence of $\chi(\mathbf{k})r_j/(2r_e f_0)$ in eqns. 2.25, 2.26 on α for $kr_j = 5\pi$. The function $-\cos(5\pi(1-\cos\alpha))(1+\cos^2\alpha)$ is displayed as a dashed line, and $-\cos(5\pi(1-\cos\alpha))$ as a solid line.

much as possible of a full 4π sphere should be measured in order to record the holographic intensity variations for all directions $\mathbf{r}_j$. According to the sampling theorem, a frequency limited signal $f(t)$ can be described completely by the signal

values at discrete points. These points must not have larger distances from each other than $1/(2f_g)$ where f_g is the highest frequency in $f(t)$.

A rough estimate of the frequencies in $\chi(\mathbf{k})$ can be made in the following way: Neglecting polarization, the functional dependence of $\chi(\mathbf{k})$ is given by $-\cos(kr_j(1-\cos\alpha))$ (eq. 2.26). The argument of this cosine function contains the term $(1-\cos\alpha)$. If α varies from 0 to π then $(1-\cos\alpha)$ increases monotonically from 0 to 2, and the more simple function $2\alpha/\pi$ also increases monotonically from 0 to 2 so that $-\cos(kr_j(1-\cos\alpha))$ can be roughly approximated by $-\cos(2kr_j\alpha/\pi)$. These two functions are shown for $kr_j = \pi/2$ in fig. 2.4. According to the sampling theorem, in this approximation at least

$$2 \times \frac{2kr_j}{\pi} = \frac{8r_j}{\lambda} \tag{2.27}$$

steps need to be measured if α changes by 2π. If $\lambda = 1$ Å and $r_j = 20$ Å, this corresponds to 160 steps in 360°. Since in fact higher frequencies contribute to $-\cos(kr_j(1-\cos\alpha))$ than to $-\cos(2kr_j\alpha/\pi)$, more steps will be necessary. According to [Tegze91], it "is evident that the high-frequency components are coming from atoms far from the source and the low frequency ones from the atoms close to the source". This seems plausible when comparing fig. 2.4 with fig. 2.5. These figures show $\chi(\mathbf{k}) \cdot r_j/(2r_e f_0)$ for $kr_j = \pi/2$ and for $kr_j = 5\pi$, respectively. If k is the same in both cases then r_j is 10 times as large in the latter case than in the former case. High-frequency components are more dominant for large kr_j but they are also present for small kr_j so that the statement in [Tegze91] does not strictly hold.

At fixed α, $\cos(kr_j(1-\cos\alpha))$ does not change if $(1-\cos\alpha) = 0$ and changes most if $(1-\cos\alpha) = 2$. If k is changed, the highest frequency is therefore obtained if $\cos(kr_j(1-\cos\alpha)) = \cos(2kr_j)$. If the incident energy changes from $E_1 = \hbar k_1 c$ to $E_2 = \hbar k_2 c$ then the argument of this cosine function changes for fixed r_j by 2π if $2(k_1 - k_2)r_j = 2\pi$. Then $\Delta E \equiv E_1 - E_2 = hc/(2r_j) \approx 12.398$ keV Å $/(2r_j)$. This condition corresponds to $\Delta E \approx 3.1$ keV for $r_j = 2$ Å and to $\Delta E \approx 310$ eV for $r_j = 20$ Å. The argument of the cosine function will change only slowly with energy for small distances. $r_j = 2$ Å is an estimate for a small distance between atoms in a solid and requires an energy range of ≈ 3.1 keV in order to change the argument of the cosine function by a full 2π period. According to the sampling theorem, the energy step size must not exceed

$$\frac{\Delta E}{2} = \frac{hc}{4r_j}. \tag{2.28}$$

In XFH, the available interference energies are the x-ray emission line energies of atoms in the structure and cannot be chosen arbitrarily. Therefore it will usually not be possible to fulfil this requirement.

2.3.2 Multiple Energy X-Ray Holography (MEXH)

In MEXH, the reference wave is given by the incident x-ray radiation. This has the following consequences.

- The angular resolution of MEXH is determined by the divergence of the incident beam. The divergence of monochromatic x rays from a synchrotron radiation source is on the order of 0.003°, making MEXH experiments at a high angular resolution possible.
- MEXH allows the energy of the reference wave to be chosen freely above an absorption edge of the detecting atom. A number of MEXH holograms can be obtained at several wavelengths to suppress in the reconstruction the misleading twin images that are inherent to the method at single energies (section 2.6).
- The object and detector are in the far field of the source while the detector is in the intermediate or far field of the object.
- In the MEXH experiments published so far [Gog96a, Gog96b, Adams98, Gog98, Hayashi98, Kawai98, Novikov98, Adams00b], the characteristic fluorescence radiation of atoms was used to detect the local field intensity inside the sample. The local field intensity can be detected also via emitted electrons. Electrons can be detected in a full hemisphere above the sample surface as done in reciprocal γ ray holography [Korecki97, Korecki99].

Formation of the Holographic Intensity

A rigorous quantum electrodynamical treatment is given in [Fonda97] for MEXH, in [Miller97] for Bremsstrahlung holography, XFH and MEXH, and in [Nishino99] for photoelectron holography, extended x-ray absorption fine structure (EXAFS), XFH and MEXH. The quantum electrodynamical results obtained for XFH and MEXH are consistent with the results from classical electrodynamics [Nishino99] and will not be treated here. The following theoretical treatment of MEXH is analogous to that of XFH in sec. 2.3.1. Consider again two atoms, a fluorescence atom at the origin $\mathbf{0}$, and another atom at position $\mathbf{r}_j$. Let the plane wave

$$\mathbf{E}_p(\mathbf{r},t) = \mathbf{E}_{0p} e^{i(\mathbf{k}_i \mathbf{r} - \omega_i t)} \tag{2.29}$$

impinge on the system, where $\mathbf{k}_i$ is the wave vector of the incident wave and $\omega_i = ck_i$. Synchrotron radiation is strongly polarized in the plane of orbit [Jackson75] so that eq. 2.29 is a good approximation for monochromatic synchrotron radiation. We want to calculate the resulting electric field

$$\mathbf{E}_i(\mathbf{0},t) = \mathbf{E}_p(\mathbf{0},t) + \mathbf{E}_d(\mathbf{0},t), \tag{2.30}$$

where $\mathbf{E}_d(\mathbf{0},t)$ is the field that originates at the position $\mathbf{r}_j$ of the scattering atom and that is caused by $\mathbf{E}_p(\mathbf{r}_j,\tau)$, where $\tau = t - r_j/c$. The scattering will again be described by eq. 2.11, but for $\mathbf{k} = \mathbf{k}_i$, $\omega = \omega_i$, $\mathbf{u} = -\mathbf{r}_j/r_j$. The electric dipole moment $\mathbf{p}$ is induced at the position of the scattering atom $\mathbf{r}_j$ by the incident $\mathbf{E}_p(\mathbf{r}_j,\tau)$,

$$\mathbf{p}(\mathbf{r}_j,\tau) = -\frac{r_e f(\mathbf{r}_j,\mathbf{k}_i)}{k_i^2}\mathbf{E}_p(\mathbf{r}_j,\tau). \tag{2.31}$$

The electric field at the origin is then given by

$$\mathbf{E}_i(\mathbf{0},t) = \mathbf{E}_{0p}e^{-i\omega_i t} + \frac{r_e f(\mathbf{r}_j,\mathbf{k}_i)}{r_j}e^{i(\mathbf{k}_i\mathbf{r}_j + k_i r_j - \omega_i t)}\mathbf{E}_j \tag{2.32}$$

$$\mathbf{E}_j \equiv F_j\frac{\mathbf{r}_j}{r_j}\left(\frac{\mathbf{r}_j}{r_j}\mathbf{E}_{0p}\right) - G_j\mathbf{E}_{0p}. \tag{2.33}$$

The intensity at the origin is the interference intensity for MEXH,

$$I_i(\mathbf{0}) = \langle|\mathbf{E}_i(\mathbf{0},t)|^2\rangle. \tag{2.34}$$

Summation over different scattering atoms and neglecting multiple scattering yields

$$I_i(\mathbf{0}) = \left|\mathbf{E}_{0p} + r_e\sum_{j=0}^{n}\frac{f(\mathbf{r}_j,\mathbf{k}_i)}{r_j}e^{i(k_i r_j + \mathbf{k}_i\mathbf{r}_j)}\mathbf{E}_j\right|^2 \tag{2.35}$$

$$= E_{0p}^2\left\{1 - 2r_e\mathrm{Re}\sum_{j=0}^{n}\frac{f(\mathbf{r}_j,\mathbf{k}_i)}{r_j}e^{i(k_i r_j + \mathbf{k}_i\mathbf{r}_j)}\left[G_j - F_j\frac{(\mathbf{r}_j\mathbf{E}_{0p})^2}{r_j^2E_{0p}^2}\right]\right\} \tag{2.36}$$

$$= E_{0p}^2\left\{1 - 2r_e\mathrm{Re}\sum_{j=0}^{n}\frac{f(\mathbf{r}_j,\mathbf{k}_i)}{r_j}e^{i(k_i r_j + \mathbf{k}_i\mathbf{r}_j)}\right.$$
$$\left.\times\left[1 - \frac{(\mathbf{r}_j\mathbf{E}_{0p})^2}{r_j^2E_{0p}^2} - \left(\frac{1}{k_i^2r_j^2} - \frac{i}{k_i r_j}\right)\left(1 - \frac{3(\mathbf{r}_j\mathbf{E}_{0p})^2}{r_j^2E_{0p}^2}\right)\right]\right\} \tag{2.37}$$

$$\equiv E_{0p}^2\left\{1 - 2r_e\mathrm{Re}\sum_{j=0}^{n}\frac{f_S(\mathbf{r}_j,\mathbf{k}_i)}{r_j}e^{i(k_i r_j + \mathbf{k}_i\mathbf{r}_j)}\right\}, \tag{2.38}$$

where eq. 2.38 defines $f_S(\mathbf{r}_j,\mathbf{k}_i)$ as an effective scattering factor that includes polarization and near-field effects. [5] If $r_j \gg \lambda_i$, then $F_j \approx 1$, $G_j \approx 1$. Then the interference pattern has a maximum if $\mathbf{r}_j \perp \mathbf{E}_{0p}$ and vanishes if $\mathbf{r}_j||\mathbf{E}_{0p}$. These polarization effects occur in MEXH if synchrotron radiation is used. Polarization effects in MEXH were investigated by P. M. Len et al [Len97b].

The near field terms become especially important if the far field term vanishes for $\mathbf{r}_j||\mathbf{E}_{0p}$. In this case, the last term in eq. 2.37 becomes $2/k_i^2r_j^2 - 2i/k_i r_j$. For a typical incident energy of 9 keV, $k_i = 4.56/\text{Å}$ and for the nearest-neighbor distance $r_j = 2.49$ Å in bcc Fe, $1/k_i r_j = 8.8\%$, and the last term becomes $2\% - i18\%$ so that near field effects are not always negligible.

[5] The same was obtained except for a typing error in the phase of the exponential in [Adams98].

Discussion of the Holographic Intensity

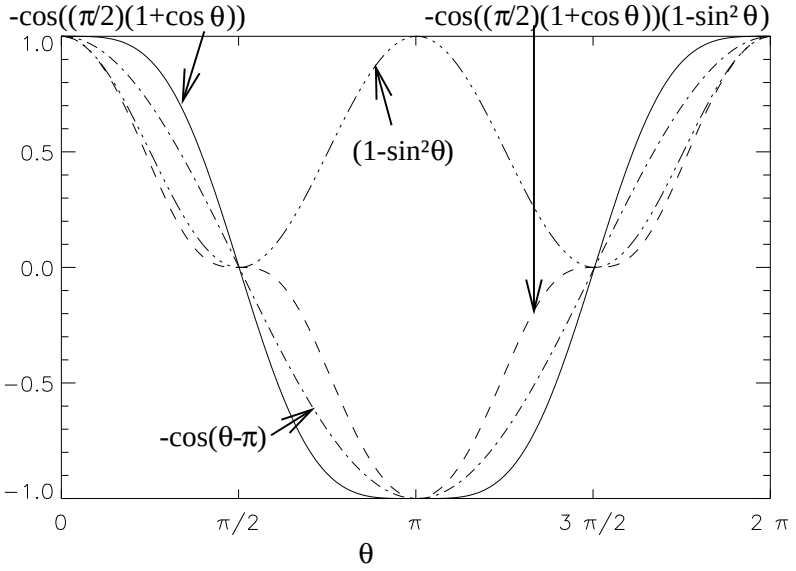

Figure 2.6: The dependence of $\chi(\mathbf{k})r_j/(2r_e f_0)$ in eqns. 2.40, 2.41 on θ for $kr_j = \pi/2$. $-\cos((\pi/2)(1+\cos\theta))(1-\sin^2\theta\cos^2\varphi)$ is shown for the polarized case ($\cos^2\varphi = 1$) as a dashed line. $-\cos((\pi/2)(1+\cos\theta))$ does not contain polarization effects and is shown as a solid line. The function $-\cos(\theta-\pi)$ is shown for comparison as a dash-dotted line, and the polarization dependence $(1-\sin^2\theta)$ is shown as a dash-dot-dotted line.

The holographic signal $\chi(\mathbf{k})$ is obtained from the interference intensity $I(\mathbf{k})$ of eq. 2.38 using the normalization of eq. 2.8. Under the assumptions leading to eq. 2.38, $\chi(\mathbf{k})$ is given by

$$\chi(\mathbf{k}) \;=\; -2r_e \mathrm{Re} \sum_{j=0}^{n} \frac{f_S(\mathbf{r}_j, \mathbf{k}_i)}{r_j} e^{i(k_i r_j + \mathbf{k}_i \mathbf{r}_j)}, \tag{2.39}$$

where $f_S(\mathbf{r}_j, \mathbf{k}) = f(\mathbf{r}_j, \mathbf{k})[1 - (\mathbf{r}_j \mathbf{E}_{0p})^2/(r_j E_{0p})^2]$ in the far field approximation. For a single scatterer at position $\mathbf{r}_j$ and for $\mathbf{k}\mathbf{r}_j = kr_j\cos\theta$, the term $\mathbf{r}_j\mathbf{E}_{0p}$ can be calculated since the electric field vector $\mathbf{E}_{0p}$ and the wavevector $\mathbf{k}$ of the incident plane wave are perpendicular to each other. If $\mathbf{r}_j$, $\mathbf{E}_{0p}$ and $\mathbf{k}$ lie in one plane then $\mathbf{r}_j\mathbf{E}_{0p} = r_j E_{0p}\sin\theta$. If $\mathbf{E}_{0p}$ is perpendicular to the plane containing $\mathbf{r}_j$ and $\mathbf{k}$ then $\mathbf{r}_j\mathbf{E}_{0p} = 0$. This leads to $\mathbf{r}_j\mathbf{E}_{0p} = r_j E_{0p}(\sin\theta)(\cos\varphi)$ in the general case. $E_{0p}\cos(\varphi)$ is the projection of $\mathbf{E}_{0p}$ on the plane containing $\mathbf{r}_j$ and $\mathbf{k}$. Under these assumptions and for a real and constant $f = f^* = f_0$, eq. 2.24 becomes

$$\chi(\mathbf{k}) \;=\; -\frac{2r_e f_0}{r_j}\left(1 - \sin^2\theta\cos^2\varphi\right)\cos(kr_j(1+\cos\theta)). \tag{2.40}$$

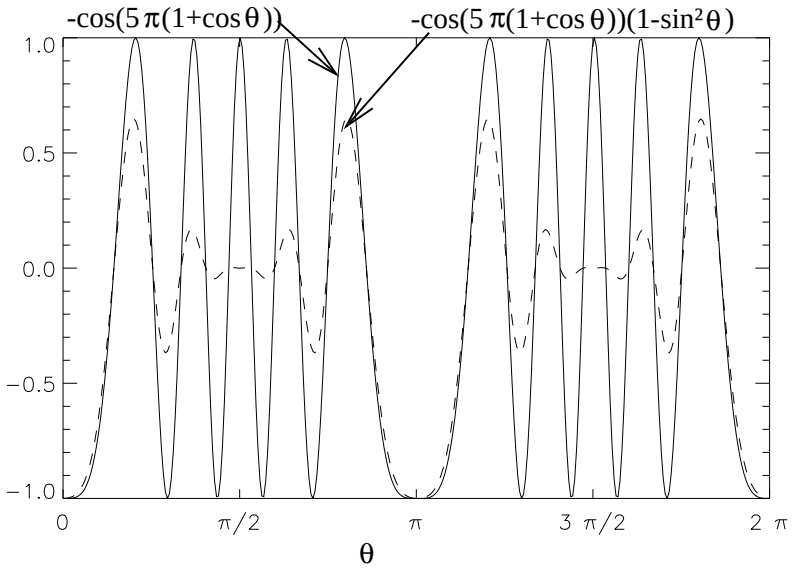

Figure 2.7: The dependence of $\chi(\mathbf{k})r_j/(2r_e f_0)$ in eqns. 2.40, 2.41 on θ for $kr_j = 5\pi$. $-\cos(5\pi(1+\cos\theta))(1-\sin^2\theta\cos^2\varphi)$ is shown for the polarized case ($\cos^2\varphi = 1$) as a dashed line. $-\cos(5\pi(1+\cos\theta))$ does not contain polarization effects and is shown as a solid line.

Neglecting polarization leads to

$$\chi(\mathbf{k}) \;=\; -\frac{2r_e f_0}{r_j}\cos(kr_j(1+\cos\theta)). \tag{2.41}$$

The function $\chi(\mathbf{k})r_j/(2r_e f_0)$ of eq. 2.40 is depicted in fig. 2.6 for $kr_j = \pi/2$ and in fig. 2.7 for $kr_j = 5\pi$ for the two extreme cases $\cos^2\varphi = 0$ and $\cos^2\varphi = 1$. The function $\cos(kr_j(1+\cos\theta))$ can roughly be approximated by $\cos(2-2kr_j\theta/\pi)$. Both functions are shown in fig. 2.6 for $kr_j = \pi/2$. In this case, the same requirements for the angular and energy ranges and step sizes are obtained as for XFH (section 2.3.1). It should be noted, however, that the interference energy in MEXH can be chosen freely above an electron binding energy of an atom incorporated in the structure so that sufficiently small energy steps can be realized in MEXH.

2.3.3 Comparison of XFH and MEXH

A theoretical comparison of XFH and MEXH is given in [Len97a]. The positions of detector and source in XFH are interchanged in MEXH. Time reversal causes also opposite signs of $\mathbf{k}$ in the exponentials of eq. 2.23 and eq. 2.38. XFH and MEXH have fundamental differences. The most important ones are summarized in the following:

- XFH does not require the fluorescence to be excited by x rays while MEXH does not require that the local field inside the sample is registered through

the fluorescence yield. Therefore the experiments may use different kinds of incident radiation and different detection systems. XFH uses and MEXH can use the characteristic fluorescence radiation of atoms. Both methods are element specific. MEXH can also use photoelectrons or Auger electrons.

- Wavelength range and step size can be chosen in MEXH but in XFH only the wavelengths corresponding to the x-ray emission lines of atoms in the investigated structure can be used.

- If the same fluorescence line is detected in XFH and MEXH then XFH is performed at a larger interference wavelength than MEXH since fluorescence is an inelastic process. In this case a direct comparison of experimental results is not possible.

- The polarization effects in XFH and MEXH are different due to the polarization averaging in XFH. In the far field approximation $r_j \gg \lambda$, the holographic interference term in XFH does not become zero, but may vanish in MEXH.

- The validity of the far field approximation in eq. 2.11 depends upon the wavelength used. For a given structure, the approximation becomes more valid for decreasing λ. If the same fluorescence line is detected in XFH and MEXH then the validity of the approximation will differ in XFH and MEXH since the interference wavelengths will be different.

- The far field terms in XFH and MEXH are different. The far field terms in MEXH may be more important than in XFH, since in MEXH the near field terms may cancel each other due to polarization effects.

- The resolutions in angle and wavelength will usually differ for XFH and MEXH experiments.

In the following, the terminology for the atomic resolution x-ray holographies is used in the same way as in the first experimental papers [Tegze96], [Gog96a]. Inside source or direct x-ray holography is called XFH. Inside detector or reciprocal x-ray holography is called MEXH. Note however that it is possible to measure in XFH at multiple energies if different characteristic lines are available and that MEXH can be performed at one fixed energy.

2.3.4 XFH and MEXH as Two Aspects of the Same Process

In atomic resolution holography, atoms of a structure are excited by incident radiation and emit radiation which is detected in the far field. If the incident *and* emitted radiations have such coherence properties that elastic scattering of each of them from atoms produces an interference pattern then both patterns have to be taken into account. For simplicity, it will be assumed in this section that a plane wave of monochromatic x rays is incident on a structure and that the outgoing fluorescence radiation is monitored. This was the case for most x-ray fluorescence holography experiments [Adams98, Adams99, Gog96a, Gog96b, Gog98, Hayashi98, Hiort00, Kawai98, Novikov98, Tegze96, Tegze99]. In this case, the equations of

sections 2.3.1, 2.3.2 apply and MEXH and XFH can be treated as two aspects of the same process. This is schematically shown in fig. 2.3.

Consider an x-ray fluorescence holography experiment at a fixed incidence energy and direction as well as fixed sample and detector positions. The electric field at the position of the fluorescence atom is the interference field of the incident reference wave and the waves scattered from neighboring atoms. It can be expressed in a very general way as $|\mathbf{R}_i + \mathbf{O}_i|^2 = |R_i|^2 \cdot |1 + \mathbf{O}_i/|R_i||^2$, where $\mathbf{R}_i$ and $\mathbf{O}_i$ are reference and object wave of the incoming radiation (compare eq. 2.1). The resulting fluorescence intensity is proportional to the local interference intensity of this field. The fluorescence wave is in turn scattered from neighboring atoms and reaches the detector in the far field directly and after scattering, thus producing the fluorescence interference pattern $|\mathbf{R}_f + \mathbf{O}_f|^2 = |R_f|^2 \cdot |1 + \mathbf{O}_f/|R_f||^2$, where $\mathbf{R}_f$ and $\mathbf{O}_f$ are reference and object wave of the fluorescence radiation. The measured intensity is then obtained from the product of the intensities

$$I = I_0 \left| 1 + \frac{\mathbf{O}_i}{|R_i|} \right|^2 \left| 1 + \frac{\mathbf{O}_f}{|R_f|} \right|^2 , \tag{2.42}$$

where any proportionality constants are included in I_0. $\mathbf{O}_i/|R_i|$ and $\mathbf{O}_f/|R_f|$ contain single and multiple scattering terms. If the sample is rotated relative to a stationary detector and relative to an incident beam of fixed direction and energy, then the detector will measure a product of a MEXH scan taken at the energy of the incident beam and an XFH scan taken at the fluorescence energy. If only single scattering needs to be considered, then the product can be approximated by a sum, and only the single scattering contributions $\mathbf{O}_i'$ and $\mathbf{O}_f'$ occur, so that

$$I = I_0 \left\{ 1 + 2\mathrm{Re} \left[\frac{\mathbf{O}_i'}{|R_i|} + \frac{\mathbf{O}_f'}{|R_f|} \right] \right\} . \tag{2.43}$$

Using eqns. 2.10 and 2.34, eq. 2.42 can be expressed as

$$I(\mathbf{k}, \mathbf{r}) = \sigma_p w_f \langle |\mathbf{E}_i(\mathbf{0}, \mathbf{t})|^2 \rangle \cdot \langle |\mathbf{E}_f(\mathbf{r}, \mathbf{t})|^2 \rangle \tag{2.44}$$

For single scattering from point scatterers, one obtains from eqns. 2.23, 2.38

$$\begin{aligned} I(\mathbf{k}, \mathbf{r}) &= I_0 \left\{ 1 - 2r_e \mathrm{Re} \sum_{j=0}^{n} \frac{f_S(\mathbf{r}_j, \mathbf{k}_i)}{r_j} e^{i(k_i r_j + \mathbf{k}_i \mathbf{r}_j)} \right\} \\ &\quad \times \left\{ 1 - 2r_e \mathrm{Re} \sum_{m=0}^{n} \frac{f_S(\mathbf{r}_m, \mathbf{k}_f)}{r_m} e^{i(k_f r_m - \mathbf{k}_f \mathbf{r}_m)} \right\} \qquad (2.45) \\ &\approx I_0 \left\{ 1 - 2r_e \mathrm{Re} \sum_{j=0}^{n} \frac{1}{r_j} \left[f_S(\mathbf{r}_j, \mathbf{k}_i) e^{i(k_i r_j + \mathbf{k}_i \mathbf{r}_j)} \right. \right. \\ &\qquad \left. \left. + f_S(\mathbf{r}_j, \mathbf{k}_f) e^{i(k_f r_j - \mathbf{k}_f \mathbf{r}_j)} \right] \right\} , \qquad (2.46) \end{aligned}$$

where near field and polarization effects are taken into account in the effective scattering factors $f_S(\mathbf{r}_j, \mathbf{k}_{i,f})$. The intensity of eq. 2.45 can be directly interpreted as a holographic intensity if one of its interference terms is constant. Otherwise, one of the terms must be removed from the intensity in order to obtain the other term as the holographic interference intensity (section 2.4.2).

2.4 Inherent Background

It follows from sections 2.3.1, 2.3.2 that the holographic signal is measured together with the reference wave which can be considered as a background inherent to the method. Effects due to the reference wave will be treated in section 2.4.1. Additionally, a mixing of XFH and MEXH can occur in holograms as was shown in section 2.3.4. Ways to separate the two holographic signals in mixed holograms are discussed in section 2.4.2.

2.4.1 Reference Wave and Absorption Effects

An intensity $I(\mathbf{k}) = |R(\mathbf{k}) + O(\mathbf{k})|^2$ (eq. 2.1) is measured in a holography experiment. $I(\mathbf{k})$ contains contributions from the reference wave $R(\mathbf{k})$ and from the object wave $O(\mathbf{k})$ so that the intensity $|R(\mathbf{k})|^2$ of the reference wave alone cannot be accessed directly. The reference wave $|R(\mathbf{k})|^2$ can be considered as a background to the holographic signal. It is removed from the observed intensity $I(\mathbf{k})$ according to eq. 2.8 in order to obtain the normalized holographic signal. A fit to the experimental data that takes only a constant background and angular dependent absorption in the crystal into account can be used to determine $|R(\mathbf{k})|^2$ [Tegze96, Adams98, Novikov98, Faigel99].

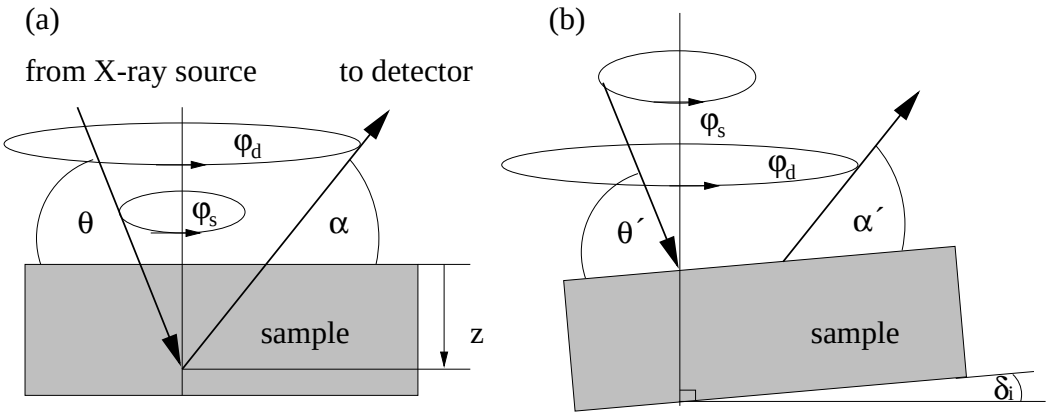

Figure 2.8: Geometry relevant for absorption in the case of a flat sample surface. (a) Depth z, incidence angle θ, detection angle α, rotation φ_s of the sample around its surface normal (relative to the incident beam), rotation φ_d of the detector around the sample surface normal (relative to the sample). (b) Possible misorientations of sample, beam, or detector. For details, see text.

For a large sample with a flat surface, the measured fluorescence intensity can be determined as a function of the incidence angle θ and the angle α between sample surface plane and detector entrance window. The angles are defined in fig. 2.8 (a). Consider the case where the sample is excited to fluorescence radiation by monochromatic x rays and the fluorescence radiation is monitored. The x-ray intensity $I(z)$ that reaches a depth z in a sample of constant density is given by

$$I(z) = I(0) \exp\left(-\frac{\mu_i}{\sin\theta} z\right) \tag{2.47}$$

where $I(0)$ is the incident x-ray intensity at position $z = 0$, and μ_i is the linear absorption coefficient at the energy of the incident x rays. At depth z, $dI(z)/dz$ is removed from the intensity by absorption. A fraction $\sigma_p \cdot w_f$ of $-dI(z)/dz$ is converted to fluorescence radiation (section 2.3.1, following eq. 2.10).

The fluorescence radiation created at a depth z is attenuated when leaving the sample by the factor $\exp(-\mu_f z/\sin\alpha)$, where μ_f is the linear absorption coefficient at the energy of the fluorescence radiation. The total fluorescence radiation leaving a sample of thickness d is obtained from

$$I_f = 4\pi I(0)\sigma_p w_f \frac{\mu_i}{\sin\theta} \int_0^d \exp\left(-\left(\frac{\mu_i}{\sin\theta} + \frac{\mu_f}{\sin\alpha}\right) z\right) dz \tag{2.48}$$

$$= -4\pi I(0)\sigma_p w_f \left(1 + \frac{\mu_f}{\mu_i}\frac{\sin\theta}{\sin\alpha}\right)^{-1} \left[\exp\left(-\left(\frac{\mu_i}{\sin\theta} + \frac{\mu_f}{\sin\alpha}\right) d\right) - 1\right] \tag{2.49}$$

For our case of a thick sample $d \to \infty$ so that

$$I_f = 4\pi I(0)\sigma_p w_f \left(1 + \frac{\mu_f}{\mu_i}\frac{\sin\theta}{\sin\alpha}\right)^{-1}. \tag{2.50}$$

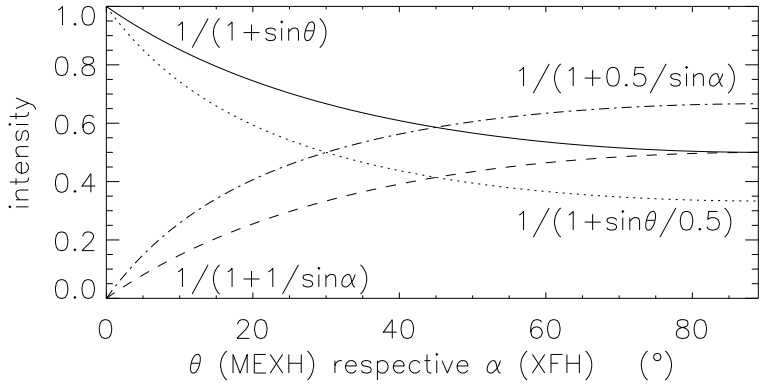

Figure 2.9: $I_f(\theta)$ in MEXH for two values of $\mu_f/(\mu_i \sin\alpha)$, and $I_f(\alpha)$ in XFH for two values of $\mu_f \sin\theta/\mu_i$ according to eq. 2.50 for $4\pi I(0)\sigma_p w_f = 1$.

The dependence of I_f on θ and α is depicted in fig. 2.9. For a detector with acceptance solid angle Ω, detector area d_a, distance from the beamspot on the sample

surface r, detection efficiency d_f for fluorescence radiation and deadtime correction factor d_d, the detected intensity is

$$I_d = \Omega d_f d_d I_f = \frac{d_a d_f d_d I_f}{4\pi r^2}. \tag{2.51}$$

If the sample surface normal is not parallel to the φ rotation axis, then θ and α have to be corrected when φ_s and φ_d are changed, see fig. 2.8 (b). Even if the sample surface normal is parallel to the φ_s rotation axis, a correction may be necessary if the radiation is detected in a limited solid angle. Then the detection angle α' will depend upon φ_d if the incident beam does not hit exactly the diffractometer rotation axis or if the detector entrance window does not exactly point at the beam spot on the sample surface. This way, the maximum misorientation angles on the incident and exit sides can be different. Let the maximum misorientation angles δ_i on the incident and δ_f on the exit side occur at angles $\varphi_s = p_i$ and $\varphi_d = p_f$, respectively. Let δ_d, the maximum change in r, occur at p_d. Then θ and α in eq. 2.50 and r in eq. 2.51 have to be replaced by

$$\begin{aligned}
\theta' &= \theta - \arctan\left((\tan\delta_i)\cos\left(\varphi_s - p_i\right)\right) && (2.52)\\
\alpha' &= \alpha - \arctan\left((\tan\delta_f)\cos\left(\varphi_d - p_f\right)\right) && (2.53)\\
r' &= r - \arctan\left((\tan\delta_d)\cos\left(\varphi_d - p_d\right)\right) && (2.54)
\end{aligned}$$

In the treatment of the experimental data, the minimum necessary number of fit parameters should be used. A numerical fit will converge more reliably if a more simple function is used for fitting. The following simplifications are possible. Since $\tan\delta_{i,f} \ll 1$ for slight misorientations and $\arctan x \approx x$ for $x \ll 1$

$$\begin{aligned}
\theta' &\approx \theta - (e_i\cos\varphi_s + f_i\sin\varphi_s) && (2.55)\\
\alpha' &\approx \alpha - (e_f\cos\varphi_d + f_f\sin\varphi_d) && (2.56)\\
r' &\approx r - (e_d\cos\varphi_d + f_d\sin\varphi_d), && (2.57)
\end{aligned}$$

where $e_{i,f,d} = (\sin\delta_{i,f,d})\cos p_{i,f,d}$ and $f_{i,f,d} = (\sin\delta_{i,f,d})\sin p_{i,f,d}$. For small $e_{i,f}$ and $f_{i,f}$,

$$\begin{aligned}
\sin\theta' &\approx \sin\theta - \cos\theta(e_i\cos\varphi_s + f_i\sin\varphi_s) && (2.58)\\
\sin\alpha' &\approx \sin\alpha - \cos\alpha(e_f\cos\varphi_d + f_f\sin\varphi_d). && (2.59)
\end{aligned}$$

In an experiment, the incident beam has a finite size and often an ellipsoidal or rectangular footprint on the sample. To avoid complications in the removal of the reference wave, a small circular beam footprint on the sample is desirable. If the beam footprint on the sample becomes larger than the sample, then only a fraction of it contributes to $I(0)$. In our data evaluation, it was not necessary to take these effects into account.

In order to remove the background from the experimental data, a multi-parameter fit $I_f(A_0, A_1, ..., A_n)$ to the data is performed.

$$I_f = \frac{A_0}{r'^2}\left(1 + A_1\frac{\sin\theta'}{\sin\alpha'}\right)^{-1}. \tag{2.60}$$

Up to nine additional fit parameters may enter the equation if θ, α, r, $e_{i,f,d}$ and $f_{i,f,d}$ are not known with sufficient accuracy to determine them directly from the experiment. A matrix inversion algorithm and a simplex algorithm were used for fitting. The results depend only weakly upon the algorithm, the exact fit function or the initial fit parameters. The number of free fit parameters depends upon the holography method used. In a mixed scheme, variations of θ' with φ_s and of α' with φ_d may have to be taken into account.

For a MEXH experiment, α is constant and also α' if the incident x-ray beam hits exactly the rotation axis and if the detector points at the beam footprint on the sample surface. This allows additional simplifications in the fitting functions. For a single MEXH scan along φ_s, θ is constant so that

$$I_f^{MEXH}(\varphi_s)|_{\theta,\alpha',r'=const} = A_0\,(1 - A_1\cos\varphi_s - A_2\sin\varphi_s)^{-1}. \tag{2.61}$$

Using different parameters, this can be approximated by the Fourier expansion

$$I_f^{MEXH}(\varphi_s)|_{\theta,\alpha',r'=const} \approx A_0 + A_1\cos\varphi_s + A_2\sin\varphi_s. \tag{2.62}$$

Eq. 2.62 takes one kind of misalignment into account. This can be a misalignment of the sample or a beam that does not exactly hit the φ_s rotation axis.

For an XFH experiment, θ is constant and for a stable incident beam also θ'. For a single XFH scan along φ_d, α is constant. If r' is not constant then

$$\begin{aligned} I_f^{XFH}(\varphi_d)|_{\theta',\alpha,r=const} &= \frac{A_0}{(1 - A_4\cos\varphi_d - A_5\sin\varphi_d)^2} \\ &\quad\cdot\left(1 + \frac{A_1}{1 - A_2\sin\varphi_d - A_3\cos\varphi_d}\right)^{-1}. \end{aligned} \tag{2.63}$$

This fitting function is not linear in its parameters A_i so that a fit using a matrix inversion algorithm may not converge. For a reliable convergence of the fit with one parameter less, the Fourier expansion

$$I_f^{XFH}(\varphi_d)|_{\theta',\alpha,r=const} \approx A_0 + A_1\sin\varphi_d + A_2\cos\varphi_d + A_3\cos(2\varphi_d) + A_4\sin(2\varphi_d) \tag{2.64}$$

can be used instead of eq. 2.63.

2.4.2 Mixed MEXH, Mixed XFH

In an experiment, care has to be taken that the interference due to either the incident or outgoing radiation is measured. Otherwise, a mixture of direct and reciprocal holograms is obtained (section 2.3.4). These have to be separated in the data evaluation in order to allow a holographic data interpretation. A separation may not be possible in the case of an unknown structure where no knowledge is present a priori. These aspects will be explained in more detail below.

Mixed MEXH

In the experiments described in [Adams98, Adams99, Gog96a, Gog96b, Gog98, Hayashi98, Kawai98, Novikov98, Tegze99] the sample was moved relative to the incident beam in incidence angle θ and azimuthal angle around the surface normal φ_s in order to record a direct or a reciprocal hologram. The schematic geometry is shown in fig. 2.8 (a). A detector of limited acceptance angle was rotated together with the sample in θ, leaving the detection angle α for fluorescence radiation constant, but when the sample moved in φ_s, the detector moved in azimuthal angle φ_d with respect to the sample. This way, "mixed" MEXH holograms were recorded in which each MEXH scan is multiplied by the same XFH scan (section 2.3.4). The XFH scan can easily be visualized by summing the mixed hologram over θ, thus forming an average mixed (φ_s , φ_d) scan (section 5.3.3, fig. 5.4). The XFH scan in a mixed MEXH hologram is itself a holographic scan that contains information on the sample structure (section 2.3.4). The specific shape of the XFH scan corresponds to the symmetry of the structure, and also upon the detector acceptance angle. This scan has a systematic effect on the hologram and must be removed before a mixed MEXH hologram can be interpreted as a MEXH hologram. The shape of the XFH scan can be very complicated so that a complete removal of the XFH scan is - especially in the case of unknown structures - unlikely and systematic artefacts may remain in the holograms.

In order to remove the XFH scan from a mixed MEXH hologram, different attempts can be made. One idea is to "measure very precisely" the unwanted scan and subtract it from the mixed holograms after removal of reference wave and absorption effects [Faigel99, Tegze99]. In a mixed MEXH hologram at $\theta = 90°$ the MEXH scan is constant. Therefore any variation in the mixed MEXH hologram at $\theta = 90°$ can be attributed to the XFH scan. The mixed MEXH scan at $\theta = 90°$ can be measured and then subtracted from the mixed MEXH hologram. It is simpler to remove an XFH scan of low angular resolution. In [Kossel98, Adams99] the shape of the XFH scan in mixed MEXH holograms was determined from the average mixed (φ_s, φ_d) scan in which the MEXH signal partly cancels out but in which the XFH signal is enhanced. The XFH scan was in one case approximated by a sine function of period 4 in 360° in (φ_s, φ_d). It was approximated in another case by the sum of two sine functions of periods 4 and 8. The so-determined XFH scan was then subtracted from the mixed hologram (section 5.3). Mixed MEXH holograms were measured for 10 values of φ_d in [Novikov98]. This way, 10 different mixed MEXH holograms were measured. The MEXH contribution was the same in these 10 holograms but the XFH scans were shifted along φ_d. In the sum over the 10 mixed MEXH holograms, the MEXH hologram is therefore enhanced but the XFH scans partly cancel each other (section 5.3).

Removing the XFH scan from mixed MEXH holograms increases the statistical experimental error in the resulting MEXH holograms and is also from this point of view not the best solution. A separate measurement of the unwanted scan takes time that could be used in a pure experiment to increase directly the number of counts in the hologram. In [Faigel99, Tegze99] and in [Kossel98, Adams99] the XFH

scan was *subtracted* from mixed holograms. This procedure is not valid if multiple scattering has to be taken into account (eq. 2.42).

Pure MEXH

In a "pure" MEXH experiment the data evaluation is straightforward and all the counts contribute directly to the MEXH hologram. The first γ-ray holography experiment [Korecki97, Korecki99] was performed in a pure reciprocal setup where a 4π electron detector was moved together with the sample. Pure MEXH experiments are described in this text (chapters 4, 5, 6) and in [Adams00b]. Pure MEXH requires that the interference intensity caused by the fluorescence radiation is kept constant in the detected signal. In MEXH, the sample is rotated relative to the incident beam. A 4π detector with isotropic efficiency can be kept stationary or rotated together with the sample to fulfil this requirement. A detector of limited acceptance angle or anisotropic efficiency must be moved together with the sample. Another approach was used in [Adams00b]. The detector is placed above the sample in the φ_s rotation axis so that it is sufficient for a pure MEXH experiment to move the detector together with the sample in θ, keeping $\alpha = 90°$ constant. The XFH signal is constant for $\alpha = 90°$ so that the detector may in this case rotate relative to the sample in φ_d. This way, it is possible to obtain a pure MEXH hologram with the same experimental setup that is normally used for mixed MEXH, by installing the detector directly above the φ_s axis.

Mixed XFH

In the experiments described in [Tegze96, Tegze99] the sample is fixed with respect to the incident beam in θ but varies in φ_s in order to record a direct hologram. A detector is rotated relative to the sample in α and φ_d. This way, "mixed" XFH holograms are recorded in which each XFH scan is multiplied by the same MEXH scan. Removing a MEXH scan from mixed XFH holograms may be especially difficult since MEXH scans are recorded at the angular resolution of the incident beam which is high for synchrotron radiation sources. This may lead to a complicated shape of the MEXH scan. If a mixed setup has to be used then the incidence angle should be $\theta = 90°$ so that the MEXH scan that multiplies the XFH hologram in mixed XFH is constant, and the angular resolution of the incident beam should be reduced.

Pure XFH

"Pure" XFH requires that the interference intensity caused by the incident beam is kept constant. This can be achieved with a sample that is fixed with respect to the incident beam and a detector that is rotated around it. Pure XFH experiments can be performed in a large angular range (chapter 5) which is important for a high spatial resolution (section 2.6).

For future hologram measurements of unknown structures, recording pure holograms is strongly advisable. Then the systematic and statistical errors of mixed experiments are avoided and the data analysis becomes straightforward (chapter 5).

2.5 Structural Aspects

The goal of atomic resolution x-ray holography is to provide information on the local environment of an atom incorporated in a structure. The influences of short- and long-range order of a structure on the resulting holograms are treated in the following. For simplicity, fluorescence detection is assumed which is necessary in XFH whereas in MEXH electrons can be detected instead.

2.5.1 Short-Range Order and Long-Range Rotational Order

In atomic resolution holography, the incoherent superposition of the holograms obtained from each fluorescing atom of a structure is measured. In order to obtain the neighborhood of just one fluorescence atom, an ideal structure would therefore contain only one fluorescing atom and a few non-fluorescing atoms as depicted schematically in fig. 2.10 (a). The holographic reconstructed image would be equivalent to this in the ideal case where twin-image effects (section 2.6) are completely suppressed. A real structure that consists of only few atoms may contain multiple fluorescing atoms. Fig. 2.10 (b) shows an example in which two fluorescing atoms have different environments. The corresponding reconstructed image is the sum over the neighborhoods of both fluorescing atoms. It is shown in part (c). It does not resemble the structure so that the interpretation of reconstructions in such cases is ambiguous. In order to avoid such effects, a simple structure should be used for an evaluation of the methods. All fluorescing atoms should have the same local environment in such a test structure.

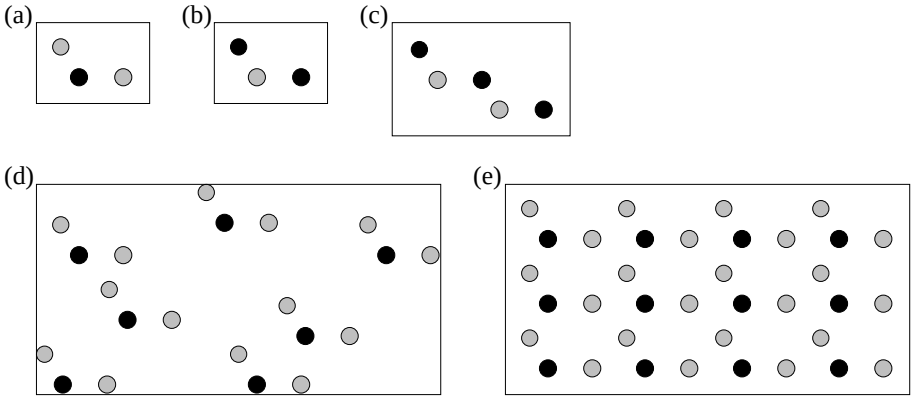

Figure 2.10: Schematic illustration of different types of structures. (a) Structure containing one fluorescing atom (black circle) and two non-fluorescing atoms (grey circles). This is the same as the ideal holographic image of the structure. (b) Structure containing two fluorescing atoms with different neighborhoods and one non-fluorescing atom. (c) Holographic image of structure (b). (d) Structure with long-range rotational but without long-range translational order, consisting of many substructures (a). (e) Structure with long-range rotational and long-range translational order, consisting of many substructures (a).

The fluorescence yield of a structure that contains few fluorescing atoms is very weak so that it is currently not possible to perform x-ray fluorescence holography on such structures. Instead, large structures that contain many fluorescing atoms have to be used. Fig. 2.10 (d) shows a case where all local environments have the same short-range order and the same long-range rotational order while no long-range translational order is present. The reconstructed image will show the local environment of part (a) so that this case is ideal for holography in yielding unambiguous information on the local environment of the average fluorescing atom. The condition of rotational order is fulfilled for example by crystals. Crystals additionally provide long-range translational order as depicted in fig. 2.10 (e). Crystals will be treated in section 2.5.2.

If the local environments are oriented within an angle δ, then the incoherent superposition of the holograms originating in different atoms produces a single hologram that resolves the local environment within distances r that are much smaller than λ/δ [Szoeke86]. For the typical values $\lambda = 1$ Å, $\delta = 1°$, this condition is $r \ll 57$ Å. An additional condition is that the crystal size L has to be smaller than $R\lambda/r_j$ [Szoeke86, Tegze91]. R is the distance from the emitter to the detector in the far field, and r_j is a typical distance from the emitter to a scattering atom. [6] For the typical values $R = 10$ cm, $\lambda = 1$ Å, and $r = 10$ Å the condition is $L < 1$ cm which is easily fulfilled.

2.5.2 Long-Range Translational Order

If monochromatic x rays of wavelength λ are incident on a crystal at an incidence angle θ, sharp peaks in the intensity occur if the x rays reflected from successive lattice planes with an angle of reflection θ interfere constructively. The geometry is shown schematically in fig. 2.11 (a). This is expressed by the Bragg condition

$$n\lambda = 2d \sin\theta_B. \tag{2.65}$$

$\theta = \theta_B$ is the so-called Bragg angle, n is an integer representing the order of reflection, and d is the distance between lattice planes. Eq. 2.65 does not depend upon the azimuthal angle φ around the lattice planes so that the Bragg condition is fulfilled for incidence directions on a cone $(\theta_B, \varphi = 0...2\pi)$.

For a point source inside the sample, e.g. fluorescence radiation, and a set of lattice planes, the Bragg condition is also fulfilled on a cone. This is schematically depicted in fig. 2.11 (b). The resulting lines of extreme intensity in $(\theta_B, \varphi = 0...2\pi)$ that are measured by a detector, for example a photographic plate, are called Kossel lines [Kossel35]. An internal source emits radiation into all directions, producing different Kossel cones that correspond to different sets of lattice planes and orders of reflection.

[6] Only the illuminated parts of the crystal are relevant. The condition can be understood as follows. Atoms have distances up to $\pm L/2$ from the center of the crystal. For a coherent superposition of the interference pattern caused by atoms at the center of the crystal with that caused by atoms $L/2$ distant from the center, $L/2$ should be smaller than the lateral coherence length $\lambda R/(2r_j)$ so that the condition $L < \lambda R/r_j$ is obtained.

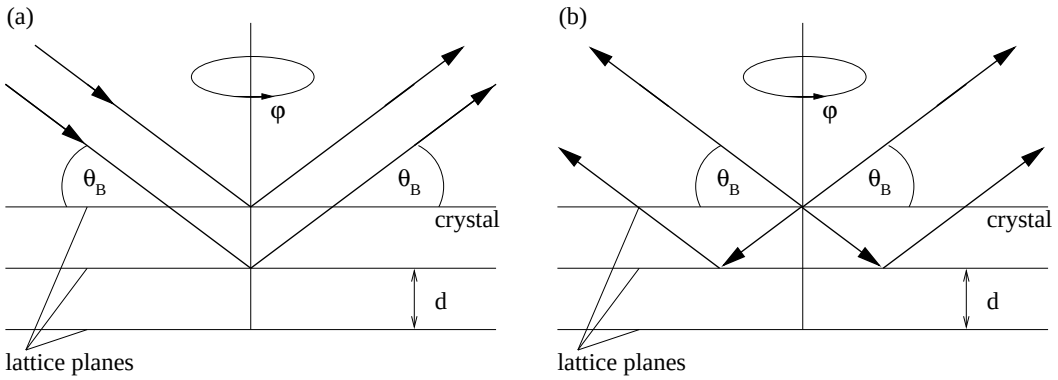

Figure 2.11: (a) A Bragg reflection from a family of lattice planes that are separated by a distance d. Incident and reflected rays are shown for two neighboring planes. (b) A Kossel cone is produced from a fluorescence source inside a crystal.

Elastic scattering of monochromatic incident x rays produces a stationary electric field in the sample. Consider two plane, linearly polarized waves with parallel electric field vectors. It will be assumed that the electric field of the waves are given by $\mathcal{E}_0(\mathbf{r},t) = E_0 \exp[i(\omega t - \mathbf{k_0 r})]$ and $\mathcal{E}_H(\mathbf{r},t) = E_H \exp[i(\omega t - \mathbf{k}_H \mathbf{r})]$, respectively, and that $|\mathbf{k_0}| = |\mathbf{k_H}|$. ω is the angular frequency of the waves and $\mathbf{r}$ is a position vector. An incident x-ray wave can be described by $\mathcal{E}_0$, and a Bragg reflected wave in a crystal by $\mathcal{E}_H$. The complex amplitude E_H can be written as $E_H = \sqrt{R} E_0 \exp(i\nu)$, where ν defines the phase relationship of E_0 to E_H and R is the reflectivity, $R = |E_H|^2/|E_0|^2$. The normalized intensity of a superposition of these waves $\mathcal{E}_0$ and $\mathcal{E}_H$ can be written as

$$I(\mathbf{r}) = 1 + R + 2\sqrt{R}\cos(\nu - \mathbf{H r}). \tag{2.66}$$

where $\mathbf{H} = \mathbf{k}_H - \mathbf{k}_0$. This expression is independent of time and describes an x-ray standing wave (XSW). The intensity at a position $\mathbf{r}$ depends upon $\mathbf{H}$ and ν. The phase ν changes from 0 to π when the crystal is rotated through the angular range of the Bragg reflection. [Zegenhagen93]

Constructive interference of the waves scattered from many atoms of a crystal close to Bragg angles causes high intensities in Kossel and XSW lines. M. von Laue calculated the XSW intensities and, using the optical reciprocity theorem, the Kossel line intensities in the frame of the dynamical theory of x-ray diffraction [Laue60]. Experimentally, the reciprocity of XSW and Kossel lines was demonstrated by T. Gog, D. Bahr, and G. Materlik [Gog95]. The phase of the XSW is directly related to the phase of the structure factor as shown by M. J. Bedzyk and G. Materlik [Bedzyk85a]. A review of the XSW method was given by J. Zegenhagen [Zegenhagen93].

In atomic resolution x-ray holography, intensities are measured over a large angular range. Holograms are measured to obtain information on the local neighborhood of

the fluorescence atom and do not require a high angular resolution. The step size is usually on the order of 1°. In XFH, the detector integrates the holographic signal over its acceptance angle which has usually been on the order of 1° or larger in order to obtain a sufficiently high count rate. This step size and this angular resolution are not sufficient to resolve the detailed line shape in intensity-versus-angle-plots of an XSW or Kossel line but at a step size and angular resolution of $\lesssim 1°$, line patterns can be seen in two-dimensional angle-versus-angle-plots of holograms taken from crystals: In XFH intensities of crystals, Kossel line patterns are seen as extreme values (section 6.1.1, fig. 6.2) and in MEXH intensities of crystals, XSW line patterns are seen as extreme values (section 6.2.1, fig. 6.11).

XSW and Kossel lines contain multiple scattering components. These should be taken into account in a rigorous theory of atomic resolution holography on crystals or they should be removed from the MEXH and XFH intensities. In [Adams98] it is suggested that the detailed line shape of XSW or Kossel lines should be determined experimentally. XSW or Kossel lines could then be removed by a fit to the line shape. A first step in this direction has been taken by measuring MEXH holograms in small angular steps [Adams00b]. This way, hologram and detailed XSW line shapes were obtained simultaneously. Removing XSW or Kossel lines in this way is presently not practical because too many high XSW and Kossel line intensities occur in holograms of crystals. If line shapes are known in detail for a few reflections, they could be evaluated to get structural information using the XSW method or a Kossel line shape analysis.

In [Tegze91] the possibility of XFH was theoretically analysed. It was found that the highest frequency component in a holographic intensity pattern is proportional to $\max(r_j)/\lambda_f$, where $\max(r_j)$ is the largest source-scatterer distance and λ_f is the x-ray fluorescence wavelength. This becomes clear from section 2.3.1, eq. 2.22, where intensity oscillations are mostly due to the exponential of phase $((2\pi r_j/\lambda_f)$ $\times(1-\mathbf{k}_f\mathbf{r}_j/(k_f r_j))$. M. Tegze and G. Faigel suggested to apply a low-pass filter to remove contributions to the intensity from atoms at larger distances which would remove Kossel lines [Tegze91, Faigel99]. A low-pass Fourier filter to remove XSW or Kossel lines from holograms of crystals is used in [Tegze96, Tegze99]. The filtering is done by a convolution of the hologram with a Gaussian of width $\sigma \approx \lambda/(2\pi \max(r_j))$, where $\max(r_j)$ is the radius of the region to be imaged, for example $\max(r_j) = 5$Å in [Tegze99]. In the first XFH experiment an additional "high-pass filter was applied to reduce noise" [Tegze96].

In atomic resolution holography, real space images are obtained by a numerical reconstruction of the holograms. The reconstruction is essentially a Fourier transform (section 2.6). The Fourier transform of a convolution of two functions is proportional to the product of the Fourier transformed functions. The Fourier transform of a Gaussian is another Gaussian. This means that a convolution of the hologram with a Gaussian will multiply in real space the reconstruction with another Gaussian. A low pass filter enhances the image at small distances from the emitter and a high pass filter enhances it at large distances from the emitter. A low pass filter will have a similar effect as a small image region around the emitter.

A low pass *and* a high pass filter together enhance the image at a certain distance from the emitter. This may cause misleading results if an unknown structure is to be imaged and is therefore not advisable.

For an angular step size of about 1° and the present state of data evaluation, it is not necessary to remove x-ray standing wave or Kossel patterns from the holograms. On the contrary, the information about the structure symmetry obtained from XSW or Kossel patterns can be used to extend experimental holograms to a full 4π sphere by copying holographic intensities measured at some angular coordinate to symmetry-equivalent coordinates where no intensities were measured [Novikov97]. This makes an isotropic spatial resolution in the reconstructed images possible [Tonner91].

2.6 Reconstructing Atomic Images

A numerical reconstruction of atomic resolution holograms was already suggested in [Szoeke86]. The numerical reconstruction corresponds to irradiating the hologram with the reference wave in order to reproduce the object wave [Barton90, Adams98]. Different reconstruction algorithms are defined in the following section 2.6.1. The effect of twin images is explained in section 2.6.2. Analytical expressions for the reconstructions are developed for simple holograms in section 2.6.3.

2.6.1 Reconstruction Algorithms

Barton's Single Energy Reconstruction Algorithm

J. J. Barton developed the following reconstruction algorithm using the Helmholtz-Kirchhoff integral theorem and the far-field approximation for large distances R between emitter atom and detector. For typical distances r between atoms, $|\mathbf{R}-\mathbf{r}| \approx R - \mathbf{rR}/R$. The reconstruction $\psi_k(\mathbf{r})$ at a single energy is obtained via the Fourier integral

$$\psi_k(\mathbf{r}) \;=\; \frac{1}{2\pi R^2}\int\int_A \chi(\mathbf{k}) e^{-i\mathbf{kr}} d\sigma_k, \tag{2.67}$$

where the integration is carried out on a sphere A of radius R around the emitter. [Barton88], [Barton90]

Inserting a constant background $\chi(\mathbf{k}) = B = const$ into eq. 2.67 leads to $\psi_k(\mathbf{r}) = (2B/R^2)[\sin(kr)/(kr)]$ which peaks at the origin $\mathbf{r} = \mathbf{0}$ (table 2.1) and makes smaller peaks at atom positions invisible. This shows that any constant background must be removed from $\chi(\mathbf{k})$ before the reconstruction.

The holographic intensity $\chi(\mathbf{k})$ in XFH is given by

$$\chi(\mathbf{k}) \;=\; -2r_e \mathrm{Re}\sum_j \frac{f_S(\mathbf{r}_j,\mathbf{k})}{r_j} e^{i(kr_j - \mathbf{kr}_j)}, \tag{2.68}$$

where $\mathbf{r}_j$ are the atom positions and $f_S(\mathbf{r}_j, \mathbf{k})$ is a generalized scattering factor (eq. 2.23). For MEXH, the same holds with a different $f_S(\mathbf{r}_j, \mathbf{k})$ and with an inverted sign of $\mathbf{k}$ (eq. 2.36). For MEXH, the sign of $\mathbf{k}$ must be inverted in the reconstruction algorithms in order to obtain the same influence on the phase as in XFH. In the following, only the algorithms for XFH will be treated. If the assumptions leading to eq. 2.68 are justified, then

$$\psi_k(\mathbf{r}) = -\frac{r_e}{\pi R^2} \sum_j \frac{1}{r_j} \int\int_A \left[f_S(\mathbf{r}_j, \mathbf{k}) e^{i(kr_j - \mathbf{kr}_j - \mathbf{kr})} + f_S{}^*(\mathbf{r}_j, \mathbf{k}) e^{-i(kr_j - \mathbf{kr}_j + \mathbf{kr})} \right] d\sigma_k. \tag{2.69}$$

For an angle-independent $f_S(\mathbf{r}_j, \mathbf{k}) \equiv f_0$, the single-energy reconstruction $\psi_k(\mathbf{r})$ oscillates for most $\mathbf{r}$ and is stable at positions $\pm\mathbf{r}_j$. The first term in the sum contributes to the twin images at positions $-\mathbf{r}_j$ and the second term contributes to the real images at atom positions $+\mathbf{r}_j$ (section 2.6.2).

Barton's Multiple Energy Reconstruction Algorithm

In order to suppress multiple scattering and twin images an additional integration is introduced in [Barton91]

$$\psi(\mathbf{r}) = \int_{|k|} \psi_k(\mathbf{r}) e^{-ikr} dk. \tag{2.70}$$

The resulting single-scattering image $\psi(\mathbf{r})$ at atom positions $\mathbf{r}_j$ does not oscillate with k while multiple-scattering and twin-image terms do oscillate with k and are suppressed. This way, a single-scattering image with reduced artefacts is obtained [Barton91]. A reliable image reconstruction requires a *wide range* of energies [Barton91, Len94].

Fourier Transform as Reconstruction Algorithm

The algorithm of eq. 2.70 is still Fourier-like, but is not a Fourier transform of $\chi(\mathbf{k})$

$$\psi_{FT}(\mathbf{r}) = \int_k \psi_k(\mathbf{r}) k^2 dk. \tag{2.71}$$

Comparison of eq.2.71 with the Barton algorithm of eq. 2.70 shows that the Barton algorithm is equal to the Fourier transform of a modified $\chi'(\mathbf{k})$:

$$\psi(\mathbf{r}) \equiv \frac{1}{2\pi R^2} \int_k \int\int_A \chi(\mathbf{k}) e^{-i\mathbf{kr}} e^{-ikr} d\sigma_k dk \tag{2.72}$$

$$\equiv \frac{1}{2\pi R^2} \int_k \int\int_A \chi'(\mathbf{k}) e^{-i\mathbf{kr}} d\sigma_k k^2 dk, \tag{2.73}$$

which is the Fourier transform of a modified holographic function

$$\chi'(\mathbf{k}) = \frac{\chi(\mathbf{k})e^{-ikr}}{k^2}. \quad (2.74)$$

$\psi_{FT}(\mathbf{r})$ is similar to $\psi(\mathbf{r})$ especially if only few energies are available. The weights of the reconstructions at single energies are different and an additional phase factor is included in $\psi(\mathbf{r})$. This leads to different relative and absolute peak heights for the multiple-energy Barton algorithm (eq. 2.70) and a multiple-energy Fourier transform (eq. 2.71) as reconstruction algorithm.

In this text, the algorithm of eq. 2.67 will be used at single energies and the algorithm of eq. 2.70 will be used at multiple energies. The integrations are replaced by summations for the numerical reconstructions of calculated (chapter 3) and experimental holograms (chapters 5, 6).

Other Reconstruction Algorithms

Eqns. 2.67, 2.70 have been used to reconstruct atomic images from XFH and MEXH holograms. More complicated algorithms are used in electron holography in order to take into account the more anisotropic and more intense scattering of electrons compared to x rays [Len94]. A review of image reconstruction methods used in photoelectron holography is given in [Len97c]. A comparison of atomic holography with electrons and x rays is given in [Len97d]. The data evaluation in photoelectron holography is described, for example, in [Zharnikov95]. Fourier filtering of experimental holograms and a reconstruction algorithm more complicated than in eqns. 2.67, 2.70 were used in this case. An algorithm for holographic low energy electron diffraction (LEED) is developed in [Saldin95]. Many algorithms contain free parameters that can be adjusted to optimize the reconstructions. Free parameters allow the manipulation of the reconstructions so that simple algorithms without free parameters should be used in a first evaluation step. Filtering changes the peak heights in the reconstructions depending on the distance from the fluorescence atom (section 2.6.3). Filtering should be avoided if the goal is to evaluate peak heights in the reconstructions quantitatively.

The goal of these presently used reconstruction algorithms is to obtain peaks at atom positions. For simple cases, the highest peaks occur at atom positions $\mathbf{r}_j$ or at positions $-\mathbf{r}_j$ (section 2.6.3). F. N. Chukhovskii derived a different reconstruction algorithm where $\chi(\mathbf{k})$ is inverted to obtain the electron charge density [Chukhovskii98]. Once this algorithm is established in practice, peak positions as well as relative and absolute peak heights in the reconstructions will be physical quantities.

Image Functions

Applying a reconstruction algorithm to a hologram function $\chi(\mathbf{k})$ produces a complex quantity $\psi_k(\mathbf{r})$ or $\psi(\mathbf{r})$. In order to display these in real space, one of the following expressions can be used to obtain a real atomic image

$$|\psi_k(\mathbf{r})|, \quad |\psi_k(\mathbf{r})|^2, \quad |\psi(\mathbf{r})|, \quad \text{or} \quad |\psi(\mathbf{r})|^2. \quad (2.75)$$

In this text, $|\psi_k(\mathbf{r})|^2$ and $|\psi(\mathbf{r})|^2$ will be used. The term "single-energy reconstruction" will be used for $\psi_k(\mathbf{r})$ and for $|\psi_k(\mathbf{r})|^2$. The terms "energy-added reconstruction" or "multiple-energy reconstruction" will be used for $\psi(\mathbf{r})$ and for $|\psi(\mathbf{r})|^2$.

2.6.2 Twin Images

Single Energy, One Scattering Atom at $\mathbf{r}_j$

For a simple structure that consists of a fluorescing atom at the origin and of a single scatterer at position $\mathbf{r}_j$, eq. 2.69 gives at the position $\mathbf{r} = \mathbf{r}_j$

$$\psi_k(\mathbf{r}_j) = -\frac{r_e}{\pi R^2 r_j} \int\int_A \left[f_S(\mathbf{r}_j, \mathbf{k}) e^{i(kr_j - 2\mathbf{kr}_j)} + {f_S}^*(\mathbf{r}_j, \mathbf{k}) e^{-ikr_j} \right] d\sigma_k \quad (2.76)$$

and at the position $\mathbf{r} = -\mathbf{r}_j$

$$\psi_k(-\mathbf{r}_j) = -\frac{r_e}{\pi R^2 r_j} \int\int_A \left[f_S(\mathbf{r}_j, \mathbf{k}) e^{ikr_j} + {f_S}^*(\mathbf{r}_j, \mathbf{k}) e^{-i(kr_j - 2\mathbf{kr}_j)} \right] d\sigma_k . \quad (2.77)$$

Comparison of eq. 2.76 with eq. 2.77 shows that

$$\psi_k(-\mathbf{r}_j) = [\psi_k(\mathbf{r}_j)]^* . \quad (2.78)$$

The single atom at the position $\mathbf{r} = \mathbf{r}_j$ produces an image at the position $\mathbf{r}_j$ and as another image its complex conjugate at the position $-\mathbf{r}_j$. This twin image does not correspond to an atom of the structure.

Single Energy, Scattering Atoms at $\mathbf{r}_j$ and at $-\mathbf{r}_j$

For a fluorescing atom at the origin and a *pair* of scattering atoms at positions $\pm\mathbf{r}_j$, the atomic image at the special point $\mathbf{r} = \mathbf{r}_j$ is the superposition of the actual image from the atom at $+\mathbf{r}_j$ and the twin image from the atom at $-\mathbf{r}_j$,

$$\begin{aligned} \psi_k(\mathbf{r}_j) = -\frac{r_e}{\pi R^2 r_j} \Bigg[& e^{ikr_j} \int\int_A f_S(-\mathbf{r}_j, \mathbf{k}) + f_S^*(-\mathbf{r}_j, \mathbf{k}) e^{-2i(kr_j + \mathbf{kr}_j)} d\sigma_k \\ & + e^{-ikr_j} \int\int_A {f_S}^*(+\mathbf{r}_j, \mathbf{k}) + f_S(+\mathbf{r}_j, \mathbf{k}) e^{2i(kr_j - \mathbf{kr}_j)} d\sigma_k \Bigg] . \end{aligned} \quad (2.79)$$

If the two terms in eq. 2.79 that contain the phase $-2i\mathbf{kr}_j$ are neglected, then

$$\psi_k(\mathbf{r}_j) = -\frac{r_e}{\pi R^2 r_j} \left[e^{ikr_j} \int\int_A f_S(-\mathbf{r}_j, \mathbf{k}) d\sigma_k + e^{-ikr_j} \int\int_A {f_S}^*(+\mathbf{r}_j, \mathbf{k}) d\sigma_k \right] \quad (2.80)$$

If near-field and polarization effects are neglected then $f_S(\mathbf{r}_j, \mathbf{k}) \approx f(\mathbf{r}_j, \mathbf{k})$. For a pair of equally illuminated scatterers in a plane perpendicular to the symmetry axis of the hologram

$$\int\int_A f(\mathbf{r}_j,\mathbf{k})d\sigma_k = \int\int_A f(-\mathbf{r}_j,\mathbf{k})d\sigma_k. \quad (2.81)$$

In the case of x-ray scattering, $f(\mathbf{r}_j,\mathbf{k}) \approx f^*(\mathbf{r}_j,\mathbf{k})$ so that

$$\psi_k(\mathbf{r}_j) = -\frac{2r_e}{\pi R^2 r_j}\cos(kr_j)\int\int_S f(\mathbf{r}_j,\mathbf{k})d\sigma_k. \quad (2.82)$$

$\psi_k(\mathbf{r}_j)$ is proportional to $\cos(kr_j)$ even under slightly different assumptions. If the scattering factor $f_S = f_s^* = f_0$ is real and isotropic, then the two terms in eq. 2.79 that contain the phase $-2i\mathbf{k}\mathbf{r}_j$ do not need to be neglected in order to obtain $\psi_k(\mathbf{r}_j) \propto \cos(kr_j)$ (section 2.6.3). The image at $\mathbf{r}_j$ vanishes for

$$\begin{aligned}\cos(kr_j) = 0 \iff kr_j &= (2m+1)\pi/2, m \in \mathbb{Z} \\ r_j &= (2m+1)\lambda/4, m \in \mathbb{Z}\end{aligned} \quad (2.83)$$

This second kind of twin image effect can suppress the image at atom positions. Thus, if holograms are measured only at a few energies, images may appear where no atoms are or images at atom positions may be cancelled [Len94]. This consideration does not take atoms at other positions into account and evaluates $\psi_k(\mathbf{r})$ only at atom positions $\mathbf{r} = \mathbf{r}_j$. Polarization effects as well as near-field effects are neglected.

Multiple Energies, Scattering Atoms at $\mathbf{r}_j$ and at $-\mathbf{r}_j$

Inserting $\psi_k(\mathbf{r}_j)$ of eq. 2.82 into the multiple-energy algorithm of eq. 2.70 leads to

$$\psi(\mathbf{r}_j) = -\frac{2r_e}{\pi R^2 r_j}\int_{k_1}^{k_2} dk e^{-ikr_j}\cos(kr_j)\int\int_S f(\mathbf{r}_j,\mathbf{k})d\sigma_k. \quad (2.84)$$

The integration over k can be performed only if the k dependency of $f(\mathbf{r}_j,\mathbf{k})$ is known. For $f(\mathbf{r}_j,\mathbf{k}) = f_0 = const$, $\Delta_k \equiv k_2 - k_1$, and $K \equiv k_2 + k_1$, one obtains

$$\psi(\mathbf{r}_j) = -\frac{4f_0 r_e}{R^2 r_j}\left[\Delta_k + \frac{e^{-2iKr_j}}{r_j}\sin(\Delta_k r_j)\right] \quad (2.85)$$

$$|\psi(\mathbf{r}_j)|^2 = \left(\frac{4f_0 r_e \Delta_k}{R^2 r_j}\right)^2\left[1 + \left(\frac{\sin(\Delta_k r_j)}{\Delta_k r_j}\right)^2 + 2\frac{\sin(\Delta_k r_j)}{\Delta_k r_j}\cos(2Kr_j)\right] \quad (2.86)$$

$\psi(\mathbf{r}_j)$ grows with Δ_k but still has an oscillating term. The dependence of $|\psi(\mathbf{r}_j)|^2 \times [(R^2 r_j)/(4f_0 r_e \Delta_k)]^2$ of eq. 2.86 on the argument $x \equiv \Delta_k r_j$ is shown in fig. 2.12 for three cases. The asymptotic values are given by the functions $s(x)$ and $t(x)$ that are defined in fig. 2.12. The case $\Delta_k = K = k_2$ occurs for $k_1 = 0$ and is shown as the function $w(x)$. The figure shows that $|\psi(\mathbf{r}_j)|^2 \times [(R^2 r_j)/(4f_0 r_e \Delta_k)]^2$ oscillates around 1 and is at least 0.5 for $x \gtrsim 3\pi/4$. The oscillation has a high amplitude for $x \lesssim 3\pi/4$. If $\Delta_k = K = k_2$ then $x = k_2 r_j = 2\pi r_j/\lambda_2$, and the condition $x > 3\pi/4$ corresponds to $\lambda_2 < 8r_j/3$ which can be easily fulfilled. This shows that the cancellation of image and twin image at a single energy (eq. 2.82) can be avoided if multiple energies (eq. 2.85) are used.

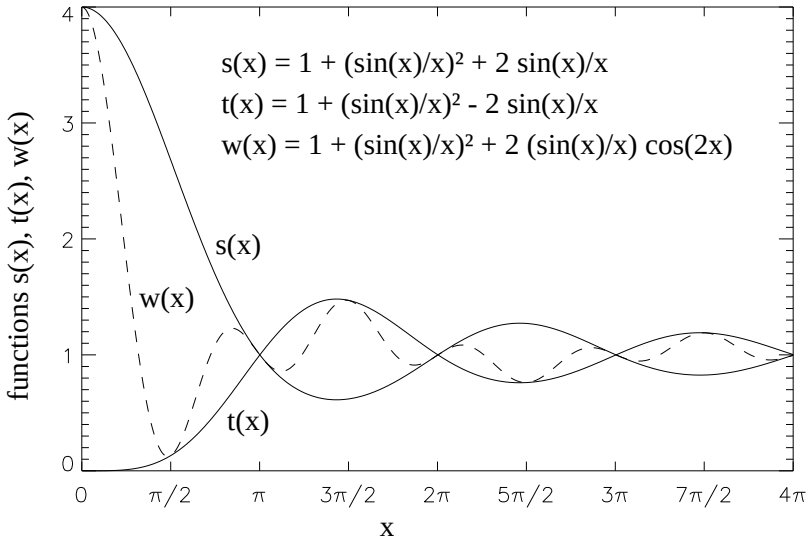

Figure 2.12: The dependence of $|\psi(\mathbf{r}_j)|^2 \times [(R^2 r_j)/(4 f_0 r_e \Delta_k)]^2$ of eq. 2.86 on the argument $x \equiv \Delta_k r_j$. $s(x) = 1 + (\sin(x)/x)^2 + 2\sin(x)/x$ and $t(x) = 1 + (\sin(x)/x)^2 - 2\sin(x)/x$ are the asymptotic limits. $w(x) = 1 + (\sin(x)/x)^2 + 2(\sin(x)/x)\cos(2x)$ occurs for $\Delta_k = K = k_2$.

2.6.3 Analytical Reconstructions of Simple Holograms

In [Tonner91], [Saldin91] the holographic image reconstruction is described for electrons and an analytical expression for reconstructed images is obtained. The discussion for x rays in this section partly follows [Tonner91]. $\psi_k(\mathbf{r})$ and $\psi(\mathbf{r})$ are evaluated at general positions $\mathbf{r}$ and not only at atom positions as was the case in section 2.6.2. This makes it possible to analyse the reconstructed images for simple holograms and to determine the spatial resolution from them. The spatial resolution of atomic resolution holography has first been estimated by A. Szöke to be $\approx \lambda$ for a hologram on a full 4π sphere [Szoeke86].

4π-Hologram at Single Energy, One Scattering Atom at $\mathbf{r}_j$

For the case of an angle-independent scattering factor $f_S(\mathbf{r}_j, \mathbf{k}) = f_0 \exp(i\phi_0)$, the holographic intensity in XFH due to a single scatterer at $\mathbf{r}_j$ is given by (eq. 2.68)

$$\chi(\mathbf{k}) \;=\; -r_e \frac{f_0}{r_j} \left[e^{i(kr_j - \mathbf{k}\mathbf{r}_j + \phi_0)} + e^{-i(kr_j - \mathbf{k}\mathbf{r}_j + \phi_0)} \right]. \qquad (2.87)$$

Inserting this into eq. 2.67 yields

$$\psi_k(\mathbf{r}) \;=\; -\frac{r_e f_0}{2\pi R^2 r_j} \int\int_A \left[e^{i(kr_j + \phi_0 - \mathbf{k}\mathbf{r}_j - \mathbf{k}\mathbf{r})} + e^{-i(kr_j + \phi_0 - \mathbf{k}\mathbf{r}_j + \mathbf{k}\mathbf{r})} \right] d\sigma_k. \qquad (2.88)$$

The integration has to be performed over the surface A of the measured hologram. The evaluation is straightforward if the hologram is known in the full 4π angular

range. Experimental holograms can usually only be measured in a limited angular range. Nearly a hemisphere can be covered (chapter 5). For crystals it may be possible to extend holograms to the full 4π range using XSW or Kossel lines (section 2.5.2). For 4π holograms, the two terms of 2.88 may be evaluated separately, yielding

$$\begin{aligned}
\psi_k(\mathbf{r}) &= -\frac{r_e f_0}{2\pi R^2 r_j}\left[e^{i(kr_j+\phi_0)}\int_0^{2\pi}d\varphi\int_0^{\pi}\sin\theta d\theta e^{-i(k|\mathbf{r}_j+\mathbf{r}|\cos\theta)}\right. \\
&\qquad \left. +e^{-i(kr_j+\phi_0)}\int_0^{2\pi}d\varphi\int_0^{\pi}\sin\theta d\theta e^{i(k|\mathbf{r}_j-\mathbf{r}|\cos\theta)}\right] \qquad (2.89)\\
&= -\frac{r_e f_0}{R^2 r_j}\left[e^{i(kr_j+\phi_0)}\int_{-1}^{1}dx e^{-ik|\mathbf{r}_j+\mathbf{r}|x}+e^{-i(kr_j+\phi_0)}\int_{-1}^{1}dx e^{-ik|\mathbf{r}_j-\mathbf{r}|x}\right] \qquad (2.90)\\
&= -\frac{2r_e f_0}{R^2 r_j}\left[e^{i(kr_j+\phi_0)}\frac{\sin(k|\mathbf{r}+\mathbf{r}_j|)}{k|\mathbf{r}+\mathbf{r}_j|}+e^{-i(kr_j+\phi_0)}\frac{\sin(k|\mathbf{r}-\mathbf{r}_j|)}{k|\mathbf{r}-\mathbf{r}_j|}\right]. \qquad (2.91)
\end{aligned}$$

For a single scattering atom at $\mathbf{r}_j$ the image

$$\begin{aligned}
|\psi_k(\mathbf{r})|^2 &= \left(\frac{2r_e f_0}{R^2 r_j}\right)^2\left[\left(\frac{\sin(k|\mathbf{r}-\mathbf{r}_j|)}{k|\mathbf{r}-\mathbf{r}_j|}\right)^2+\left(\frac{\sin(k|\mathbf{r}+\mathbf{r}_j|)}{k|\mathbf{r}+\mathbf{r}_j|}\right)^2\right. \\
&\qquad \left. +2\frac{\sin(k|\mathbf{r}-\mathbf{r}_j|)}{k|\mathbf{r}-\mathbf{r}_j|}\frac{\sin(k|\mathbf{r}+\mathbf{r}_j|)}{k|\mathbf{r}+\mathbf{r}_j|}\cos(2kr_j+2\phi_0)\right] \qquad (2.92)
\end{aligned}$$

is obtained. $|\psi_k(\mathbf{r})|^2$ is proportional to $(f_0/r_j)^2$ so that higher peaks are obtained for stronger scattering atoms and for atoms that have a small distance r_j to the fluorescence atom.

x	x is	$g(x)=\sin(x)/x$	$g^2(x)$
0	first maximum of g and g^2	1	1
$n\pi, n\in\mathbb{Z}^*$	first minima of g^2	0	0
$\approx\pm 3\pi/2$	first min. of g, second max. of g^2	-0.212	0.045
$\approx\pm\sqrt{2}$	$\approx 0.5\ r_{FWHM}$ of g^2	0.698	0.488
± 1.40	$\approx 0.5\ r_{FWHM}$ of g^2	$0.704\approx 1/\sqrt{2}$	$0.495\approx 1/2$
± 1.90	$\approx 0.5\ r_{FWHM}$ of g	$0.498\approx 1/2$	$\approx 1/4$

Table 2.1: Characteristic values of the even image function $g(x)=(\sin x)/x = 1-x^2/3!+x^4/5!-+..., |x|<\infty$ and its square $g^2(x)=(\sin^2 x)/x^2$. r_{FWHM} denotes the full width at half maximum of the central maximum.

The functions $(\sin x)/x$ and $[(\sin x)/x]^2$ are plotted in fig. 2.13 and a few characteristic values are given in table 2.1. $|\psi_k(\mathbf{r})|^2$ peaks at the atom position $|\mathbf{r}-\mathbf{r}_j|=0$ and at the twin position $|\mathbf{r}+\mathbf{r}_j|=0$. At $\mathbf{r}=\mathbf{r}_j$, the last term in eq. 2.92 becomes proportional to $[\sin(2kr_j)]/(2kr_j)$. For $2kr_j\approx 3\pi/2$, it becomes as large as $2\cdot 0.212\approx 40\%$

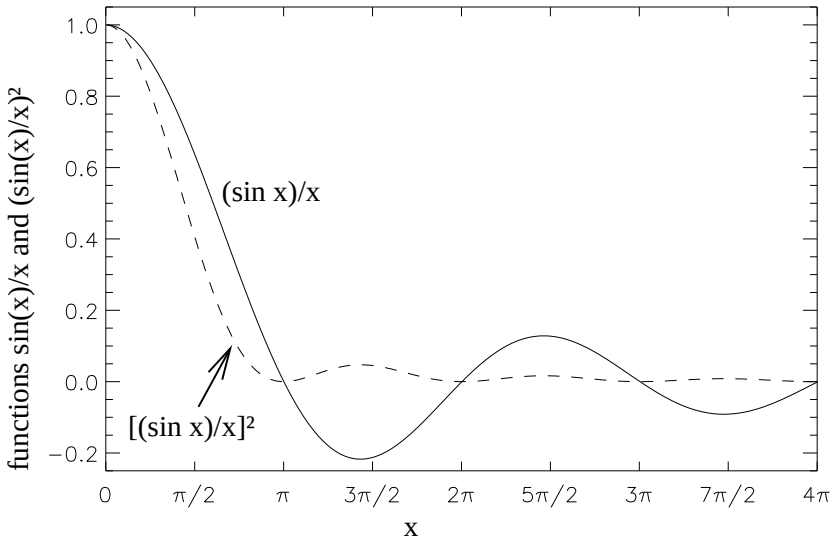

Figure 2.13: The dependence of the functions $(\sin x)/x$ and $[(\sin x)/x]^2$ on x.

of the first term. The phase ϕ_0 of the atomic scattering factor is approximately zero for x-ray energies far from absorption edges which corresponds to a real scattering factor ($\phi_0 = 0$). For $\phi_0 = 0$ and for $2kr_j \approx 3\pi/2$, the function $\cos(2kr_j + 2\phi_0) \approx 0$, so that the last term in eq. 2.92 becomes zero and may be neglected for a single scattering atom. At $\mathbf{r} = \mathbf{r}_j$, the second term of eq. 2.92 becomes proportional to $(\sin(2kr_j))^2/(2kr_j)^2$ which is only $\approx 5\%$ of the first term for $2kr_j \approx 3\pi/2$ so that mostly the first term of eq. 2.92 is relevant. The full width at half maximum r_{FWHM} of this peak at position $\mathbf{r} = \mathbf{r}_j$ is

$$r_{FWHM} \approx 2.8/k \approx 2\sqrt{2}/k = \sqrt{2}\lambda/\pi \approx \lambda/2, \tag{2.93}$$

which can be compared to the spatial resolution of a microscope (section 2.1.1, eq. 2.2). r_{FWHM} can be taken as a measure for the distance necessary to resolve peaks in the reconstructed image. The first and second terms peak at a distance $|(\mathbf{r} - \mathbf{r}_j) - (\mathbf{r} + \mathbf{r}_j)| = 2r_j$ from each other and can be resolved if $2r_j \geq r_{FWHM}$. Another measure would be the distance r_{Mm} from the central intensity maximum to the first intensity minimum. The minimum occurs for $kr_{Mm} = \pi$ so that $r_{Mm} = \lambda/2 \approx r_{FWHM}$. As an example, at the Fe K_α line $E \approx 6.4$ keV and $\lambda \approx 1.94$ Å, so that $r_{FWHM} \approx 0.9$ Å. Typical interatomic distances are larger than this. For example, the nearest neighbor distance in bcc Fe is 2.49 Å, so that the condition $2r_j > r_{FWHM}$ is valid for this case and for larger energies or distances.

4π-Hologram at Single Energy, Scattering Atoms at $\mathbf{r}_j$ and $-\mathbf{r}_j$

For a pair of scattering atoms at positions $\pm\mathbf{r}_j$ one obtains from eq. 2.91

$$\psi_k(\mathbf{r}) = -\frac{4r_e f_0}{R^2 r_j}\cos(kr_j + \phi_0)\left[\frac{\sin(k|\mathbf{r} - \mathbf{r}_j|)}{k|\mathbf{r} - \mathbf{r}_j|} + \frac{\sin(k|\mathbf{r} + \mathbf{r}_j|)}{k|\mathbf{r} + \mathbf{r}_j|}\right]. \tag{2.94}$$

The image is then

$$|\psi_k(\mathbf{r})|^2 = \left(\frac{4r_e f_0}{R^2 r_j}\right)^2 \cos^2(kr_j+\phi_0)\left[\left(\frac{\sin(k|\mathbf{r}-\mathbf{r}_j|)}{k|\mathbf{r}-\mathbf{r}_j|}\right)^2 + \left(\frac{\sin(k|\mathbf{r}+\mathbf{r}_j|)}{k|\mathbf{r}+\mathbf{r}_j|}\right)^2 + 2\frac{\sin(k|\mathbf{r}-\mathbf{r}_j|)}{k|\mathbf{r}-\mathbf{r}_j|}\frac{\sin(k|\mathbf{r}+\mathbf{r}_j|)}{k|\mathbf{r}+\mathbf{r}_j|}\right]. \quad (2.95)$$

Peak heights at atom positions can deviate from the physically relevant amplitude factor $(4r_e f_0)^2/(R^2 r_j)^2$ due to twin image effects and due to cross terms: $\psi_k(\mathbf{r})$ is proportional to $\cos(kr_j+\phi_0)$ and becomes zero for a real scattering factor $\phi_0 = 0$ if $kr_j = (2m+1)\pi/2, m \in \mathbb{Z}$ (compare eq. 2.83 of section 2.6.2). At $\mathbf{r} = \mathbf{r}_j$, the last term in eq. 2.95 becomes $\propto 2\sin(2kr_j)/(2kr_j)$, and the second term becomes $\propto (\sin(2kr_j))^2/(2kr_j)^2$. For $2kr_j \approx 3\pi/2$, these terms become $\approx 40\%$ and $\approx 5\%$ of the first term, respectively, showing that the value of $|\psi_k(\mathbf{r})|^2$ at an atom position $\mathbf{r} = \mathbf{r}_j$ depends upon cross-terms which may enhance or reduce peak heights at atom positions.

4π-Hologram at Single Energy, Many Scattering Atoms

The reconstruction $\psi_k(\mathbf{r})$ of eq. 2.91 was calculated for a hologram in which only one single scattering atom was taken into account. For many atoms, $\chi(\mathbf{k})$ is a sum over single atom contributions of the form given by eq. 2.87. The reconstruction algorithm of eq. 2.67 is a linear transform. In order to obtain the reconstructed image for a structure of many atoms, eq. 2.91 therefore has to be summed over different atom positions $\mathbf{r}_j$.

The reconstruction $\psi_k(\mathbf{r})$ of a hologram that contains contributions of many scattering atoms is obtained as a sum over the reconstructions of eq. 2.91 obtained from single atoms, i.e.

$$\psi_k(\mathbf{r}) = -\sum_j \frac{2r_e f_{0j}}{R^2 r_j}\left[e^{i(kr_j+\phi_{0j})}\frac{\sin(k|\mathbf{r}+\mathbf{r}_j|)}{k|\mathbf{r}+\mathbf{r}_j|} + e^{-i(kr_j+\phi_{0j})}\frac{\sin(k|\mathbf{r}-\mathbf{r}_j|)}{k|\mathbf{r}-\mathbf{r}_j|}\right]. \quad (2.96)$$

The reconstruction $\psi_k(\mathbf{r})$ depends on all atom positions $\mathbf{r}_j$. Cross terms in $|\psi_k(\mathbf{r})|^2$ may not be negligible as in eq. 2.92. Peaks at atom positions may be enhanced, reduced or even cancelled as in eq. 2.95 so that the image may not be ideal, even for the simple case of isotropic scattering. Central maxima and side extrema due to atoms at different positions may sum to high values or may be diminished in this sum. Therefore high peaks may occur not only at atom positions; peaks can be shifted away from atom positions or peaks can be cancelled. These effects will usually increase with the number of atoms contributing to a hologram. For a large number of atoms, an analytical analysis of eq. 2.96 becomes impractical. Holograms can be calculated numerically and then reconstructed in order to estimate these effects for a known or postulated structure (chapter 3).

4π-Holograms at Multiple Energies, One Scattering Atom at $\mathbf{r}_j$

$\psi_k(\mathbf{r})$ of eq. 2.91 can be inserted into the multiple-energy algorithm of eq. 2.70. This yields

$$\psi(\mathbf{r}) = -\frac{2r_e f_0}{R^2 r_j}\int_k dk\left[e^{i(k(r_j-r)+\phi_0)}\frac{\sin(k|\mathbf{r}_j+\mathbf{r}|)}{k|\mathbf{r}_j+\mathbf{r}|}+e^{-i(k(r_j+r)+\phi_0)}\frac{\sin(k|\mathbf{r}-\mathbf{r}_j|)}{k|\mathbf{r}-\mathbf{r}_j|}\right] \tag{2.97}$$

$$= -\frac{2r_e f_0}{R^2 r_j}\left[\frac{e^{i\phi_0}}{|\mathbf{r}_j+\mathbf{r}|}\int_{k_1}^{k_2}\frac{dk}{k}\left(e^{ikm}-e^{ikn}\right)+\frac{e^{-i\phi_0}}{|\mathbf{r}_j-\mathbf{r}|}\int_{k_1}^{k_2}\frac{dk}{k}\left(e^{ikp}-e^{ikq}\right)\right], \tag{2.98}$$

where the abbreviations $m = r_j - r + |\mathbf{r}_j+\mathbf{r}|$, $n = r_j - r - |\mathbf{r}_j+\mathbf{r}|$, $p = r_j + r - |\mathbf{r}_j-\mathbf{r}|$, and $q = r_j + r + |\mathbf{r}_j-\mathbf{r}|$ were used. The integrals can be solved using [Bronstein91] (integral #451)

$$I(k,x) \equiv \int_k \frac{dk}{k}e^{ikx} = \ln k + \frac{kx}{1\cdot 1!}+\frac{(kx)^2}{2\cdot 2!}+\frac{(kx)^3}{3\cdot 3!}+... \tag{2.99}$$

so that

$$\psi(\mathbf{r}) = -\frac{2r_e f_0}{R^2 r_j}\left[\frac{e^{i\phi_0}}{|\mathbf{r}_j+\mathbf{r}|}\left(I(k,m)-I(k,n)\right)+\frac{e^{-i\phi_0}}{|\mathbf{r}_j-\mathbf{r}|}\left(I(k,p)-I(k,q)\right)\right]_{k_1}^{k_2} \tag{2.100}$$

$$\psi(\mathbf{r}=r\mathbf{r}_j/r_j) = -\frac{2r_e f_0}{R^2 r_j}\left[\frac{e^{i\phi_0}}{r_j+r}\left(I(k,2r_j)-I(k,-2r)\right)+\frac{e^{-i\phi_0}}{r_j-r}\left(I(k,2r)-I(k,2r_j)\right)\right]_{k_1}^{k_2}, \tag{2.101}$$

where the last equality holds for radial directions $\mathbf{r} = r\mathbf{r}_j/r_j$. For $\mathbf{r} = \mathbf{r}_j$, eq. 2.85 is again obtained.

If a Fourier transform of $\chi(\mathbf{k})$ were calculated instead of the Barton algorithm of eq. 2.70, then eq. 2.97 would still hold with the following modifications: the integrands on the right side of eq. 2.97 would have to be multiplied by k^2, and m, n, p, and q would have to be replaced by $m' = r_j + |\mathbf{r}_j+\mathbf{r}|$, $n' = r_j - |\mathbf{r}_j+\mathbf{r}|$, $p' = r_j - |\mathbf{r}_j-\mathbf{r}|$, and $q' = r_j + |\mathbf{r}_j-\mathbf{r}|$, respectively. The integrals can be solved using [Bronstein91] (integral #448)

$$J(k,x) \equiv \int_k dk\, k\, e^{ikx} = \frac{e^{ikx}}{(ix)^2}\left(ikx-1\right). \tag{2.102}$$

Thus, eq.2.100 will still hold if I is replaced by J, and if m, n, p, q are replaced by m', n', p', q'.

Only a few energies are available in present atomic resolution x-ray holography experiments due to the long data acquisition times for a hologram at a fixed energy (chapter 5). The integration over k is then replaced by a summation. Inserting eq. 2.91 into eq. 2.70 yields

$$\begin{aligned}\psi(\mathbf{r}) &= -\frac{2r_e f_0}{R^2 r_j}\sum_k \left[e^{i(k(r_j-r)+\phi_0)}\frac{\sin(k|\mathbf{r}+\mathbf{r}_j|)}{k|\mathbf{r}+\mathbf{r}_j|}\right. \\ &\quad \left. + e^{-i(k(r_j+r)+\phi_0)}\frac{\sin(k|\mathbf{r}-\mathbf{r}_j|)}{k|\mathbf{r}-\mathbf{r}_j|}\right]. \end{aligned} \tag{2.103}$$

At a fixed energy, the image terms are the same as in eq. 2.91 except for an additional phase $\exp(-ikr)$. This corresponds to a weighted sum over single-energy reconstructions. For a single scattering atom at $\mathbf{r}_j$, $|\psi(\mathbf{r})|^2$ will be given by eq. 2.92, and for a pair of atoms at $\pm\mathbf{r}_j$, $|\psi(\mathbf{r})|^2$ will be given by eq. 2.95. In the following, the single-energy algorithm of eq. 2.67 will be discussed further.

2π-Holograms at Single Energy, One Scattering Atom at $\mathbf{r}_j$

Consider the case where a hologram is only known on a hemisphere that covers a range in the polar coordinates θ and φ above the scattering atom at position $\mathbf{r}_j = (\sin\theta\cos\varphi, \sin\theta\sin\varphi, \cos\theta)$. Two cases of atom positions below a hemisphere are illustrated in fig. 2.14: first, $\theta = [0,\pi]$, $\varphi = [0,\pi]$ and second, $\theta = [0,\pi/2]$, $\varphi = [0,2\pi]$. For simplicity, $\psi_k(\mathbf{r})$ is only evaluated for radial positions $\mathbf{r} = r\mathbf{r}_j/r_j$. For these, $\mathbf{k}(\mathbf{r}_j \pm \mathbf{r}) = \mathbf{k}\mathbf{r}_j(1 \pm r/r_j) = k(r_j \pm r)\cos\theta$.

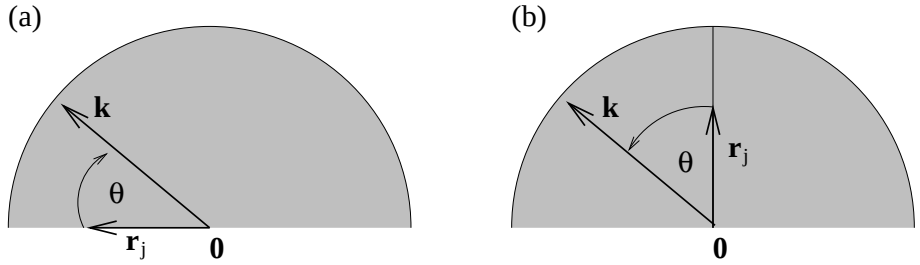

Figure 2.14: Two cases for hemispheres above the scattering atom at position $\mathbf{r}_j$. (a) $\theta = [0,\pi]$, $\varphi = [0,\pi]$, (b) $\theta = [0,\pi/2]$, $\varphi = [0,2\pi]$.

The first case $\theta = [0,\pi]$, $\varphi = [0,\pi]$ is directly obtained from the above results for the case of a 4π hologram. The difference is that the integration over φ yields π here instead of 2π there, so that the expression for $\psi_k(\mathbf{r})$ of eq. 2.91 needs to be divided by two. The spatial resolution is that of eq. 2.93.

The second case $\theta = [0, \pi/2]$, $\varphi = [0, 2\pi]$ can be easily generalized to the case $\theta = [\alpha, \beta]$, $0 \leq \alpha < \beta \leq \pi$, $\varphi = [0, 2\pi]$:

$$\begin{aligned}\psi_k(\mathbf{r} = r\mathbf{r}_j/r_j) &= -\frac{r_e f_0}{r_j \pi R^2}\left[e^{i(kr_j+\phi_0)}\int_0^{2\pi} d\varphi \int_\alpha^\beta \sin\theta d\theta e^{-ik(r_j+r)\cos\theta)}\right. \\ &\left. + e^{-i(kr_j+\phi_0)}\int_0^{2\pi} d\varphi \int_\alpha^\beta \sin\theta d\theta e^{i(k(r_j-r)\cos\theta)}\right]. \quad (2.104)\end{aligned}$$

With the abbreviations $a = kr_j + \phi_0$, $c = k(r_j + r)\cos\alpha$, $d = k(r_j + r)\cos\beta$, $e = k(r_j - r)\cos\alpha$, $f = k(r_j - r)\cos\beta$, this becomes

$$\begin{aligned}\psi_k(\mathbf{r} = r\mathbf{r}_j/r_j) &= -\frac{r_e f_0}{r_j R^2}\left[e^{i(a+(c+d)/2)}(\cos\alpha + \cos\beta)\frac{\sin((c-d)/2)}{(c-d)/2}\right. \\ &\left. + e^{-i(a-(e+f)/2)}(\cos\alpha - \cos\beta)\frac{\sin((e-f)/2)}{(e-f)/2}\right]. \quad (2.105)\end{aligned}$$

For a hemisphere, $\cos\alpha = 1$ and $\cos\beta = 0$ so that one obtains

$$\begin{aligned}\psi_k(\mathbf{r} = r\mathbf{r}_j/r_j) &= -\frac{r_e f_0}{r_j R^2}\left[e^{i(k(3r_j+r)/2+\phi_0)}\frac{\sin(k(r_j+r)/2)}{k(r_j+r)/2}\right. \\ &\left. + e^{-i(k(r_j-r)/2+\phi_0)}\frac{\sin(k(r_j-r)/2)}{k(r_j-r)/2}\right]. \quad (2.106)\end{aligned}$$

These equations show that ψ_k and therefore the spatial resolution depends upon the reconstructed angular range of a hologram. The expression of eq. 2.106 for a 2π hologram is similar to eq. 2.90 for a 4π hologram. Here, the argument of the $(\sin x)/x$ function is half that of the same function for the 4π hologram, so that the r_{FWHM} here is twice that of eq. 2.93 [Tonner91]. For an unknown structure, atom positions are not known so that the spatial resolution obtained from a hemisphere may vary between $\approx \lambda$ and $\approx \lambda/2$. An isotropic resolution is only obtained from 4π holograms.

Spatial Resolution of Atomic Resolution Holography and of Young's Double Slit Experiment

The spatial resolution of atomic resolution holography can be compared to that of Young's double slit experiment [Born97], see fig. 2.15. Consider two coherent point sources S_1 and S_2 of equal wavelength λ. Let $\mathbf{r}_{1,2}$ point from $S_{1,2}$ to a point in the far field on a screen. The phase difference of the two waves is $\delta = k(r_2 - r_1)$ (section 2.1). In an atomic resolution holography experiment, S_1 would be the source and S_2 would be the object. An additional path length difference kd would be introduced into the phase δ. If the screen is *parallel* to the line connecting S_1 and S_2 and is a distance $a \gg d$ from it, the central maximum is obtained for $r_1 = r_2$. The first minimum is obtained for $\lambda/2 = r_1 - r_2 \approx d\sin\theta$ for small θ, $\theta \ll \pi/2$. Then the two sources can be resolved on the screen if

$$d \gtrsim \frac{\lambda}{2\sin\theta}. \tag{2.107}$$

This corresponds to the ideal resolution obtained by a microscope of aperture θ (eq. 2.2 for $b = 0.5$). The value $\lambda/2$ is not reached here since eq. 2.107 was derived for small θ. On a screen that is *perpendicular* to the line connecting S_1 and S_2, eq. 2.107 does not hold. In this case, for small θ, the path difference $q_1 - q_2 \approx d$ is nearly independent of the distance x on the screen and the point sources cannot be resolved for small θ.

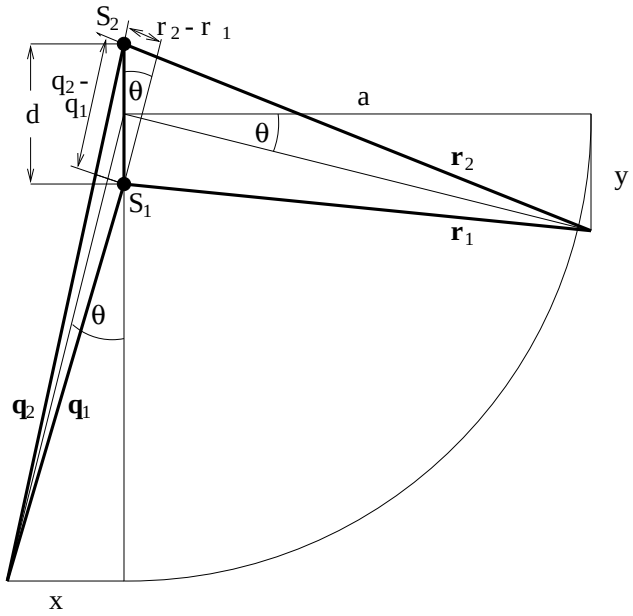

Figure 2.15: Two coherent point sources S_1 and S_2, separated by a distance d, produce an interference pattern at a distance $a \gg d$. The figure is not to scale. $\mathbf{r}_{1,2}$ go from $S_{1,2}$ to one point on a circular screen, $\mathbf{q}_{1,2}$ go from $S_{1,2}$ to another point on the screen. For small angles θ, $r_1 - r_2 \approx yd/a \equiv d\tan\theta \approx d\sin\theta$, while $q_1 - q_2 \approx d\cos\theta \approx d \neq xd/a \equiv d\tan\theta \approx d\sin\theta$.

The sources S_1 and S_2 in Young's double slit experiment are like two atoms of a structure in atomic resolution holography. The positions of S_1 and S_2 are known in fig. 2.15 but the atom positions are not known in atomic resolution holography. In order to record an interference pattern for arbitrary atom positions, the interference pattern is recorded on a sphere around S_1 and S_2 in atomic resolution holography. If the full sphere is covered then an isotropic spatial resolution of about $\lambda/2$ is obtained.

Chapter 3

Numerical Reconstructions of Calculated Holograms

The hologram formation was described in section 2.3 and analytical reconstructions of simple holograms were discussed in section 2.6.3. As shown there, such reconstructions can be used to demonstrate the effect of twin images, to calculate the spatial resolution of the method, and to analyse reconstruction algorithms for simple structures that contain only a few atoms. Real structures usually contain many atoms. In order to take many atoms into account and to allow to handle more realistic assumptions, holograms can be calculated and reconstructed numerically. Numerical calculations can be used to study systematically the holographic methods and the calculated results can be compared with experimental results. This can improve the understanding of the methods and can be used for a refinement of the results.

The assumptions made in the numerical hologram calculations are given in section 3.1 and examples of calculated holograms are shown. Several holograms were reconstructed numerically. These reconstructions are shown and discussed in section 3.2.

3.1 Numerical Hologram Calculations

Interference intensities were calculated for small clusters of atoms using

$$I_c = I_0 \left| 1 + \sum_{j=1}^{n} \frac{r_e f(\mathbf{r}_j, \mathbf{k})}{r_j} e^{i(kr_j - \mathbf{k}\mathbf{r}_j)} \right|^2 \tag{3.1}$$

under the following assumptions.

- The local field intensity is calculated in the frame work of classical electrodynamics [Adams98].
- Atoms are treated as point scatterers.

- The superposition of a plane incident wave of intensity $I = I_0$ and scattered waves originating in atom positions is calculated.

- Multiple scattering which is present but very weak for x rays [Len94, Len97d] is neglected as are polarization and near-field effects [Adams98]. Polarization effects in MEXH are taken into account in calculations in [Len97a]. The square of the object waves $|O(\mathbf{k})|^2$ is taken into account.

- In order to account for the amplitude and angular distribution of the scattering power of the atoms, the real parts of the atomic form factors are included. The tabulated values of the scattering factor are defined for plane wave scattering so that their use implies an approximation. [IUC85] (p. 201 ff)

Under these assumptions, XFH and MEXH holograms are very similar except for the opposite signs of the phases $\mathbf{kr}$ (eqns. 2.23, 2.38). The XFH phase $(kr_j - \mathbf{kr}_j)$ is used for all hologram calculations in this chapter: XFH and MEXH are treated as equivalent. They only differ in interference energy and in the interpretation of the central atom of the cluster, which is the fluorescence emitter atom in XFH and the detector atom in MEXH.

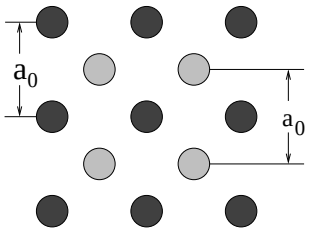

Figure 3.1: Schematic illustration of the bcc Fe structure. The lattice constant is $a_0 = 2.87$ Å. The dark circles correspond to atom positions in a $\{001\}$ lattice plane and in planes that have distances of $n \cdot a_0$, $n \in \mathbb{Z}$ from this plane. The light circles correspond to positions of atoms in planes $(2n+1)a_0/2$, $n \in \mathbb{Z}$ above and below this plane.

Such hologram calculations can be used to study systematically the spatial resolution and peak positions in the images as functions of the hologram energy and angular range for an ideal theoretical case in which statistical fluctuations do not occur [Adams98, Kossel98, Adams99]. The computer program for calculating holograms was written by B. Adams [Adams98]. For comparison with the experimental results of chapter 6, the calculations discussed here were performed for a body-centered cubic (bcc) Fe cluster. The structure of bcc Fe is shown schematically in fig. 3.1. The cluster is spherical and has a radius of two lattice constants ($2a_0 = 2 \times 2.87$ Å) so that effects caused by the long range translational order of crystals do not arise.

Holograms are calculated for different energies on an angular grid of incidence angle $\theta = -90°, ... + 90°$ and azimuthal angle $\varphi = 0°, ...359°$. The step size in both angles

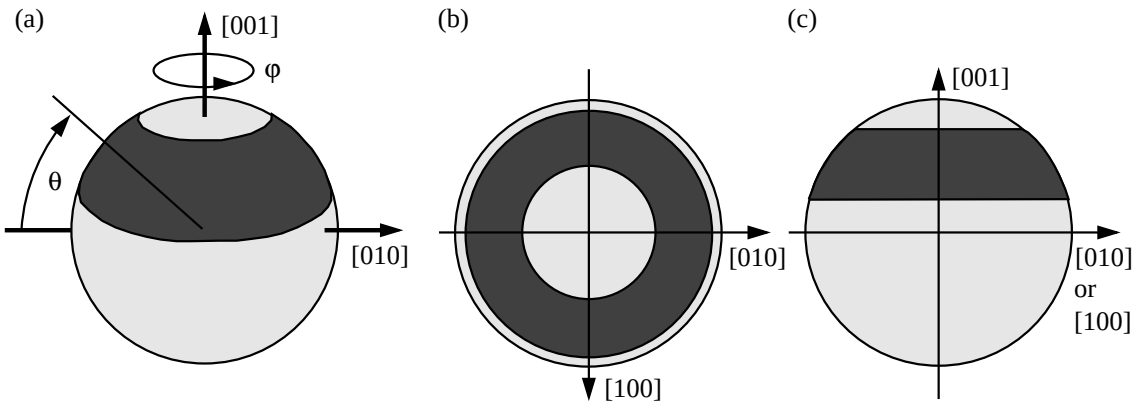

Figure 3.2: (a) Schematic illustration of the angular range in an x-ray holography experiment. θ is the incidence angle in MEXH or the detection angle in XFH. φ is the azimuthal angle. The dark area of the sphere indicates a typical angular range for an experimental hologram. In this case, the φ rotation axis and the crystal [001] axis coincide. (b) The projection of the hologram on the (001) lattice planes keeps the symmetry around the [001] axis. (c) The projection of the hologram on the (010) or (100) lattice planes is not symmetric with respect to the [100] axis.

was in all cases 1° as in the bcc Fe experiments (chapter 5). The angles θ and φ are illustrated in fig. 3.2 (a). For experimental holograms, there is a difference between the incidence angles θ and φ_s that are relevant in MEXH and the detection angles α and φ_d that are relevant in XFH (compare fig. 2.8 (a)). In this chapter, the angles θ and α will be treated as equivalent. The azimuthal angles φ, φ_d, and φ_s will also be treated as equivalent as consequence of the assumptions made in the hologram calculations. A theoretical investigation on optimized $\mathbf{k}$ space sampling was given by P. M. Len et al for electron emission holography [Len96]. An estimate for necessary angular and energy ranges and step sizes is given in section 2.3.1.

The constant background of intensity $I = I_0$ due to the reference wave is removed from the numerically calculated intensities using eq. 2.8. Resulting holograms are shown in fig. 3.3. These holograms were calculated for the interference energies $E_1 = 6.400$ keV and $E_2 = 7.058$ keV. The φ_d rotation axis was parallel to the [001] direction of the bcc Fe cluster for all hologram calculations discussed here. The holograms have a fourfold symmetry along the azimuthal angle φ_d that corresponds to the fourfold symmetry of the structure.

3.2 Numerical Reconstructions

The holograms were reconstructed according to eqns. 2.67, 2.70, where the integrations were replaced by summations. Volumes of (16 Å)^3 and, for a higher spatial resolution, of (7 Å)^3 are reconstructed on a spatial grid of (61 points)^3 with the fluorescence atom at the center. In this chapter, the fluorescence atom will be called emitter atom, corresponding to its function in XFH but it could also be called detector atom in correspondence with its function in MEXH. A

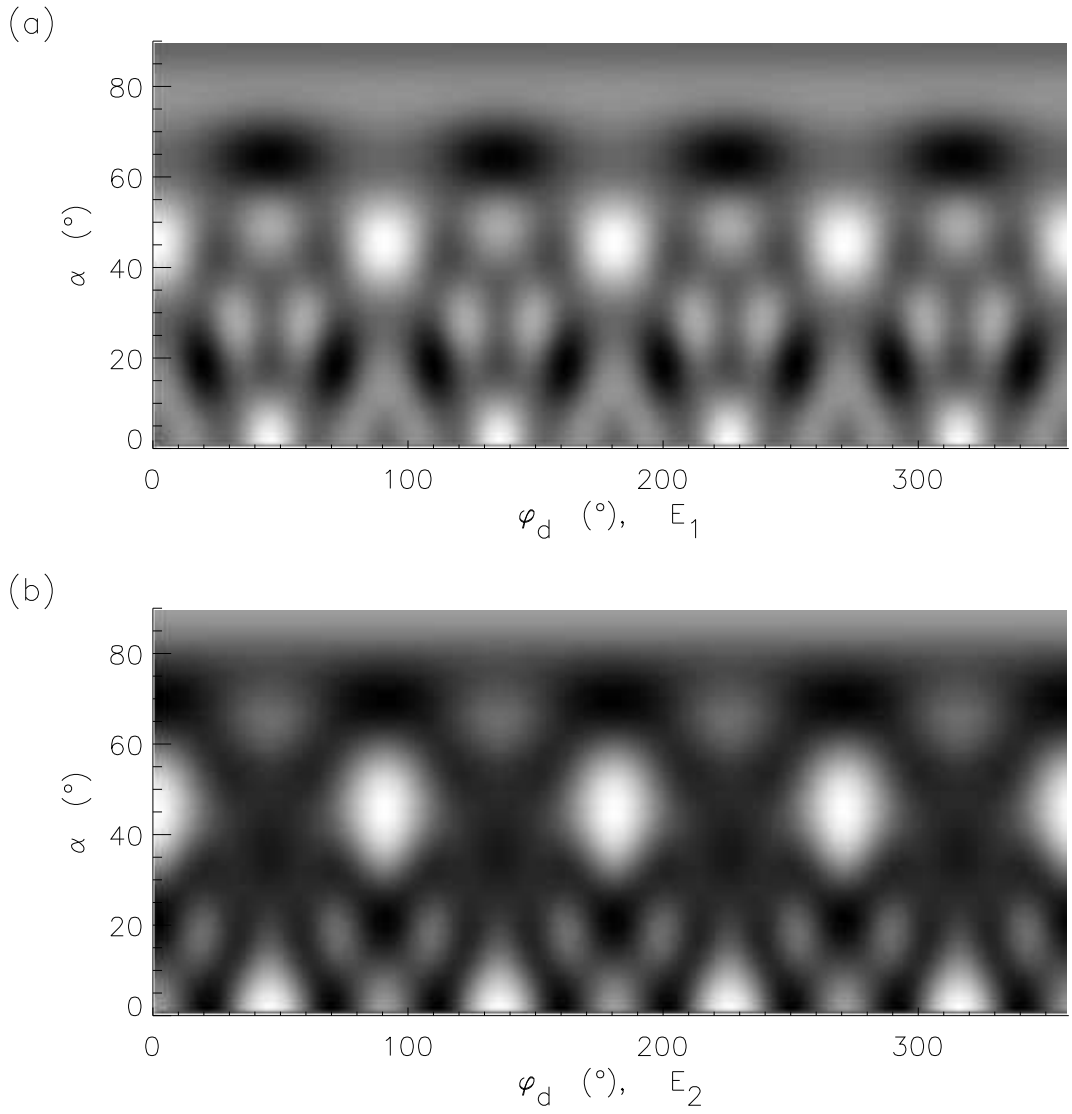

Figure 3.3: Holograms calculated at the interference energies (a) $E_1 = 6.400$ keV and (b) $E_2 = 7.058$ keV. The holograms are displayed in a linear greyscale where black corresponds to the maximum intensity and white to the minimum intensity of each hologram.

constant background in the holograms leads to a high peak at the emitter atom position in the reconstruction (section 2.6.1, following eq. 2.67). Due to the removal of the reference wave, no high peak occurs at the position of the emitter atom.

The reconstructions $\psi_k(\mathbf{r})$ at a single energy and $\psi(\mathbf{r})$ at multiple energies depend upon three spatial coordinates. Such a three-dimensional reconstruction cannot easily be displayed. Image intensities $|\psi_k(\mathbf{r})|^2$ and $|\psi(\mathbf{r})|^2$ can best be visualized in two-dimensional cuts where intensities are visualized using color and where information on the third spatial coordinate is lost. Such two-dimensional cuts are shown for example in fig. 3.4. In this chapter, all such two-dimensional cuts show

$|\psi_k(\mathbf{r})|^2$ or $|\psi(\mathbf{r})|^2$ without any cutoff in a linear greyscale where black corresponds to maximum peak intensity. For a quarter of each image, positions of atoms in bcc Fe in the image plane are indicated by the crosspoints of lines. If the full information on peak positions and heights is desired, one-dimensional cuts can be evaluated. The information on the two remaining spatial coordinates is lost in this case. Such one-dimensional cuts are shown for example in fig. 3.6.

The coordinate system in atomic resolution holography usually has the emitter respective detector atom at the origin (in the center) and a volume around this atom is reconstructed. The position of this atom is at the coordinate origin (in the center of most images). The images show the local neighborhood of this atom or in the case of many such atoms, the sum over their local neighborhoods (section 2.5.1). Even if crystals are imaged there is no reason to display only one unit cell in atomic resolution holography as might be expected from crystallography. The goal is to image the *local* environment of the emitter respective detector atom in atomic resolution holography. This is different from crystallography where the unit cell of a crystal structure is solved and where the full information is contained in the unit cell so that it would not be useful to display more than one unit cell. Atomic resolution holography is not based on the concept of a crystal unit cell and does not require a structure to have long-range translational order (section 2.5). An ideal reconstruction of the local environment of an atom incorporated in a crystal would have peaks at the neighbor atom positions. This ideal case may not even be met in reconstructions of calculated holograms since reconstructions at a single energy or at few energies may be misleading (section 2.6).

3.2.1 Reconstructions at Two Energies

Fig. 3.4 presents two-dimensional cuts through three-dimensional images $|\psi_k(\mathbf{r})|^2$, $|\psi(\mathbf{r})|^2$ obtained by reconstructing calculated holograms of different angular ranges and energies. The images are also shown in appendix B, fig. B.1 in a larger area. The image planes are parallel to the (001) lattice planes and pass through the emitter atom at the origin (0,0). This corresponds to the situation of fig. 3.2 (b) where the projection of the hologram on the (001) lattice planes keeps the symmetry around the [001] axis. The hologram energies 6.400 keV and 7.058 keV correspond to the energies of the Fe K_α and K_β lines, respectively, which are available in a XFH experiment of Fe. The complex reconstructions $\psi_{k1}(\mathbf{r})$ and $\psi_{k2}(\mathbf{r})$ at the single energies were combined using eq. 2.70 to obtain a multiple-energy reconstruction $\psi(\mathbf{r})$ which can be called "energy-added" reconstruction. The integration in eq. 2.70 was replaced by a summation. $\psi(\mathbf{r})$ depends upon the relative weights of the single-energy reconstructions which present the extreme possibilities for the combined image. For calculated holograms, there is no reason to use different weighting factors for $\psi_{k1}(\mathbf{r})$ and $\psi_{k2}(\mathbf{r})$, so that relative weights of 1 were used here in order to sum the two single-energy reconstructions in the combined image with equal weights.

The angular ranges $\Delta\theta_1 = 0°...59°$ and $\Delta\theta_2 = 24°...83°$ were available in our bcc Fe XFH experiment (chapter 5) while the 4π range corresponds to the ideal case which allows isotropic spatial resolution. In fig. 3.4 (e) the spatial resolution along

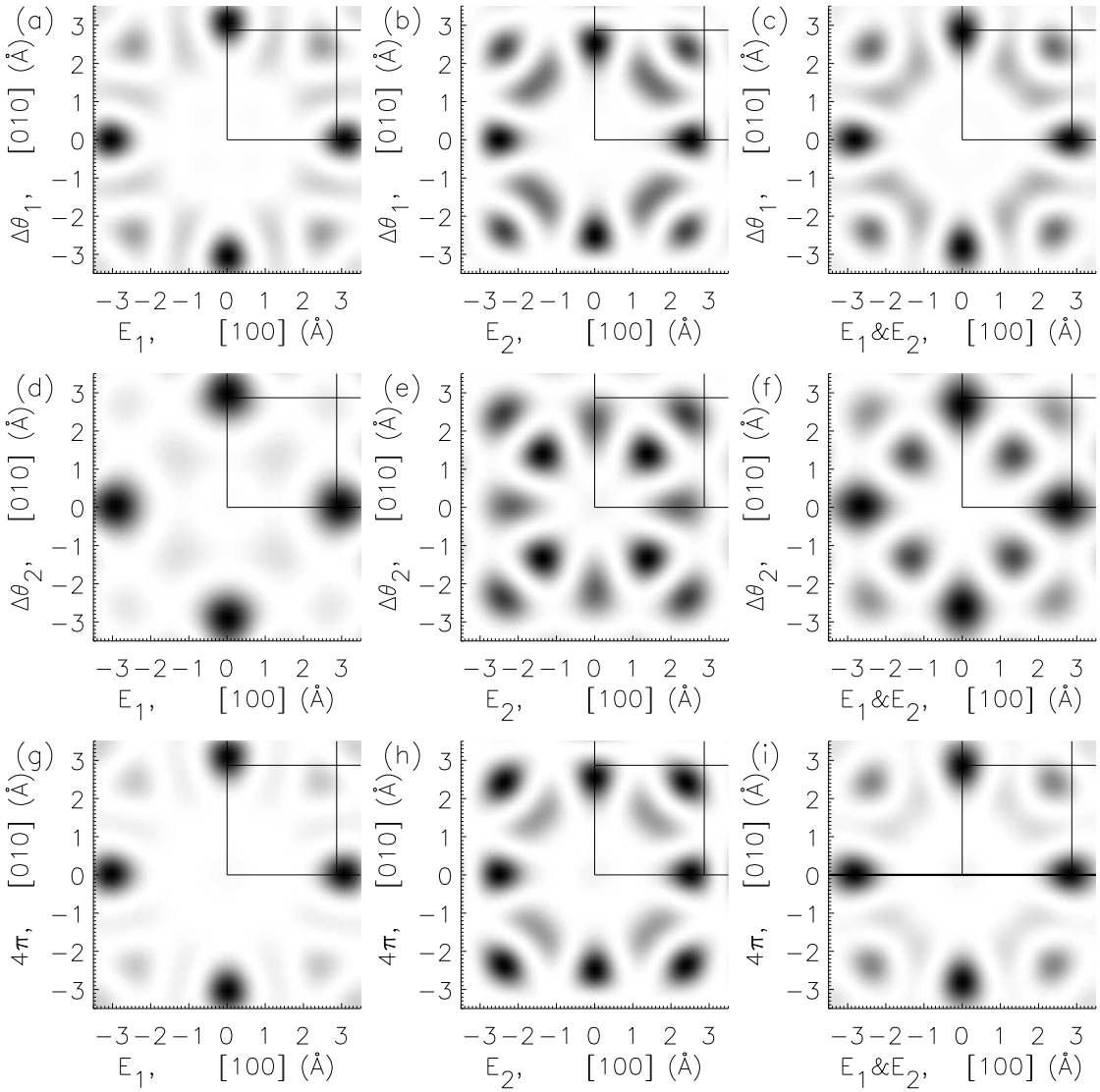

Figure 3.4: Reconstructions of calculated holograms in a plane parallel to the (001) lattice planes and passing through the emitter atom. The hologram range $\Delta\theta_1 = 0°...59°$ was reconstructed in (a)-(c), the range $\Delta\theta_2 = 24°...83°$ in (d)-(f), and a full 4π sphere in (g)-(i). In all cases, $\varphi = 0°...359°$ was used. The hologram energies are $E_1 = 6.400$ keV in (a), (d), (g), $E_2 = 7.058$ keV in (b), (e), (h), and both energies were added according to eq. 2.70 in (c), (f), (i). The thick line in (i) indicates the position of a cut (cut_1 of fig. 3.6).

the [001] direction is so low that the highest peaks occur at positions of atoms that are half a lattice constant above or below the image plane (fig. 3.1, grey circles). In all other cases of fig. 3.4 the highest peaks appear close to atom positions of the image plane (fig. 3.1, black circles). The spatial resolution within the image plane is similar for the different angular ranges and energies used while the spatial resolution perpendicular to the image plane, the exact peak positions, and the image background depend upon energy and angular range.

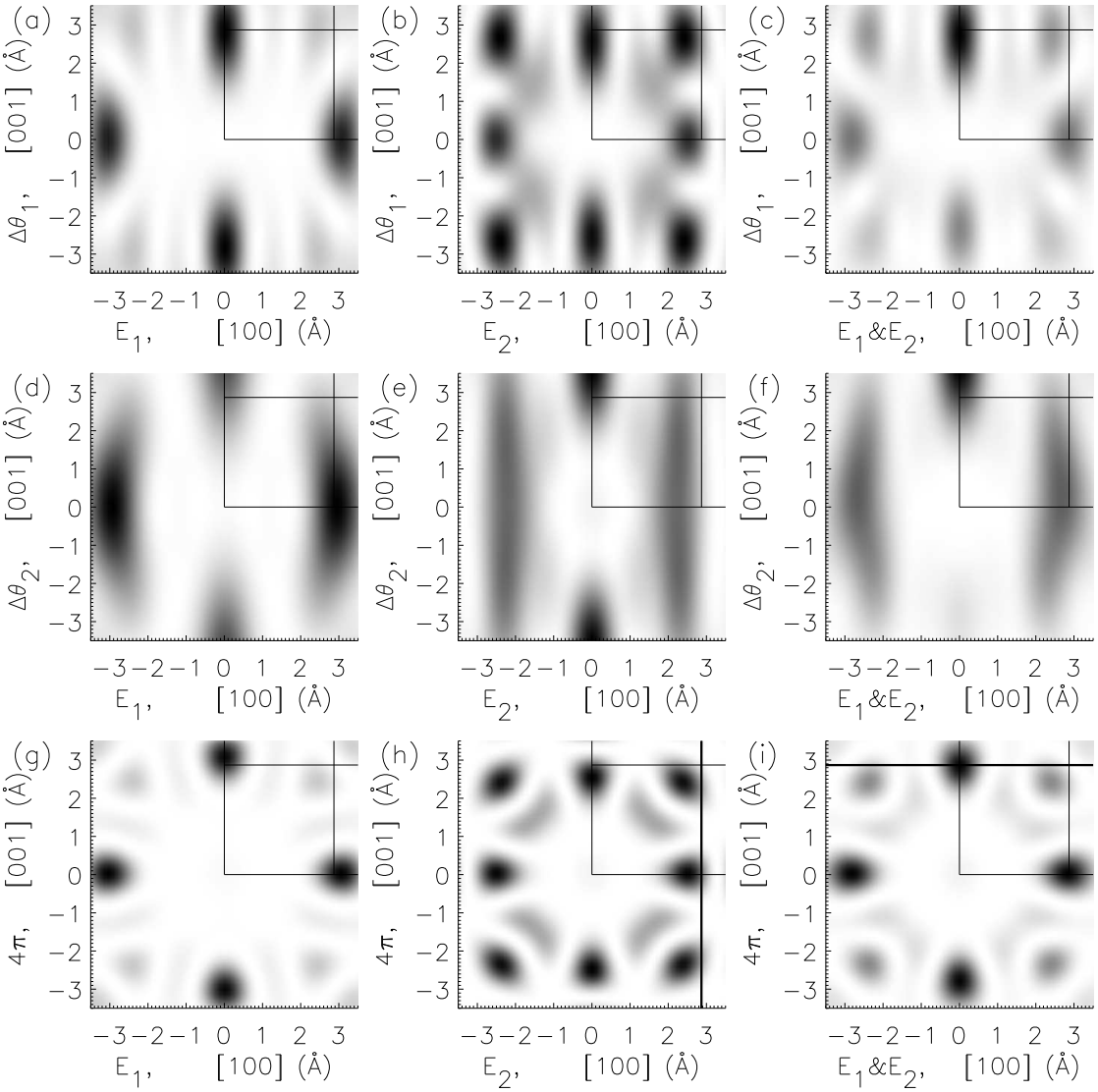

Figure 3.5: Reconstructions of calculated holograms in a plane parallel to the (010) lattice planes and passing through the emitter atom. The hologram range $\Delta\theta_1 = 0°...59°$ was reconstructed in (a)-(c), the range $\Delta\theta_2 = 24°...83°$ in (d)-(f), and a full 4π sphere in (g)-(i). In all cases, $\varphi = 0°...359°$ was used. The hologram energies are $E_1 = 6.400$ keV in (a), (d), (g), $E_2 = 7.058$ keV in (b), (e), (h), and reconstructions from both energies were added according to eq. 2.70 in (c), (f), (i). The thick lines in (h), (i) indicate the positions of cuts (cut_2, cut_3 of fig. 3.6, respectively).

The corresponding reconstructions in planes parallel to the (010) lattice planes and passing through the emitter atom at (0,0) are shown in fig. 3.5. For a limited θ range as in parts (a)-(f), the spatial resolution in planes perpendicular to the φ rotation axis (fig. 3.4) is higher than in planes containing it (fig. 3.5). The limited θ ranges of these holograms do not correspond to the symmetry of the structure (fig. 3.2 (c)). The peaks in fig. 3.5 along the [001] direction are much

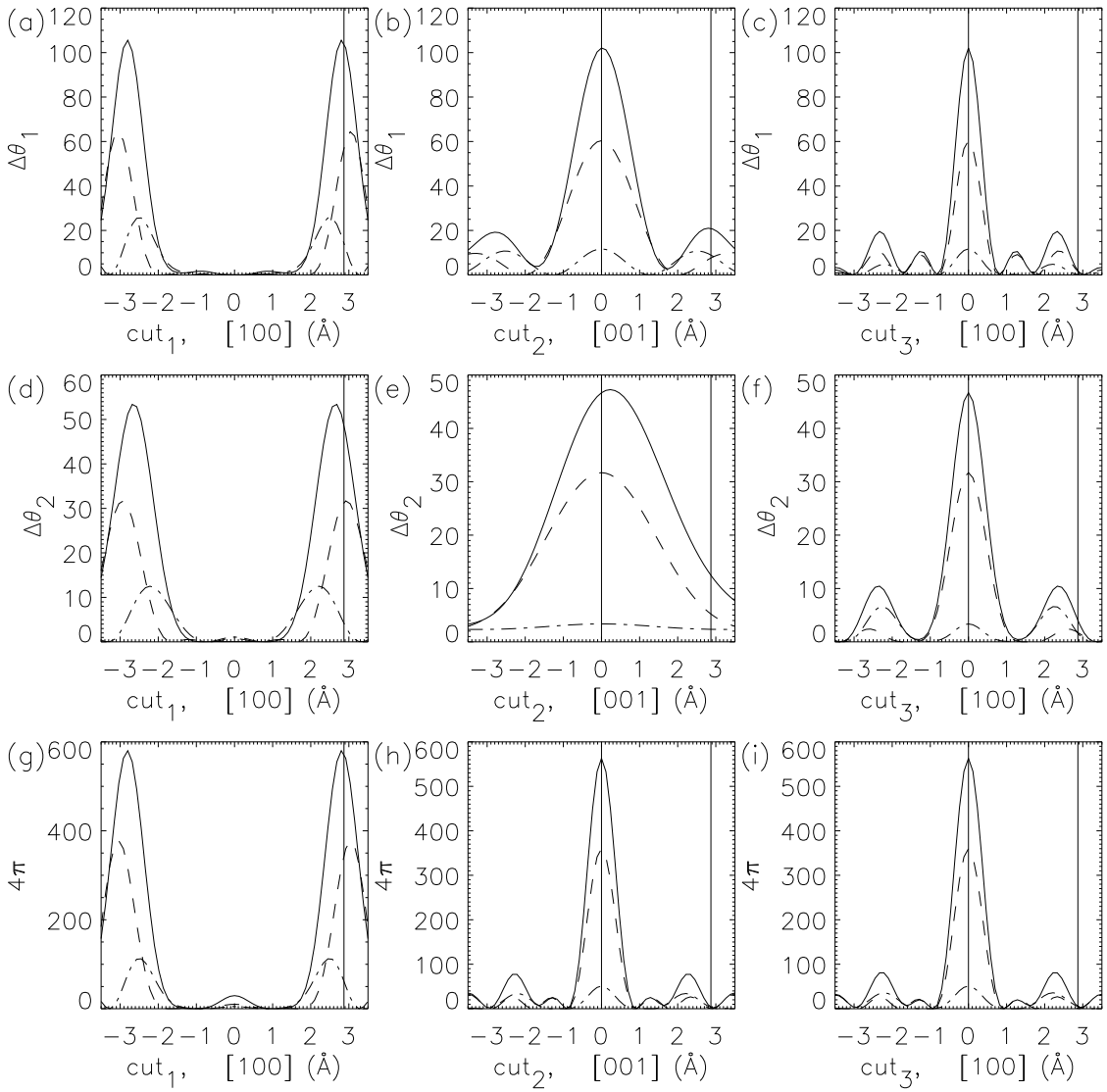

Figure 3.6: One-dimensional cuts through the reconstruction planes of figs. 3.4, 3.6. Parts (a), (d), (g) show cuts parallel to the [100] axis, passing through the emitter at the origin 0 as indicated in fig. 3.4 (i). (b), (e), (h) are cuts parallel to the [001] axis, at a distance of 2.8 Å $\sim a_0 = 2.87$ Å from the emitter as shown in fig. 3.5 (h). (c), (f), (i) are cuts parallel to the [100] axis, at a distance of 2.8 Å from the emitter as shown in fig. 3.5 (i). The holograms cover $\varphi = 0°...359°$ in all cases, $\Delta\theta_1 = 0°...59°$ in (a)-(c), $\Delta\theta_2 = 24°...83°$ in (d)-(f), and a full 4π sphere in (g)-(i). The hologram energies are indicated by different lines: $E_1 = 6.400$ keV by dashed lines, $E_2 = 7.058$ keV by dash-dotted lines, and both combined energies by solid lines. Vertical lines are drawn for positive x-values at the atom positions in bcc Fe.

wider for the angular range $\Delta\theta_2 = 24°...83°$ than for the range $\Delta\theta_1 = 0°...59°$. This explains that peaks from atoms half a lattice constant above or below the image plane of fig. 3.5 (e) can be higher than the peaks of that image plane. In order to obtain a high spatial resolution in three dimensions from a limited angular

range, the range should be measured close to the equator $\theta = 0°$. Experimental intensities change with θ due to absorption. For the geometry of section 2.4.1 and at the equator, the MEXH intensity becomes maximal while the XFH intensity vanishes. For this geometry, it is more practical to obtain high hologram intensities close to the equator in MEXH than in XFH - and in this way a high spatial resolution in three dimensions from a limited angular range. This shows that different absorption conditions can be relevant for the holograms in XFH and MEXH experiments. As expected from section 2.6.3, the images obtained from 4π holograms are the same in planes parallel (fig. 3.4 (g)-(i)) and perpendicular (fig. 3.5 (g)-(i)) to the (100) lattice planes. In this case, resolution, peak height and distance to the fluorescence emitter atom are the same for atoms that have the same position relative to the emitter atom, independent of the image plane.

For a quanitative evaluation, one-dimensional cuts through the reconstructions were evaluated. Fig. 3.6 shows one-dimensional cuts at three different positions (indicated in fig. 3.4 (i), fig. 3.5 (h), (i)) for the angular ranges and energies of figs. 3.4, 3.5. It can be clearly seen that the exact peak heights, positions and widths depend on hologram energy and angular range. The one-dimensional cuts of fig. 3.6 pass through atom positions of bcc Fe. Since the peak positions in the reconstructed images depend upon energy and angular range, these cuts may miss the exact peak positions. In order to perform a reliable evaluation, the peak heights and positions were determined not from these scans but directly as the values and positions of the maxima in the three-dimensional reconstructions. One-dimensional radial scans through the emitter and the so-obtained peak positions were used to determine the peak widths. The widths were determined as the full widths at half maximum of the peaks. These values depend upon the choice $|\psi(\mathbf{r})|^2$ of image function (section 2.6.1).

The reconstructions shown in this chapter use a spatial grid of 61 points/16Å which corresponds to 0.26Å per point or a grid of 61 points/7Å which corresponds to 0.12Å per point. Not all peaks are completely symmetric with respect to their maximum so that peak positions and widths were determined with an accuracy of about ± 0.2 Å for the finer grid. The best positions and widths are obtained from 4π holograms: Their reconstructions peak at the correct *directions* relative to the emitter but their *distances* may differ from the ideal values, and the spatial resolution is nearly isotropic. The reconstructed volume of (7 Å)^3 centered around the emitter contains its nearest, next-nearest, third-nearest and fifth-nearest neighbors. They can be seen in the one-dimensional cuts of fig. 3.7 (c), (a), (b) and (c), respectively.

Table 3.1 gives the distances d_c between emitter and neighbors obtained from the three-dimensional reconstructions together with the peak widths r_c and *heights* max_c. These values are obtained by reconstructing calculated holograms according to eqns. 2.67, 2.70, and then forming the absolute value $|\psi_k(\mathbf{r})|^2$ or $|\psi(\mathbf{r})|^2$. For a simple structure that consist only of two or three atoms, the highest peaks occur at atom positions $\mathbf{r}_j$ and at twin image positions $-\mathbf{r}_j$, while weaker peaks may occur elsewhere (section 2.6.3). The highest peaks will therefore usually be interpreted as peaks that correspond to atoms or to their twins. Therefore the relative heights

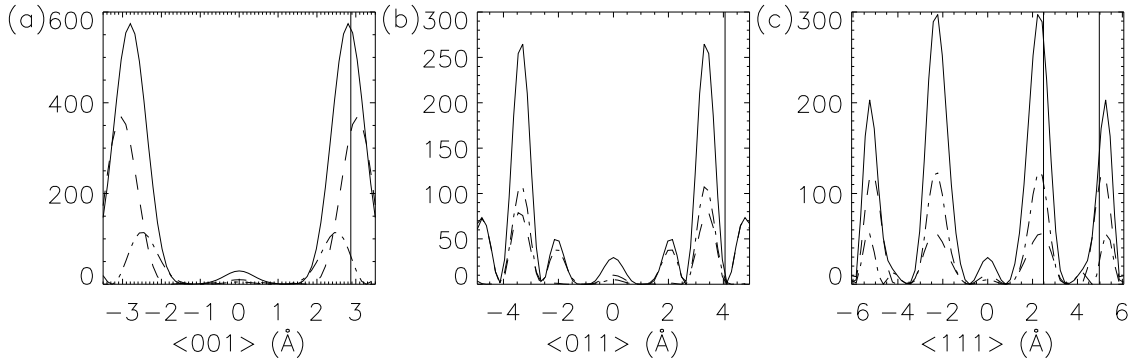

Figure 3.7: One-dimensional radial cuts through the three-dimensional reconstructed images $|\psi_k(\mathbf{r})|^2$, $|\psi(\mathbf{r})|^2$ of calculated 4π holograms. The emitter is in the center of all cuts which pass (a) parallel to the <001> directions through its next-nearest neighbors, (b) parallel to the <011> directions through its third-nearest neighbors, (c) parallel to the <111> directions through its nearest and fifth-nearest neighbors. The hologram energies are indicated by different lines: $E_1 = 6.400$ keV by dashed lines, $E_2 = 7.058$ keV by dash-dotted lines, and both energies combined by solid lines. Part (a) is the same as fig. 3.6 (g).

nn	$E_1 = 6.400$ keV			$E_2 = 7.058$ keV			E_1 & E_2			
	max_c	d_c	r_c	max_c	d_c	r_c	max_c	d_c	r_c	d_k
1^{st}	60	2.4	1.3	120	2.2	1.0	300	2.2	1.1	2.49
2^{nd}	370	3.0	0.9	110	2.4	0.8	570	2.8	1.0	2.87
3^{rd}	80	3.4	0.8	110	3.2	0.8	260	3.2	0.7	4.06
5^{th}	120	5.0	0.8	60	5.2	0.7	200	5.2	0.8	4.97

Table 3.1: Distances d_c from emitter to its 1^{st}, next- (2^{nd}), third- (3^{rd}) and fifth- (5^{th}) nearest neighbors (nn), determined from three-dimensional reconstructed images $|\psi_k(\mathbf{r})|^2$ of calculated holograms at the energies $E_1 = 6.400$ keV, $E_2 = 7.058$ keV, and from the energy-added reconstructed image $|\psi(\mathbf{r})|^2$ using E_1 and E_2. The full widths at half maximum r_c and the maximum values max_c are also given. d_c and r_c were determined with an accuracy of about ± 0.2 Å. The values d_k are obtained from the tabulated lattice constant $a_0 = 2.87$ Å of bcc Fe which was used for the hologram calculations.

of different peaks within one reconstruction are important. The relative heights of peaks in different reconstructions are important when two or more reconstructions are to be combined. The peak heights depend upon the reconstruction algorithm and the image function chosen. The reconstruction algorithm and image function used here do not reproduce the electron density: For a single scattering atom at $\mathbf{r}_j$ and at a single energy, a peak height of $|\psi_k(\mathbf{r}_j)|^2 \approx (2r_e f_0)^2/(R^2 r_j)^2$ is obtained at the atom position $\mathbf{r}_j$ under simple assumptions (section 2.6.3, eq. 2.92). The peak height is proportional to $1/r_j^2$, where r_j is the distance from the emitter atom to the position of the neighbor atom. Therefore it can be expected that the peak

heights decrease for increasing distances r_j. Twin image effects and effects due to many atoms in a structure can lead to deviations from this simple prediction for peak heights. Between the hologram calculations shown here and the simple cases of section 2.6.3, additional deviations can be due to different assumptions: here, the square of the object waves and the real parts of the atomic scattering factors are taken into account while they are neglected in section 2.6.3. In the future, a different algorithm may allow to reconstruct the electron density and give direct meaning to the peak heights.

At 6.400 keV, the highest peaks occur at the second-nearest neighbor positions. At 7.058 keV, the peaks at first- to third-nearest neighbor positions have approximately the same heights. The peak heights in the reconstructed images $|\psi_{k1}|^2$ at 6.400 keV and $|\psi_{k2}|^2$ at 7.058 keV do not *sum* up in the image $|\psi|^2$ because the complex ψ_{k1} and ψ_{k2} are added according to eq. 2.70 and then the absolute square $|\psi|^2$ is formed.

The peak *distances* d_c from the emitter to its nearest, third- and fifth-nearest neighbors obtained at 6.400 keV correspond to those at 7.058 keV, while the distances to its second-nearest neighbors are different. Many distances are close to the tabulated values d_k but others differ significantly from the tabulated values as can be seen from the third-nearest neighbors of the emitter. These peak positions occur at a distance of nearly 1 Å from the correct atom positions. The effect can be explained by effects caused by many atoms in a structure (section 2.6.3). All peak *widths* r_c are between (0.7 ± 0.2) Å and (1.3 ± 0.2) Å and do not differ significantly for 6.400 keV and 7.058 keV. Peak widths of 0.9 Å at 6.4 keV and of 0.8 Å at 7.1 keV would be expected from eq. 2.93.

These results for calculated holograms show that reconstructions at one or two energies can give some information about a structure but do not not exactly resemble the structure. Therefore, a refinement is needed to achieve a better agreement between positions obtained in the reconstructions of calculated holograms and the positions used in the hologram calculations. Distances obtained from holograms at different energies can be compared in order to check if they agree with each other but an agreement between the distances obtained for two different energies does not necessarily lead to the correct values for the structure as can be seen from the third-nearst neighbor distances. Such calculations can also be used to estimate how much the positions determined from reconstructions may deviate from the actual positions in a certain structure.

3.2.2 Reconstructions at Multiple Energies

In order to evaluate further the energy-dependence of the reconstructions, holograms were also calculated for bcc Fe clusters for interference energies from 7.9 keV to 11.3 keV in steps of 0.2 keV. This energy range was available in a MEXH experiment (chapter 5). The calculations were performed for the experimentally available $\Delta\theta_1 = 19°, ...90°$, $\varphi = 0°, ...359°$ and for the ideal 4π angular range, using $\Delta\theta_2 = -90°, ...90°$, $\varphi = 0°, ...359°$. A volume of (16 Å)^3 on a grid of (61 points)^3 was reconstructed for an overview of the reconstructions.

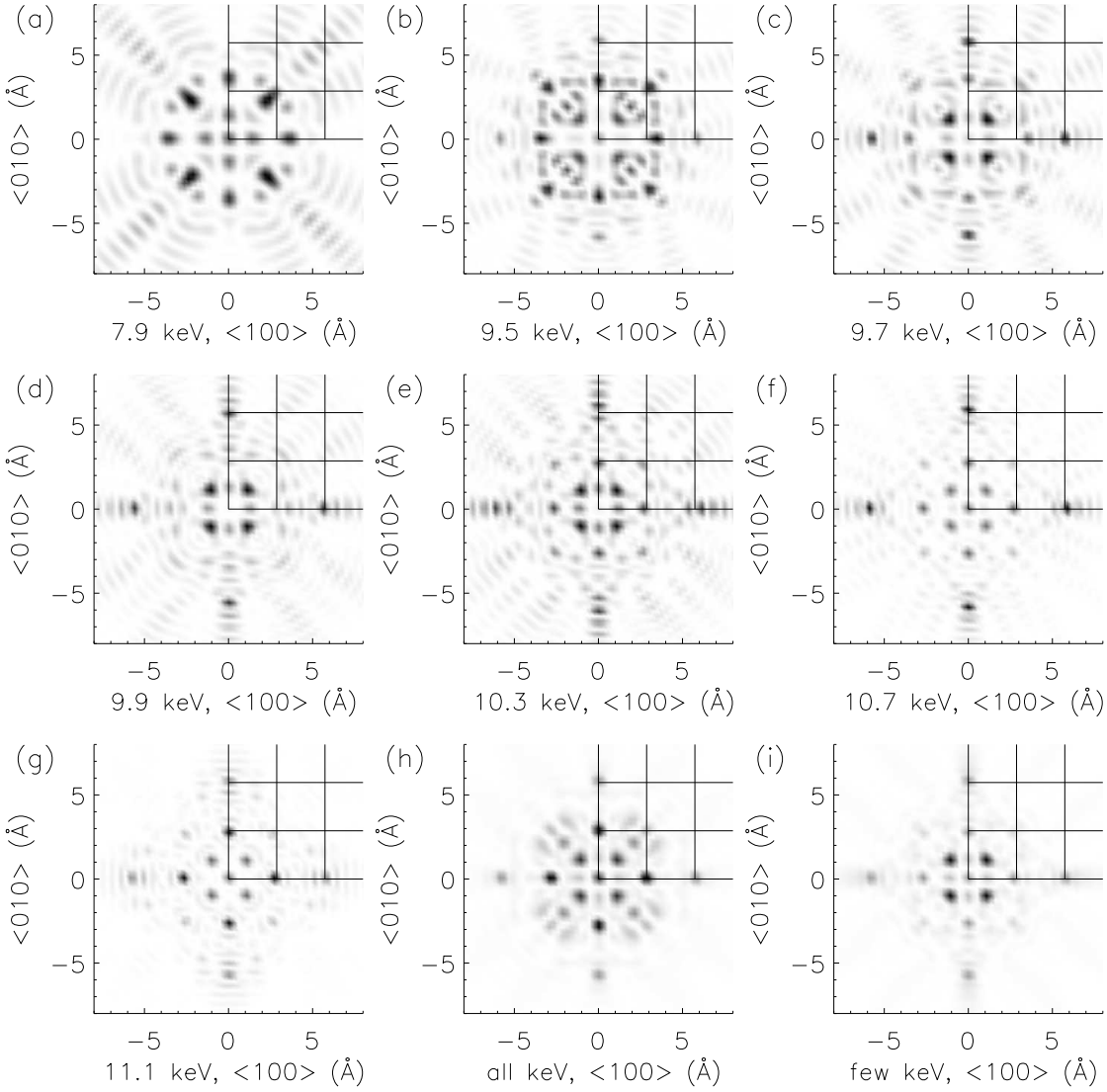

Figure 3.8: Reconstructions of calculated holograms in a plane parallel to the {001} lattice planes and passing through the emitter atom at (0,0). 4π holograms were reconstructed for the energies from 7.9 keV to 11.1 keV in steps of 0.2 keV. (h) shows the energy-added image of all single-energy reconstructions from 7.9 keV to 11.1 keV in steps of 0.2 keV. (i) shows the energy-added image of the single-energy reconstructions from 9.5 keV to 11.1 keV in steps of 0.4 keV. The constant background of intensity $I = I_0$ was subtracted from each calculated hologram before the reconstruction.

Fig. 3.8 shows reconstructions of calculated 4π holograms in a plane parallel to the {001} lattice planes and passing through the emitter atom. The images $|\psi_k(\mathbf{r})|^2$ may vary considerably for energy differences of only 0.2 keV, as the comparison of figs. 3.8 (b) and (c) at the energies of 9.5 keV and 9.7 keV shows. Fig. 3.8 (b) has the highest peaks close to the positions of the second and third nearest neighbors

of the emitter atom. These peaks are weak in fig. 3.8 (c), where peaks at positions of neighbors in about $2a_0$ distance from the emitter and peaks very close to the emitter dominate. High peaks very close to the emitter also occur at other energies, for example in fig. 3.8 (d), (e). A high peak at the origin can be caused by a constant offset in a hologram (section 2.6.3). Such an offset occurs if the sum over all angular points in the hologram is not equal to zero. In the case of the calculated holograms described here, a limited angular range, the squared object waves, or numerical errors can cause an offset. In experimental holograms, an offset can also be caused by multiple scattering, by insufficient sampling (of Kossel or XSW lines), or by errors in background removal. If a constant equal to the average value of a hologram is subtracted from the hologram, then the high peak at the origin of the reconstruction vanishes.

The single-energy reconstructions of fig. 3.8 (a)-(g) demonstrate that a structure determination from single-energy reconstructions is usually not straightforward. An improved image $|\psi(\mathbf{r})|^2$ is obtained in fig. 3.8 (h), where all single-energy reconstructions from 7.9 keV to 11.1 keV in steps of 0.2 keV were combined according to eq. 2.70. The highest peaks appear close to the positions of the second-nearest neighbors of the emitter which are the closest neighbors of the emitter in this image plane (compare fig. 3.1). High peaks occur usually close to the emitter since $|\psi_k(\mathbf{r})|^2 \propto 1/r_j^2$ but they may be suppressed by twin-image and many-atom effects as discussed in section 2.6.3 and in section 3.2.1, following table 3.1. In fig. 3.8 (i) the single-energy reconstructions from 9.5 keV to 11.1 keV in steps of 0.4 keV were combined. The peaks close to the emitter dominate the image so that peaks due to atoms of the image plane are present but hardly visible.

The corresponding reconstructions for the limited θ range $\Delta\theta_1 = 19°...90°$ are shown in appendix B. In the plane parallel to the (001) lattice planes and passing through the emitter atom (fig. B.2) they are very similar to the reconstructions of fig. 3.8. In planes perpendicular to the (001) lattice planes and passing through the emitter atom (fig. B.4) they differ from fig. 3.8 due to their reduced spatial resolution along the [001] direction. Fig. 3.9 (a) and (b) show as an example such image planes at 7.9 keV.

It may not be possible to determine the background dependence on two angular coordinates from experimental intensities (chapter 5). If the background can only be determined for single φ scans, the average information along θ may get lost during background removal. In order to investigate this situation, the following background removal was used: Instead of subtracting the constant background of intensity $I = I_0$ from the calculated intensities, for each φ scan the average value of this scan was subtracted. This average value may deviate from 1. Images obtained from these holograms are shown in fig. 3.9 (c), (d). They correspond to those of fig. 3.9 (a), (b) where the background $I = I_0$ was subtracted from the calculated intensities. Appendix B (figs. B.2, B.3, B.4, B.5) presents the corresponding reconstructions for all energies of fig. 3.8. The images of fig. 3.9 can be compared with each other. In the images (c) and (d) no peaks occur at or close to an axis that passes through the emitter atom and is parallel to the [001] direction. This

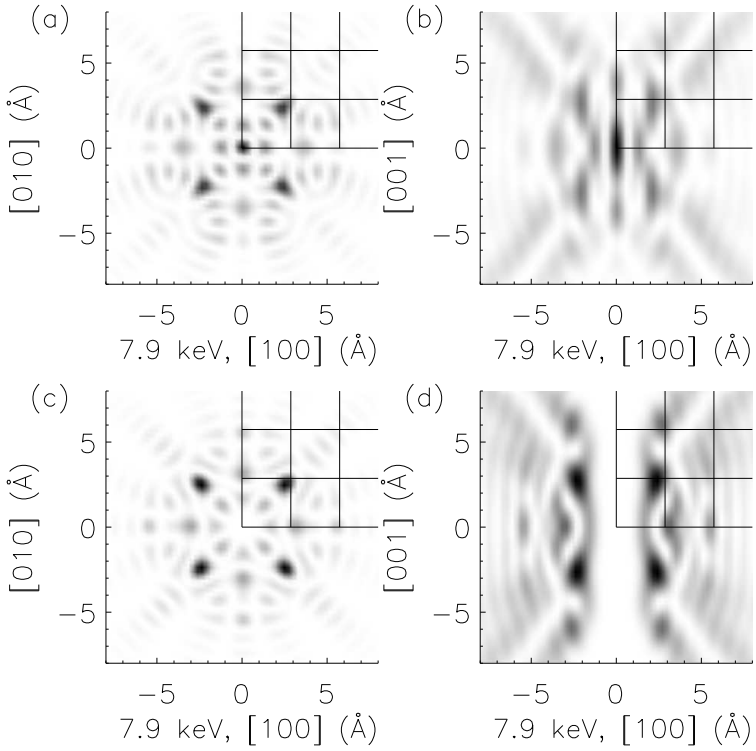

Figure 3.9: Reconstructions of holograms calculated at 7.9 keV (a), (c) in a plane parallel to the (001) lattice planes and passing through the emitter atom at (0,0). (b), (d) in a plane perpendicular to the (001) lattice planes and passing through the emitter atom. (a), (b) The constant background of intensity $I = I_0$ was subtracted from the calculated intensities. (c), (d) The average value of each φ scan was subtracted individually. The θ range of the holograms used for these reconstructions is $\Delta\theta_1 = 19°...90°$.

axis is the φ rotation axis. The angles θ and φ are defined as in fig. 3.2. Thus, the information along and close to the φ rotation axis is lost if the average value is subtracted from each single φ scan. This can also be understood directly from the holograms (section 2.3.1): If the dependence on $(kr_j - \mathbf{k}\mathbf{r}_j)$ is removed from a hologram for certain atom positions $\mathbf{r}_j$ then no information on these atom positions can be present in the corresponding reconstruction. This different background removal changes the relative intensities in the images by removing the information close to the φ rotation axis. Apart from this, the reconstructed images are very similar for both methods of background removal. For the reconstructions shown in the following, the constant background of intensity $I = I_0$ was subtracted from the calculated intensities.

Different reconstruction planes through three-dimensional energy-added reconstructions of 4π holograms are shown in appendix B (figs. B.6, B.7). For a quantitative evaluation, a volume of (7 Å)^3 was reconstructed on a grid of (61 points)^3 for the single energies. One-dimensional radial cuts through three-dimensional energy-added reconstructions $|\psi(\mathbf{r})|^2$ of the 4π holograms are shown in figs. 3.10, 3.11.

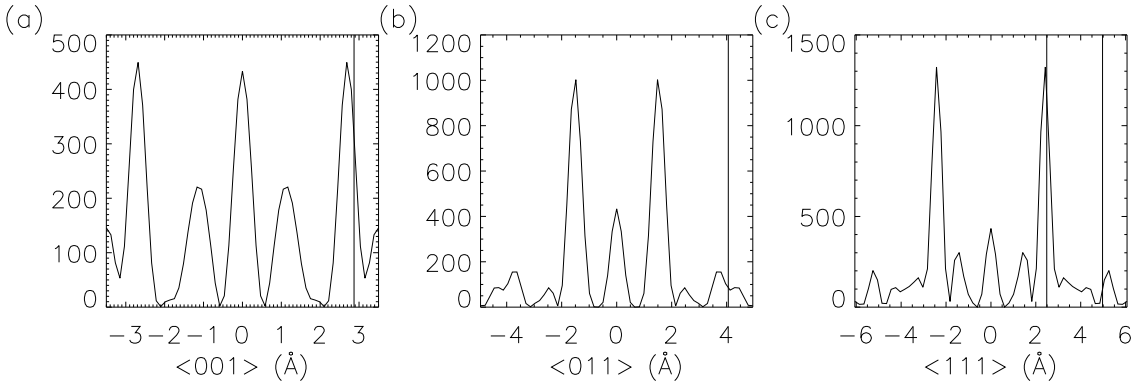

Figure 3.10: One-dimensional radial cuts through the three-dimensional energy-added reconstructed image $|\psi(\mathbf{r})|^2$ of calculated 4π holograms. The holograms were calculated at the energies 9.5 keV, 9.9 keV, ...11.1 keV. The emitter is in the center (0) of all cuts which pass (a) parallel to the <001> directions through its next-nearest neighbors, (b) parallel to the <011> directions through its third-nearest neighbors, (c) parallel to the <111> directions through its nearest and fifth-nearest neighbors. Atom positions in bcc Fe are indicated by vertical lines for positive x-values.

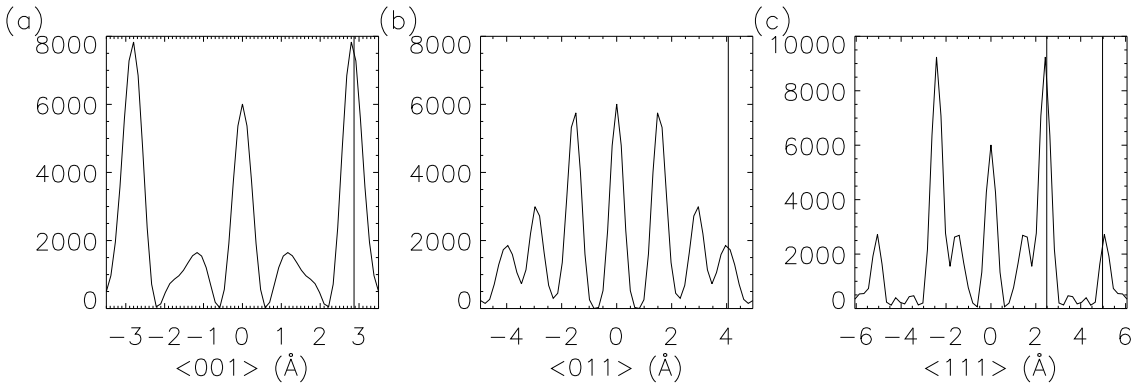

Figure 3.11: The same as in fig. 3.10 but here the holograms were calculated at the energies 7.9 keV, 8.1 keV, ...11.3 keV.

They are taken through the energy-added reconstructions obtained for the energies from 9.5 keV to 11.1 keV and from 7.9 keV to 11.3 keV, respectively. The cuts for the two energy ranges are similar but the peaks have different relative weights. For both energy-ranges, peaks appear not only at atom positions but the highest peaks at atom positions are for most cuts higher than other peaks. Such scans were used to determine the peak widths for the reconstructions $|\psi_k(\mathbf{r})|^2$ at the single energies 9.5 keV, 9.9 keV, ...11.1 keV and for the two energy-added reconstructions. The cuts pass through the emitter atom and its neighbors.

Peak distances d_c to the emitter and peak heights m_c were determined from the three-dimensional reconstructions. The values are given in table 3.2 together with the peak widths r_c. A detailed discussion of peak distances, heights and widths for two energies is given in section 3.2.1. Peak positions and widths were determined

with an accuracy of about ± 0.2 Å. In a few cuts that were used to determine the peak-widths, the highest peaks are not close to atom positions (figs. 3.10 (b), 3.11 (b)). In these cases, the table lists the parameters of peaks that are close to atom positions.

nn	9.5 keV			9.9 keV			10.3 keV			10.7 keV		
	m_c	d_c	r_c	m_c	d_c	r_c	m_c	d_c	r_c	m_c	d_c	r_c
1^{st}	70	2.5	0.6	200	2.4	0.5	180	2.4	0.5	44	2.2	0.5
2^{nd}	48	3.3	0.8	17	2.8	0.5	53	2.6	0.5	46	2.6	0.5
3^{rd}	42	4.2	0.7	18	4.5	0.4	32	3.7	0.5	17	3.6	0.6
5^{th}	35	5.3	0.6	42	5.2	0.5	46	5.2	0.8	22	4.2	0.5

nn	11.1 keV			(9.5, ...11.1) keV			(7.9, ...11.3) keV			d_k
	m_c	d_c	r_c	m_c	d_c	r_c	m_c	d_c	r_c	
1^{st}	16	2.8	0.5	1300	2.4	0.6	9200	2.4	0.7	2.49
2^{nd}	52	2.6	0.5	450	2.6	0.5	7800	2.8	0.6	2.87
3^{rd}	14	3.6	0.6	160	3.6	0.7	1700	4.1	0.9	4.06
5^{th}	10	5.0	0.7	200	5.2	0.6	2700	5.0	0.6	4.97

Table 3.2: Distances d_c from emitter to its 1^{st}, next- (2^{nd}), third- (3^{rd}) and fifth- (5^{th}) nearest neighbors (nn), determined from three-dimensional reconstructed images $|\psi_k(\mathbf{r})|^2$ of calculated holograms at the energies 9.5 keV, 9.9 keV, ...11.1 keV, and from the energy-added reconstructed image $|\psi(\mathbf{r})|^2$ using these energies or the energies 7.9 keV, 8.1 keV, ...11.3 keV. The full widths at half maximum r_c and the maximum values m_c (arbitrary units) are also given. d_c and r_c were determined with an accuracy of about ± 0.2 Å. The values d_k are obtained from the tabulated lattice constant $a_0 = 2.87$ Å of bcc Fe which was used for the hologram calculations. In a few cuts along the <001>, <011> or <111> directions, the highest peaks are not close to atom positions. In these cases, the parameters of peaks close to atom positions are listed.

The peak heights obtained here from the single-energy reconstructions at energies from 7.9 keV to 11.3 keV are comparable to those obtained at 6.400 keV and 7.058 keV (table 3.1). All reconstructions can be combined to obtain an energy-added image which depends upon the relative weights used for the single-energy reconstructions. The Barton algorithm used here has relative weights of $1/k^2$ compared to a Fourier transform and an additional phase factor (section 2.6.1) so that energy-added reconstructions differ for the Barton algorithm and a Fourier transform as reconstruction algorithm. The relative peak heights obtained in a reconstructed image depend also upon the choice of image function $|\psi(\mathbf{r})|^2$ (section 2.6.1). Hologram calculations can be used to investigate the dependence of the reconstructed images on hologram energy and angular range. Different methods of background removal can be evaluated and an estimate for peak positions, heights, and widths is obtained. The energy-added reconstructions show for the case of a bcc Fe cluster that high peaks are not only obtained close to atom positions. This holds even for the large range of energies from 7.9 keV to 11.3 keV in steps of 0.2 keV.

Chapter 4

Experiments

The signal in atomic resolution x-ray holography is on the order of $\lesssim 10^{-4}$ times the background (section 2.3). This signal is very weak but it should be larger than the statistical noise. The measurement of sufficient photon numbers within a reasonable amount of time requires a high incident flux, a high detection efficiency, and - presently - structures that provide a high signal. The experiments will be described in the following.

4.1 Experimental Setup

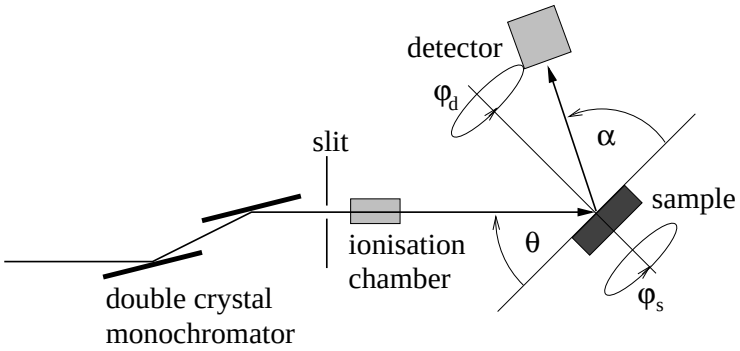

Figure 4.1: Schematic setup for atomic resolution x-ray holography. See text for details. θ: incidence angle, α: detection angle for fluorescence radiation, φ_s: rotation of the sample around its surface normal, φ_d: rotation of the detector relative to the sample rotation φ_s.

The experiments described here were carried out at the Hamburger Synchrotronstrahlungslabor HASYLAB at the Deutsches Elektronen-Synchrotron DESY. Experiments were performed in mixed MEXH, in pure MEXH and in pure XFH. The schematic setup is the same for XFH, MEXH and the mixed methods and is shown in fig. 4.1. The positron energy of the DORIS III storage ring was 4.44 GeV for the experiments described here. The synchrotron radiation from DORIS III (section 4.2) was monochromatized by two symmetric Si (111) crystals and passed a slit to define the beam spot size on the sample and to reduce background. The

incident intensity as monitored by an ionisation chamber was kept constant in order to minimize detector deadtime effects. The incident intensity was stabilized using the ionisation chamber signal in a feedback loop (MOSTAB) together with a piezo crystal acting on the angular alignment of the first monochromator crystal [Krolzig84]. Sample and detectors were mounted on a multi circle diffractometer. Different single crystals served as sample structures (section 4.4). Energy dispersive silicon drift detectors (section 4.3) were used to measure the fluorescence yield of the sample.

Holograms were measured in incremental scans in two angular coordinates. The monochromator and diffractometer movements were controlled by a computer. In the most recent experiments, an angular step size of 1° was chosen so that Kossel or XSW line patterns became visible in the holograms, thereby allowing an extension of the holograms to the full 4π angular range (chapter 6). In the mixed MEXH experiments, the incidence angle θ was varied while the detection angle α was kept constant. The sample was rotated around its surface normal relative to the incident beam and to the detector. In the pure MEXH experiments, sample and detectors were rotated together relative to the incident beam, changing the incidence angle θ and the rotation angle φ_s of sample and detector around the sample surface normal. Additionally, the energy was changed using the monochromator. In the pure XFH experiments, the detectors were rotated in detection angle α and in φ_d around the sample surface normal. Parameters of different experiments are given and discussed in chapter 5.

4.1.1 Sample Alignment

The alignment was performed in several steps. A needle on a goniometer head was aligned at the center of rotation of a multi-circle diffractometer using a microscope with a crosshair. The alignment error was about ± 0.2 mm in θ due to an error in the diffractometer θ rotation stage and smaller than ± 0.1 mm in φ_s. The silicon drift detectors were aligned optically, aiming them at the needlepoint. The center of rotation of the diffractometer was translated to the center of the beam spot in order to align the diffractometer with respect to the beam along the beam propagation direction. If the beam spot does not hit exactly the rotation axis or if the detector does not aim exactly at the rotation axis, then the distance between the beamspot on the sample surface and the detector window will change during a φ_d rotation. This will lead to a variation in the detected intensity (section 2.4.1). As an example, distances of (100 ± 1) mm lead to relative intensity variations of ± 2 % according to eq. 2.60, and distances of (50 ± 1) mm lead to relative intensity variations of ± 4 %.

The needle position indicating the center of rotation of the beam-aligned diffractometer was marked using telescope crosshairs. The sample was fixed on a goniometer head which was placed on the diffractometer instead of the needle. The midpoint of the sample surface was placed at the center of rotation of the diffractometer. The sample surface plane was aligned optically using a laser beam as shown schematically in fig. 4.2. The laser beam hit the sample surface and was reflected from it. The sample was rotated by 360° around its normal and the laser

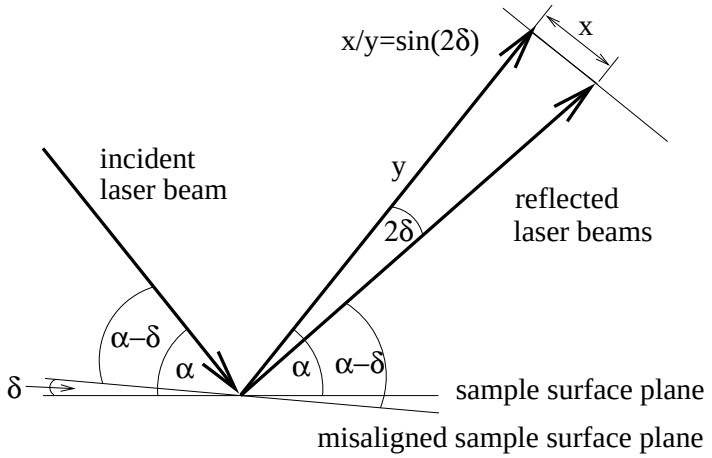

Figure 4.2: Alignment of the sample surface using a laser beam. If the sample is misaligned by an angle $\pm\delta$ then the reflected beam direction changes from α to $\alpha \pm 2\delta$.

beam spot was watched a few meters away on a wall. The sample surface plane was then aligned using the two perpendicular tilts of the goniometer head. The incident direction of the laser beam was kept constant. If the maximum tilt angle of the sample is given by $\pm\delta$ then the direction of the beam reflected by the sample changes by $\pm 2\delta$. The distance between sample surface and wall was typically 3 m and the beam spot position on the wall did not change by more than about ± 1 mm so that $\sin(2\delta) \approx 1/300$ and $\delta \approx 0.1°$.

A misalignment angle δ of the sample surface will change the intensity (section 2.4.1). For example, if $\alpha = (30 \pm 1)°$ in XFH then one obtains relative intensity variations of ± 2 % for $\mu_f \sin\theta/\mu_i = 1$, ± 1.5 % for $\mu_f \sin\theta/\mu_i = 0.5$, and ± 1 % for $\mu_f \sin\theta/\mu_i = 0.25$ according to eq. 2.60. If $\theta = (30 \pm 1)°$ in MEXH then one obtains relative intensity variations of ± 1 % for $\mu_f/(\mu_i \sin\alpha) = 1$, and smaller variations for smaller $\mu_f/(\mu_i \sin\alpha)$. Angular variations on the order of $\delta \approx 0.1°$ but not of $\pm 1°$ are expected from the sample surface plane alignment.

A considerable part of the relative intensity variations in φ scans may be attributed to a deviation between the center of rotation of the diffractometer and the position on the sample surface where the beam spot is or at which the detectors aim. Since the detectors are rotated together with the sample in MEXH but rotated around the sample in XFH, the detector alignment plays in principle a more important role in XFH than in MEXH. Nevertheless, if the detectors are for practical reasons not mounted on the same rotation stage as the sample in MEXH then a misalignment may be caused. Future detector geometries should allow an improved detector alignment. The experimental alignment also depends upon the position of the incident beam which could not be monitored at beamlines BW1 and CEMO so that we could not improve the alignment of our experiments. In principle, the variations in the experimental intensities that are caused by misalignment could be used to optimize the alignment of holography experiments. In practice, it is hardly possible to reduce

intensity variations due to misalignment to an order of magnitude that is comparable to the holographic signal which is typically smaller than 10^{-4} of the reference wave. A misalignment causes small variations of low frequency in experimental interference intensities. These effects can be separated from the holographic signal which contains typically higher frequencies (section 2.3.1). Geometric functions can be used to determine reference wave and absorption effects and to remove them from the experimental intensities (section 2.4.1).

4.1.2 Data Acquisition

The schematic data acquisition scheme is shown in fig. 4.3. The signals from the silicon drift detectors sdd1 and sdd2 are preamplified within the detector housings. They are shaped and amplified by ORTEC 579 Fast-Filter Amplifiers with differentiation and integration times of 200 ns or 500 ns. The amplitude of the output pulses is proportional to the energy of the radiation. For each detector, the shaped and amplified signals can be analysed alternatively by a multi channel analyser (MCA), an oscilloscope or by two single channel analysers (SCA) in parallel. A CAMAC computer controls the data acquisition. Since the fluorescence photons leave the sample at irregular intervals, a peak detecting MCA has to be used. A LeCroy 3512 High Performance Buffered Spectroscopy ADC with histogramming memory was the fastest available peak detecting MCA for the CAMAC system. Its deadtime was $d = 7.8\mu$s for 1000 MCA channels so that about 1 pulse/$(7.8\mu\text{s}) \approx 1.3 \cdot 10^5$ pulses/s could be recorded if the intervals between pulses were regular. Fluorescence pulses occur at random times so that the number of counts N recorded in a time t is given by $N/t = (N_0/t)\exp(-dN_0/t)$, where N_0 is the number of counts at the input of the device. For $N_0/t = 10^5/s$ and $d = 7.8\mu$s one obtains $N/N_0 = \exp(-0.78) \approx 46\%$ so that more than half of the available counts are not recorded and do not contribute to the statistics in the holograms. In order to allow for higher throughput rates than this MCA, fast SCAs (ORTEC 583 Constant Fraction Differential Discriminators) discriminated the holographic signals. For pulse widths ≥ 10 ns, their deadtime is given by the pulse width at the arming threshold +40 ns. The pulse widths at the threshold were approximately equal to the shaping times of the amplifiers. These were about 200 ns or 500 ns in our experiments so that one obtains at least $N/N_0 = \exp(-0.054) \approx 95\%$ of the incident counts for $N_0/t = 10^5/s$ and $d \leq 540$ ns. An oscilloscope was used to set the SCA energy windows to the desired values. For each detector, two SCAs were used in parallel to discriminate two different signals simultaneously.

4.2 Radiation Source

Since the signal in atomic resolution x-ray holography is on the order of $\lesssim 10^{-4}$ times the background (section 2.3), a high incident flux is necessary in order to produce a sufficiently strong signal within a reasonable amount of time. Therefore, most atomic resolution x-ray holography experiments have been performed at synchrotron radiation facilities. The physics of synchrotron radiation sources is described for example in [Wille96]. The spectral angular flux of insertion devices at HASYLAB can be found in [HASYLAB97, HASYLAB99].

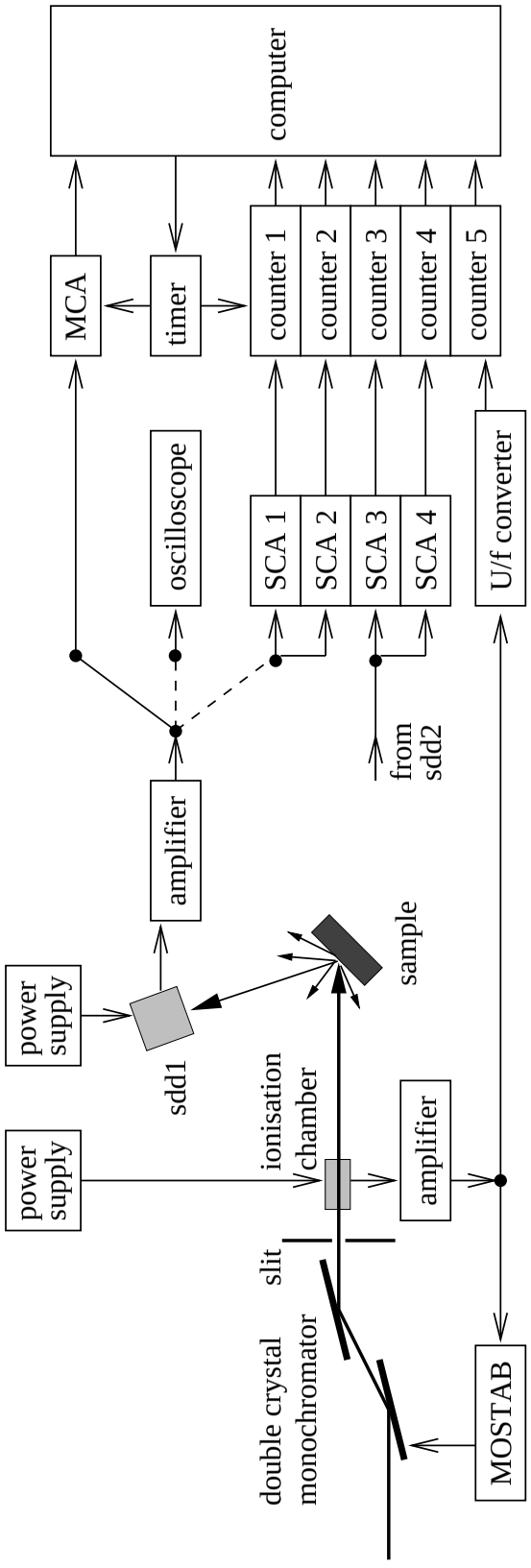

Figure 4.3: The incident intensity is monitored by an ionisation chamber. The ionisation chamber current is amplified and used together with a piezo crystal acting on the angular alignment of the first MOnochromator crystal to STABilize the incident intensity in a feedback loop (MOSTAB). The ionisation chamber voltage is also converted to a frequency which is registered by a counter. The signals from the silicon drift detectors sdd1 and sdd2 are preamplified within the detector housings. For each detector, they are shaped and amplified and can be analysed alternatively by a multi channel analyser (MCA), an oscilloscope or by two single channel analysers (SCA) in parallel. The SCA signals are registered by counters. A computer controls the beamline, the stepping motors of the diffractometer, and a timer. The timer sets the counting time for the MCA and the counters. MCA and counters are read out by the computer.

Figure 4.3: Schematic setup of the readout electronics.

In XFH, the incident radiation is only used to excite the sample to fluoresce and the fluorescence radiation of an atom is the holographic reference wave. In MEXH, the properties of the incident radiation are much more important for the holographic intensity since the incident radiation serves as the holographic reference wave. Synchrotron radiation has a continuous energy spectrum [Jackson75] (p. 678, fig. 14.11). From these energies, an energy that is suitable for an experiment can be chosen using an x-ray monochromator. This provides a unique opportunity for MEXH experiments: The interference energy can be varied continuously and can be chosen freely above an electron binding energy of an atom incorporated in the structure.

The coherence requirement is easy to fulfil in the atomic resolution x-ray holographies (compare sections 2.1.2, 2.2): the coherence length of incident x rays from a storage ring and monochromatized by a Si double-bounce monochromator or of fluorescence radiation is typically on the order of 1μm. This is much larger than necessary for imaging the local neighborhood of an atom which requires only a coherence length of a few interatomic distances, for example about 50 Å.

4.3 Detectors

A review of radiation detectors is for example given in [Leo94]. In the following, the semiconductor detectors and an ionization detector that were used at HASYLAB for atomic resolution x-ray holography are described.

4.3.1 Silicon Drift Detectors

Two fast energy dispersive silicon drift detectors were used for most atomic resolution x-ray holography experiments at HASYLAB. [1] Silicon drift detectors are energy dispersive. They allow the separation of the fluorescence signal from the elastic line of the incident radiation and element-specific measurements. The detection principle and operative detectors were first described by E. Gatti and P. Rehak [Gatti84a, Gatti84b, Rehak85]. The schematic cross section of a cylindrical silicon drift detector with integrated n-channel junction field effect transistor (JFET) is shown in fig. 4.4. The charge amplifier integrated on the detector wafer is described in [Rehak90]. The silicon drift detector principle has been applied to pn CCDs [Strueder90, Pinotti93, Soltau96, Strueder96] as well as to cylindrical detectors for energy resolution experiments [Lechner95, Lechner96, Strueder95] that were used here.

The device consists of an n-type device substrate, an implanted p+ backcontact, and a structured front side with p+ field rings, an n+ implanted anode and an integrated JFET transistor [Strueder98] (fig. 4.4). The n-type device substrate is

[1] The detector chips were fabricated by MPI Halbleiterlabor & KETEK GmbH [KETEK]. Detector housing and power supply were produced by RÖNTEC Röntgenanalyse-Technik GmbH [ROENTEC96]. A silicon drift detector prototype [ROENTEC96] was used in the experiments performed between August and November 1996. A six-pixel silicon drift detector [Gauthier96] was used in December 1996.

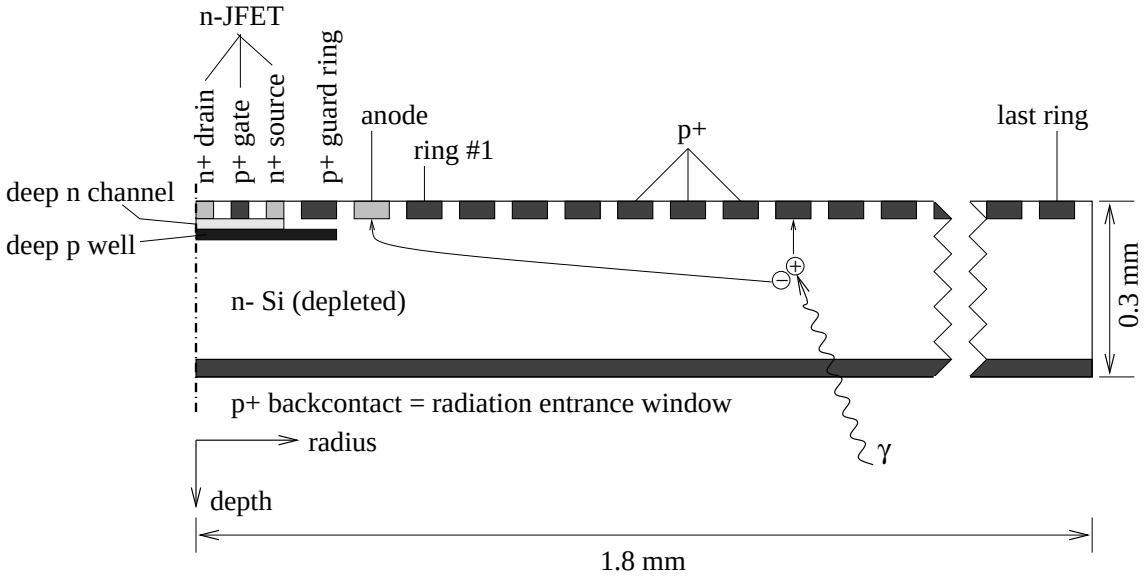

Figure 4.4: Schematic cross section of a cylindrical silicon drift detector with integrated n-channel JFET. The figure is not to scale. Depth and radius are given as in fig. 4.5 where the potentials at the p+ backcontact and at the p+ drift rings are shown.

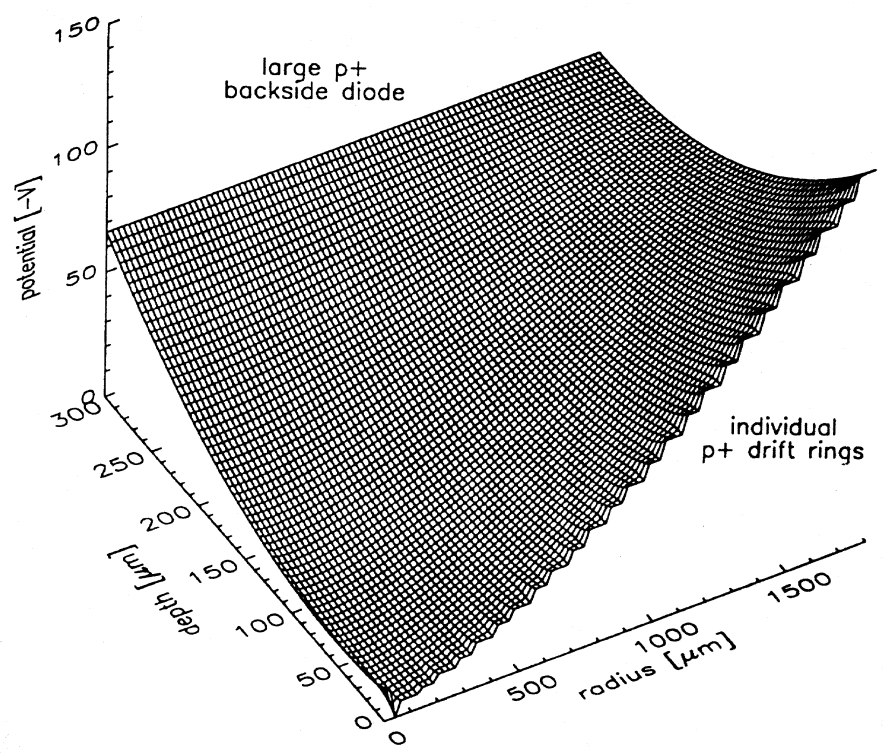

Figure 4.5: Numerical simulation of the potential for electrons in a silicon drift detector, from [Lechner96]. 25 p+ drift rings were used in this simulation. Electrons are driven towards the anode at (0,0).

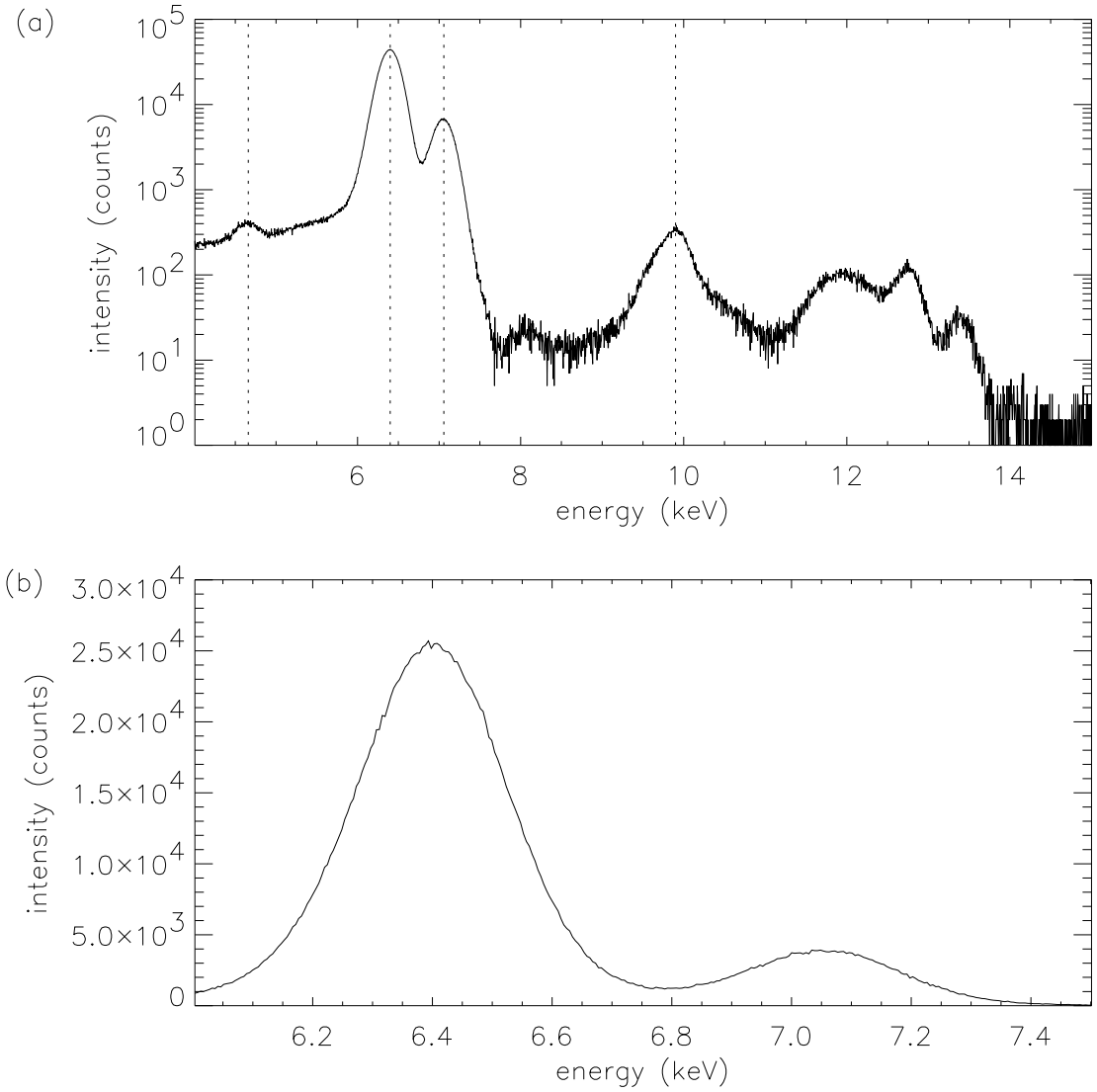

Figure 4.6: MCA spectrum taken during the MEXH beamtime in 03/1999 at CEMO in 100 s. An Fe single crystal served as a sample. The energy of the incident radiation was 9.900 keV. The detector temperature was stabilized to 10°C using a Peltier cooler. The total number of counts in the spectrum is 2.18×10^6 and the maximum number of counts is 2.57×10^4 at the Fe K_α line. (a) Spectrum in a logarithmic intensity scale. Dotted vertical lines indicate the energies of the Fe K_α line at 6.400 keV, the Fe K_β line at 7.058 keV, the elastic line at 9.900 keV, and the Si escape peak at (6.400 − 1.740) keV. The Fe K_α fluorescence excites the Si of the detector chip to fluorescence and causes the Si escape peak. The peak at $\approx$ 8.2 keV is probably the Si escape peak of the elastic line at 9.900 keV. The peak at $\sim$ 12.8 keV is due to signal pileup of the Fe K_α line. The other peaks at energies above $\sim$ 11 keV are not identified. (b) Close up view of the Fe K_α and K_β lines in a linear intensity scale. The full width at half maximum of the Fe K_α line was $\sim$ 250 eV for all MCA spectra of this beamtime.

fully depleted by applying a negative voltage with respect to the collecting anode to the p+ back contact and the p+ field strips. The backside of the device is the entrance window for ionizing radiation. A photon that is absorbed in the device will cause the creation of electron hole pairs. The number of pairs is proportional to the absorbed energy. The voltages at the backcontact and at the field strips are adjusted in such a way that electrons are driven towards the anode and holes move towards the p+ contacts. The potential for electrons in the device is shown in fig. 4.5. The potential is minimal at the anode and large at large radii and at the backcontact. The anode current is preamplified by the JFET close to the anode. As the device is fully depleted, electrons created at any depth inside the detector can be collected at the anode so that the number of recorded electrons is proportional to the absorbed energy but for x rays with low energies (below $\approx$ 1 keV), the number of recorded electrons deviates from this proportionality [Lechner95]. The devices that were used here have a thickness of 300μm. For x rays this gives more than 90% detection efficiency at 10 keV and more than 50% at 15 keV. The active area of each device was 3.5 mm^2. [Lechner96]

Silicon drift detectors do not require liquid nitrogen cooling so that their housings are relatively small (figs. 5.16, 5.17) compared to those of other semiconductor detectors such as Si(Li) detectors that do require a cryostat. Therefore silicon drift detectors can be rotated around the sample in pure XFH or together with the sample around the incident beam direction in pure MEXH. A larger detection system with a cryostat would not easily allow this.

Peltier cooling to 150 K gives an energy resolution of 139 eV (2.4 %) at the Mn K_α line (5.90 keV) which changes to 170 eV (2.9 %) at 273 K and to 220 eV (3.7 %) at 300 K [Lechner96]. For our experiments, the energy resolution was at least $\sim$ 250 eV (4 %) at 283 K at the Fe K_α line and at count rates up to 10^5/s. Fig. 4.6 shows a typical MCA spectrum taken during the MEXH beamtime at CEMO in 1999.

4.3.2 An Electron Yield Detector

In MEXH it is possible to integrate the detected signal over a large angular range and to use electrons or x rays for detection. In the frame of this work, an electron detector was developed and used for the first time in a MEXH experiment. This detector can detect electrons in a large angular range above the sample surface, which is in MEXH an advantage over the presently available silicon drift detectors that have a small active area. The operation principle of the electron detector is that of an ionization detector [Leo94]. The various electronic excitation channels that contribute to the production of photoelectrons and Auger electrons following x-ray absorption in a solid are discussed in [Stoehr84]. Ionization detectors of different geometies have been described and used for example in [Shevchik79, Kordesch84] for electron-yield extended x-ray absorption fine structure (EXAFS), in [Bedzyk85b] for x-ray absorption spectroscopy (XAS), and in [Korecki97, Korecki99] for reciprocal γ-ray holography.

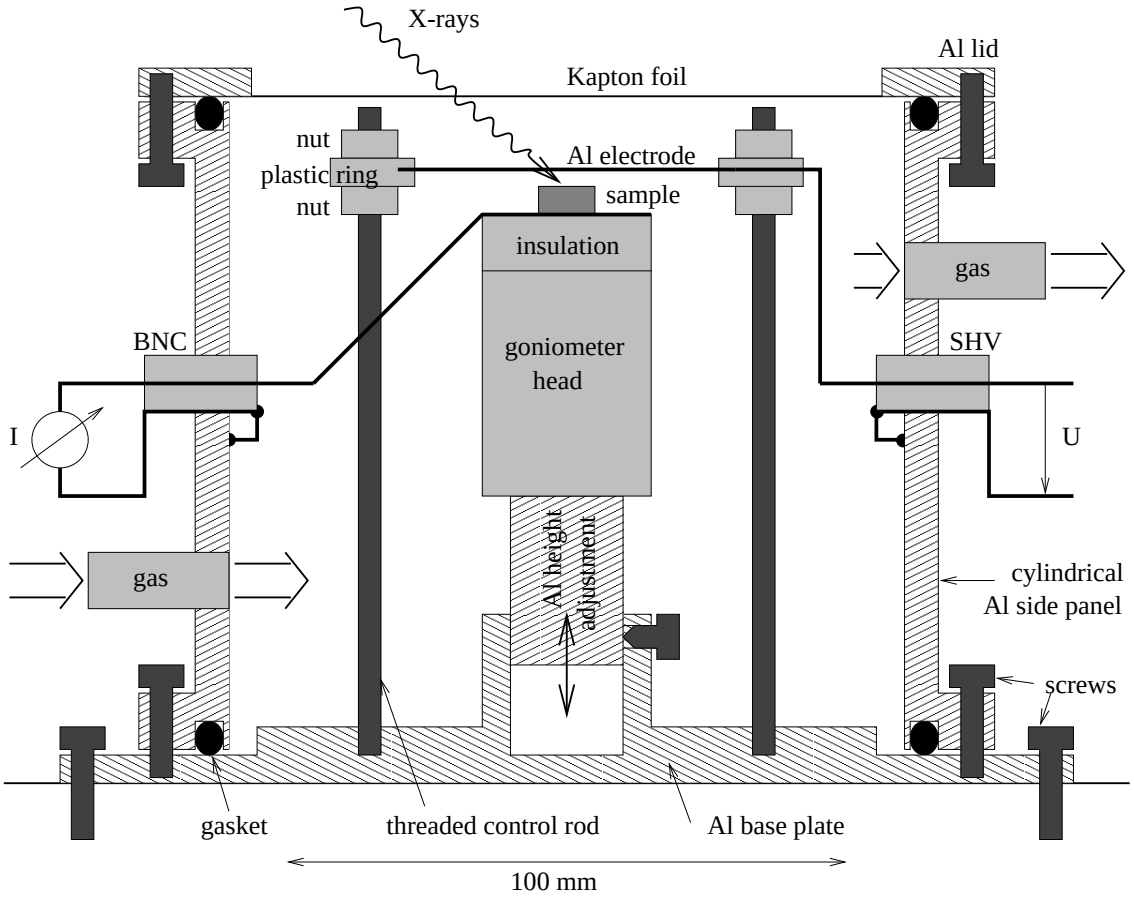

Figure 4.7: Schematic drawing of the ionization detector that has a geometry optimized for MEXH experiments.

The detector is shown schematically in fig. 4.7. He gas flows through the detector at atmospheric pressure. X rays enter the detector through a Kapton window on the detector lid and are absorbed by the sample. The sample is fixed inside the detector on a goniometer head and its height can be varied using a height adjustment cylinder. This way, the sample surface can be positioned very close to the Kapton window and a large range of angular incidence directions can be measured. A dc voltage U is applied between the detector housing and an Al foil that is fixed on a plastic ring above the sample. The Al foil serves as a collecting anode. A foil, wire, or ring can be fixed on the plastic ring and serve as anode. We chose a circular foil as anode in order to retain a circular symmetry. This is important in order to measure the angular dependence of the MEXH signal which should not be disturbed by an angular dependence of the anode. In an initial experiment, an Al foil of thickness $\sim 20\mu$m was used. It was difficult to fix the foil very flatly to the plastic ring since the foil was not very stiff. Therefore the anode did have an angular dependence. A stiff and therefore flat Al foil can replace it in the future. Also, instead of a circular foil that is hit by the incident beam, a ring-shaped anode can be used that is not hit by the beam. In this case, the incident beam is not absorbed in the anode, and an angular dependence due to absorption is avoided.

The distance between the sample and the plastic ring holding the anode can be changed using nuts that fix the plastic ring on threaded control rods in order to choose the distance between anode and sample. This distance was about 3 mm in our experiment. The current I between sample and detector housing is the measured signal. It depends upon the voltage U and the distance between anode and sample.

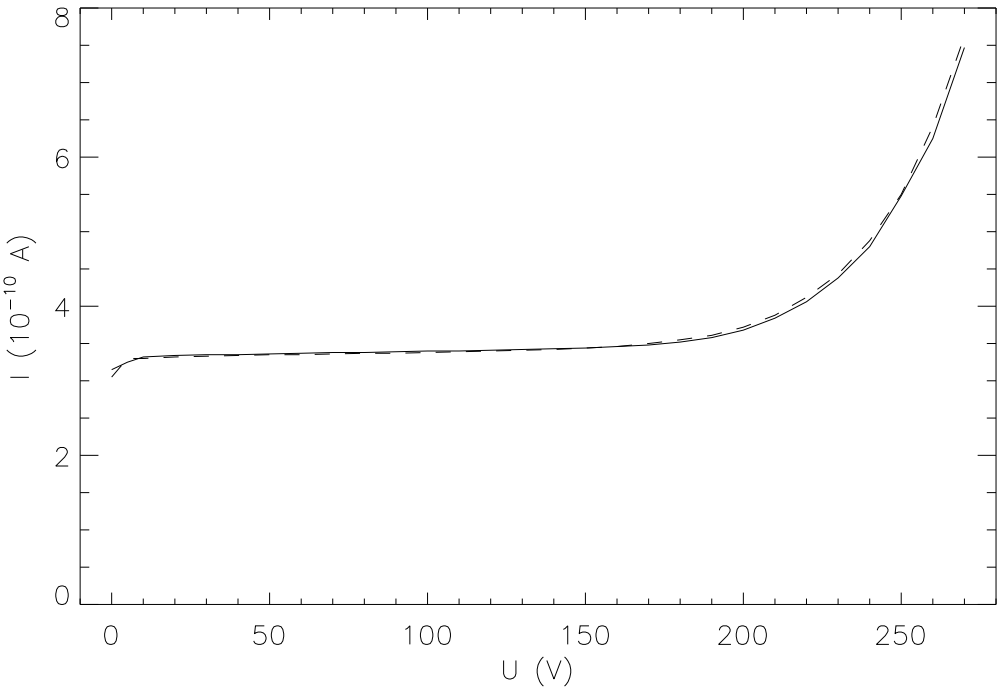

Figure 4.8: Dependence of the sample current I on the voltage U applied at the Al foil electrode. $I(U)$ is shown as a solid line for positive U and $-I(-U)$ is shown as a dashed line.

The dependence $I(U)$ was measured for U ranging from -270 V to $+270$ V at fixed angles θ and φ_s. $I(U)$ is shown in fig. 4.8 as a solid line for positive U and $-I(-U)$ is shown as a dashed line. The energy of the incident photons was 11.1 keV and the incident flux was 4×10^9 (photons/s)/(0.4 mm)^2.

For the initial MEXH experiment with this detector (section 5.4.3) the anode voltage was set to $U = 50$ V. The signal current I was nearly constant between $U \approx 10$ V and $U \approx 160$ V so that possible voltage instabilities can be neglected. In this region all created electons will be collected and a detector working in this region is called an ionization chamber. The detector can also be operated at higher voltages $U \gtrsim 200$ V where the current increases with voltage. The detector design is flexible: sample, housing, and anode can be contacted in different ways.

The detector was designed in such a way that the lid and side panel can be removed

without removing the socket. This makes it possible to use the same experimental setup with either silicon drift detectors or this electron yield detector. This was done in the beamtime at CEMO in March 1999. The experiment is described in section 5.4.3 and the experimental parameters are given in appendix C.2, table C.3. MEXH holograms were measured with the electron detector at incidence energies of 9.5 keV, 9.9 keV, 10.3 keV, and 11.1 keV.

4.3.3 Future Detectors and Sources

A higher incident flux together with faster energy-resolving detectors will help to improve the experimental statistics. In order to allow detection in a large angular range, the active area of detectors should be large. At low count numbers, it is useful to increase the active area of each pixel while the use of many small pixels in parallel is advantageous at high count numbers. The active area of single-pixel silicon drift detectors has been increased from 3.5 mm^2 to 5 mm^2 [Strueder97]. Multi-pixel detectors have many detection pixels on one chip. A six-pixel silicon drift detector array described in [Gauthier96] was used for a mixed MEXH experiment [Novikov98]. [2] The layout of a 39-pixel detector array is shown in [Strueder97, Strueder98]. Current developments of multi-pixel silicon drift detectors can improve the statistics or reduce the data acquisition time at least by a factor of 100. In MEXH, the fluorescence yield may be integrated over the full hemisphere above the sample surface or at least over 360° in φ in order to obtain higher count rates. The integration over 360° in φ can be achieved using highly oriented pyrolytic graphite (HOPG) cylindrical monochromators [Grigoryeva90, Dolbnya95a, Dolbnya95b, Beckhoff94, Beckhoff97], compare also [Gog96a, Faigel99].

For the experimental geometries used here, the number of detector counts per second was restricted by the incident photon flux and for the silicon drift detectors by the small detection angles used. If the fluorescence intensity from crystalline samples is integrated over a large angular range in MEXH, present-day synchrotron radiation sources can already provide fluorescence intensities which can hardly be handled fast enough by state-of-the-art detectors. Problems of reduced dimension - e.g. the study of surfaces, interfaces, impurities, or defects - will require higher source brilliances. In the future they can be supplied by x-ray free-electron-lasers using the excitation principle of self-amplified spontaneous emission [Kondratenko80, Bonifacio84, Arthur95, Brinkmann97]. These sources can emit in one 100 fs long x-ray flash a similar number of photons as is presently provided by the best x-ray undulator sources in one second. The source diameter is only 20 μm and the photon beam divergence 1 μrad. In XFH, the sample is fixed with respect to the incident beam so that multi-pixel silicon drift detectors will then make it possible to generate a full XFH hologram with one pulse only, allowing an extreme time resolution.

[2] The geometry of this first six-pixel silicon drift detector prevented pure XFH or MEXH experiments in a large angular range so that two smaller single-pixel detectors were used for pure experiments (chapter 5).

4.4 Choice of Structure

At the present development state of atomic resolution x-ray holography, well-known structures are investigated in order to develop and evaluate XFH, MEXH and the mixed methods. The results obtained from experimental holograms can be compared with the known structure and with the results from calculated holograms (chapter 3). In order to obtain an acceptable fluorescence yield at current synchrotron radiation facilities, a structure should contain many fluorescence atoms (section 2.5). These should have a sufficiently high atomic number Z since the real part of the atomic scattering factor increases far from any absorption edges approximately as Z. Presently sufficient holographic intensities are only obtained from experiments with crystalline samples. This is not an ideal choice from the holographic point of view since the long-range translational order in single crystals leads in certain directions to high object-wave intensities that cannot be neglected. The goal of holography is to image the local neighborhood of an atom incorporated in the structure so that a hologram would ideally only contain information on the local neighborhood of an atom. The effect of long-range translational order on holograms is discussed in section 2.5.2.

The local environments of Fe in Fe_2O_3 in [Gog96a, Gog96b, Gog98] of Sr in $SrTiO_3$ [Tegze96, Kawai98], of Co in CoO in [Tegze99], of Cu in Cu_2O [Novikov98], of Cu and Au in Cu_3Au [Kossel98, Adams98, Adams99, Adams00b], and of Fe in bcc Fe [Hiort00] have been investigated using atomic resolution x-ray holography. An exception is a hologram measurement of 0.02 wt% (200ppm) Zn in GaAs [Hayashi98]. The structures used at HASYLAB for atomic resolution x-ray holography experiments are described in the following.

4.4.1 bcc Fe

For the experiments and results that will be described in detail (sections 5.4.2, 5.4.3, 6.1, 6.2), a body-centered cubic (bcc) Fe crystal was used. The structure is shown schematically in figs. 3.1, 4.9. Different atom positions relative to the fluorescence atom are labeled in fig. 4.9 by letters. Since the crystal consists entirely of Fe atoms, a strong fluorescence signal is obtained. Atomic resolution holography measures the sum over the local environments of the fluorescence atoms. All fluorescence atoms in bcc Fe have the same local environment so that the summed neighborhood obtained in the reconstructed image should correspond to that of just one bcc Fe neighborhood (section 2.5.1, fig. 2.10 (a)). [3]

Small distances in the reconstructed images correspond to low frequencies in the holograms. Therefore the removal of the constant or low-frequency reference wave from the holograms may affect small distances in the reconstructions (sections 2.3.1, 2.4). If too few frequencies are removed, the huge maximum at the origin of the reconstructions (section 2.6) cannot sufficiently be suppressed. If too many frequencies are removed, neighbors close to the emitter cannot be imaged. The lattice constant of bcc Fe is $a_0 = 2.87$Å [Wyckoff63] (p. 16) and the smallest

[3] This neglects effects caused by long-range translational order.

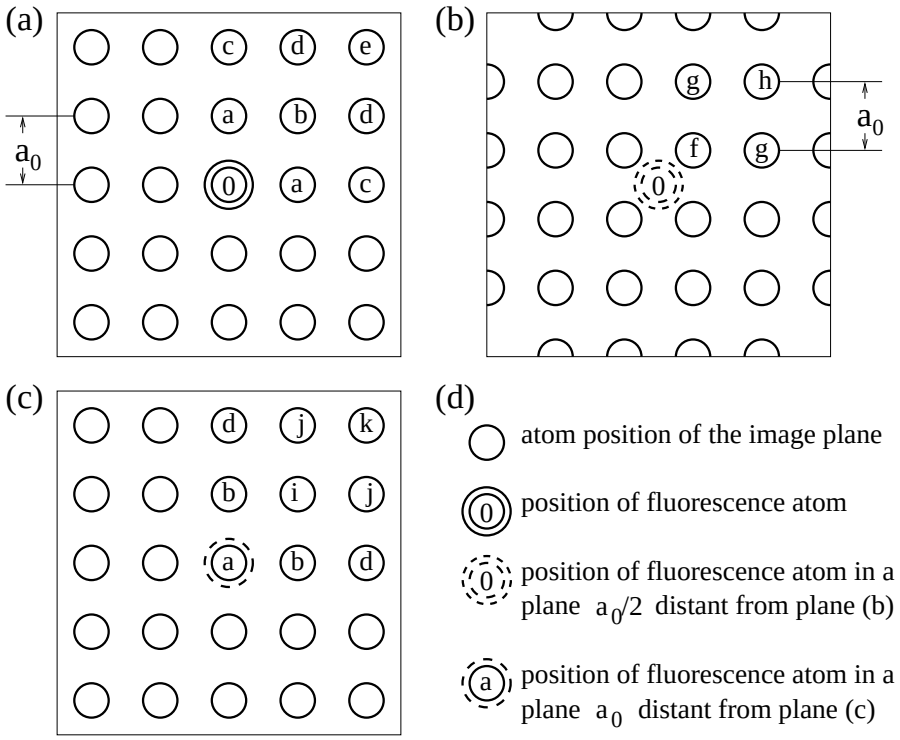

Figure 4.9: Schematic structure of bcc Fe. (a), (b), (c) show different planes of the structure. The planes are parallel to the 001 lattice planes of bcc Fe. The fluorescence atom is at the center of plane (a). Plane (b) is taken at a distance $a_0/2$ from plane (a). Plane (c) is taken at a distance a_0 from plane (a). The neighbors of the emitter are labeled with letters in a quarter of the images. This way, different neighbor positions can be identified. (d) explains the symbols used in (a)-(c). The distances of the neighbors to the fluorescence atom are a: $\sqrt{1}$, b: $\sqrt{2}$, c: $\sqrt{4}$, d: $\sqrt{5}$, e: $\sqrt{8}$, f: $\sqrt{3/4}$, g: $\sqrt{11/4}$, h: $\sqrt{19/4}$, i: $\sqrt{3}$, j: $\sqrt{6}$, and k: $\sqrt{9}$ in units of the lattice constant $a_0 = 2.87$ Å.

interatomic distance is 2.49Å which is a small distance for solid matter. This makes bcc Fe a critical test structure for the imaging of neighbors that are close to the emitter.

The bcc Fe single crystal used here was characterized in [Treusch95]. The crystal is cylindrical with a radius of 8 mm and a thickness of 2 mm. The flat polished surface is oriented parallel to the (001) lattice planes. The mosaicity is approximately $0.01° - 0.02°$ [Treusch95].

4.4.2 Cu_3Au

Cu_3Au has a face-centered cubic (fcc) lattice with lattice constant $a_0 = 3.75$ Å. Au atoms occupy the corners of the cubic unit cell and Cu atoms occupy the face centers of the cell in ordered Cu_3Au as shown schematically in fig. 4.10. Two different kinds of planes exist parallel to the {001} lattice planes: One plane contains Cu atoms and the other plane contains Cu and Au atoms as depicted

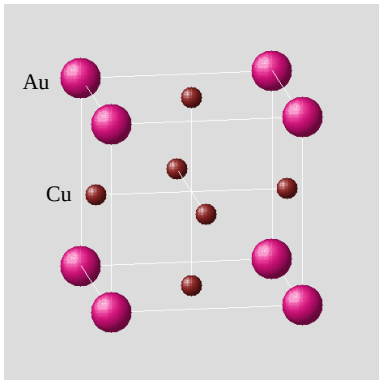

Figure 4.10: Schematic structure of ordered Cu_3Au. Au atoms are at the corners of the cubic unit cell and Cu atoms are at the face centers, from [Kossel98].

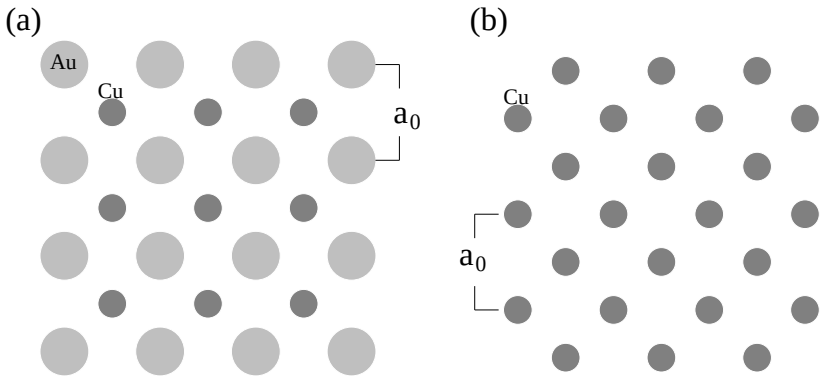

Figure 4.11: Two different kinds of planes exist parallel to the {001} lattice planes in ordered Cu_3Au. (a) One kind of planes contains Cu and Au atoms. (b) The other kind contains only Cu atoms, from [Kossel98].

schematically in fig. 4.11. All Au atoms in ordered Cu_3Au have the same local environment so that the summed neighborhood of all Au atoms that is obtained in the reconstructed image should correspond to just one neighborhood. The Cu atoms of the different planes have different kinds of neighbor atoms but at the same relative positions so that a mixture of the different neighbor atoms will be obtained and the nearest neighbor of such an "average" Cu atom is a mixture of Cu and Au atoms (compare section 2.5.1, fig. 2.10 (b), (c)).

Cu_3Au allows to obtain high fluorescence intensities from the Cu K and the Au L lines. The reconstructions of holograms detected at these lines can be compared with each other. An average Cu atom has a mixture of Cu and Au atoms at certain neighbor positions so that the interpretation of the results obtained from the Cu atoms may not be as simple as from the Au atoms.

The cylindrical Cu_3Au crystal used here has a height of 2 mm and a diameter of 8 mm. The sample surface normal is oriented parallel to the [001] direction at least

to 0.1°. The crystal consists of ~ 76 % Cu and of ~ 24 % Au with a homogenity of ± 5 % and a mosaicity of 0.2° in the [001] direction. [Adams95]

4.4.3 Cu_2O, Cu

Copper oxide (cuprite, Cu_2O) has a cubic ($Pn3$) unit cell of lattice constant $a_0 = 4.27$ Å. In the unit cell, oxygen atoms are at the positions 000 and $\frac{1}{2}\frac{1}{2}\frac{1}{2}$, and copper atoms are at the positions $\frac{1}{4}\frac{1}{4}\frac{1}{4}$, $\frac{3}{4}\frac{3}{4}\frac{1}{4}$, $\frac{3}{4}\frac{1}{4}\frac{3}{4}$, and $\frac{1}{4}\frac{3}{4}\frac{3}{4}$. Each Cu atom has only two close O neighbors while each O atom is surrounded by a tetrahedron of Cu atoms. The Cu-Cu separation is 3.01 Å. [Wyckoff63] (p. 331f)

Not all Cu atoms have the same local environment in Cu_2O so that an average neighborhood should be obtained in reconstructed images (section 2.5.1, fig. 2.10 (b), (c)). The crystal used here has a height of 2 mm and has a surface size of about 5 mm $\times$11 mm. The crystal has a mosaicity of 0.2° and (111) surface orientation.

Cu has an fcc lattice with a lattice constant of 3.61 Å [Wyckoff63] (p. 10). The cylindrical single crystal used here had a diameter of 9 mm and was 7 mm thick. Its surface was oriented parallel to the (100) lattice planes.

Chapter 5

Experimental Results: Establishing the Relevant Parameters

The experimental parameters such as the angular and energy ranges and step sizes have an important influence on the reconstructed images. This becomes clear not only from the theoretical results of chapters 2, 3 but also from experimental data where additional difficulties arise. The atomic resolution x-ray holography experiments performed at HASYLAB in the context of this work will be described in this chapter. An overview over the experiments and the corresponding parameters is given in section 5.1. The standard data treatment is described in section 5.2.

Until April 1997, experiments were performed in a mixed MEXH setup which is much easier to implement than a pure XFH or a pure MEXH setup. These experiments are discussed in section 5.3. It became necessary to perform pure experiments in order to avoid the complications in the data evaluation that arise in mixed experiments. Pure XFH and MEXH were performed for the first time in the context of this work. These experiments are discussed in section 5.4. A conclusion how atomic resolution x-ray holography experiments should be performed is given in section 5.5.

5.1 Experimental Overview

Table 5.1 gives an overview over the atomic resolution x-ray holography experiments performed at HASYLAB relevant to this thesis. [1] The experiments are listed in chronological order to reflect the experimental improvements. XFH, MEXH and mixed MEXH experiments were performed at the HASYLAB beamlines BW1 and CEMO. The evaluation status of the data is shortly given in the table together with citations where the data are published. Detailed information on the data evaluation is found in sections 5.3, 5.4. The data were evaluated in the context of this thesis unless noted otherwise in the text.

[1] All of the *experiments* discussed here were performed in a collaboration of the holography people in the group of Professor Dr. G. Materlik.

date	structure	beamline	method	status
08/96	Cu_3Au	BW1	mix	cannot be evaluated as hologram
10/96	Cu_3Au	BW1	mix	evaluated [Adams98]
10/96	Cu	BW1	mix	evaluated (this text)
10/96	Cu_2O	BW1	mix	evaluated (this text)
11/96	Cu_3Au	BW1	mix	evaluated (this text)
12/96	Cu_2O	BW1	mix	evaluated [Hiort97, Novikov98]
04/97	Cu_3Au	CEMO	mix	evaluated [Kossel98]
05/97	Cu_3Au	BW1	XFH	evaluated [Hiort98]
06/97	Cu_3Au	BW1	MEXH	evaluated [Hiort98]
07/98	Fe	CEMO	MEXH	evaluated [Hiort99a]
10/98	Fe	BW1	XFH	evaluated [Hiort00]
03/99	Fe	CEMO	MEXH	evaluated [Hiort99b]

Table 5.1: Overview over the atomic resolution x-ray holography experiments performed at HASYLAB in the frame of this work. The experiments are listed in chronological order and can be identified using the date (month/year) when they were performed and the sample structure. The experiments were performed in mixed MEXH (denoted by "mix" in the table), in XFH or MEXH. In the status column it is noted if the data are evaluated and where they are published. More detailed information on the status is given in the text.

date	structure	θ or α (°)	φ_s or φ_d (°)	energies (keV)
10/96	Cu_3Au	45, 50, ... 85	0, 1, ... 360	9.350, 10.285, 11.000
10/96	Cu	45, 50, ... 85	0, 1, ... 360	9.350, 10.285, 11.000
10/96	Cu_2O	45, 50, ... 85	0, 1, ... 360	9.350, 10.285, 11.000
11/96	Cu_3Au	40, 43, ... 85	0, 1, ... 360	9.100, 9.200, 10.050, 11.000
12/96	Cu_2O	30, 32, ... 88	0, 1, ... 360	11.000, 12.000, 13.000
04/97	Cu_3Au	19, 20, ... 90	0, 1, ... 360	15.000, 18.000, ... 30.000
05/97	Cu_3Au	8, 9, ... 90	0, 1, ... 120	9.350, 10.050
06/97	Cu_3Au	20, 21, ... 90	0, 1, ... 120	9.350, 10.050
07/98	Fe	20, 21, ... 90	0, 1, ... 150	7.900, 8.100, ... 11.300
10/98	Fe	0, 1, ... 83	0, 1, ... 360	9.000
03/99	Fe	44, 45, ... 90	0, 1, ... 360	9.500, 9.900, ... 11.100
03/99	Fe	1, 2, ... 43	0, 1, ... 95	9.500, 9.900, ... 11.100

Table 5.2: Overview over the most important parameters used in the atomic resolution x-ray holography experiments of table 5.1. The energies given are the energies of the incident x rays and have errors of ± 0.003 keV. The energy of the incident radiation is the interference energy in MEXH. For mixed MEXH, the angular ranges of θ and of the mixed coordinate (φ_s, φ_d) are given. The angular ranges of θ and φ_s are given for MEXH and the ranges of α and φ_d for XFH. (The angular coordinates are defined in fig. 4.1.) The accuracy of the diffractometers was better than 0.01°.

The most important parameters of the holographic data sets are the angular and energy ranges and step sizes. The energies of incidence and the angles are listed in

Z	element	binding energies (keV)	x-ray emission lines (keV)		
		K 1s	K_alpha$_1$	K$_{\alpha_2}$	K$_{\beta_1}$
26	Fe	7.112	6.404	6.391	7.058
29	Cu	8.979	8.048	8.028	8.905

Z	el.	binding energies (keV)			x-ray emission lines (keV)				
		L$_I$ 2s	L$_{II}$ 2p$_{1/2}$	L$_{III}$ 2p$_{3/2}$	L$_{\alpha_1}$	L$_{\alpha_2}$	L$_{\beta_1}$	L$_{\beta_2}$	L$_{\gamma_1}$
79	Au	14.353	13.734	11.919	9.713	9.628	11.442	11.585	13.382

Table 5.3: Electron binding energies for a few elements in their natural forms and energies of principal x-ray emission lines, from [Xraydata86]. Z = atomic number. The interference energy in XFH is given by the detected x-ray emission line.

table 5.2 for the experiments of table 5.1. The energy of the interfering wavefields is the incidence energy in MEXH and the fluorescence energy in XFH. Therefore the energies listed in table 5.1 only correspond to the interference energies for the MEXH experiments and for the MEXH contribution to the mixed MEXH holograms. Table 5.3 lists electron binding energies and energies of principal x-ray emission lines [Xraydata86] for a few elements. The x-ray emission lines are the relevant interference energies in XFH.

5.2 Data Treatment

The standard data treatment was the following: The measured fluorescence intensities were divided by the ionisation chamber signal to remove incident intensity fluctuations and to obtain the intensity $I(\mathbf{k})$. The background $|\mathbf{R}(\mathbf{k})|^2$ was determined using fits to $I(\mathbf{k})$ as discussed in section 2.4.1. One-dimensional fits to single φ scans were performed using eqns. 2.61, 2.64 for MEXH and XFH, respectively. The holographic signal was then obtained by the normalization of eq. 2.8, repeated here:

$$\chi(\mathbf{k}) \simeq \frac{I(\mathbf{k}) - |\mathbf{R}(\mathbf{k})|^2}{|\mathbf{R}(\mathbf{k})|^2}. \tag{5.1}$$

The holograms were reconstructed according to the Barton algorithm (eqns. 2.67, 2.70), where the integrations were replaced by summations. As reconstructed images, $|\psi_k(\mathbf{r})|^2$ and $|\psi(\mathbf{r})|^2$ were displayed for single-energy and multiple-energy reconstructions, respectively. Additional data treatments that were performed in some cases are described below together with the corresponding data.

5.3 Mixed MEXH Experiments

Most x-ray holography experiments [Tegze96, Gog96a, Gog96b, Adams98, Gog98, Novikov98, Kawai98, Hayashi98, Faigel99, Tegze99] were mixed x-ray holography experiments because pure experiments are much more complicated to implement. The first experiments at HASYLAB were performed in a mixed MEXH setup (sec-

tion 4.1). The data interpretation and evaluation is complicated for mixed holograms as described theoretically in sections 2.3.4, 2.4.2. This became evident from the holograms discussed in this section.

5.3.1 Cu_3Au Data Recorded in August 1996

An experiment performed in August 1996 could not be evaluated as a hologram since abrupt intensity variations within single mixed (φ_s, φ_d) scans prevented a sufficient removal of the reference wave (section 2.4.1). The duration of a single mixed (φ_s, φ_d) scan was about 16 h in this case. These intensity variations were due to intensity variations between different synchrotron radiation runs that have a typical duration of 8 h at DORIS III. Therefore the duration of single scans was reduced in the following experiments so that single scans could be measured within one synchrotron radiation run.

5.3.2 Cu_3Au, Cu, and Cu_2O Data Recorded in October and November 1996

Mixed MEXH holograms were measured for three structures, Cu_3Au, Cu, and Cu_2O, at three incident energies in October 1996 and for Cu_3Au at four incident energies in November 1996. These experiments were performed with very similar setups and will be discussed in this section.

The interference intensities were measured on polar caps where θ varied from 45° to 85° in steps of 5° and from 40° to 85° in steps of 3°, respectively. The sampling along θ was coarser than along (φ_s, φ_d) where the stepsize was 1°. The large stepsize in θ made it impossible to see XSW line patterns in the holograms obtained from these mixed MEXH experiments. Therefore, the patterns cannot be extended to a full 4π sphere (section 2.5.2) and it is not possible to obtain a high spatial resolution in planes perpendicular to the sample surface plane. The small angular range leads also to a decreased spatial resolution in planes parallel to the sample surface plane (section 2.6.3, [Kossel98, Adams99]).

Point-to-point scans were measured in the angular coordinate (φ_s, φ_d) at fixed θ and fixed α. The scan duration was about 30 min for a single mixed (φ_s, φ_d) scan. The incident intensity was sufficiently stable within this time. No intensity steps occur in most of the scans so that the background due to the reference wave and absorption effects could be removed according to section 2.4.1 from single (φ_s, φ_d) scans. The net measurement time was only 12 min per scan corresponding to 2 s per angular point so that most of the scan duration was used for the motor movements. Therefore, faster motors were installed after these experiments in order to use the time more effectively.

The background could only be determined for single scans in one angular coordinate but not from full holograms. This was the case in all experiments discussed in this text. The reason was that the measurement time of the full holograms was typically on the order of a day. The incident radiation was not stable enough to allow the

determination of background and absorption effects from two angular coordinates simultaneously: steps occured in the interference intensities between different single scans and within a few single scans. This way, the average information was lost along the second scan direction which was θ in mixed MEXH, usually θ in MEXH, and α in XFH. The effect of background removal from single φ scans is demonstrated for reconstructions of calculated holograms in fig. 3.9 of section 3.2.2: The information along an axis that passes through the fluorescence atom and is parallel to the φ axis is lost in the reconstruction. The most recent x-ray holography experiments [Tegze99, Adams00b] were performed in fast scan modes that allow the measurement of a full hologram within a few hours, thereby making a simultaneous removal of the background from two angular coordinates possible. Such experiments require very fast motors and a fast data acquisition system which are now available at HASYLAB so that future experiments can be performed under these further improved conditions.

Short scans were repeated in order to obtain a sufficient number of total counts. Before repeating the mixed (φ_s, φ_d) scans, the detectors were rotated in φ_d by 1° in October 1996 and by 5° in November 1996. This way, mixed MEXH holograms were recorded at 10 different detector start-positions along φ_d in October 1996 and at 4 different detector start-positions in November 1996. After repeating the scans, θ was changed. A slight improvement in the angular sampling was made in November 1996 by using a stepsize of 3° in θ instead of 5° as in October 1996. Two data sets measured in October 1996 will be discussed in the following.

Cu_3Au - A Hologram and its Reconstruction

Figure 5.1: A hologram of Cu_3Au after background removal. Horizontal axis: $\varphi_s = 0°, 1°, ...359°$; vertical axis: $\theta = 45°, 50°, ...85°$. The data were symmetrized to four-fold symmetry along φ_s. [Adams98]

An example of a hologram measured on a Cu_3Au single crystal is shown after background removal in fig. 5.1. The energy of the incident beam was 9.35 keV. The Cu K_α fluorescence intensity was detected using a prototype silicon drift detector. The holograms obtained at the 10 different φ_d start-positions of the detector were added which corresponds to averaging the XFH scan that is present in the mixed

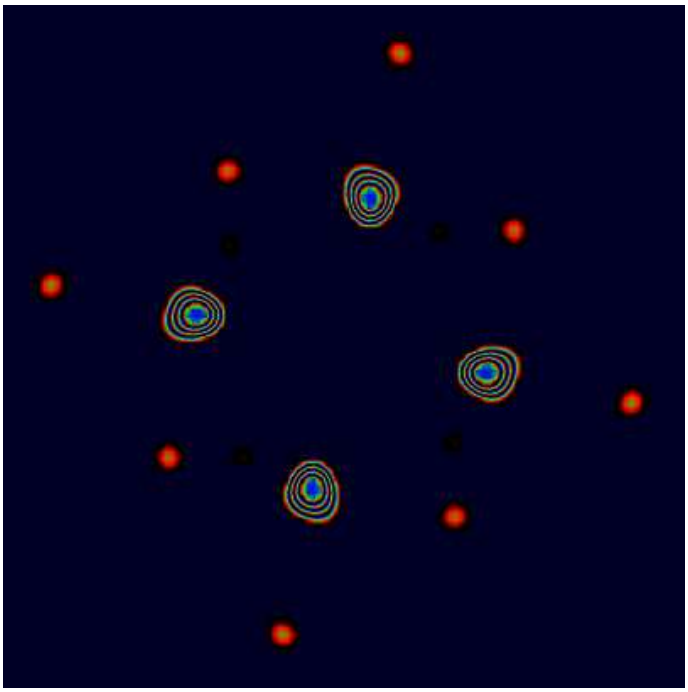

Figure 5.2: Reconstruction of the hologram of fig. 5.1 in a plane cutting through the Cu detector atom and parallel to the (001) lattice planes. The smaller spots occur close to Cu atom positions in Cu_3Au. The larger spots occur close to positions of Cu and Au neighbors (see text) of the detecting Cu atom at the center of the image. [Adams98]

MEXH holograms over 10 φ_d positions. The summed hologram was symmetrized along (φ_s, φ_d) according to a fourfold symmetry: The hologram was added to the same hologram after shifting it by 90°, by 180°, and by 270°. The initial position $(\varphi_s, \varphi_d) = 0°$ was chosen arbitrarily so that the symmetry axes of the hologram do not coincide with $(\varphi_s, \varphi_d) = 0°$, 90°, 180°, or 270°.

The hologram was reconstructed according to eq. 2.67, where the integration was replaced by a summation. The reconstruction $|\psi_k(\mathbf{r})|^2$ of the Cu_3Au hologram of fig. 5.1 is shown in fig. 5.2 in a nonlinear intensity scale using background cutoff. The highest peaks can be seen. This reconstruction was obtained by D. V. Novikov. The image plane passes through the average Cu detector atom at the center of the image and is parallel to the (001) lattice planes which were oriented parallel to the sample surface plane in the experiment. No high peak ocurs at the center since the background was removed from the hologram. The image can be compared to the Cu_3Au structure (section 4.4.2). The smaller spots occur close to Cu atom positions. The larger spots occur close to positions of Cu and Au atoms. A mixture of Cu and Au atoms produces these spots since an average over the neighborhoods of all Cu atoms in the Cu_3Au structure is measured. This is presently the best reconstruction of the holograms measured in October 1996 and November 1996 at HASYLAB. No three-dimensional information has been obtained from these holograms.

Cu - Mixing of XFH and MEXH in Mixed MEXH

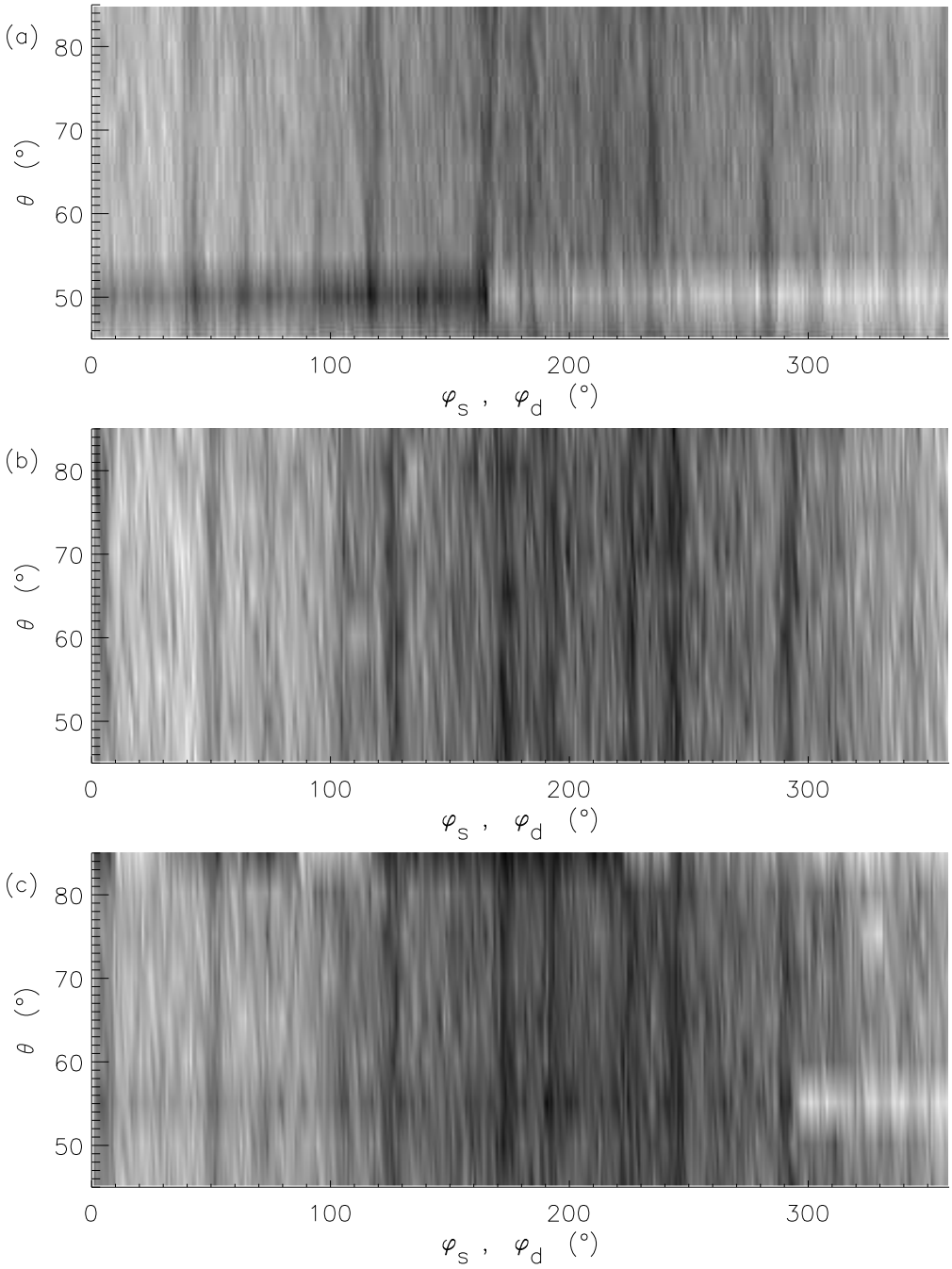

Figure 5.3: Mixed MEXH Cu data after dividing each (φ_s, φ_d) scan by its average value. The data were measured in an angular range $\varphi_s = 0°, 1°, ...359°$, $\theta = 45°, 50°, ...85°$. The Cu K_α line was used for fluorescence detection. The energy of the incident x rays was 9.350 keV in (a) and (b). It was 10.285 keV in (c). The detector start-position was $\varphi_d = 0°$ in (a) and 9° in (b) and (c).

Mixed MEXH data measured on a Cu single crystal are shown in fig. 5.3. The Cu K_α fluorescence intensity was detected using a prototype silicon drift detector. For

these plots, each mixed (φ_s, φ_d) scan was divided by its average value in order to remove the intensity variations for different values of θ that occur due to absorption. In parts (a) and (b) the energy of the incident x rays was 9.350 keV. The detector start-position was at an arbitrary angle $\varphi_d = 0°$ in (a). The dominant pattern is given by lines of extreme intensity that are parallel to the θ direction. The detector start-position was $\varphi_d = 9°$ in (b). The dominant pattern in the data (a) is shifted by 9° in (b). In part (c) the energy of the incident x rays was 10.285 keV and the detector start-position was $\varphi_d = 9°$ as in (b). The line patterns in (b) and (c) are very similar, showing that they do not depend upon the energy of the incident x rays. In these holograms it was discovered how dominant the effect of mixing can be in a mixed hologram. These lines can be interpreted as an XFH φ_d-scan at constant α that is measured together with the (φ_s, θ) MEXH hologram in mixed MEXH. Such a dominant XFH scan in a mixed MEXH hologram is not an exception as will be seen in the next section.

5.3.3 Cu_2O Data Recorded in December 1996

The Cu_2O experiment performed in December 1996 is described in and the data are partly published in [Novikov98]. The beam from the BW1 x-ray undulator source was monochromatized by two Si(111) Bragg reflecting crystals and limited by a slit of size $(0.5\ \text{mm})^2$. The energy of the incident beam was set to 11 keV, 12 keV, and 13 keV. The photon flux incident on the sample was $\approx 5 \times 10^{10}$/s, $\approx 4 \times 10^{10}$/s, and $\approx 2 \times 10^{10}$/s, respectively. A six-pixel silicon drift detector [Gauthier96] with an energy resolution of about 320 eV at 10 keV and at 1.2×10^5 counts/s was used to detect the Cu K fluorescence of the sample. Five pixels were used in this experiment. 4.8×10^{10} total counts were recorded at 11 keV, 3.9×10^{10} total counts at 12 keV, and 3.3×10^{10} total counts at 13 keV. The detector was rotated together with the sample in θ, keeping α constant. Only the sample was rotated around its surface normal so that φ_d and φ_s changed.

Intensities obtained from one detector pixel are shown in fig. 5.4. The incident energy was 11.0 keV in this case. The mixed MEXH hologram is shown in fig. 5.4 (a) after removal of reference wave and absorption effects. The dominant structure in this hologram (a) consists of high or low intensity lines with little variation along θ. Shifting the detector start-position by some amount in φ_d in the experiment shifts these lines by the same amount which shows that they are generated by the fluorescence radiation (compare fig. 5.3). These lines are caused by an XFH scan which is measured at constant α and does not depend upon θ. The evaluation of these data is difficult due to the strong effect of the XFH scan in the mixed MEXH data. Part (b) shows the hologram (a) averaged over θ. Since the MEXH contributions to the hologram (a) vary with θ, they partly cancel in this scan while the XFH contributions to the hologram (a) do not depend upon θ and are enhanced. [2]

This way of determining the XFH scan should work better for this hologram that was measured in 30 comparatively small steps of 2° in θ and where an average over

[2] The XFH contributions depend upon the detection angles α and φ_d. In this mixed MEXH experiment, α was constant but φ_d was not constant.

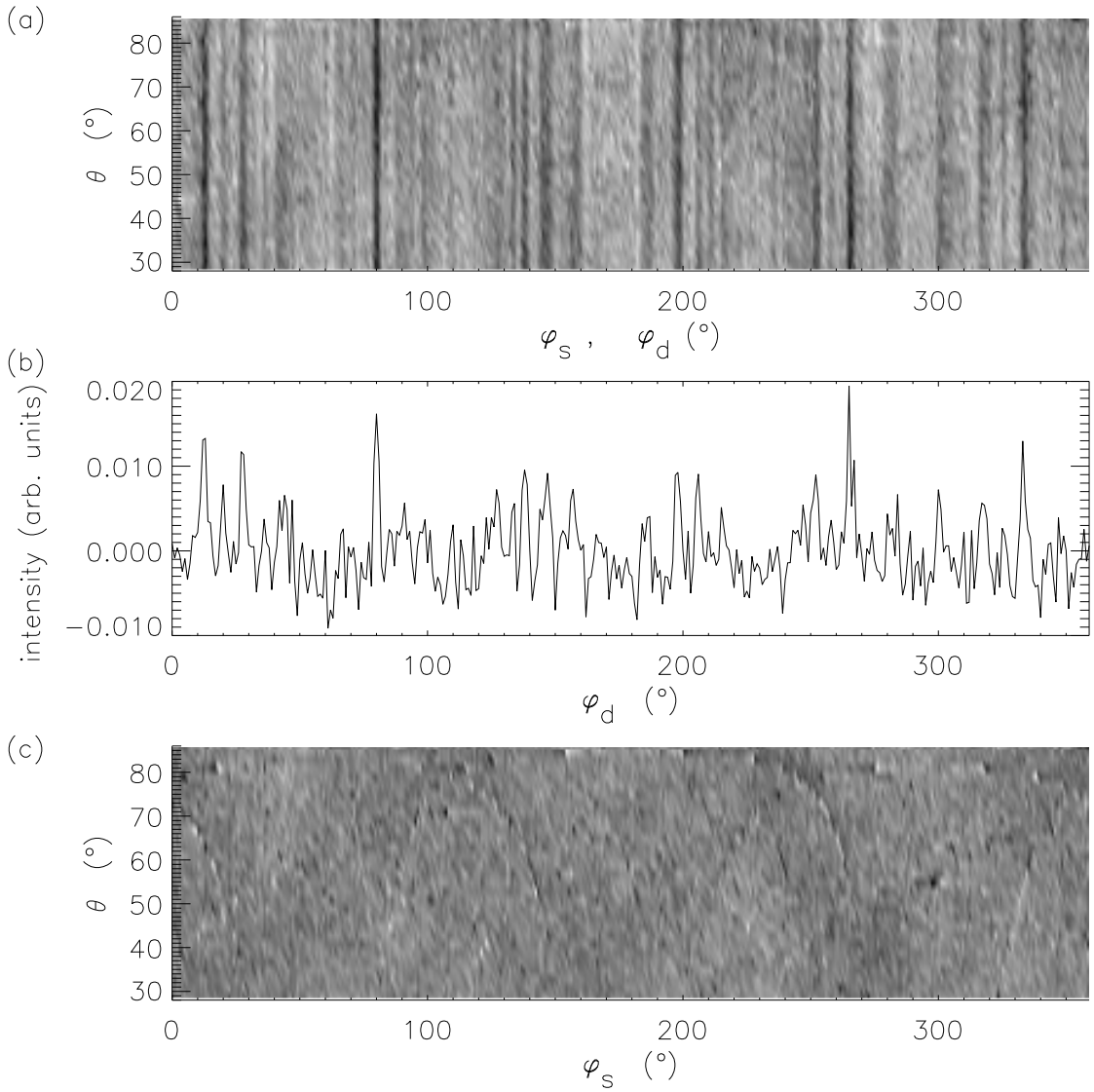

Figure 5.4: Intensities obtained from one pixel of a six-pixel detector in the mixed MEXH experiment on Cu_2O in December 1996. The incident energy was 11.0 keV and the Cu K fluorescence intensity was detected. (a) Mixed MEXH hologram that depends upon the position φ_s of the sample relative to the incident beam and upon the position φ_d of the detector relative to the sample. Only the hologram measured at one start-position $\varphi_d = 0°$ is shown here. (b) The array (a) averaged over θ. This scan mainly depends upon φ_d while the dependence on φ_s is nearly cancelled so that this scan is mostly an XFH scan. The scan (b) was subtracted from each (φ_s, φ_d) scan of the hologram (a) to yield the hologram (c).

30 MEXH scans is formed than for the holograms measured until November 1996 in only few steps of larger size in θ. The number of counts in scan (b) is larger than in a single scan so that this scan shows the XFH contribution to the hologram (a) more clearly than the single scan at $\theta = 90°$. If scan (b) is subtracted from the mixed MEXH hologram (a), then hologram (c) is obtained. This hologram contains mostly

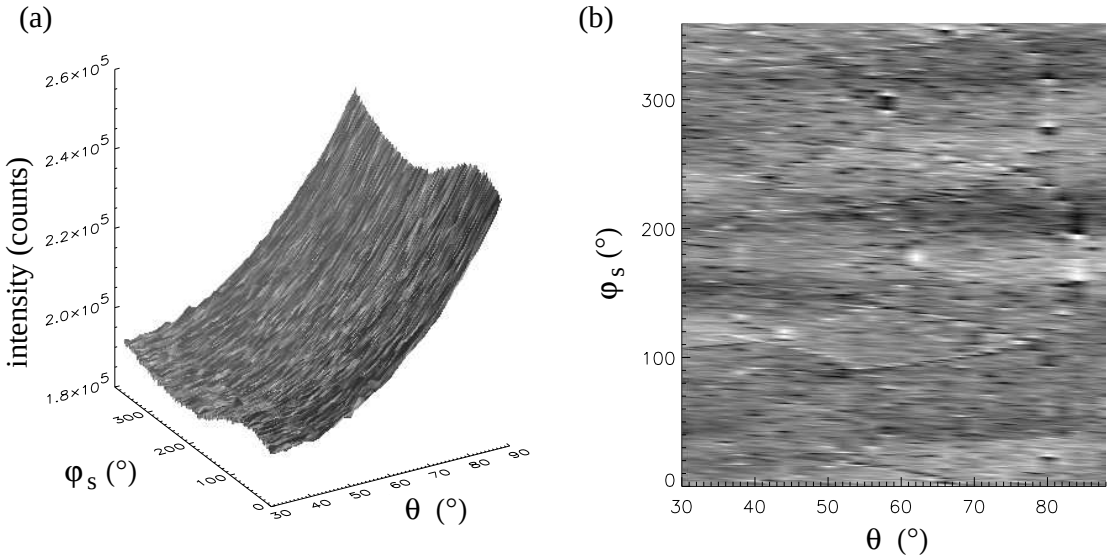

Figure 5.5: Experimental MEXH hologram of Cu_2O, measured at BW1 at 13 keV. (a) The original data set summed over the signals measured by 5 detection pixels and over 3 start-positions in φ_d. (b) The data set (a) after removal of the elastic background and absorption effects. [Novikov98]

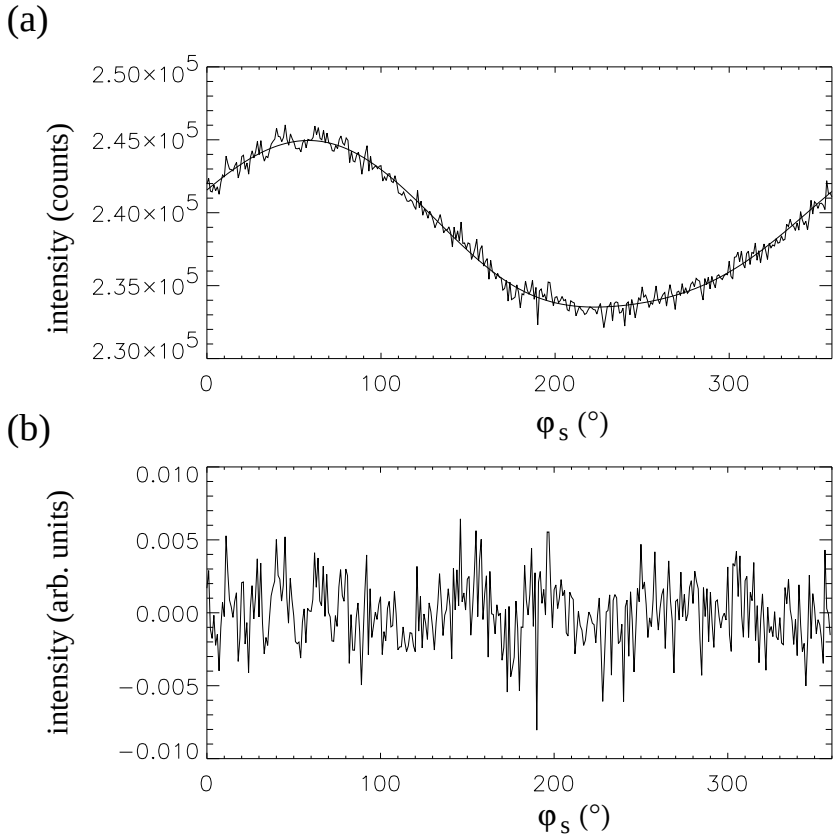

Figure 5.6: A singe azimuthal φ_s scan from the data set of fig. 5.5. (a) original, (b) corrected for reference wave and absorption effects. [Novikov98]

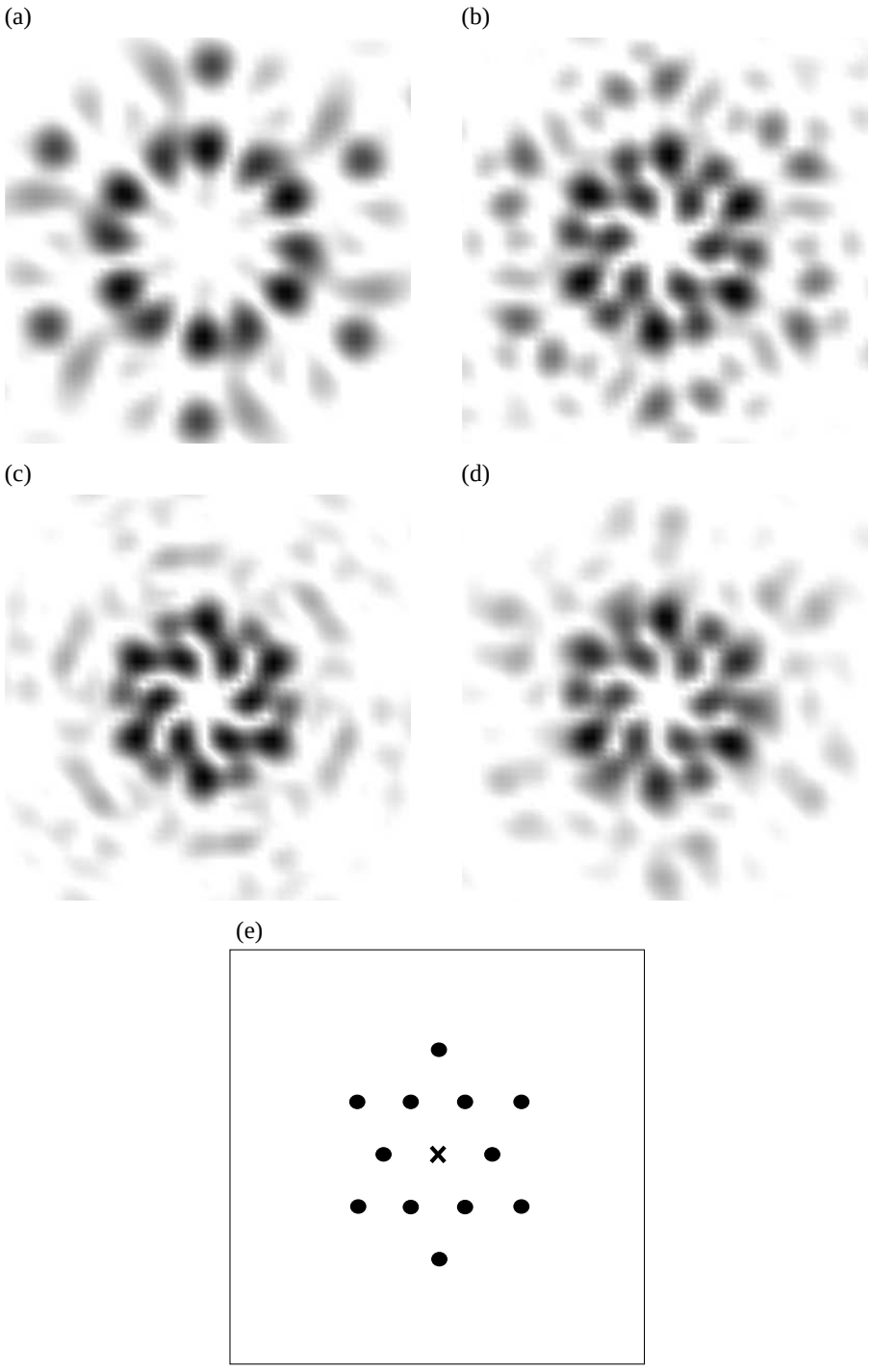

Figure 5.7: Reconstructed images of a plane parallel to the Cu_2O (111) plane and passing through the average detecting Cu atom. Single-energy reconstructions are shown at (a) 11 keV, (b) 12 keV, (c) 13 keV. (d) The energy-added reconstruction. The images (a)-(d) are displayed in a greyscale where black corresponds to maximum peak intensity and white to minimum intensity. Low image values were removed. (e) Peak positions expected in the image plane for reconstructions of Cu_2O holograms. The position of the detecting atom is marked with a cross. [Novikov98]

MEXH information since the XFH scan was determined carefully and removed, but small effects due to the XFH scan may still remain in the hologram. It is therefore highly desirable to carry out pure MEXH or pure XFH measurements. The stepsize in θ was only 2° so that an XSW line pattern becomes weakly visible in hologram (c).

A different way to "remove" the XFH scan was used in [Novikov98]. Mixed MEXH holograms were measured by 5 detection pixels for 3 different φ_d start-positions, namely 0°, 5°, and 10°. Averaging over these 5×3 values was used to diminish the effect of the XFH scan. Averaging over different φ_d positions was also used in the Cu_3Au hologram of section 5.3.2. In fact, averaging over all 360 positions in φ_d would completely remove the XFH scan but the corresponding 360-fold mixed MEXH experiment would be more complicated to perform than one pure MEXH experiment. The interference intensity that was measured at an incidence energy of 13 keV and summed over 5 pixels and 3 φ_d start-positions is shown in fig. 5.5 (a). The same intensity is shown after removal of reference wave and absorption effects in fig. 5.5 (b). An XSW line pattern becomes weakly visible in this hologram.

A single azimuthal φ_s scan from the data set of fig. 5.5 is shown in fig. 5.6. The original scan is shown in (a) and the scan is shown after removal of reference wave and absorption effects in (b). The sinusoidal shape in (a) is due to a slight misalignment as explained in section 2.4.1. The holograms were symmetrized along φ_s according to a threefold symmetry before reconstruction. The symmetrization procedure was described in section 5.3.2 for Cu_3Au and a fourfold symmetry.

Reconstructions at single and multiple energies were performed as described in section 5.2. Reconstructions in a plane parallel to the Cu_2O (111) plane and passing through the average detecting Cu atom are shown in fig. 5.7. Single-energy reconstructions are shown at (a) 11 keV, (b) 12 keV, (c) 13 keV. Part (d) shows the energy-added reconstruction. Oxygen scatters so weakly that the oxygen neighbors of the Cu atoms are not visible in the reconstructions. The Cu atom positions expected for the Cu_2O structure from the holographic method are indicated in part (e). Different Cu atoms in Cu_2O have different neighborhoods so that a mixture of these neighborhoods is expected (fig. 2.10 (b), (c) of section 2.5.1).

5.3.4 Cu_3Au Data Recorded in April 1997

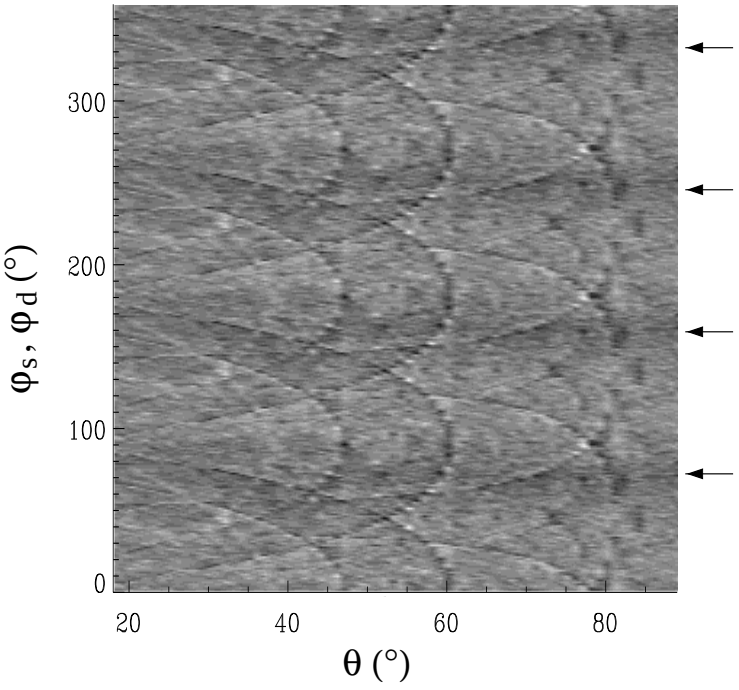

Figure 5.8: A mixed MEXH Cu_3Au hologram after removal of reference wave and absorption effects. The incidence energy was 24 keV and the Cu K_α fluorescence was used for detection. The hologram was symmetrized according to a fourfold symmetry along (φ_s, φ_d). Arrows are drawn to indicate an intensity variation along (φ_s, φ_d) that does not vary much in θ. [Kossel98]

Mixed MEXH holograms were measured at energies from 15 keV to 30 keV in steps of 3 keV on a Cu_3Au single crystal in April 1997. Two silicon drift detectors were used. For each detector, one SCA discriminated the Cu K_α line and another SCA discriminated the Au L fluorescence line. The data were evaluated by E. Kossel in the context of her Diplomarbeit [Kossel98]. The data are also discussed in [Adams99]. The step size was only 1° in θ so that XSW line patterns are clearly visible in the holograms. An example of a mixed hologram measured by one detector is shown after removal of reference wave and absorption effects in fig. 5.8. The hologram was measured at an incidence energy of 24 keV and the Cu K_α fluorescence was used for detection. The hologram was symmetrized according to a fourfold symmetry along (φ_s, φ_d) in order to emphasize in the image a slight intensity variation along (φ_s, φ_d) that does not vary much in θ. Arrows are drawn to indicate this barely visible intensity variation which can be interpreted as the XFH scan of this mixed MEXH hologram. A similar intensity variation was found in all holograms measured by this detector.

The intensity variation can be visualized more clearly if the hologram is summed

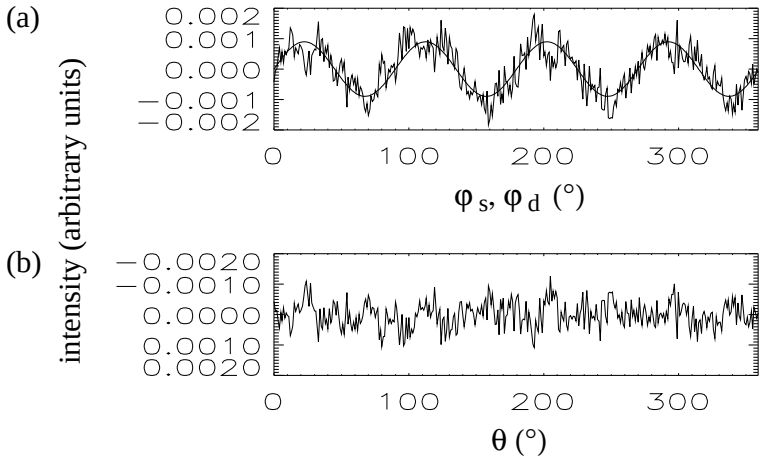

Figure 5.9: (a) The mixed MEXH hologram measured at the Cu K_α line and an incidence energy of 24 keV was summed over θ. A sine function of period 4 in 360° was fitted to this summed scan. The phase of this sine function was determined from the fit. A fourfold sine function of variable amplitude and this phase was fitted to each (φ_s, φ_d) scan of the mixed hologram and subtracted from it. (b) shows the resulting hologram summed over θ. [Kossel98, Adams99]

over θ. The resulting scan is shown in fig. 5.9 (a). The hologram was not symmetrized along (φ_s, φ_d) in this case. The summed scan is similar to a fourfold sine function. In order to remove this average scan from the mixed hologram, a sine function of period 4 in 360° was fitted to the summed scan of fig. 5.9 (a). The fitted sine function is also drawn in fig. 5.9 (a). Then a fourfold sine function was fitted to each scan of the mixed MEXH hologram with variable amplitude and the fixed phase that was determined from the fit to the summed scan. These fitted scans were subtracted from the mixed MEXH scans. The resulting hologram was summed over θ to check if the average modulation of the (φ_s, φ_d) scans was successfully removed. This summed scan is shown in fig. 5.9 (b). Such a periodic function could also be removed using filtering. This is not advisable since sinusoidal components of all phases would be removed in that case and too much of the MEXH contribution to the mixed MEXH hologram might be removed. Traces of the XFH scan will remain in the hologram unless the XFH scan was truly a fourfold sine function in this case.

The shape of the XFH scan depends upon the detection angle α. The detection angle was different for the second detector. In this case, the sum of a fourfold and an eightfold sine function was removed from the mixed holograms.

The removal of the XFH scan has a large influence on the reconstructions as can be seen from fig. 5.10 where reconstructions of the unsymmetrized hologram measured at an incidence energy of 24 keV are shown. The Cu K_α fluorescence was used for detection and the holograms measured by both detectors were added after removal of reference wave and absorption effects. The images are reconstructed in a plane parallel to the (001) lattice planes that passes at the image center through the fluorescing Cu atom. Part (a) shows the reconstruction of the mixed hologram.

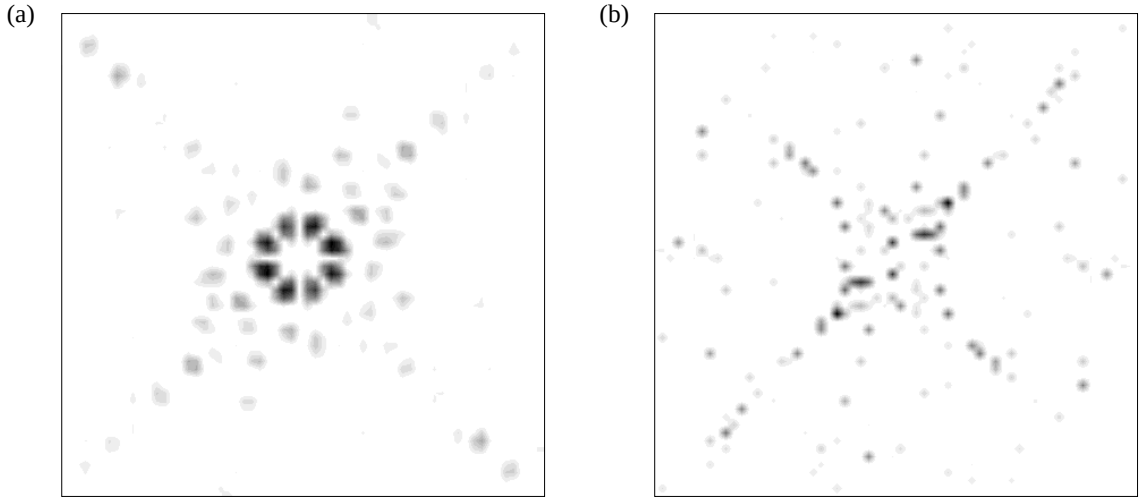

Figure 5.10: (a) Reconstruction $|\psi_k(\mathbf{r})|^2$ of the hologram measured at an incidence energy of 24 keV. The Cu K_α fluorescence was used for detection. Reference wave and absorption effects were removed from the hologram before reconstructing but not the XFH scan. The hologram was not symmetrized but is otherwise the hologram of fig. 5.8. (b) Reconstruction of the same hologram but after removing the XFH scan. The images are reconstructed in a plane parallel to the (001) lattice planes that passes at the image center through the fluorescing Cu atom. The image size is (15 Å)^2. The images are displayed in a greyscale where black corresponds to maximum peak intensity. Low image values were removed. [Kossel98]

High peaks occur close to the center of the image and at positions that do not correspond to atom positions in Cu_3Au. Part (b) shows the reconstruction of the hologram after removing the XFH scan from the hologram. The dominant peaks that occur in (a) are not present here. The number of counts varied between 6×10^4 and 7×10^5 per angular point and energy in this experiment and was on average 1.2×10^5. The total number of counts in this hologram was about $9 \cdot 10^9$. Statistical noise in the hologram leads to peaks that do not correspond to atom positions (section 6.1.2) so that the image (b) does not resemble the Cu_3Au structure.

Improved images are obtained if all holograms measured at the energies from 15 keV to 30 keV are reconstructed and if the reconstrcutions are combined according to eq. 2.70. The total number of counts measured by both detectors at both fluorescence lines in all holograms was about 7×10^{10} so that the influence of statistical noise is lower in the energy-added reconstruction than at a single energy. Such an energy-added reconstruction is shown in fig. 5.11 (a). In this case, the holograms measured at the Au L fluorescence line were used. The corresponding reconstruction of holograms measured at the Cu K_α line is very similar [Kossel98]. This is not surprising because the holograms are very similar for both detection energies [Kossel98, Adams99]. The image plane is parallel to the (001) lattice planes and passes at the center through the Au emitter atom. The image does not quite correspond to the neighborhood of the Au emitter atom which is shown in fig. 5.11 (c). In order to understand the experimental reconstruction better, holograms were

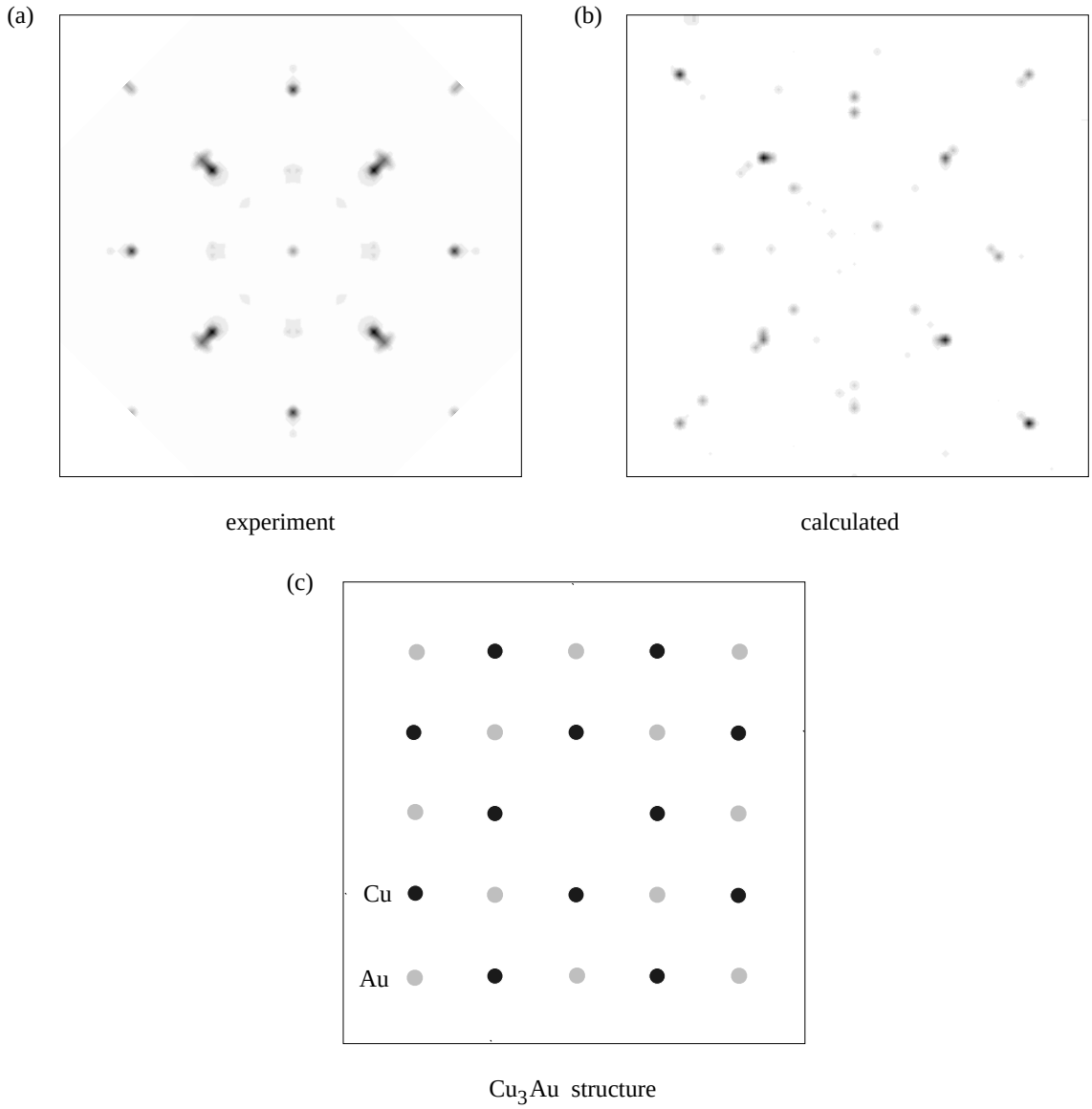

Figure 5.11: (a) Energy-added reconstruction $|\psi(\mathbf{r})|^2$ of experimental holograms measured at the incidence energies 15 keV, 18 keV, ...30 keV. The Au L line was detected. The image plane is parallel to the (001) lattice planes and passes at the center through the Au emitter atom. The image size is (15 Å)^2. (b) The corresponding energy-added reconstruction of holograms that were calculated for the experimental energies and angles. The images (a) and (b) are displayed in a greyscale where black corresponds to maximum peak intensity. Low image values were removed. (c) Illustration of the neighborhood of the Au fluorescence atom in the image plane of (a) and (b). [Kossel98, Adams99]

calculated for a Cu_3Au cluster with a radius of $2a_0 = 7.5$ Å. The calculations were performed according to section 3.1 and for the energies and angles that were used in the experiment. The resulting energy-added reconstruction is shown in fig. 5.11 (b). The highest peaks that occur in the reconstruction of calculated holograms occur also in the reconstruction of experimental holograms showing that the experimental

reconstruction was successful.

The evaluation [Kossel98] of this experiment was complicated because the data were measured in a mixed mode and the number of counts was small. The angular step size was small enough to make XSW lines visible. The same step size was therefore chosen for all following experiments described in this text. The energy steps were large in this experiment (section 2.3.1) so that an energy integration could not be performed. Smaller energy steps were used in the following experiments. The evaluation of these data took E. Kossel about half a year mostly because it was not easy to determine and remove the XFH contribution to the mixed MEXH holograms and because the time required for reconstructing holograms was limited by computer speed. Faster computers now allow a faster reconstruction of holograms. The examples of mixed experiments given in this chapter show that the separation of XFH and MEXH contributions to mixed holograms is necessary but very complicated or even impossible.

5.4 Pure Experiments

The measurements performed in the frame of this work since May 1997 were carried out in pure XFH or MEXH. This was a consequence of the problems encountered with the mixed data sets and it was necessary to allow a comparison of XFH and MEXH. The experiments performed in May and June 1997 are the first pure XFH and pure MEXH experiments, respectively. They will be discussed in the following.

5.4.1 Cu_3Au XFH Data Recorded in May 1997, Cu_3Au MEXH Data Recorded in June 1997

The angular range was comparatively small and only two incidence energies were used in these x-ray holography experiments on Cu_3Au. The Cu K_α fluorescence was detected by two silicon drift detectors d1 and d2.

Cu_3Au, XFH

In this XFH experiment, both detectors covered an angular range of 120° in φ_d. The step size was 1°. One detector (d1) covered an angular range $-21°, -20°, ...50°$ in α while the other detector (d2) covered $19°, 20°, ...90°$ in α. No intensity can be detected in our experimental geometry for negative α values. In this geometry, the XFH intensity is zero for $\alpha = 0°$ due to absorption. The intensities for $\alpha < 8°$ were too low to be useful. Therefore, for d1 only the α range from 8° to 50° was used in the evaluation. Two incidence energies were used, 9.350 keV and 10.050 keV. A total number of 1.8×10^{10} counts was recorded in this XFH experiment at the Cu K_α fluorescence line. 2.8×10^9 counts were recorded at the incident beam energy 9.350 keV by d1, 5.2×10^9 counts at 9.350 keV by d2, 3.5×10^9 counts at 10.050 keV by d1, and 6.8×10^9 counts at 10.050 keV by d2.

Experimental XFH intensities measured by the detector d2 are shown in fig. 5.12. The incident energy was 10.050 keV in this case. The interference energy in XFH

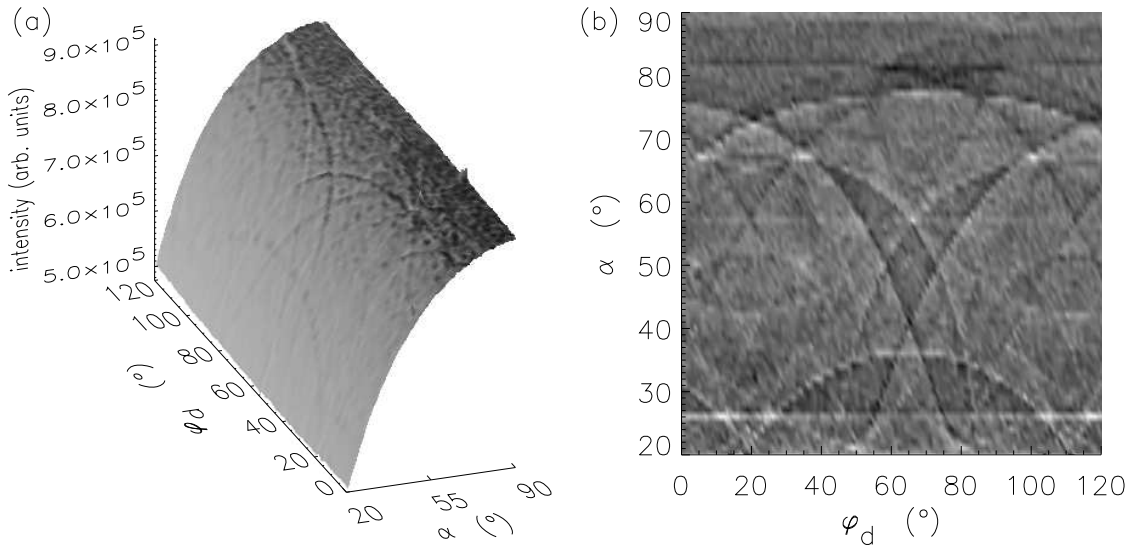

Figure 5.12: (a) XFH intensity and (b) normalized hologram measured on a Cu_3Au single crystal. Kossel lines can be seen in the raw intensities and in the hologram. The incidence energy was 10.050 keV. The interference energy in XFH is the detected fluorescence energy which was given by the Cu K_α line of 8.05 keV. In (b), a linear greyscale is used to indicate the intensities. Dark grey corresponds to a high intensity.

is the fluorescence energy so that a very similar hologram was obtained at an incidence energy of 9.350 keV. The measured intensity is shown in part (a) and the normalized hologram after removal of reference wave and absorption effects is shown in part (b). Reference wave and absorption effects were determined according to section 2.4.1.

In order to extend the holograms to 360° in φ_d, 90° of the 120° in φ_d were used: A part of the hologram covering 90° in φ_d was copied to the φ_d ranges from 0° to 89°, from 90° to 179°, from 180° to 269°, and from 270° to 359° of an extended holographic array that coveres 360° in φ_d. This extension ensures that the hologram range has a rotational symmetry around the sample surface normal which was parallel to the crystal [001] axis (compare fig. 3.2). Therefore the symmetry in reconstruction planes parallel to the (001) lattice planes corresponds to the symmetry of the structure. The symmetrization is problematic because it forces a fourfold symmetry into holograms and reconstructions. Even statistical or systematic errors in holograms will lead to a fourfold symmetry in the reconstructions of holograms that are symmetrized.

The extended holographic arrays were reconstructed according to eq. 2.67. Fig. 5.13 shows the reconstructed images $|\psi_k(\mathbf{r})|^2$ obtained from the XFH holograms. The image plane passes through the Cu emitter atom at the origin and is parallel to the (001) lattice planes. The reconstructions obtained from detector d1 are shown in (a)-(c) and from detector d2 in (d)-(f).

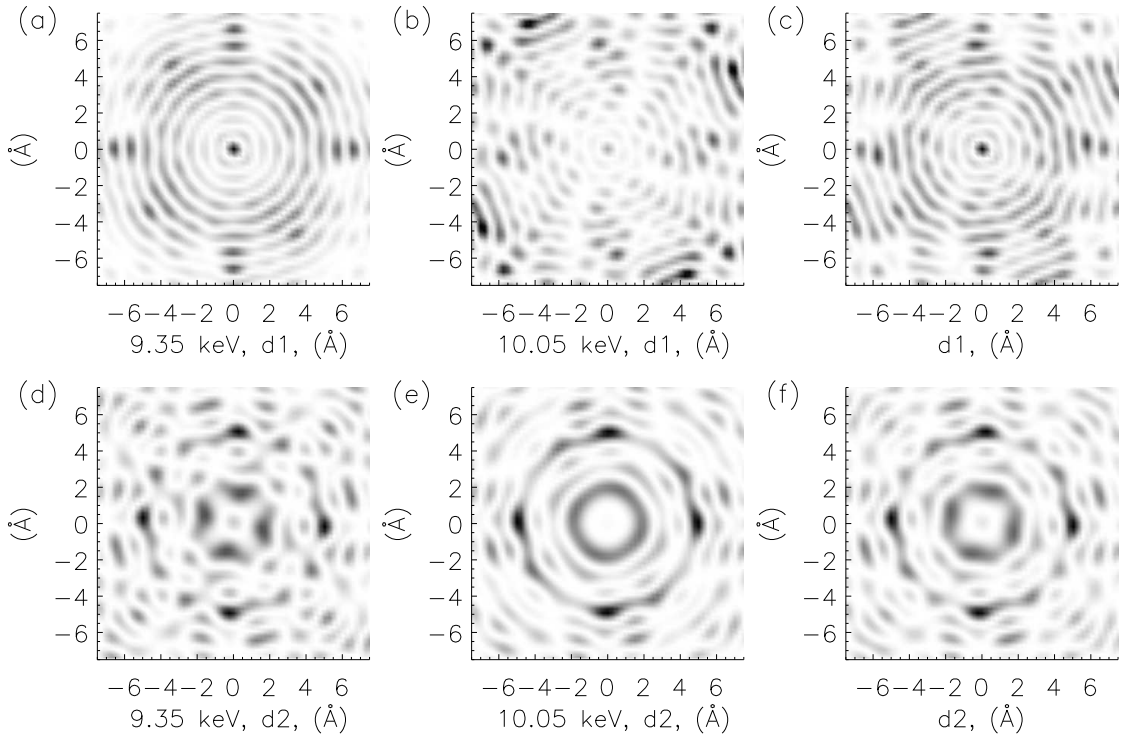

Figure 5.13: Reconstructed images $|\psi_k(\mathbf{r})|^2$ obtained from extended XFH holograms measured on Cu_3Au. The images are parallel to the (001) lattice planes and pass through the emitter atom at the origin (0,0). The corresponding holograms were measured (a) at an incidence energy of 9.350 keV by d1, (b) at an incidence energy of 10.050 keV by d1, (d) at an incidence energy of 9.350 keV by d1, and (e) at an incidence energy of 10.050 keV by d2. Parts (c) and (f) show the added reconstructions of the holograms measured by d1 and d2, respectively. The images are displayed in a linear greyscale where dark grey corresponds to high peak intensity. No background cutoff was used.

Since the interference energy is the fluorescence energy in XFH, these summed reconstructions are single-energy reconstructions and all of them should look similar. The reconstructions (a)-(c) obtained from holograms measured by d1 are similar to each other for distances $\lesssim 6$ Å from the emitter atom. The reconstructions (d)-(f) obtained from holograms measured by d2 are similar to each other but not similar to the reconstructions (a)-(c). A high peak at the origin of the reconstructions (a)-(c) shows that the removal of reference wave and absorption effects was not completely successful for the holograms measured by detector d1. Differences between the reconstructions (a)-(c) and (d)-(f) can be due to the different measuring conditions for d1 and d2: different α ranges were covered so that different reconstructions may result. The total number of counts was lower for d1 than for d2 and the statistical noise in the holograms was especially high for d1 at low α values. Therefore more reliable reconstructions can be expected for d2.

The highest peaks in the reconstructions (d)-(f) of holograms measured by d2 occur at similar positions, which they should since the corresponding holograms were measured at the same interference energy. These peaks have a distance of $\approx 2a_0 = 7.5$ Å from each other and correspond to the third nearest neighbors of the emitter in this imaging plane. (The image is rotated by 45° compared to the schematic Cu_3Au structure of fig. 4.11.) Further neighbors are not imaged which can be due to twin image effects.

As expected, the data evaluation was much more straightforward for this pure experiment than for mixed experiments and first structural information is obtained at a single interference energy.

Cu_3Au, MEXH

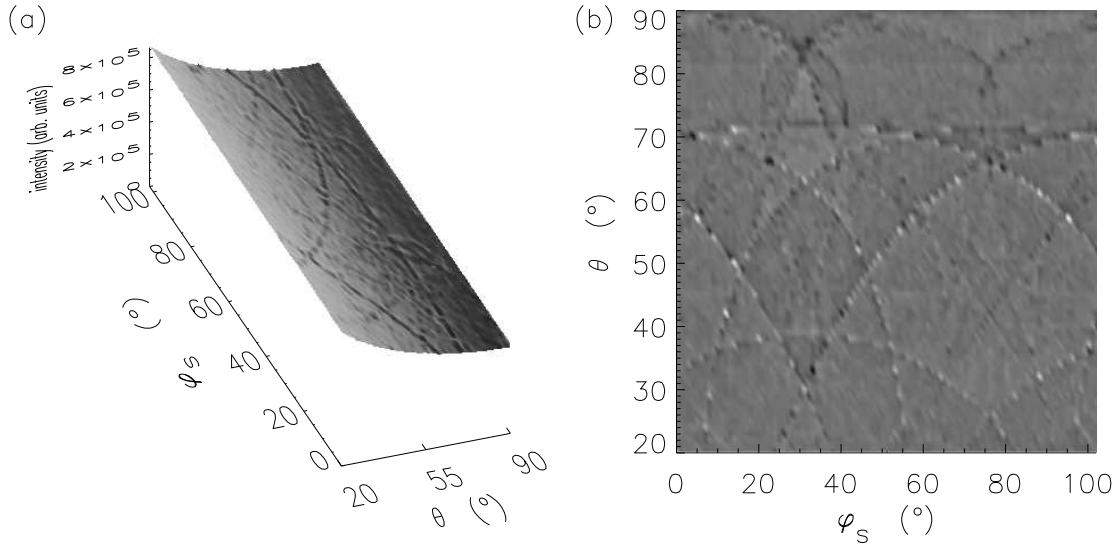

Figure 5.14: (a) MEXH intensity and (b) normalized hologram measured on a Cu_3Au single crystal. XSW lines can be seen in the raw intensities and in the hologram. The incidence energy was 10.050 keV which is the interference energy in MEXH. The Cu K_α line was detected.

In this MEXH experiment, both detectors covered an angular range of 120° in φ_d and the range 20°, ...90° in α. The step size was 1° in both angular coordinates. A total number of 3.4×10^{10} counts were recorded in the MEXH experiment at the Cu K_α fluorescence line. Of these, 1.3×10^{10} counts were recorded at the incident beam energy 9.350 keV by d1, 6.3×10^9 counts at 9.350 keV by d2, 9.9×10^9 counts at 10.050 keV by d1, and 4.6×10^9 counts at 10.050 keV by d2.

Experimental MEXH intensities measured by d2 are shown in fig. 5.14. The incident energy of 10.050 keV is the interference energy in MEXH. The measured intensity is shown in part (a) and the normalized hologram after removal of reference wave and absorption effects is shown in part (b). The absorption effects are different in XFH

and MEXH as can be seen in the raw data of figs. 5.12, 5.14. The absorption effects in XFH and MEXH are described in section 2.4.1. As for the XFH experiment, 90° of the 120° in φ_s were used to extend the holograms to 360° in φ_s.

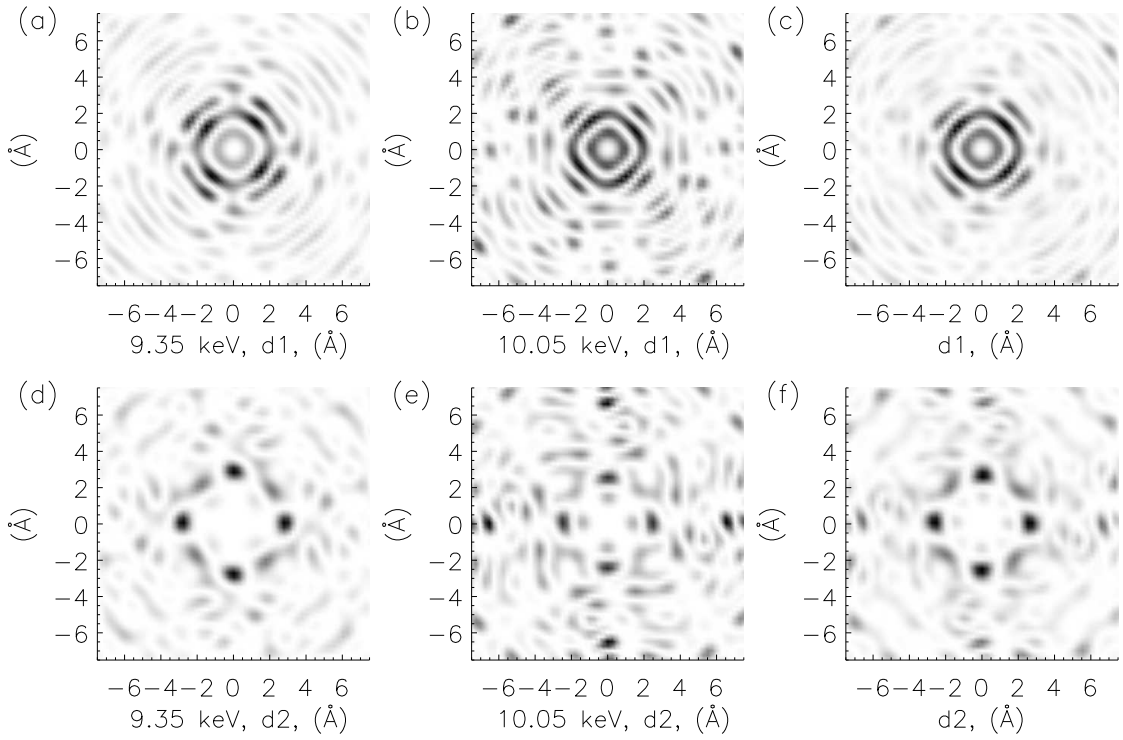

Figure 5.15: Reconstructed images $|\psi_k(\mathbf{r})|^2$ obtained from extended MEXH holograms measured on Cu_3Au. The images are parallel to the (001) lattice planes and pass through the emitter atom at the origin (0,0). The corresponding holograms were measured (a) at an incidence energy of 9.350 keV by d1, (b) at an incidence energy of 10.050 keV by d1, (d) at an incidence energy of 9.350 keV by d1, and (e) at an incidence energy of 10.050 keV by d2. Parts (c) and (f) show the energy-added reconstructions $|\psi(\mathbf{r})|^2$ of the holograms measured by d1 and d2, respectively. The images are displayed in a linear greyscale where dark grey corresponds to high peak intensity. No background cutoff was used.

The extended holograms were reconstructed according to eq. 2.67 at the single energies and according to eq. 2.70 for both energies together. Fig. 5.15 shows the reconstructed images $|\psi_k(\mathbf{r})|^2$, $|\psi(\mathbf{r})|^2$ obtained from the MEXH holograms. The image plane passes through the Cu detector atom at the origin and is parallel to the (001) lattice planes. The reconstructions obained from d1 are shown in (a)-(c) and from d2 in (d)-(f).

High peaks occur close to the origin of the reconstructions (a)-(c) and indicate problems in background removal for the holograms recorded by d1. The energy resolution of d1 was only about 0.5 keV in this experiment which can introduce an additional background in the holograms. The highest peaks in the reconstruc-

tions (d)-(f) obtained from d2 have similar positions. Deviations can be due to the different interference energies in (d) and (e). These peaks have a distance of $\approx a_0 = 3.75$ Å from each other and correspond to the nearest neighbors of the detector in the imaging plane. The best image is the energy-added reconstruction (f) of the holograms measured by d2. (The image is rotated by 45° compared to the schematic Cu_3Au structure that is shown in fig. 4.11.)

First Pure Experiments, Angular Range

The main complication in the evaluation of these first pure XFH and MEXH data was caused by fact that the φ_s range in MEXH and the φ_d range in XFH was only $\approx 120°$. Such a limited scan range can make the determination of reference wave and absorption effects from single scans complicated. For example, if scans are measured for a full 360° rotation, the intensity should be the same at 0° and after the rotation at 360°. Different intensities at 0° and at 360° can be due to a drift in intensity or position of the incident beam. Different intensities at 0° and at some arbitrary angle, for example 120°, can be due to a misalignment of sample or beam, to different interference intensities or to a drift of the incident beam. Holograms that are measured in a small φ_d range have to be symmetrized and extended along φ_d so that the full 360° range in φ_d is covered in order to produce the structure symmetry in the reconstructions. The extension and symmetrization can lead to systematic errors in the reconstructions. Therefore a large angular range was used in subsequent experiments.

5.4.2 bcc Fe XFH Data Recorded in October 1998

A photo of a pure XFH experimental setup is shown in fig. 5.16. The XFH experiment was carried out at the undulator beamline BW1 [Frahm95] in October 1998. The DORIS current in 5 bunch mode decreased from 140 mA to 80 mA during one run. Two focusing mirrors were used, one before and one after the 2 symmetric Si (111) monochromator crystals. The incident x-ray energy was 9.0 keV. The slit in front of the ionisation chamber was 1.0 mm×1.0 mm in size. The number of incident photons was stabilized for single φ_d scans within ≈ 0.5 % at $\approx 5 \times 10^{10}$ photons/s/mm^2. A bcc Fe single crystal served as a sample. All Fe atoms have the same neighborhood in bcc Fe so that complications that arise from different neighborhoods are avoided. The sample was aligned on a diffractometer and was fixed relative to the incident beam. The beam hit the sample at fixed $\theta = 90°$, $\varphi_s = const.$ The angular resolution of about 1° was determined by the beam footprint size on the sample surface and by the detector acceptance angle. Two silicon drift detectors were rotated around the sample in two angular coordinates φ_d and α. Each detector covered the full 360° in φ_d. Both detectors covered different α ranges, allowing together to measure from $\alpha = 0°$ to $\alpha = 83°$. The measuring time was 2 s per angular point. About ten holograms were obtained in a total recording time of 12 days. The net counting time was 6 days. The total recording time includes the time necessary for motor movements and could be reduced nearly to the net counting time if the point-by-point scans are replaced by continuous scans.

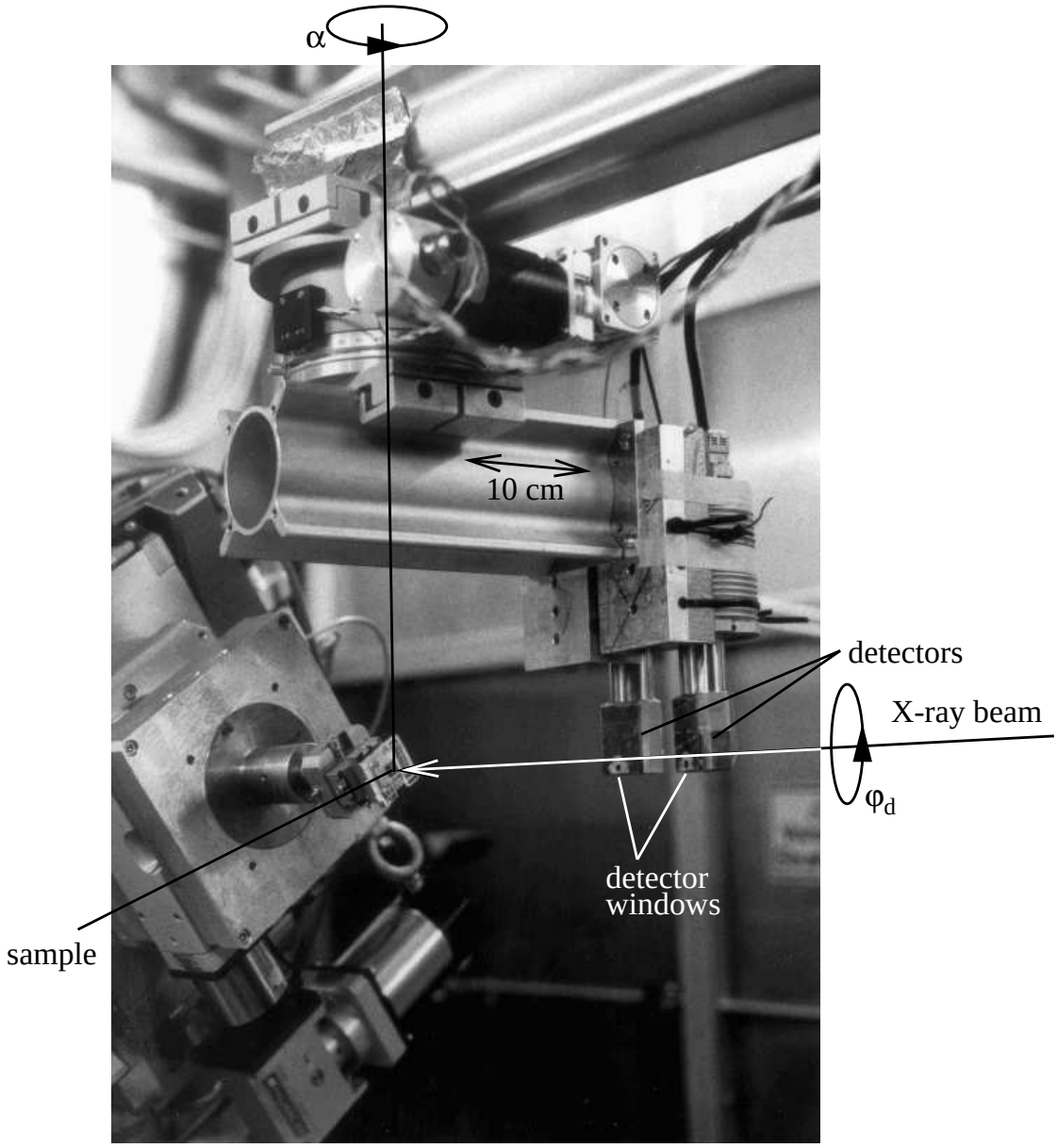

Figure 5.16: Photograph of the XFH experimental setup at BW1, October 1998. The sample is a bcc Fe single crystal. It is aligned on a diffractometer and is fixed relative to the incident beam. Two silicon drift detectors are rotated around the sample in two angular coordinates φ_d and α.

For each detector, the energy window of one SCA discriminated the Fe K_α line, and the window of another SCA discriminated the Fe K_β line. The total number of counts summed over both detectors and all data sets was $\approx 7 \times 10^9$ at the Fe K_α line and $\approx 3 \times 10^9$ at the Fe K_β line. For each of about 10 data sets, the total number of counts was 10^9. The average count rate was $\approx 10^4$ photons/s in each detector, so that the average number of counts per angular element, data set and detector was $\approx 2 \times 10^4$. Details of the XFH experiment are given in appendix C.1, table C.1. The experimental data and results are discussed in section 6.1.

5.4.3 bcc Fe MEXH Data Recorded in July 1998 and in March 1999

MEXH holograms were measured for several energies at the bending magnet beamline CEMO [HASYLAB97]. The DORIS current decreased in one run from 140 mA to 60 mA in 5 bunch mode and from 100 mA to 50 mA in 2 bunch mode. An Au coated mirror was used before the 2 symmetric Si (111) monochromator crystals. The sample was a bcc Fe single crystal. It was aligned on a diffractometer. Two silicon drift detectors were fixed with respect to the sample. Sample and detectors were rotated relative to the incident beam direction in two angular coordinates φ_s and θ.

bcc Fe MEXH Data Recorded in July 1998

Incidence energies from 7.9 keV to 11.3 keV in steps of 0.2 keV were used in a first MEXH experiment on bcc Fe in July 1998. The parameters of the first experiment were the following: The beam hit the sample at variable angles θ, φ_s. A limited φ_s range of 150° was recorded for $\theta = 20°, ...90°$. For each detector, the energy window of one SCA allowed to count the total over the Fe K lines. This signal was used as the holographic interference intensity. In order to determine the influence of the elastic line, the window of another SCA allowed to count the total over the Fe K lines and the elastic line. The total measuring time per angular element and energy varied between 2 s and 8 s. It was 3 s for most energies. The average recording time per energy was 22 hours, yielding for 18 energies a total time of 16 days. The total number of counts summed over both detectors and all data sets was $\approx 4.3 \times 10^{10}$ at the total Fe K line. Details are given in appendix C.2, table C.2.

bcc Fe MEXH Data Recorded in March 1999

A photo of a second MEXH experiment on bcc Fe is shown in fig. 5.17. The experiment was performed in March 1999. In this experiment, incidence energies from 9.5 keV to 11.1 keV in steps of 0.4 keV were used. The slit in front of the ionisation chamber was of size $(0.4\ \text{mm})^2$. The number of incident photons was $\approx 2 \times 10^{10}$ photons/s/$(0.4\ \text{mm})^2$ at 9.5 keV and $\approx 4 \times 10^9$ photons/s/$(0.4\ \text{mm})^2$ at the other energies and was stabilized within ≈ 0.5 % for single φ_s scans. The angular resolution of $\approx 0.003°$ vertical $\times \approx 0.02°$ horizontal was determined by the incident radiation. The full 360° range in φ_s could be measured for $\theta = 90°, ...44°$ and a limited 95° range in φ_s was available for $\theta = 43°, ...0°$.

The measuring time was 3 s per angular point. The holograms were obtained in a total recording time of 10 days. For each detector, the energy window of one SCA discriminated the Fe K_α line and the window of another SCA discriminated the total over the Fe K lines. The average number of counts measured per angular element and per energy by each detector was $\approx 9 \times 10^4$ in the Fe K_α line and $\approx 1.2 \times 10^5$ in the total over the Fe K lines. The hologram measurements at 9.5 keV and at 9.9 keV were repeated once respectively twice. The total number of counts summed over

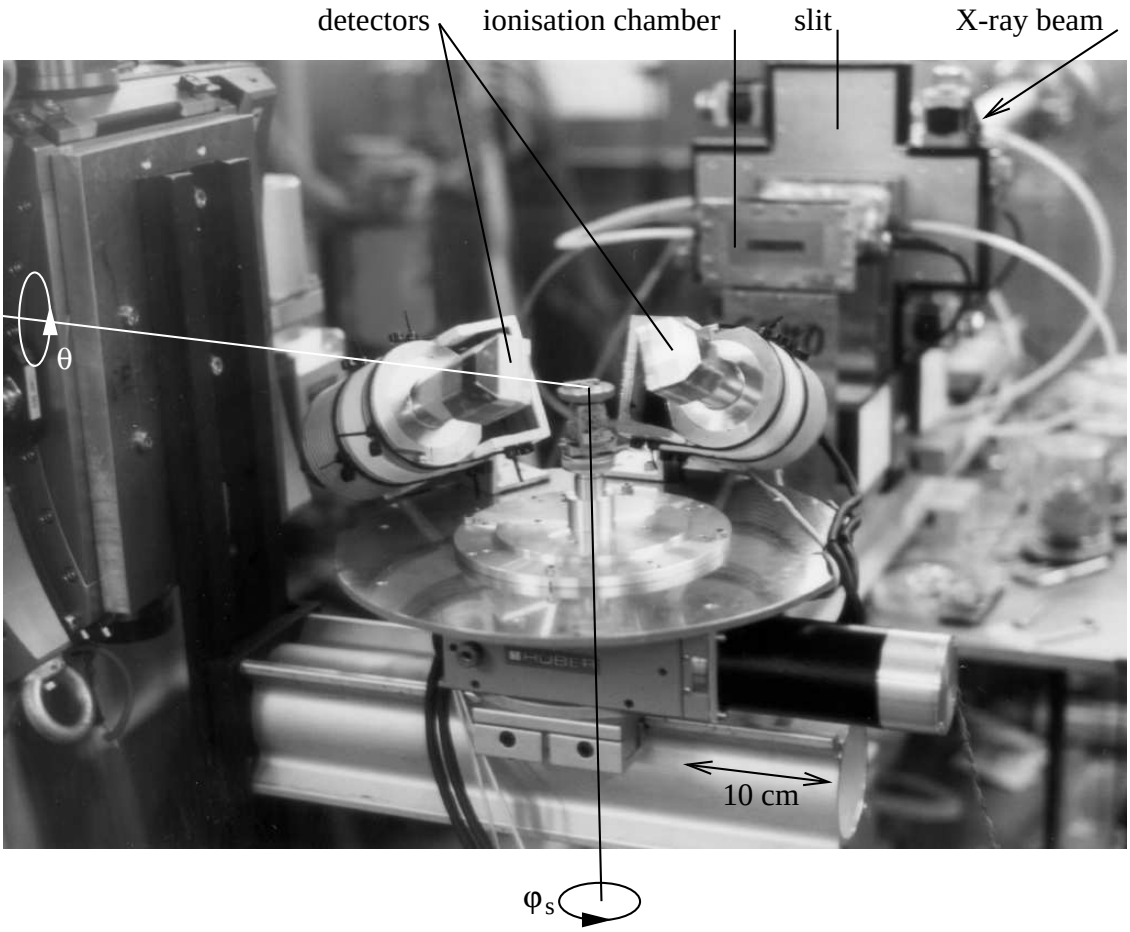

Figure 5.17: Photograph of MEXH experimental setup at CEMO, March 1999. The sample is a bcc Fe single crystal. It is aligned on a diffractometer. Two silicon drift detectors are fixed with respect to the sample. Sample and detectors are rotated relative to the incident beam direction in two angular coordinates φ_s and θ.

both detectors and all data sets was $\approx 1.6 \times 10^{10}$ at the Fe K_α line and $\approx 2.1 \times 10^{10}$ at the total Fe K line. Details are given in appendix C.2, table C.3. The MEXH data measured on bcc Fe and the results are discussed in section 6.2.

Future MEXH Experiments

The present detector geometry allowed measuring MEXH holograms in a comparatively large angular range only for a relatively small detector acceptance angle of about 1°. In order to obtain higher count rates, a different detector geometry would be desirable. It could allow integrating the fluorescence signal over a larger angular range while retaining the large range of incidence angles.

Point-to-point scans were replaced by fast continuous scans in recent experiments [Adams00b, Faigel99]. This makes it possible to integrate the signal over one angular coordinate, to perform the experiment at a stable incident beam, and to use the beamtime effectively. In these experiments, the detectors were not fixed

with respect to the sample so that only the small lightweight sample was rotated continuously. In the MEXH experiments described here, the detectors were fixed with respect to the sample in order to perform pure MEXH so that stronger motors are required for fast continuous scans. Fast continuous experiments can now be performed at HASYLAB in this pure setup.

A special characteristic of MEXH is the high angular resolution which makes a simultaneous measurement of XSW line shapes and holographic intensities possible [Adams00b]. This feature becomes a disadvantage when high sampling rates are not required. This is for example the case when only a local neighborhood of the emitter atom is of interest. The plane wave like geometry of the incident wave can be relaxed experimentally: The energy bandwidth can be increased by using multilayer or mosaic crystal monochromators or even further by using a direct undulator beam or a pink beam from a total reflecting mirror system. The angular collimation can be widened by inserting a focusing x-ray lens or an x-ray total reflecting capillary into the beam to generate a convergent monochromatic incident beam.

Electron Yield Detector

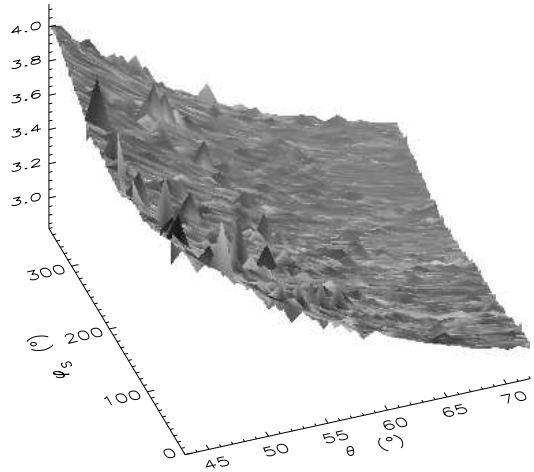

Figure 5.18: A data set recorded with the electron yield detector after dividing by the incident intensity. The energy of the incident radiation was 11.100 keV.

During the beamtime in March 1999, MEXH holograms were also recorded with the electron yield detector as described in section 4.3.2. The setup was otherwise the same as with the silicon drift detectors. An advantage of the electron detector is its acceptance angle of nearly a half sphere. A data set recorded with the electron yield detector at an incidence energy of 11.100 keV is shown in fig. 5.18. The raw data were divided by the incident intensity as recorded by a ionisation chamber.

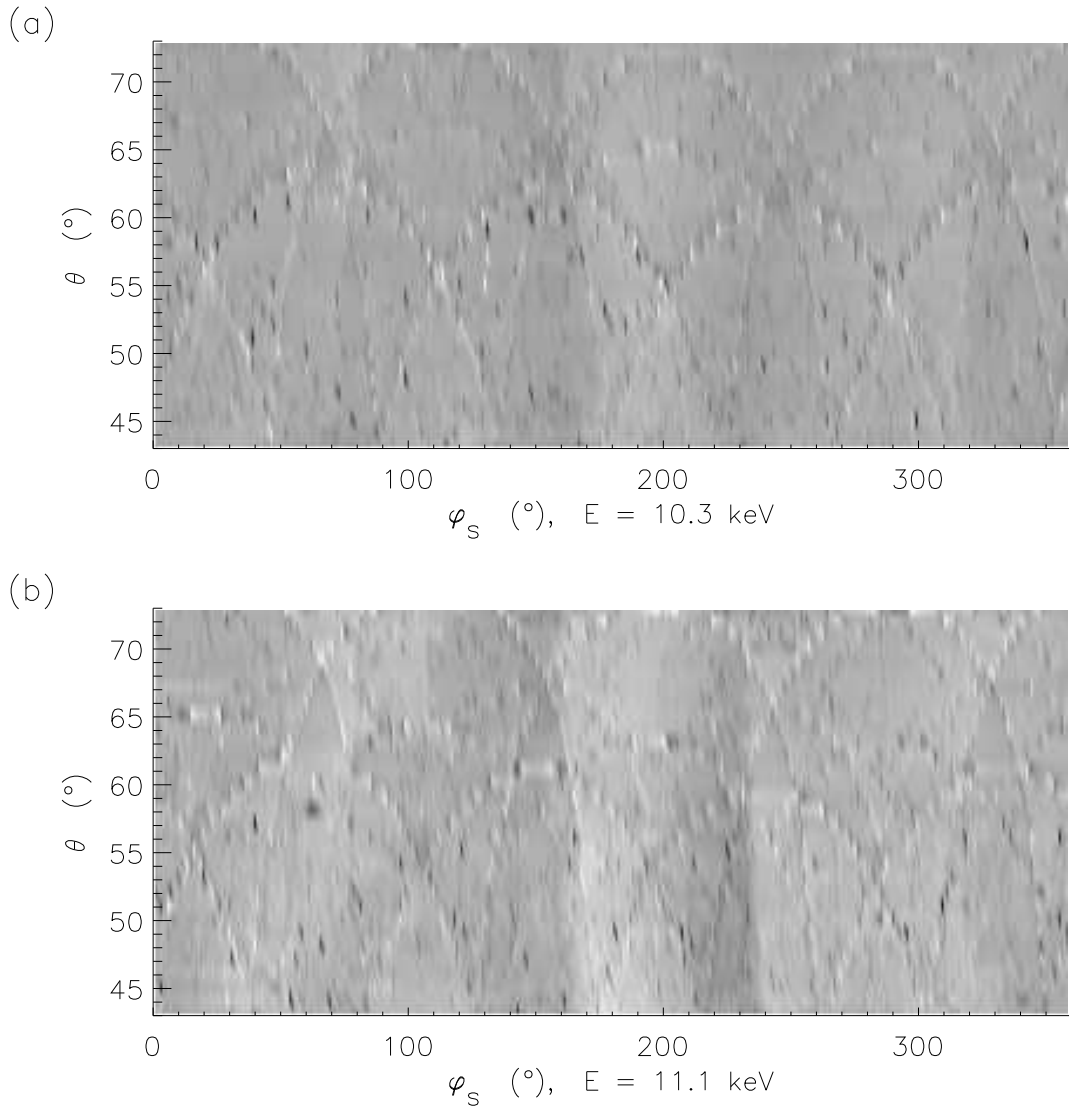

Figure 5.19: MEXH holograms recorded with the electron detector after removal of reference wave and absorption effects. The incidence energy was (a) 10.300 keV and (b) 11.100 keV.

Holograms measured at incidence energies of 10.300 keV and 11.100 keV are shown in fig. 5.19 after removal of reference wave and absorption effects. The holograms clearly show XSW patterns and are similar to holograms measured by silicon drift detectors, showing that the electron detector can be used to record holograms. These holograms are not very flat, indicating that the background removal was not very successful. The remaining background leads to artifacts in the reconstructions and prevents a successful reconstruction of the holograms. Therefore the background removal has to be improved. The background removal will be more simple in future experiments where detector details can be optimized for holography experiments (section 4.3.2). A more flat Al foil or an anode ring that is not hit by the incident beam will lead to a more constant background.

The evaluation of the data measured with the electron detector is also complicated due to very high intensities close to Bragg angles. The corresponding intensities recorded by the silicon drift detector are not so dominant close to Bragg angles due to its energy resolution and detector deadtime. Improvements will have to be made in the treatment of the high intensities, either by removing them from the holograms or by using them in a modified data evaluation, in order to use this detector for holography. This concept is especially promising if an energy-resolution is achieved that allows the separation of the incident x rays from the signal electrons.

5.5 Optimized Measurement Procedure

The goal of atomic resolution x-ray holography is to solve unknown structures in three dimensions. This requires to measure holograms in such a way that the information is obtained from a straightforward data treatment. The evaluation of experimental data together with theoretical considerations shows how the experiments should be performed:

Pure Experiments

Mixed experiments make a separation of XFH and MEXH signals in the data evaluation necessary which is hardly possible in some cases. Therefore, experiments should be performed in a pure XFH or pure MEXH mode that allows a straightforward data evaluation. This will be an advantage especially for future applications of the methods to unknown structures.

Fast Scans

Long-term variations of the incident beam lead to jumps in the holographic intensity. Jumps within single scans may prevent a successful background removal and a holographic evaluation of interference intensities. Jumps between different single scans prevent a two-dimensional determination of reference wave and absorption effects. If reference wave and absorption effects can only be determined from one-dimensional scans, then the average holographic information along the other angular coordinate is lost in the normalized holograms. Holograms should therefore be measured within a time that is short compared to the time between fluctuations of the incident beam. Typical recording times should not exceed a few hours and - at storage rings - a complete hologram should be recorded within one synchrotron radiation run. Fast scans require fast motors and a fast data acquisition system. Measurements can be repeated to increase experimental statistics.

Continuous Scans

Instead of measuring point-to-point scans, scans can be measured continuously during the angular movements in order to integrate the signal over one angular coordinate. For crystals this allows to integrate over the contributions from Kossel or XSW lines which can otherwise in MEXH not easily be sampled in a large angular

range and at sufficiently small steps. In order to integrate over two angular coordinates in MEXH, the plane-wave like geometry of the incident wave must be relaxed experimentally. An integration happens naturally in XFH for both angular coordinates where the detector acceptance angle defines the range of angular integration. Continuous scans allow a large duty cycle and therefore use the beamtime more efficiently than point-to-point scans.

High Statistics

The holographic signal is typically on the order of $\lesssim 10^{-4} \times N$ of the elastic background where N is the number of recorded photons. [3] The statistical noise is on the order of $\sqrt{N}$. The number of photon counts in the experimental holograms has to be increased so that the holographic signal becomes comparable to or larger than the statistical noise. The condition $10^{-4} \times N = \sqrt{N}$ is fulfilled for $N = 10^8$. This condition is very weak because it only requires the statistical noise to be comparable to the *extrema* of the holographic signal. If this condition is applied to each angular bin individually, then 10^8 counts per angular bin should be measured. This corresponds to 3×10^{13} total counts for 360×90 angular bins. For a wavelength of 1 Å and an atom that has a distance of 5 Å from the emitter, at least 40 angular bins should be measured in 360° under simple assumptions (section 2.3.1). If a hemisphere is measured in 40×10 angular bins, then 4×10^{10} total counts should be recorded. Photon numbers of this order are presently available only for crystals that provide high photon numbers.

Large Angular Range, High Angular Resolution

Holograms should be measured in a large angular range. This is necessary to measure the holographic interference pattern for unknown structures (section 2.3.1) and it is necessary for a high spatial resolution in the reconstructions. Holograms that are known on a full 4π sphere make three-dimensional reconstructions of nearly isotropic resolution $\approx \lambda/2$ possible, and a resolution of $\approx \lambda$ can be obtained from holograms known on a hemisphere (section 2.6.3).
A large angular range is also essential for the determination of reference wave and absorption effects. A correct determination of the background is necessary to avoid artefacts in the reconstructed images. If possible, the holograms should allow an evaluation without making a symmetrization of holograms or reconstructions necessary (chapter 6). This requires high statistics and a large angular range. The background due to reference wave and absorption effects can be determined by fitting the experimental intensities as described in section 2.4.1. The background determination is simpler for a small beam footprint on the sample surface. In this case a point-like beam footprint can be assumed as in section 2.4.1. Fourier filtering of holograms should be avoided (sections 2.3, 2.5.2, 2.6).

[3] The holographic signal is a superposition of the signals from all scattering atoms. For a single scattering atom and under simple assumptions, the holographic signal is a cosine function with amplitude $2r_e f_0/r_j$ where r_e is the classical electron radius, f_0 is a real and constant scattering factor and r_j is the distance to the scattering atom (section 2.3.1, eq. 2.26). The amplitude is proportional to $1/r_j$. As an example, $2r_e f_0/r_j \approx 4 \times 10^{-4}$ for typical values $f_0 = 26$ and $r_j = 4$ Å.

High sampling frequencies are necessary to image atoms that are far away from the emitter (section 2.3.1) so that a high angular resolution is necessary in order to provide for a sufficient sampling. If holograms of crystals are measured, an angular resolution on the order of 1° or smaller is necessary in order to make Kossel or XSW lines in the holograms visible. This allows the extension of the holograms to a full 4π sphere and makes thus three-dimensional reconstructions of nearly isotropic resolution possible even if the holograms were not measured on a full 4π sphere.

Large Energy Range, Small Energy Steps

Small energy steps are necessary for a sufficient sampling in energy. For example, energy steps of ≈ 0.3 keV are necessary to sample the energy dependence of neighbors that have a distance of 10 Å from the fluorescence atom according to section 2.3.1. A large energy range should be measured in small energy steps that allow the integration over the interference energy in the reconstruction so that systematic errors that occur in single- or few-energy reconstructions are reduced (compare section 2.6 and chapter 3). This is usually only possible in MEXH where the interference energy can be chosen freely above the absorption edge of an atom incorporated in the structure.

Chapter 6

Experimental Results from bcc Fe and Discussion

In the XFH and MEXH experiments on bcc Fe (sections 5.4.2, 5.4.3), the parameters were sufficiently optimized to allow an experimental comparison of XFH and MEXH. The data and results obtained from these experiments are dicussed in sections 6.1, 6.2, respectively. The standard data treatment is described in section 5.2. Additional data treatments that were performed in some cases are described together with the corresponding data. The results allow a comparison of XFH and MEXH experiments which is given in section 6.3.

6.1 X-Ray Fluorescence Holography

6.1.1 Experimental Data

Fig. 6.1 gives an overview over an XFH data set measured at the Fe K_α line and the corresponding data treatment. Part (a) shows a single φ_d scan of one XFH data set at $\alpha = 54°$ and a background fit to the scan according to eq. 2.64. The statistical noise in the scan is $\approx$ 0.7 %. The sine-like shape of the scan is caused by a slight misalignment (section 2.4.1). A misalignment of beam, sample or detectors can lead to relative intensity variations of a few percent (section 4.1.1). The intensity variation due to misalignment is about $\pm$0.7 % in this scan. Part (b) shows the same scan after division by the ionisation chamber signal and the background fit to this scan. The ionisation chamber signal was stabilized to $\approx$ 0.5 %. The shape of scans (a) and (b) is very similar, indicating that the division by the ionisation chamber signal has little effect on the scan.

The scans of fig. 6.1 (a) and (b) are shown after the normalization of eq. 5.1 in parts (c) and (d), respectively. The division by the ionisation chamber signal is performed for all data sets before fitting, normalizing and reconstructing. As can be expected from the small differences between the scans (c) and (d), this correction has very little influence on the reconstructed images.

Two α scans that were measured by two detectors at the same φ_d are shown in fig. 6.1 (e). The detectors cover different ranges in α (table C.1). The intensity

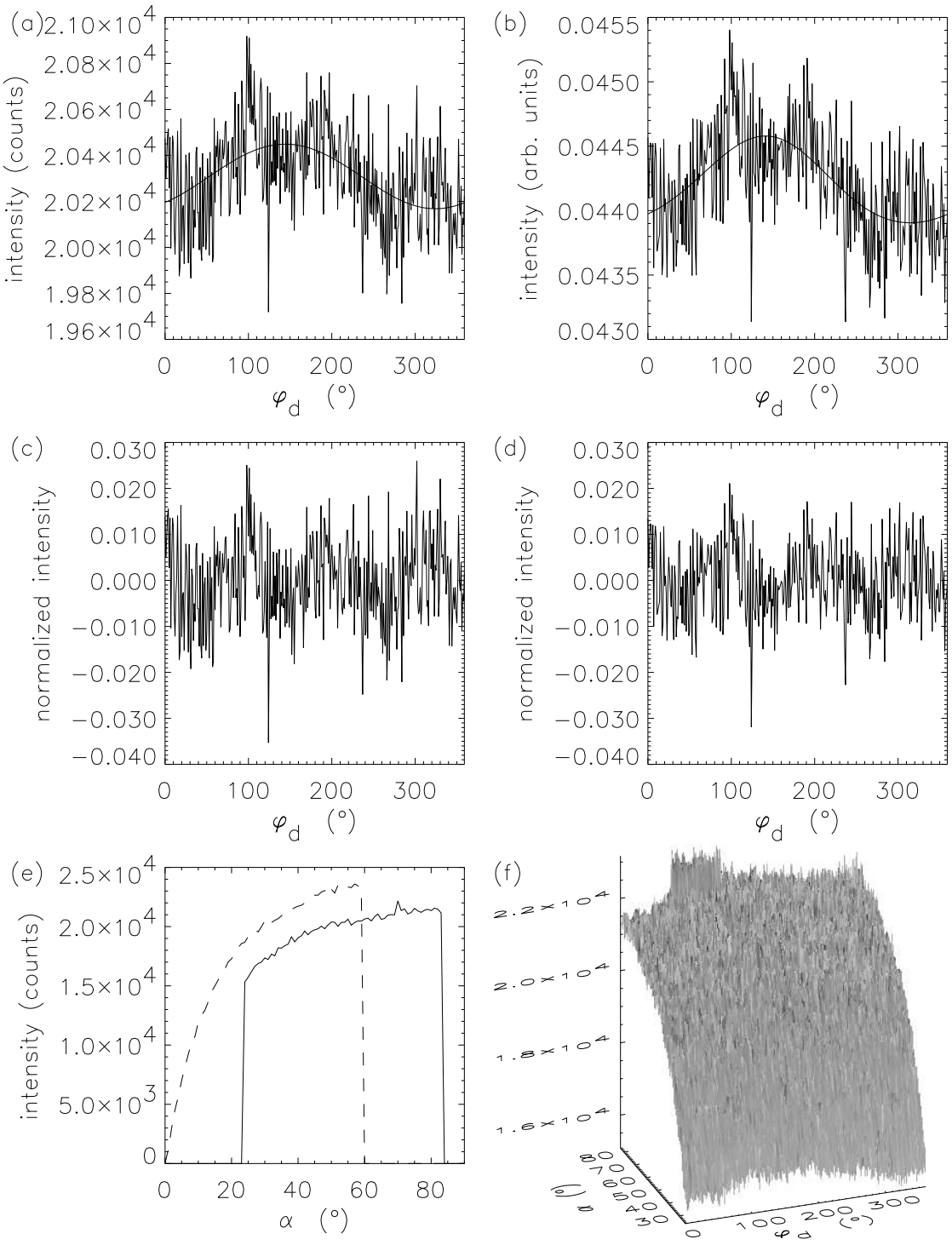

Figure 6.1: Intensities obtained from one detector in one data set at the Fe K_α line. (a) φ_d scan at $\alpha = 54°$ of one data set, and fit to the scan. The fit is used to determine the background due to reference wave and absorption effects. (b) The φ_d scan of (a) after dividing by the ionisation chamber signal, and fit to the scan. (c) The φ_d scan of (a) normalized by the fit of (a). (d) The φ_d scan of (b) normalized by the fit of (b). (e) α scans for the two detectors. (f) (α,φ_d) of one data set.

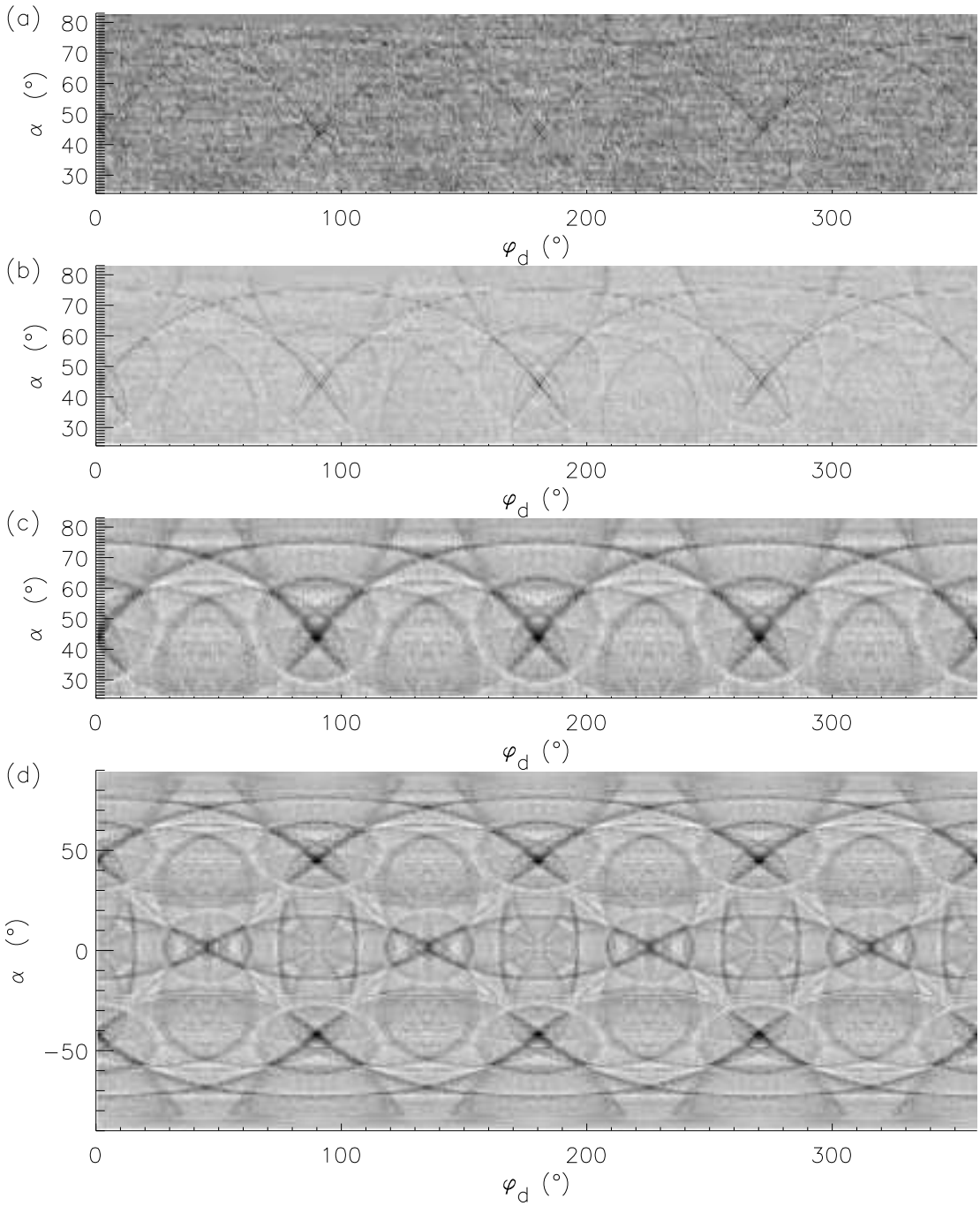

Figure 6.2: (a) The hologram obtained by normalizing one of 10 individual data sets, measured by one of two detectors in the angular range $\varphi_d = 0°, ...359°$, $\Delta\alpha_2 = 24°, ...83°$ at the energy of the Fe K_α line. (b) The sum of all 10 such holograms. (c) The rotational and mirror plane symmetries along φ_d in the hologram (b) were used to obtain this symmetrized hologram. (d) The hologram (c) extended to 4π.

at fixed α is different for both detectors since their acceptance angles were not identical. A complete data set is shown in part (f).

The normalized φ_d scans obtained for all α values form a hologram. Fig. 6.2 gives an overview over the XFH holograms obtained by one detector at the energy of the Fe K_α line. The images are displayed without any cutoff in a linear greyscale where black corresponds to maximum and white to minimum intensity. Part (a) shows one of the about 10 individually measured holograms. The total number of counts in this hologram is 4×10^8. The intensity of the single φ_d scan at $\alpha = 54°$ is that of fig. 6.1 (d). If all 10 holograms are summed, the hologram of part (b) is obtained. The total number of counts in this hologram is 4×10^9 (table C.1). The Kossel line structure becomes clearly visible in (b) while it can hardly be seen in (a). The hologram (b) shows a fourfold rotational and a mirror plane symmetry along φ_d. They can be used to obtain a symmetrized hologram: The hologram (b) is shifted by 0°, and also by 90°, 180°, and 270°. These four holograms are summed. The resulting hologram is added to itself after reflecting it at $\varphi_d = 180°$. This symmetrized hologram is shown in part (c). This hologram was extended to the full 4π sphere using the information from the Kossel lines. For known test structures the known structure can be used for the extension to 4π instead. The extended hologram is shown in part (d).

6.1.2 Reconstructions

The holograms were reconstructed according to the Barton algorithm of eqns. 2.67, 2.70, where the integrations were replaced by summations. In this chapter, all two-dimensional images of reconstructions show $|\psi_k(\mathbf{r})|^2$ at single energies and $|\psi(\mathbf{r})|^2$ at multiple energies without any cutoff in a linear greyscale where black corresponds to maximum and white to minimum intensity. For a quarter of each image, positions of atoms in bcc Fe in the image plane are indicated by the intersections of lines.

Statistical Noise

Figure 6.3 shows 9 reconstructed images obtained from 9 individual holograms measured by one detector at the Fe K_α line energy. The angular range of the holograms is the same as that of fig. 6.2 (a): $\varphi_d = 0°, ...359°$, $\Delta\alpha_2 = 24°, ...83°$. The reconstructions pass through the emitter atom in a plane parallel to the (001) lattice planes. The φ_d rotation axis was parallel to the [001] direction. The image (f) is obtained from the hologram of fig. 6.2 (a). For comparison, appendix B, fig. B.1 (d) shows the reconstructed image obtained from the corresponding calculated hologram. There, the 4 highest peaks appear on the vertical and horizontal axes through the origin at about $a_0 = 2.87$ Å distance from the origin. The 9 images of the experimental holograms look very different from this and from each other but in most of the images peaks appear also near the correct positions. The experimental setup was the same for all individual hologram measurements so that differences are mainly expected from the low statistics in the holograms. For each of these holograms, the total number of counts was about 4×10^8.

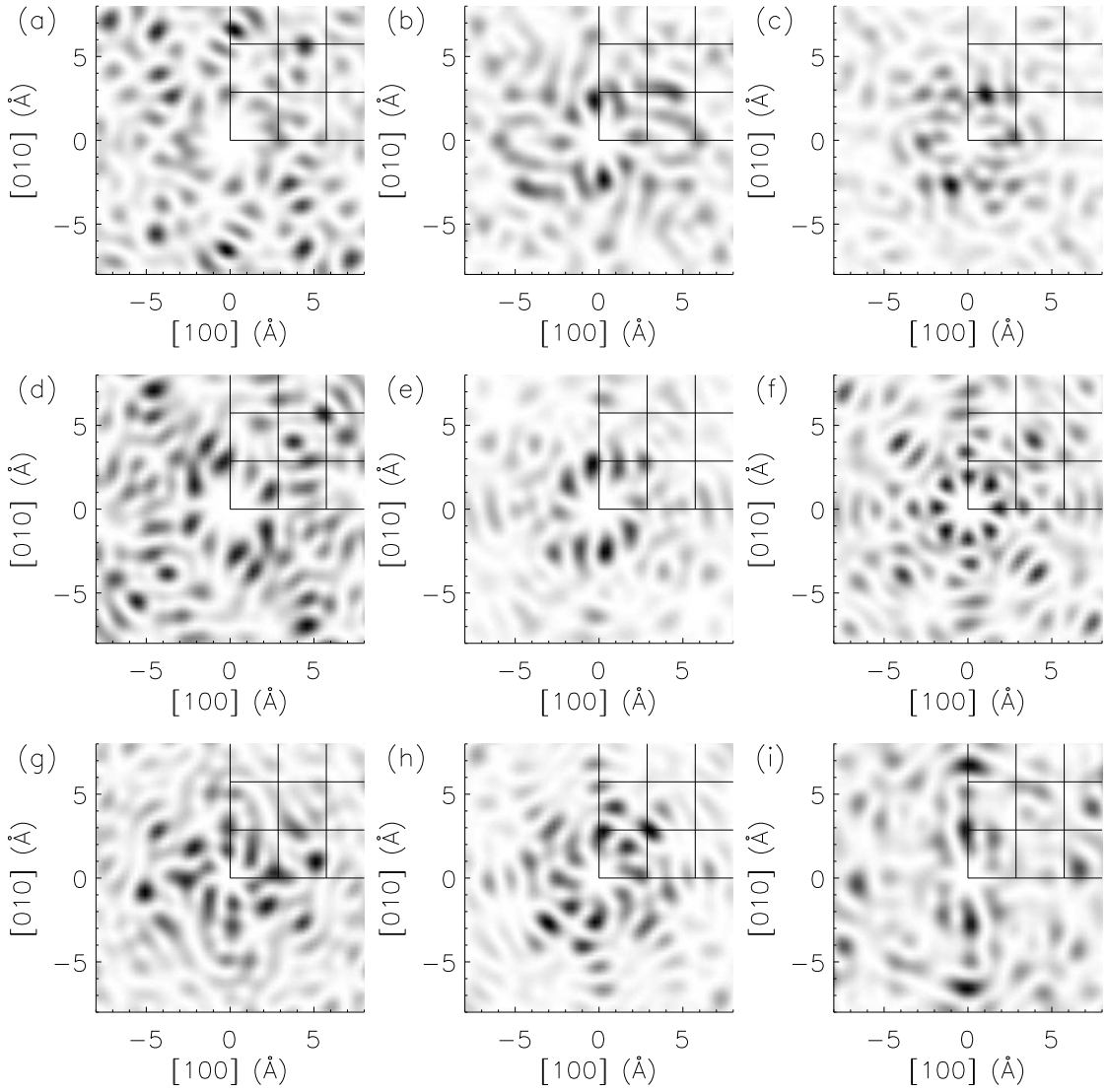

Figure 6.3: Reconstructions $|\psi_k(\mathbf{r})|^2$ of 9 different holograms measured by one detector in the angular range $\varphi_d = 0°, ...359°$, $\Delta\alpha_2 = 24°, ...83°$, at the Fe K_α line. The reconstructions pass through the emitter atom in a plane parallel to the (001) lattice planes. The φ_d rotation axis is parallel to the [001] direction. The image (f) is obtained from the hologram of fig. 6.2 (a).

According to section 2.3.1, and under simplifying assumptions, at least $8r_j/\lambda$ steps need to be measured in 360°. For a distance $r_j \approx 4$ Å and at the Fe K_α line ($\lambda \approx 1.94$ Å), $8r_j/\lambda \approx 16$. If 4×10^8 counts are distributed on a hemisphere of 16×4 relevant sampling points along $\varphi_d \times \alpha$ then the average number of counts per angular bin is $N \approx 10^8/16 = 6.25 \times 10^6$. The statistical noise at each bin is on the order of $\sqrt{N} \approx 2500$. In this text, $10^{-4}N$ will be used as an estimate for the holographic signal as explained in section 5.5. The holographic signal at each bin is on the order of $10^{-4}N \approx 625$ or smaller which is smaller than the statistical noise. In order to fulfill the requirement $10^{-4}N \approx \sqrt{N}$ at each of

16×4 bins, $16 \times 4 \times 10^8 \approx 6.4 \times 10^9$ total counts need to be recorded. [1] This is a lower limit to the necessary number of counts since a hologram contains values smaller than $10^{-4}N$ so that the requirement $10^{-4}N \approx \sqrt{N}$ may not be sufficient. Therefore many peaks in the reconstructions of fig. 6.3 are caused by statistical noise in the individually measured holograms. This was verified by summing the complex reconstructions of the individual holograms or by summing the individual holograms and then reconstructing their sum. The same result is obtained from both procedures since the reconstruction algorithm is a linear transform.

Figure 6.4 shows reconstructions of holograms that are the sum over 10 individually measured holograms. For example, part (d) shows the reconstruction of the hologram of fig. 6.2 (b). The complex reconstruction $\psi_k(\mathbf{r})$ for which $|\psi_k(\mathbf{r})|^2$ is shown in fig. 6.4 (d) is equal to the sum over the individual reconstructions $\psi_k(\mathbf{r})$ for which $|\psi_k(\mathbf{r})|^2$ are shown in fig. 6.3. The total number of counts in the sum over the holograms measured by this detector at the Fe K_α line was 4×10^9. According to the above estimate, this is about the minimum number of counts necessary for imaging atoms in 4 Å distance from the emitter. In the reconstruction of fig. 6.4 (d), peaks far away from the origin are smaller than in most images of fig. 6.3. This can be explained in the following way: Statistical noise produces high frequencies in the holograms which correspond to large distances in the reconstructions. The total number of counts is 10 times larger for the hologram reconstructed in fig. 6.4 (d) than for each individual hologram reconstructed in fig. 6.3. The reduction in statistical noise is also obvious directly from the holograms, see fig. 6.2. Thus, statistical noise in the holograms produces peaks in the reconstructions that do not correspond to the sample structure. They cannot *a priori* be separated from peaks that are caused by the structure. Only if the statistical noise in the holograms is sufficiently small then the peaks caused by statistical noise will be lower than the peaks caused by the structure and thus appear as a background.

If similar reconstructions are obtained from individual holograms and if systematic artifacts can be excluded then high peaks in the reconstructions are caused by the sample structure. The two highest peaks in the image of fig. 6.4 (d) appear near the positions of two nearest neighbors of the emitter in this image plane. The other two nearest neighbors of this image plane appear as weaker peaks. This image does not show the full fourfold rotational symmetry expected from the corresponding image obtained from the calculated hologram (appendix B, fig. B.1 (d)) which can be attributed to statistical noise in the hologram.

Fig. 6.4 (a), (b), (d), (e) show the four reconstructions $|\psi(\mathbf{r})|^2$ obtained by the two detectors and at the energies E_1 and E_2 of the Fe K_α and K_β lines. The detectors cover different angular ranges $\Delta\alpha_1$ and $\Delta\alpha_2$. The reliability of the reconstructions can be tested by comparing the reconstructions with each other. Peaks appear at similar positions but with different heights in the four images (a), (b), (d), (e). For each detector, reconstructions at two energies were combined, and for each energy,

[1] This was not done in individual holograms here. Instead, the holograms were measured fast to ensure a stable incident beam that allows a straightforward background removal, and the hologram measurement was repeated 10 times.

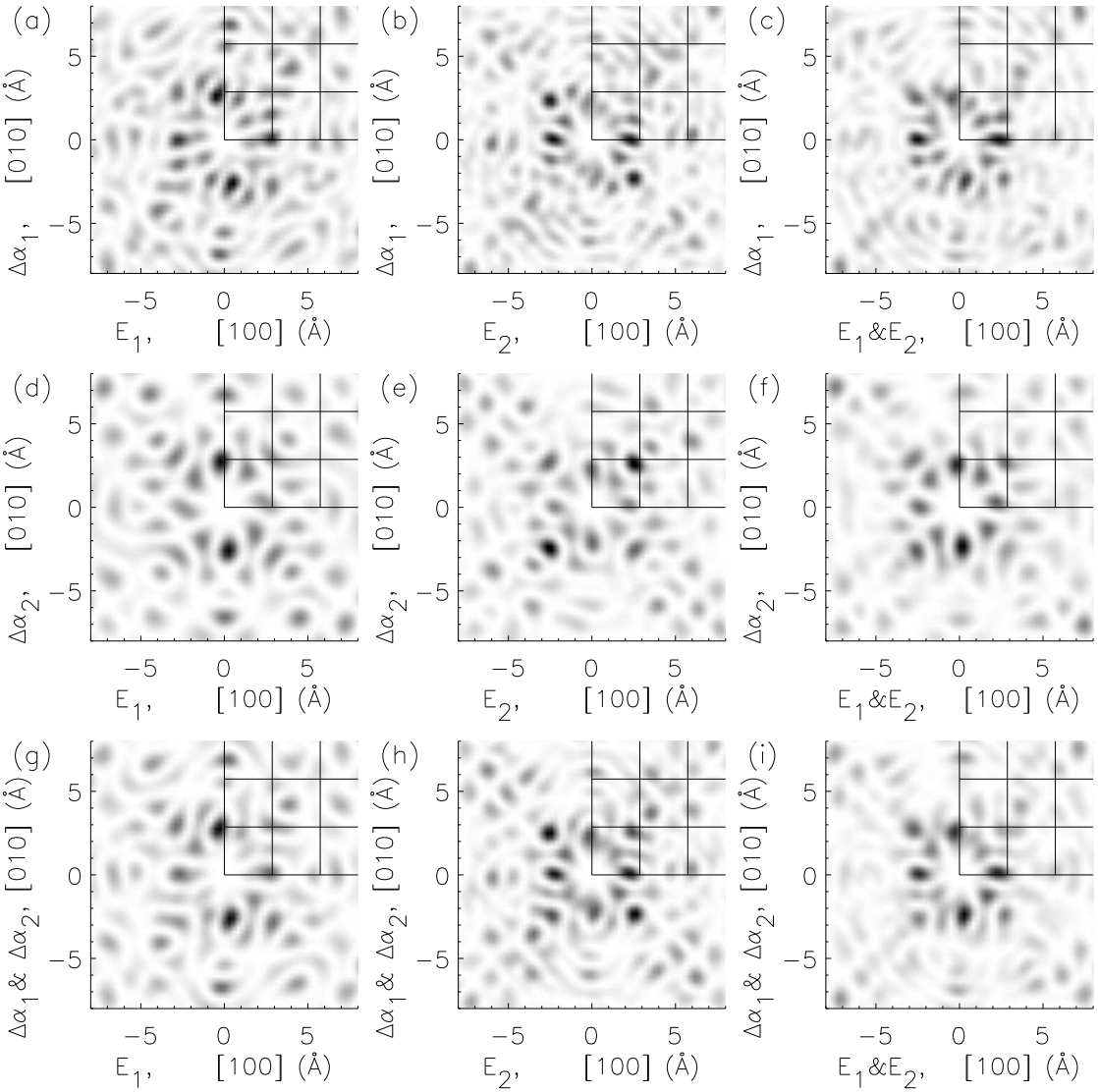

Figure 6.4: Reconstructions $|\psi_k(\mathbf{r})|^2$ of 10 summed holograms at the energies (a), (d), (g) E_1 of the Fe K_α line, (b), (e), (h) E_2 of the Fe K_β line, $E_2 = 7.1$ keV, and (c), (f), (i) energy-added reconstructions $|\psi(\mathbf{r})|^2$ using E_1 and E_2. The angular range was $\varphi = 0°, ...359°$, and (a)-(c) $\Delta\alpha_1 = 0°, ...59°$, (d)-(f) $\Delta\alpha_2 = 24°, ...83°$. (g)-(i) show the summations over the reconstructions from both angular ranges for the different energies. The image (d) is obtained from the hologram of fig. 6.2 (b). The reconstructions pass through the emitter atom in a plane parallel to the (001) lattice planes. The φ_d rotation axis was parallel to the [001] direction.

reconstructions for two detectors were added. These images are shown in parts (c), (f), (g), (h). Combining two of the four images improves their symmetry. The four single reconstructions (a), (b), (d), and (e) were combined to obtain the image (i) where a clear fourfold symmetry is visible. The total number of counts in the holograms used for this reconstruction is $\approx 10^{10}$.

Spatial Resolution

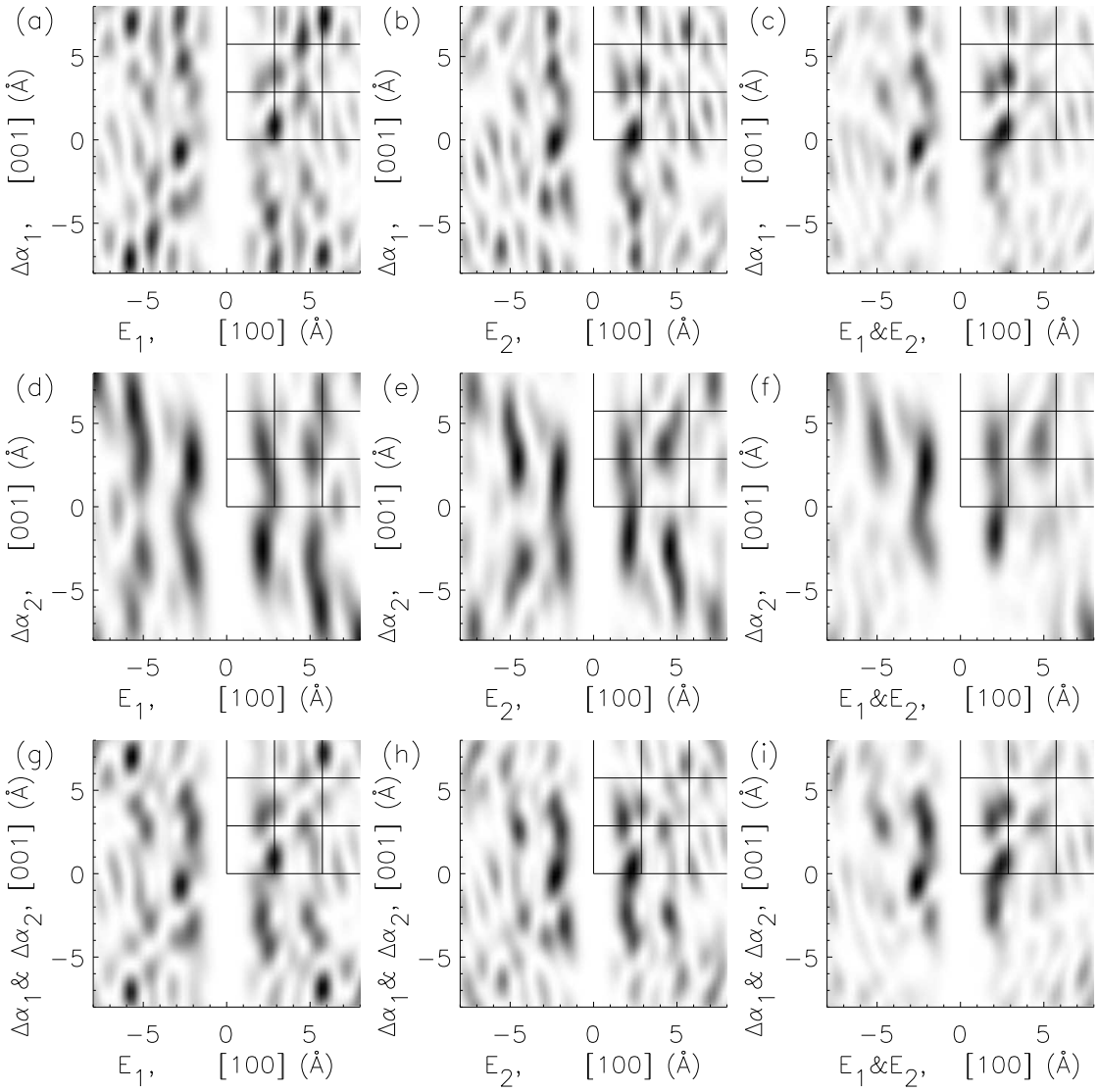

Figure 6.5: Reconstructions of 10 summed holograms measured at the energies (a), (d), (g) E_1 of the Fe K_α line, (b), (e), (h) E_2 of the Fe K_β line, and (c), (f), (i) energy-added reconstructions. The angular range was $\varphi_d = 0°, ...359°$, and (a)-(c) $\Delta\alpha_1 = 0°, ...59°$, (d)-(f) $\Delta\alpha_2 = 24°, ...83°$. (g)-(i) show the summations over the reconstructions from both angular ranges for the different energies. The image (d) is obtained from the hologram of fig. 6.2 (b). The reconstructions pass through the emitter atom in a plane parallel to the (010) lattice planes. The φ_d rotation axis was parallel to the [001] direction.

In order to investigate the dependence of the spatial resolution on energy and angular range, reconstructions were also calculated in planes perpendicular to the (001) lattice planes. Figure 6.5 shows such reconstructions in planes parallel to the (010) lattice planes. Part (d) is the reconstruction of the hologram of fig. 6.2 (b). The same holograms were reconstructed as in fig. 6.4. The corresponding images of

calculated holograms are shown for a smaller image area of (7 Å)^2 in section 3.2.1, fig. 3.5. Since the background was removed from individual experimental φ_d scans, no peaks occur along and close to the [001] direction in fig. 6.5 (section 3.2.2, fig. 3.9). As expected from the reconstructions of the calculated holograms, the spatial resolution is much better for the angular range $\Delta\alpha_1 = 0°, ...59°$ than for the range $\Delta\alpha_2 = 24°, ...83°$. The information from small α values in the holograms is especially important for a high spatial resolution in directions parallel to the [001] direction.

The spatial resolution in the reconstructions (g)-(i) summed for both angular ranges is not quite isotropic as it would be for 4π holograms. In ideal 4π holograms, each φ_d scan has the same weight. The combination of $\Delta\alpha_1$ and $\Delta\alpha_2$ nearly corresponds to a hemisphere. For a hemispere, a spatial resolution of about $\lambda/2$ is expected for atoms in the [001] plane and of about λ for atoms along the [001] axis (section 2.6.3). Thus, a different spatial resolution is expected for different image planes. In addition to this, the angular ranges $\alpha = 0°, ...23°$ and $\alpha = 60°, ...83°$ are measured by one detector, the range $\alpha = 24°, ...59°$ is measured by both detectors, and the range $\alpha = 84°, ...90°$ is not measured so that the strongest effect in the reconstructions is obtained from the range $\alpha = 24°, ...59°$. These weights enhance the effect of different resolutions.

The reconstruction planes that pass through the emitter and are parallel to the {001} axes should be mirror planes for bcc Fe. The incomplete mirror symmetry of the images in figs 6.4, 6.5 is due to the limited symmetry of the holograms along φ_d. Statistical noise in the holograms can disturb the symmetry.

Holograms Symmetrized in φ_d

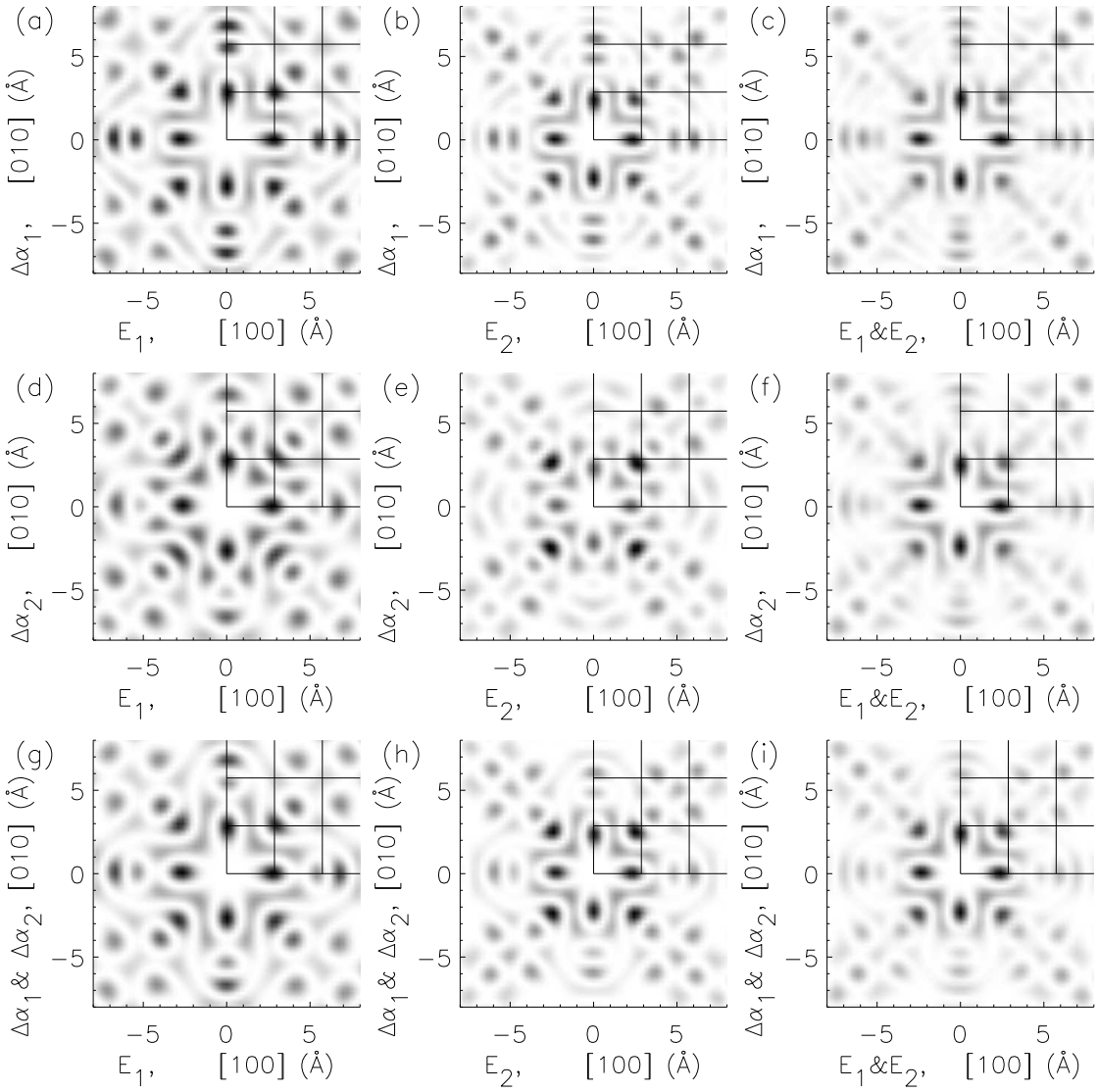

Figure 6.6: The rotational and mirror symmetries of the holograms along φ_d were used to symmetrize the holograms along φ_d. Reconstructed images obtained from 9 summed and symmetrized holograms at the energies (a), (d), (g) E_1 of the Fe K_α line, (b), (e), (h) E_2 of the Fe K_β line, and (c), (f), (i) the image of the energy-added reconstruction. The angular range was $\varphi = 0°, ...359°$, and (a)-(c) $\Delta\alpha_1 = 0°, ...59°$, (d)-(f) $\Delta\alpha_2 = 24°, ...83°$. (g)-(i) show the summations over the reconstructions from both angular ranges for the different energies. Part (d) is the reconstruction of the hologram of fig. 6.2 (c). The reconstructions pass through the emitter atom in a plane parallel to the (001) lattice planes. The φ_d rotation axis was parallel to the [001] direction.

The symmetry in the holograms along φ_d is available from the Kossel lines (fig. 6.2). Fig. 6.6 shows images that correspond to those of fig. 6.4 but are obtained from holograms that were symmetrized along φ_d. Figure 6.6 (d) is the reconstruction

of the hologram of fig. 6.2 (c). The fourfold rotational symmetry around the [001] axis and the mirror plane symmetry in the symmetrized holograms are reproduced in the reconstructions. The reconstructions at the different energies and angular ranges are very similar to each other. In all images, the highest peaks occur close to atom positions in bcc Fe. For the image (i) obtained from holograms at both energies and from both detectors, the highest peaks occur close to the second- and third-nearest neighbors of the emitter atom. These are the atom positions a and b of fig. 4.9 (a), respectively. These reconstructions are improved compared to those of fig. 6.4 since the symmetrization is performed by summing 8 holograms (section 6.1.1) which enhances the holographic signal but not the statistical noise. A similar reduction in statistical noise would be obtained by measuring an 8 times larger number of counts than for the holograms reconstructed in fig. 6.4.

Holograms Extended to 4π

Kossel lines can be used not only to symmetrize holograms along one angular coordinate but also to extend them to 4π. The images corresponding to fig. 6.6 from holograms extended to 4π are shown in appendix D.1, fig. D.2. Instead of extending the holograms, reconstructions can be symmetrized in real space for a known test structure. The images of reconstructions that were symmetrized in real space according to the bcc Fe structure are shown in appendix D.1, fig. D.1. The reconstructions of holograms that were symmetrized along φ_d or extended to 4π (figs. 6.6, D.2) and the reconstruction that was symmetrized in real space (fig. D.1) are very similar to each other and to the corresponding reconstructions of calculated holograms (appendix B, fig. B.1). In all cases, the second-nearest and third-nearest neighbors of the emitter are clearly imaged. The different methods of symmetrization have little influence on the image planes shown.

In order to obtain an isotropic spatial resolution, 4π holograms can be reconstructed. Since the background of the holograms was subtracted from individual φ_d scans, the average information along α was lost. Extending such holograms by just copying data values to equivalent sites in the holograms can extend this information loss to other directions. If the reconstructions of unsymmetrized holograms are instead symmetrized in real space according to the sample structure, the effect will be different since the relative weights of the holographic data will be different. Fig. 6.7 shows image planes through such a three-dimensional reconstruction. The image planes are parallel to the $\{001\}$ lattice planes and have distances z from the emitter atom, where (a)-(c) $z = 1.3$ Å $\approx a_0/2 = 1.44$ Å, (d)-(f) $z = 2.7$ Å $\approx a_0 = 2.87$ Å, and (g)-(i) $z = 4.0$ Å $\approx 3a_0/2 = 4.31$ Å. Single-energy reconstructions at the Fe K_α and K_β lines and energy-added reconstructions are shown. The nearest and fourth-nearest neighbors of the emitter (atom positions f and g in fig. 4.9 (b)) can be seen in parts (a)-(c) as the highest peaks. The second-, third- and fifth-nearest neighbors of the emitter (atom positions a, b, and i in fig. 4.9 (c)) are imaged in (d)-(f). Weaker peaks occur at the positions of more distant neighbors. The fourth-nearest neighbors (atom positions g in fig. 4.9 (b)) can also be seen in (g)-(i).

The holograms from both detectors measured at the Fe K_α and K_β lines, among

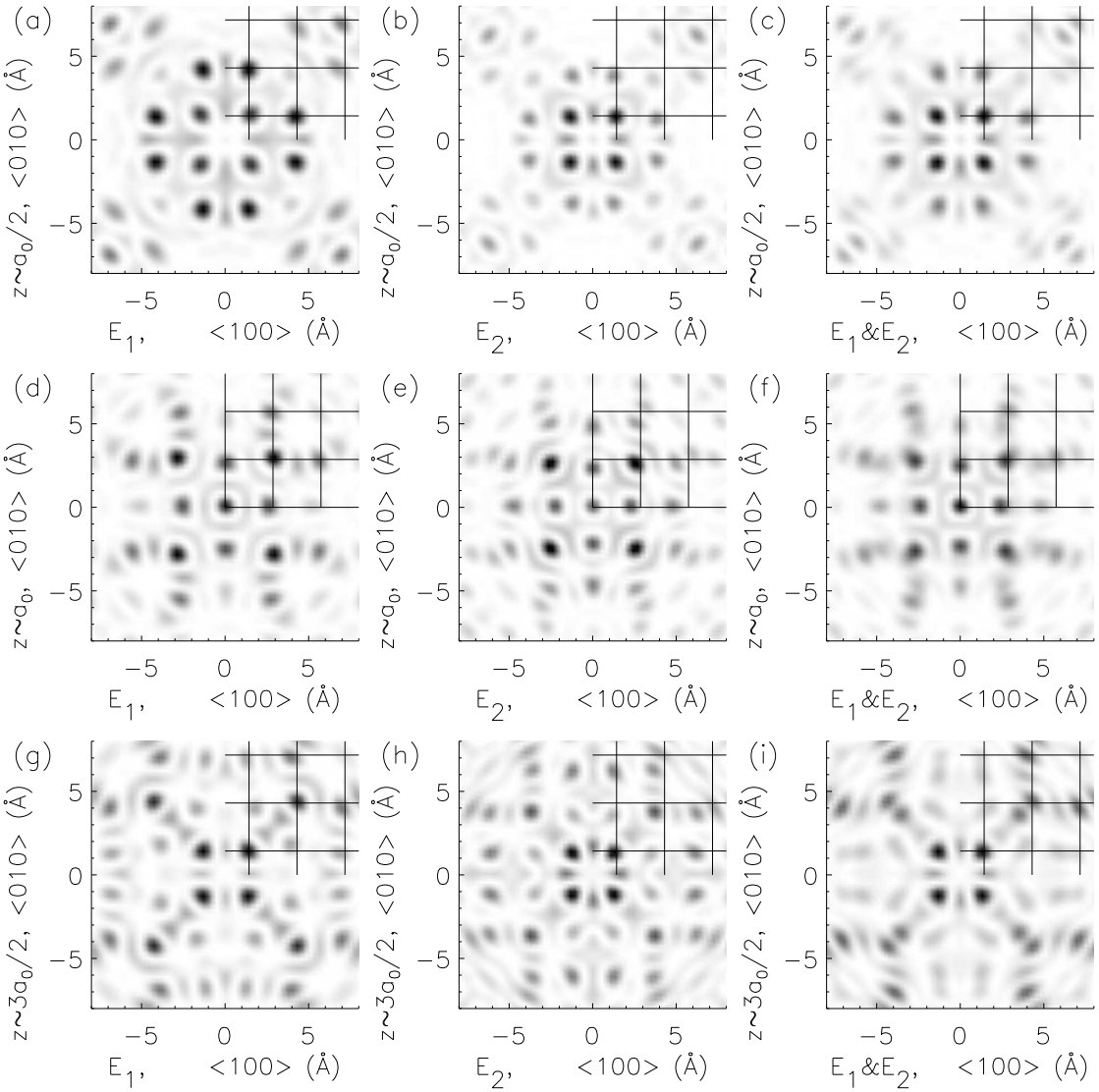

Figure 6.7: These reconstructions of unsymmetrized holograms were symmetrized in real space according to the symmetry of bcc Fe. Reconstructions of holograms measured at the energies (a), (d), (g) E_1 of the Fe K_α line, (b), (e), (h) E_2 of the Fe K_β line, and (c), (f), (i) images of the energy-added reconstruction. In all cases, the reconstructions from holograms measured at the two different angular ranges were added. Images are shown in reconstruction planes parallel to the {001} lattice planes in a distance z from the emitter atom. (a)-(c) $z = 1.3$ Å $\approx a_0/2$, (d)-(f) $z = 2.7$ Å $\approx a_0$, (g)-(i) $z = 4.0$ Å $\approx 3a_0/2$.

them the hologram of fig. 6.2 (d), were reconstructed, combined for both energies according to eq. 2.70, and symmetrized in real space. A three-dimensional iso-surface at 50% of the highest maxima of $r|\psi(\mathbf{r})|^2$ is displayed in fig. 6.8. In this plot, $r|\psi(\mathbf{r})|^2$ is displayed instead of $|\psi(\mathbf{r})|^2$ in order to make atoms at larger distances r from the emitter more visible. Atom positions in bcc Fe are indicated by intersections of lines. The emitter atom is the center $r = 0$ of the images. Its 34

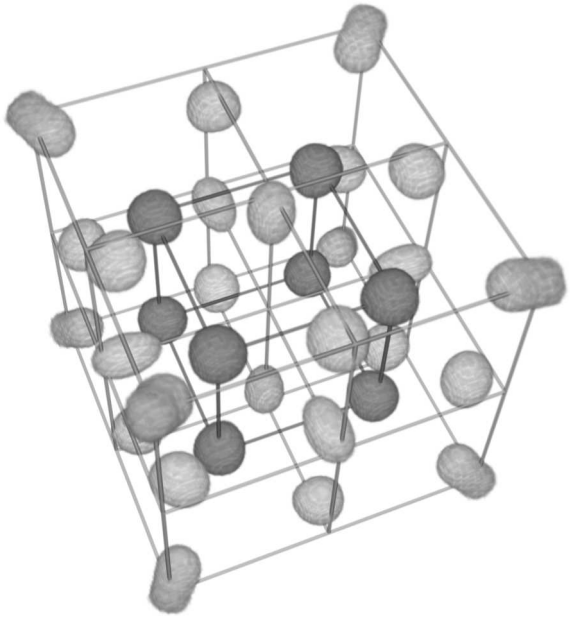

Figure 6.8: The holograms from both detectors measured at the Fe K_α and K_β lines, among them the hologram of fig. 6.2 (d), were reconstructed, energy-added and symmetrized in real space. This figure shows the resulting $r|\psi(\mathbf{r})|^2$ with 50% background cutoff in a volume of (7 Å)^3. The 8 nearest neighbors of the emitter atom are displayed in a darker grey than its more distant neighbors. Atom positions in bcc Fe are indicated by intersections of lines.

neighbors that are expected in the imaged volume of bcc Fe can be seen. The eight nearest neighbors (atom positions f in fig. 4.9 (b)) are shown in dark grey. They appear at the correct positions. The 26 more distant neighbors are shown in light grey and appear shifted towards the emitter atom. This figure gives an impression of what XFH may achieve: three-dimensional information on the sum over the neighborhoods of all fluorescence atoms with nearly-isotropic spatial resolution.

For a quantitative evaluation, fig. 6.9 shows one-dimensional radial cuts through a three-dimensional reconstruction. The reconstruction of unsymmetrized holograms was symmetrized in real space. This figure can be compared with fig. 3.7 which shows cuts through reconstructions of calculated 4π holograms. The second-nearest neighbors of the emitter are imaged in (a). Their distances to the emitter are larger for the Fe K_α line than for Fe K_β line. The third-nearest neighbors of the emitter are imaged in (b). Weaker peaks appear at distances of ≈ 2 Å from the emitter. The nearest and fifth-nearest neighbors of the emitter are imaged in (c). As discussed for the reonstructions of calculated holograms (section 3.2.1), the peak heights and positions were determined not from these scans but directly as the values and positions of the maxima in the three-dimensional reconstructions. One-dimensional radial scans through the emitter and the peak positions were used to determine the peak widths as the full widths at half maximum of the peaks. The reconstructions used for this purpose were calculated on a spatial

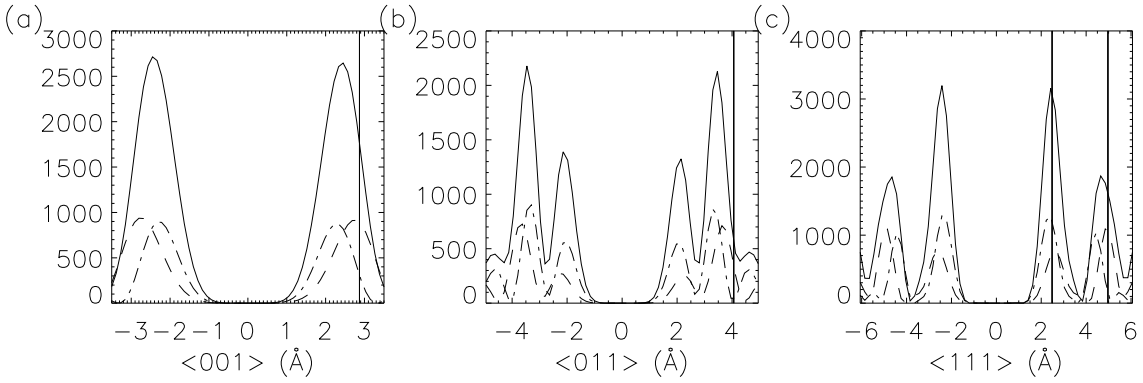

Figure 6.9: One-dimensional radial cuts through a three-dimensional reconstruction. The reconstruction of unsymmetrized holograms was symmetrized in real space. The emitter is in the center of all cuts which pass (a) parallel to the $\langle 001 \rangle$ directions through its next-nearest neighbors, (b) parallel to the $\langle 011 \rangle$ directions through its third-nearest neighbors, (c) parallel to the $\langle 111 \rangle$ directions through its nearest and fifth-nearest neighbors. The hologram energies are indicated by different lines: the Fe K_α line by dashed lines, the Fe K_β line by dash-dotted lines, and both combined energies by solid lines. Vertical lines indicate atom positions in bcc Fe for positive x-values.

grid of 61 points/7 Å which corresponds to 0.12 Å per point. Not all peaks are completely symmetric with respect to their maximum so that systematic errors of about ± 0.2 Å may occur for peak positions and widths. The reconstructions peak at the correct *directions* relative to the emitter but their *distances* may differ from the ideal values, and the spatial resolution is nearly isotropic.

Table 6.1 gives the distances d_m between emitter and neighbors obtained from the three-dimensional reconstructions together with the peak widths r_m and heights max_m. Results are given for both detectors sdd1 and sdd2 separately at the energies E_1 of the Fe K_α line and E_2 of the K_β line, for both detectors together at each energy, and for the combined reconstruction using holograms measured by both detectors at both energies. The distances and peak widths obtained from both detectors agree within the accuracy at each single energy. An exception occurs for sdd1 at E_2 for the third-nearest neighbors: two peaks are present instead of one peak. One of them has a distance of (3.2 ± 0.2) Å from the emitter that is consistent with the distance of (3.4 ± 0.2) Å obtained by sdd2 at E_2. The other peak has a distance of (4.4 ± 0.2) Å from the emitter. This distance is closer to the distance of 4.06 Å in bcc Fe but is not consistent with the distance obtained by sdd2 at E_2. Misleading peaks can be caused by statistical noise in the holograms.

All peaks *heights* from single energies and detectors have the same order of magnitude in table 6.1. A very simple estimate for a peak height at a single energy is $|\psi_k(\mathbf{r})|^2 \approx (2r_e f_0)^2/(R^2 r_j)^2$ (section 2.6.3), where r_e is the classical electron radius, f_0 is a constant real scattering factor, R is the distance to the detector, and r_j is the distance between the emitter atom and the scattering atom. All atoms

nn	sdd1, E_1			sdd1, E_2			sdd2, E_1			sdd2, E_2		
	max_m	d_m	r_m	max_m	d_m	r_m	max_m	d_m	r_m	max_m	d_m	r_m
1^{st}	160	2.7	1.2	420	2.4	0.9	250	2.5	1.0	240	2.4	0.9
2^{nd}	250	2.8	1.2	330	2.3	1.1	230	2.6	1.2	140	2.2	1.0
3^{rd}	120	3.6	0.8	210	4.4	0.8	280	3.7	0.8	280	3.4	0.8
3^{rd}				210	3.2	0.8						
5^{th}	290	5.0	0.8	420	4.4	0.8	290	4.8	0.7	120	5.4	0.7
5^{th}										150	4.2	0.7

nn	(sdd1 + sdd2), E_1			(sdd1 + sdd2), E_2			(sdd1 + sdd2), (E_1 & E_2)			
	max_m	d_m	r_m	max_m	d_m	r_m	max_m	d_m	r_m	d_k
1^{st}	780	2.6	1.0	1300	2.4	0.9	3200	2.4	1.0	2.49
2^{nd}	940	2.8	1.2	890	2.3	1.1	2700	2.4	1.2	2.87
3^{rd}	730	3.6	0.8	900	3.2	0.7	2200	3.4	0.8	4.06
5^{th}	1100	4.8	0.8	170	5.4	0.7	1900	4.6	1.2	4.97
5^{th}				1000	4.4	0.7				

Table 6.1: Distances d_m from the emitter to its 1^{st}, next- (2^{nd}), third- (3^{rd}) and fifth- (5^{th}) nearest neighbors (nn), determined from three-dimensional reconstructions of holograms measured by the detectors sdd1 and sdd2 at the energies E_1 of the Fe K_α line and E_2 of the K_β lines. The values are also given for the reconstructions at the single energies after adding the holograms measured by both detectors, and for the energy-added reconstruction using E_1 and E_2. The full widths at half maximum r_m and the maximum values max_m (arbitrary units) are also given. d_m and r_m have an accuracy of ± 0.2 Å. The values d_k are obtained from the tabulated lattice constant $a_0 = 2.87$ Å of bcc Fe.

have the same scattering factor in bcc Fe. More than just one emitter atom and one scattering atom contribute to experimental holograms. This will introduce a proportionality factor in the estimate for the peak heights so that $|\psi(\mathbf{r})|^2 \propto 1/r_j^2$ remains. Twin image effects and effects due to many atoms in a structure will usually lead to deviations from this simple proportionality (section 2.6.3). A multiple-energy reconstruction according to eq. 2.70 is a phased and weighted sum over single-energy reconstructions of eq. 2.67. In order to compare peak heights of a multiple-energy reconstruction $|\psi(\mathbf{r})|^2$ with heights of a single-energy reconstruction $|\psi_k(\mathbf{r})|^2$, $|\psi(\mathbf{r})|$ should be divided by the number of contributing energies. As expected, the peak heights in the two-energy reconstruction $|\psi(\mathbf{r})|$ are very roughly given by $|\psi_{k1}(\mathbf{r})| + |\psi_{k2}(\mathbf{r})|$.

The peak *distances* d_m from the emitter to its nearest, third- and fifth-nearest neighbors obtained at the Fe K_α line correspond to those at the K $_\beta$ line, whereas the distances to the second-nearest neighbors are different. The nearest-neighbor distances correspond to the tabulated values d_k within the accuracy while many other distances d_m are smaller than the corresponding d_k.

All peak *widths* r_c are between (0.7 ± 0.2) Å and (1.2 ± 0.2) Å and do not differ significantly for the two energies. Peak widths of 0.9Å at $E_1 \approx 6.4$ keV and of 0.8Å at $E_2 \approx 7.1$ keV would be expected from eq. 2.93 so that the peak width in reconstructions of experimental holograms agree reasonably well with the estimate of eq. 2.93.

In order to understand the experimental results better, table 6.1 can be compared with the corresponding table 3.1 for reconstructions of *calculated* 4π holograms. The *distances* and peak *widths* agree with each other for the single energies and for the energy-added reconstruction. The only exception is the distance obtained for the fifth-nearest neighbors. The distances obtained at 6.4 keV agree for calculation and experiment but at 7.1 keV the highest peak has a distance of $d_c = (5.2 \pm 0.2)$ Å from the emitter for calculated holograms and a distance $d_m = (4.4 \pm 0.2)$ Å for measured holograms. Another lower peak obtained at a distance $d_m = (5.4 \pm 0.2)$ Å for measured holograms does correspond to the distance obtained for calculated holograms. The higher, misleading peak can result from statistical noise in the holograms: As is shown in fig. 6.3, statistical noise in holograms leads to peaks in the reconstructions that cannot a priori be separated from the peaks that occur in the holograms due to the sample structure.

Many peak heights in the reconstructions of experimental holograms measured by both detectors are proportional to the corresponding peak heights of calculated holograms with a proportionality factor of about 10. The peak heights are expected to be not equal to each other but proportional since peak heights are proportional to $1/R^2$, where R is the distance from the fluorescence atom to the detector, and since R was different in calculation and experiment. Deviations from the proportionality can be explained by the effects of statistical noise in experimental holograms or by systematic differences between experiment and calculations. A list of the assumptions made in the calculations is given in section 3.1. Many-atom effects play an important role in the experimental holograms that were measured for a *crystal* while they are much less dominant in holograms calculated for a *cluster*. Kossel line patterns are dominant in the experimental holograms but they are not present in the calculated holograms. Differences between the holograms can lead to differences in the reconstructions. The reconstructions can change with the number of scattering atoms that contribute to the hologram (section 2.6.3). Under simple assumptions, high frequencies in holograms correspond to atoms at large distances from the emitter (section 2.3.1) so that many-atom effects are not very important: Since only a neighborhood around the emitter was imaged in the experiment, mostly atoms close to the emitter contributed to the hologram so that the reconstructions of calculated and experimental holograms should be similar which they are.

Except for the few cases discussed above, the reconstructions of calculated and experimental holograms agree with each other. Calculations can be used to refine experimental results. A comparison of experimental and calculated holograms shows that the effects of long-range translational order should be taken into account in refined hologram calculations in the future. These will allow investigating the dependence on sample size and contribute to the understanding of the method.

6.2 Multiple Energy X-Ray Holography

6.2.1 Experimental Data

Fig. 6.10 gives an overview of the MEXH data set measured at CEMO in March 1999. The data shown in this figure were measured by one detector at an incidence energy of 10.7 keV. The Fe K_α line was used for fluorescence detection. The results obtained from detection at both Fe K lines are very similar. Part (a) shows a single φ_s scan of one MEXH data set at $\theta = 50°$ and a background fit to the scan according to eq. 2.61. The statistical noise in this scan is ≈ 0.4 %. The sine like modulation of the scan is caused by a slight misalignment (section 2.4.1). A misalignment of beam, sample or detectors can lead to relative intensity variations of a few percent (section 4.1.1). The relative intensity variation due to misalignment is about ± 3 % in this scan.

Part (b) shows the same scan after division by the ionisation chamber signal and the background fit to this scan. The ionisation chamber signal was stabilized within ≈ 0.5 %. The scans (a) and (b) are very similar. As for the XFH experiment, the division by the ionisation chamber signal has little effect on the scan. Scan (b) is shown after the normalization of eq. 5.1 in (c). A θ scan at fixed φ_s is shown in (d) before dividing by the ionisation chamber signal and in (e) after the division. The step in scan (d) is due to a change in the incident intensity. The division by the ionisation chamber signal is performed for all data sets before fitting, normalizing and reconstructing. Experimental parameters are given in table C.3. The complete data set is shown after division by the ionisation chamber signal in (f).

The normalized φ_s scans obtained for all θ values form a hologram. Fig. 6.11 gives an overview over the MEXH holograms measured at incidence energies (a) 9.5 keV, (b) 9.9 keV, (c) 10.3 keV, and (d) 10.7 keV. The Fe K_α line was used for fluorescence detection. The results obtained from detection at both Fe K lines are very similar. The images are displayed in a linear greyscale where dark color corresponds to high intensity. The holograms measured by both detectors were added in this figure. The total number of counts at the Fe K_α line varied for the different energies from 10^9 to 5×10^9 (table C.3). The symmetry of the XSW lines along φ_s can be used to symmetrize the holograms in φ_s and to extend them to 4π. Only a polar cap $\theta = 40°, ...90°$, $\varphi_s = 0°, ...359°$ of each hologram was extended to 4π. The background removal was less straightforward for the range $\theta = 1°, ...43°$ where only 95° in φ_s were covered in the experiment so that this angular range was avoided. The symmetrization of the holograms along φ_s makes the XSW line structure clearly visible just as the Kossel lines in XFH holograms become more visible after symmetrization (compare fig. 6.2). Parts (a) to (c) show such symmetrized holograms at different interference energies. Part (d) shows a hologram that is extended to 4π. Its intensity at $\theta = 50°$ is that of the scan in fig. 6.10 (c) after symmetrization.

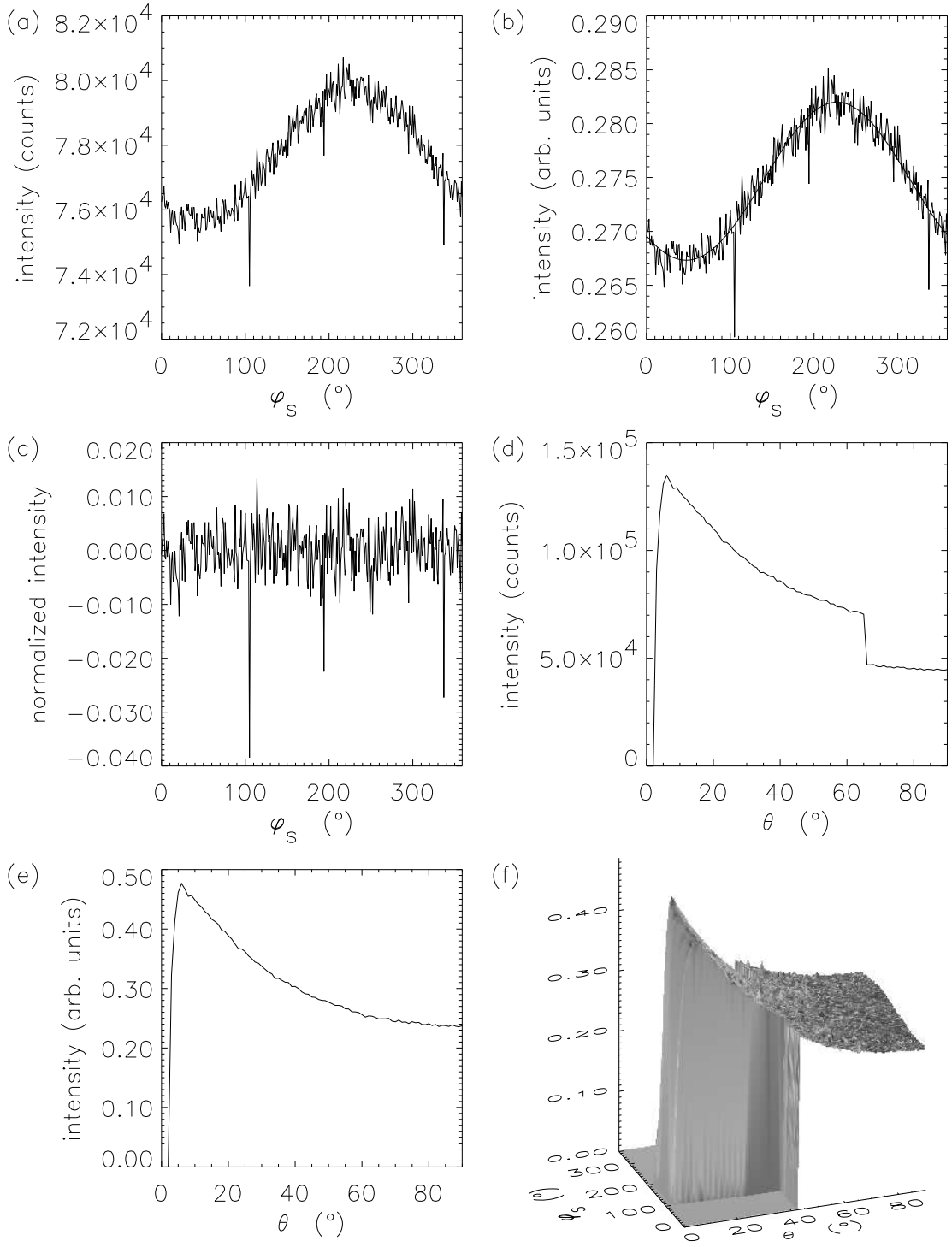

Figure 6.10: MEXH data measured by one detector at an incidence energy of 10.7 keV. The Fe K_α line was used for fluorescence detection. (a) φ_s scan measured at $\theta = 50°$. (b) The φ_s scan of (a), divided by the ionisation chamber signal, and fit to the scan. The fit is used to determine reference wave and absorption effects. (c) The φ_s scan of (b) normalized by the fit of (b). (d) θ scan measured at $\varphi_s = 150°$. (e) The θ scan of (d), divided by the ionisation chamber signal. (f) (θ,φ_s) array, divided by the ionisation chamber signal.

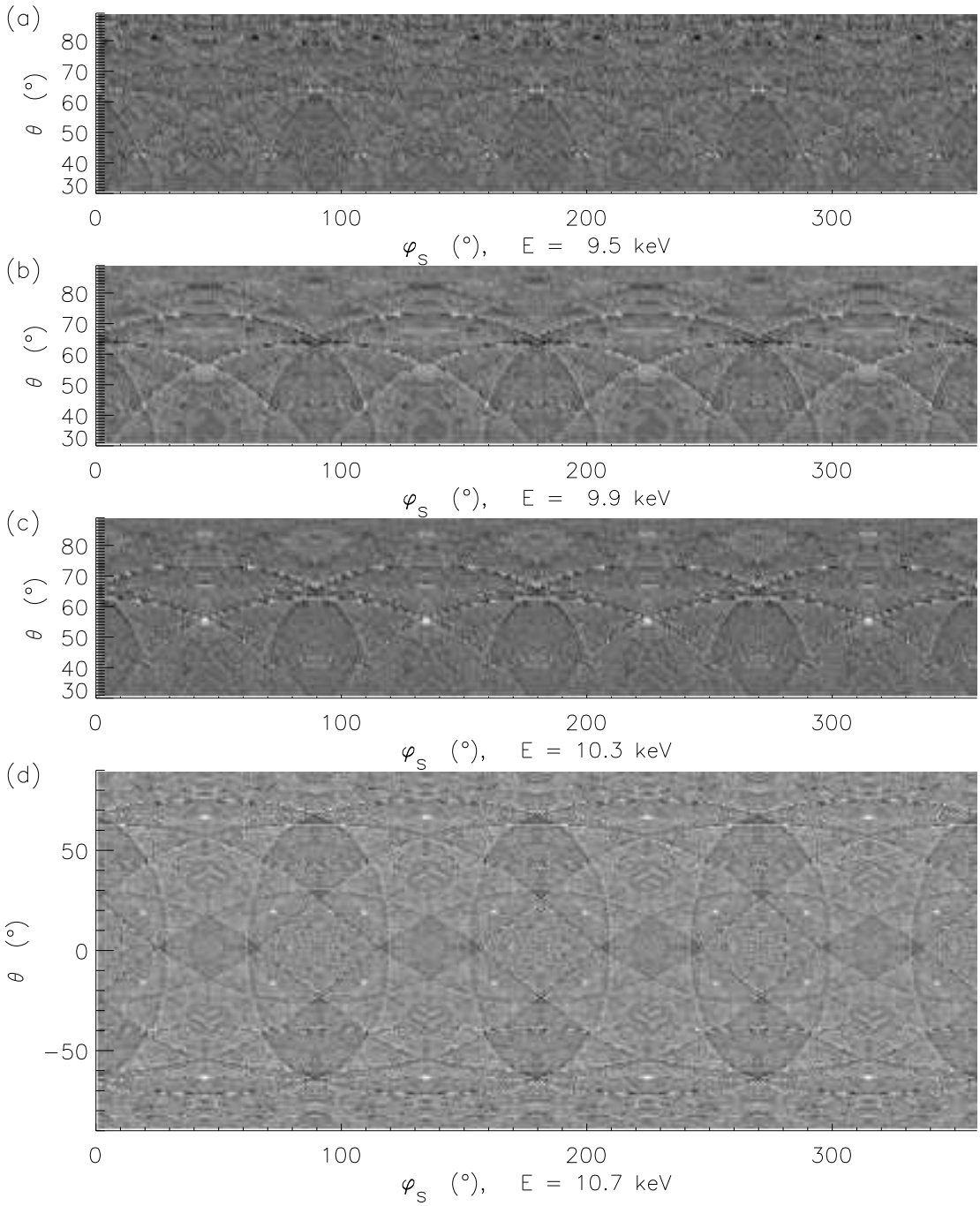

Figure 6.11: The translational and mirror plane symmetries along φ_d in the hologram were used to obtain these symmetrized holograms. The holograms were measured at the energies (a) 9.5 keV, (b) 9.9 keV, (c) 10.3 keV, (d) 10.7 keV. The holograms (a)-(c) are shown in the angular range $\varphi_s = 0°, ...359°$, $\theta = 30°, 31°, ...89°$. The hologram (d) is shown extended to 4π.

6.2.2 Reconstructions

The holograms were reconstructed according to the Barton algorithm where the integrations were replaced by summations: At single energies, eq. 2.67 was used. At multiple energies, eq. 2.70 was used with a modification. The phase factor in MEXH holograms is different from that in XFH holograms (section 2.3). In order to obtain in MEXH the same effect on the holographic phase as in XFH, the single-energy reconstructions in MEXH were multiplied by $\exp(ikr)$ instead of $\exp(-ikr)$ before summing them (section 2.6.1). The two-dimensional images show $|\psi_k(\mathbf{k})|^2$ of eq. 2.67 at single energies and $|\psi(\mathbf{k})|^2$ of the modified eq. 2.70 at multiple energies. The influence of the phase factor on the experimental reconstructions is small at few energies where the multiple-energy reconstruction of eq. 2.70 is mostly a sum of single-energy reconstructions. The detector atom is at the origin (0,0) of the images or above or below this position.

MEXH Experiment in July 1998, Holograms Extended to 4π

Reconstructions of 4π extended holograms of the MEXH experiment at CEMO in July 1998 are shown in fig. 6.12. The images are taken in a plane at a distance 2.9 Å $\approx a_0 = 2.87$ Å from the detector atom and parallel to the (001) lattice planes. The next-, third- and fifth-nearest neighbors of the detector (atom positions a, b, and i of fig. 4.9 (c)) lie in the image plane. At the center of part (a) at 7.9 keV, the highest peak occurs near the next-nearest neighbor position. The highest peaks in (b) at 9.5 keV and in (c) at 9.7 keV occur near the third- and fifth-nearest neighbor positions, respectively. High peaks close to the third- or fifth-nearest neighbor positions also appear in the other single-energy reconstructions in (d)-(g) but the single-energy reconstructions except for (b) do not correspond very well to the bcc Fe structure (fig. 4.9 (c)). The highest peaks in the energy-added reconstruction (h) that uses the energies 7.9 keV, 8.1 keV, ...11.3 keV occur close to the third- and fifth-nearest neighbor positions. Weaker peaks also occur close to positions of atoms at larger distances from the emitter. The next-nearest neighbor (atom position a of fig. 4.9 (c)) is not seen in (h) because it peaks in a plane that lies further away from the emitter atom. This multiple-energy reconstruction gives a better impression of the structure than most of the single-energy reconstructions. The energies 9.5 keV, 9.9 keV, ...11.1 keV are used in the energy-added reconstruction (i), where the highest peaks occur near the third-nearest neighbor positions. This reconstruction has much higher peaks at positions that do not correspond to atom position in bcc Fe than the reconstruction (h) obtained from all energies. Differences are due to the different energies used and to statistical noise in the holograms. The total number of counts at the single energies varied from 10^9 to 4×10^9, and is 4.3×10^{10} in part (h) but only 7×10^9 in part (i)(table C.2) .

Reconstructions obtained in three different image planes at all energies are shown in fig. 6.13. As can be seen in (a) and (b), high peaks occur close to the origin at positions that do not correspond to atom positions. Peaks close to the origin also occur in the corresponding reconstruction of calculated holograms (fig. 3.8 (h)). Since peaks close to the origin correspond to low frequencies which can be caused by the background, differences close to the origin between reconstructions of exper-

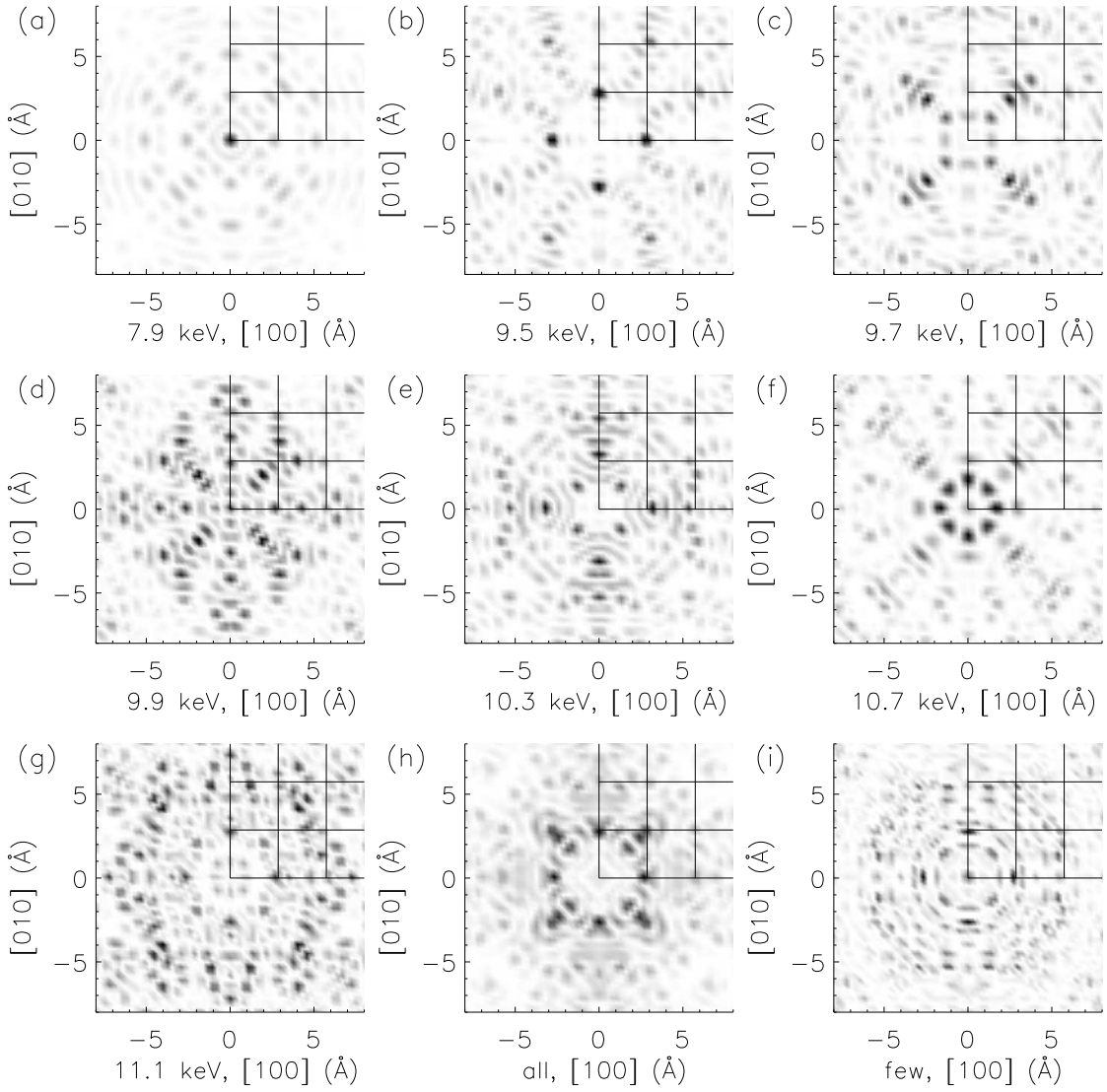

Figure 6.12: Reconstructed images obtained from holograms at the energies (a) 7.9 keV, (b) 9.5 keV, (c) 9.7 keV, (d) 9.9 keV, (e) 10.3 keV, (f) 10.7 keV, (g) 11.1 keV, that were extended to 4π. Part (h) shows the energy-added image using the energies 7.9 keV, 8.1 keV, ...11.3 keV, Part (i) shows the energy-added image using the energies 9.5 keV, 9.9 keV, ...11.1 keV. The reconstructions are taken in planes at a distance 2.9 Å $\approx a_0 = 2.87$ Å from the detector atom and parallel to the (001) lattice planes. The φ_d rotation axis is parallel to the [001] direction.

imental and calculated holograms can be due to errors in background removal. The background was determined by fitting the experimental data. In this first MEXH experiment, φ_s scans were only measured in a limited range of 150° (table C.2). This makes the fit to the background less reliable because a possible drift in background might not be fitted adequately. Also, the scans need to be symmetrized along φ_s in order to correspond to the symmetry of the structure along φ_s. Thus, reconstructions of unsymmetrized holograms cannot contain a fourfold symmetry.

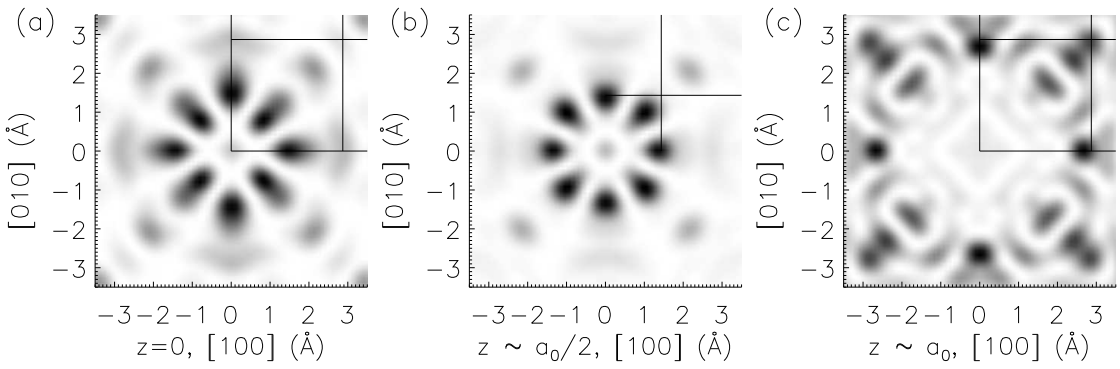

Figure 6.13: Energy-added reconstruction of holograms measured at the energies 7.9 keV, 8.1 keV, ...11.3 keV. The images are taken in planes parallel to the (001) lattice planes at a distance z from the detector atom. The image planes (a)-(c) correspond to those of fig. 4.9 (a)-(c). The φ_d rotation axis is parallel to the [001] direction. (a) $z = 0$ Å, (b) $z = 1.4$ Å $\approx a_0/2 = 1.44$ Å, (c) $z = 2.9$ Å $\approx a_0 = 2.87$ Å. (c) shows the center of fig. 6.12 (h).

Reconstructions of holograms symmetrized along φ_s will contain a fourfold symmetry even if the peaks in the reconstructions are not caused by the structure. In order to overcome these difficulties, a second MEXH experiment was performed where φ_s scans were measured in 360°.

MEXH Experiment in March 1999, Holograms Extended to 4π

In the following, reconstructions of MEXH holograms measured at CEMO in March 1999 are discussed. The φ_s scans measured in this experiment cover 360° so that the background determination is more straightforward than for φ_s scans measured in a smaller range. The holograms were extended to 4π before reconstructing them. The Fe K_α fluorescence was detected. Figure 6.14 shows reconstructions of holograms measured at the energies (a) 9.5 keV, (b) 9.9 keV, (c) 10.3 keV, (d) 10.7 keV, (e) 11.1 keV. Part (f) shows the energy-added image. The reconstructions pass through the emitter atom in a plane parallel to the (001) lattice planes. All images show high peaks at the origin or close to it. A high peak at the origin is caused by a constant offset in the hologram (section 3.2.2) that occurs if the sum over all data points is not equal to zero. A constant offset can be caused by errors in background removal or by numerical errors. The hologram may not add to zero in a limited angular range. Multiple scattering leads to quadratic terms in the hologram that do not need to add to zero in the sum over all hologram points. High intensities in insufficiently sampled XSW lines may also lead to errors. If a constant equal to the average value in the holograms is subtracted from the holograms, then the high peak at the origin vanishes. [2] High-frequency statistical noise in the holograms causes peaks at large distances from the origin (compare fig. 6.3 with fig. 6.4 (d)).

[2]Reconstructions of holograms with and without a constant offset are compared in figs. 6.19, 6.20.

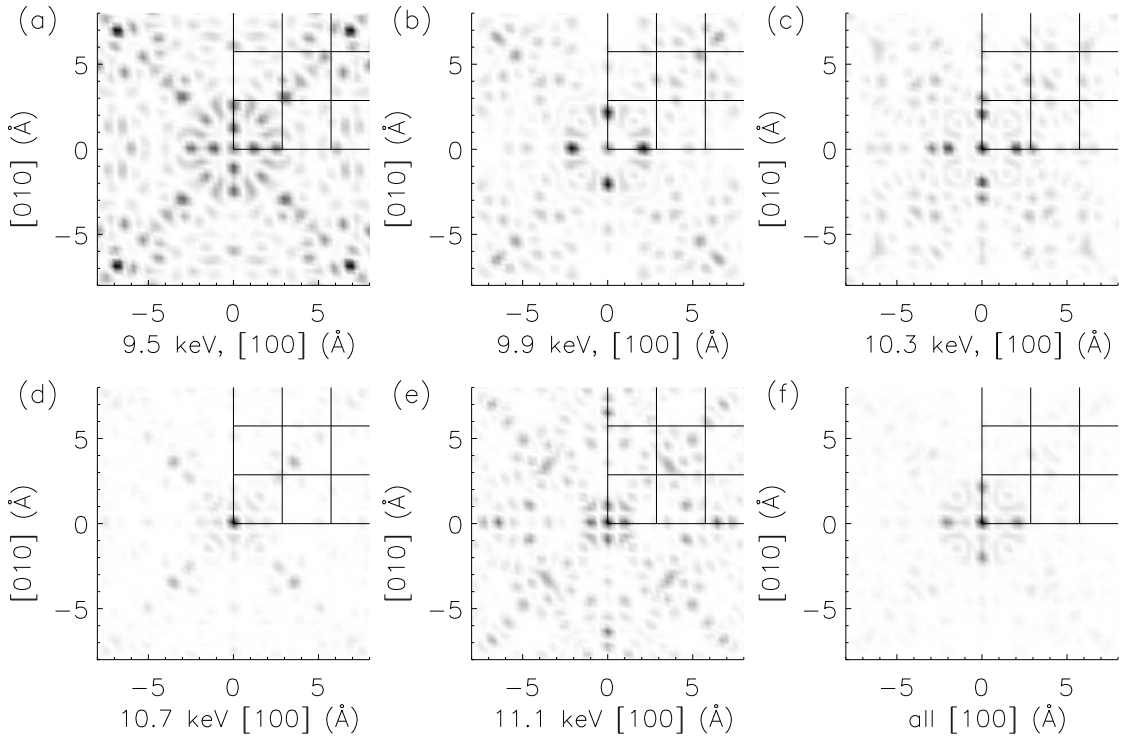

Figure 6.14: Reconstructions of holograms measured at the energies (a) 9.5 keV, (b) 9.9 keV, (c) 10.3 keV, (d) 10.7 keV, and (e) 11.1 keV, that were extended to 4π. (f) shows the energy-added image. The reconstructions pass through the detector atom in a plane parallel to the (001) lattice planes (compare fig. 4.9 (a)). The φ_d rotation axis was parallel to the [001] direction.

Fig. 6.15 shows reconstructions in a plane parallel to the (001) lattice planes, at a distance of 1.3 Å $\approx a_0/2 = 1.44$ Å from the detector atom. The image plane is that of fig. 4.9 (b). The corresponding holograms were measured at the energies (a) 9.5 keV, (b) 9.9 keV, (c) 10.3 keV, (d) 10.7 keV, (e) 11.1 keV. Part (f) shows the image of the energy-added reconstruction. The highest peaks in (b)-(f) appear at the positions of the nearest neighbors of the detector (atom position f in fig. 4.9 (b)). In (b)-(d) and especially in (f) more distant neighbors of this image plane can weakly be seen (atom positions g, h in fig. 4.9 (b)). Part (a) does not resemble the bcc Fe structure of the image plane. Misleading peaks in this image can be caused by statistical noise in the hologram or by systematic errors. The number of counts in (a) was 10^9 and at least 3 times smaller than at the other single energies (table C.3). In the energy-added reconstructions of figs. 6.14 (f) and 6.15 (f), fewer high peaks occur far from the origin than in the single-energy reconstructions of parts (a)-(e). This is due to statistical noise in the holograms. The number of counts varied from 10^9 to 5×10^9 at single energies and was 1.6×10^{10} for all holograms together. Systematic artefacts should also be reduced at multiple energies.

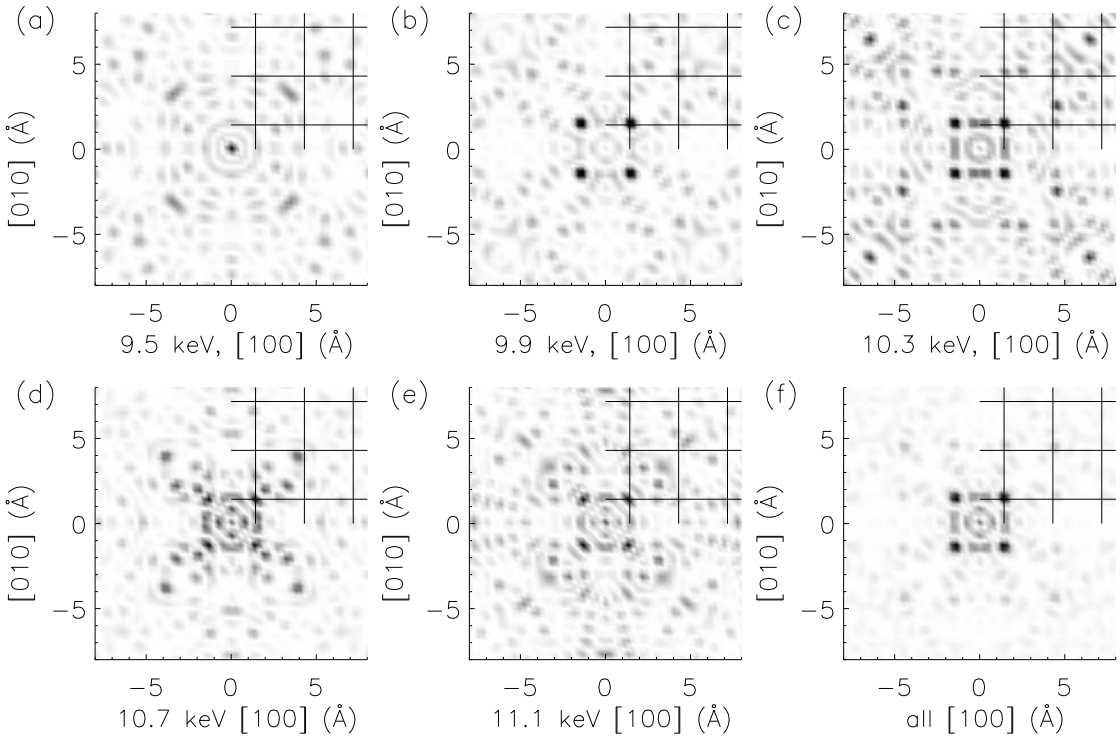

Figure 6.15: Reconstructions of holograms measured at the energies (a) 9.5 keV, (b) 9.9 keV, (c) 10.3 keV, (d) 10.7 keV, (e) 11.1 keV, that were extended to 4π. (f) shows the energy-added image. The reconstructions are taken in a plane parallel to the (001) lattice planes, at a distance 1.3 Å $\approx a_0/2 = 1.44$ Å from the detector atom (compare fig. 4.9 (b)). The φ_d rotation axis was parallel to the [001] direction.

The multiple-energy reconstruction is further investigated in fig. 6.16 where images in different planes are shown. The planes in (a), (b) pass through the emitter atom parallel to the (001) and (010) lattice planes, respectively. These images are very similar as is expected for 4π holograms. This shows that the extension of the holograms to 4π was successful. The image (a) is the same as that of fig. 6.14 (f). Parts (c)-(f) show planes parallel to the (001) lattice planes at different distances to the detector atom. The detector atom is below or above the origin (0,0) of the images. The image (c) is the same as that of fig. 6.15 (f). The nearest, fourth- and seventh-nearest neighbors of the detector are imaged (atom positions f, g, h in fig. 4.9 (b)). The image (d) shows the fifth-nearest neighbors of the detector atom (atom positions i in fig. 4.9 (c)). Only very weak peaks occur near the third-nearest neighbor positions (atom positions b in fig. 4.9 (c)). The peak near the second-nearest neighbor position (atom position a in fig. 4.9 (c)) has its maximum in a plane closer to the detector atom and is not seen. Weak peaks also occur near the ninth-nearest neighbor positions (atom positions j in fig. 4.9 (c)). In (e), the fourth- and seventh-nearest neighbors that are very weak in (c) are clearly imaged. In (f), the ninth-nearest neighbors that are very weak in (d) are imaged. The distance in bcc Fe between detector and its ninth-nearest neighbors is $\sqrt{6}a_0 = 7.03$ Å. Appendix D.2, figs. D.3, D.4, D.5 show images in the same image planes as in fig. 6.16 (d) - (f) for the single energies.

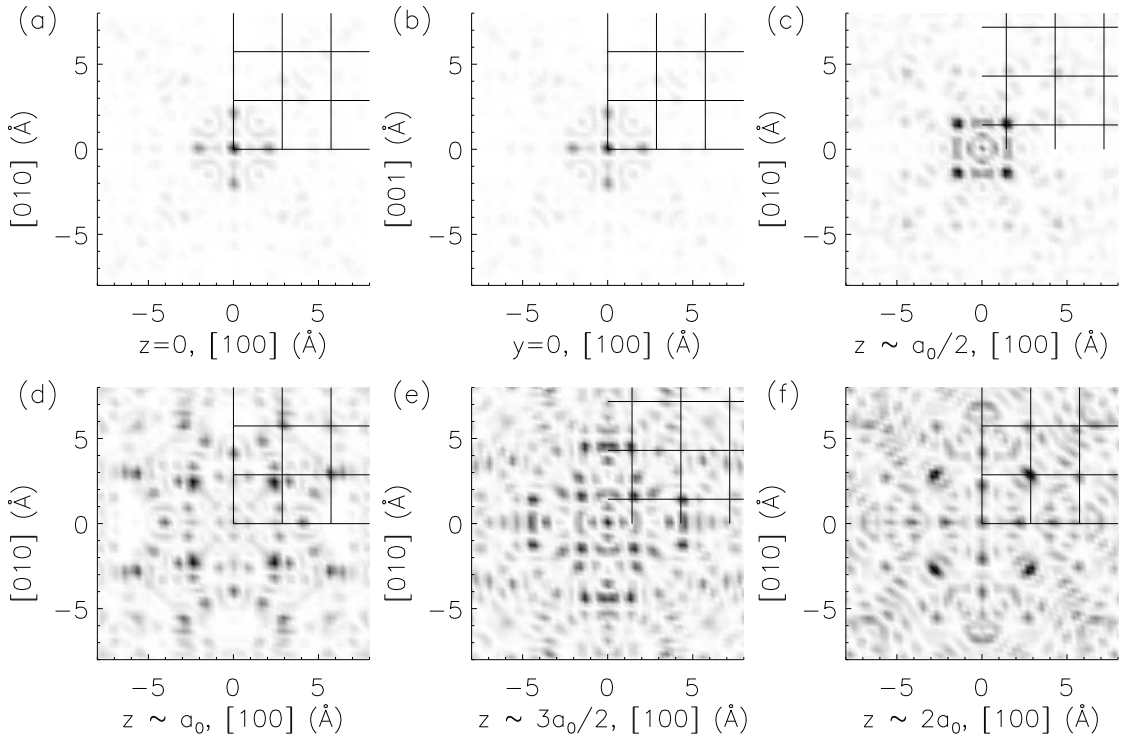

Figure 6.16: Images of the energy-added reconstruction in different planes. (a) The plane passes through the emitter atom parallel to the (001) lattice planes. (b) The plane passes through the emitter atom perpendicular to the (001) lattice planes. (c)-(f) The planes are parallel to the (001) lattice planes and have a distance z from the detector atom. (c) $z = 1.3$ Å $\approx a_0/2 = 1.44$ Å, (d) $z = 2.6$ Å $\approx a_0 = 2.87$ Å, (e) $z = 4.5$ Å $\approx 3a_0/2 = 4.31$ Å, (f) $z = 5.8$ Å $\approx 2a_0 = 5.74$ Å. The φ_d rotation axis was parallel to the [001] direction.

The three-dimensional image of the energy-added reconstruction is shown in fig. 6.17 with 50% background cutoff. In this plot, $r|\psi(\mathbf{r})|^2$ is displayed instead of $|\psi(\mathbf{r})|^2$ in order to make atoms at large distances r from the detector atom more visible. The 8 nearest neighbors of the detector atom are imaged near the correct positions. High peaks also occur close to its 6 next-nearest and 8 fifth-nearest neighbor positions. These peaks are shifted towards the detector atom. The peaks at the third-nearest neighbor positions are too small and not visible in this plot.

Three different cuts through the three-dimensional energy-added reconstruction obtained from the 4π extended holograms are shown in fig. 6.18. These one-dimensional cuts pass through the emitter at the center and (a) parallel to the $\langle 001 \rangle$ directions through its next-nearest neighbors, (b) parallel to the $\langle 011 \rangle$ directions through its third-nearest neighbors, (c) parallel to the $\langle 111 \rangle$ directions through its nearest and fifth-nearest neighbors. A constant offset in the holograms causes a high peak at the origin (0,0,0) of the reconstruction. For comparison, fig. 6.19 shows the same cuts after setting the central $\approx (0.8$ Å$)^3$ of the reconstruction to

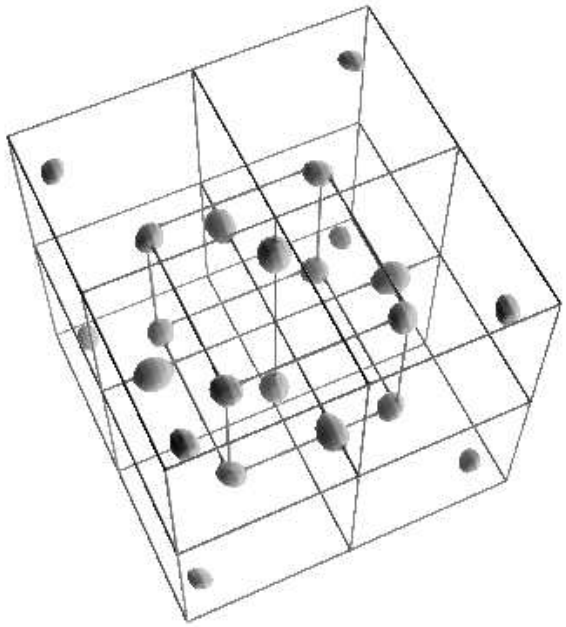

Figure 6.17: The holograms from both detectors were extended to 4π and reconstructed. This figure shows the resulting three-dimensional energy-added reconstruction $r|\psi(\mathbf{r})|^2$ with 50% background cutoff in a volume of (7 Å)^3. High peaks occur near the 8 nearest neighbor positions of the detector atom which is at the center of the image. High peaks also occur close to its 6 next-nearest and 8 fifth-nearest neighbor positions but shifted towards the detector atom. Atom positions in bcc Fe are indicated by intersections of lines.

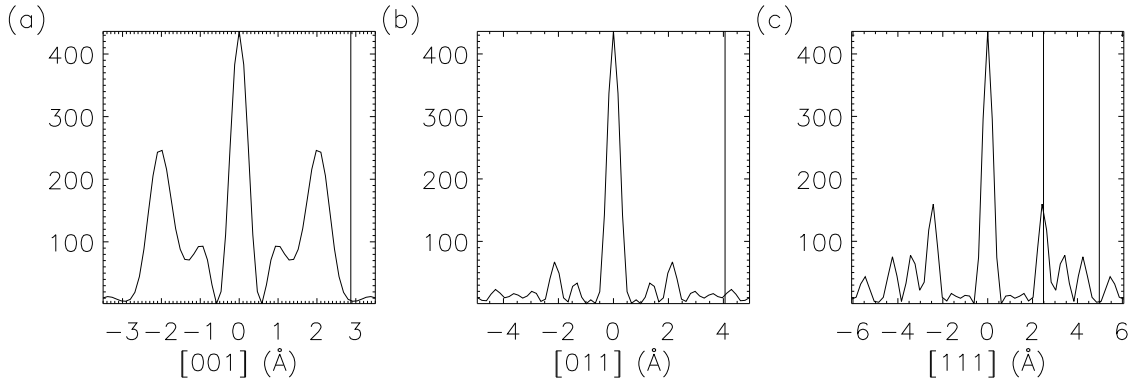

Figure 6.18: One-dimensional radial cuts through the three-dimensional reconstruction of the energy-added, 4π extended holograms. The detector atom is at the origin (0) of all cuts which pass (a) parallel to the $\langle 001 \rangle$ directions through its next-nearest neighbors, (b) parallel to the $\langle 011 \rangle$ directions through its third-nearest neighbors, (c) parallel to the $\langle 111 \rangle$ directions through its nearest and fifth-nearest neighbors. The cuts are divided by 1000.

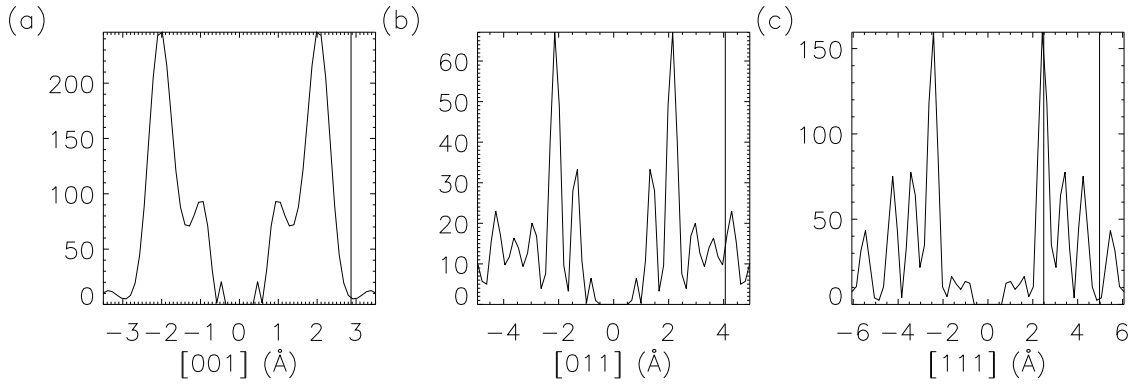

Figure 6.19: Same as fig. 6.18 after setting the central $\approx (0.8\ \text{Å})^3$ of the reconstruction to zero. Appendix D.2 shows the same cuts for the single energies in figs. D.6, D.7, D.8.

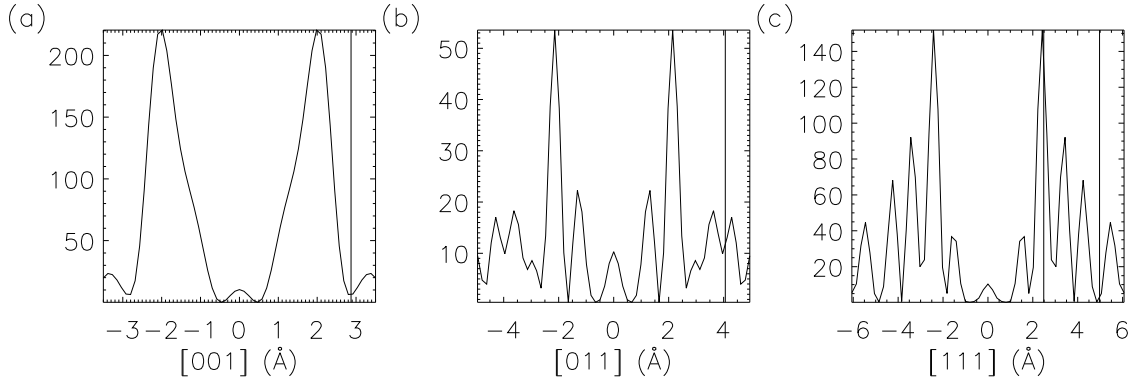

Figure 6.20: Same as fig. 6.18 but the average value was subtracted from each hologram before reconstructing the holograms.

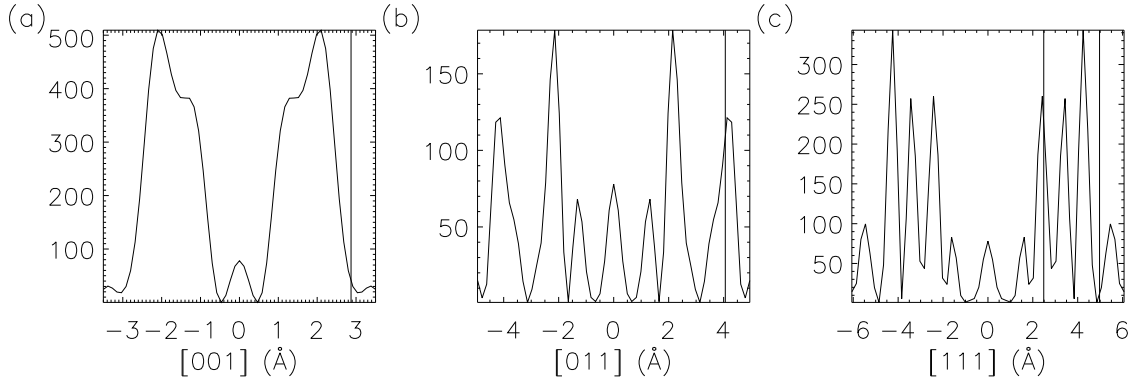

Figure 6.21: Same as fig. 6.20 but with different weights used for the single energy reconstructions (see text).

zero, and fig. 6.20 shows the same cuts for reconstructions of the same holograms after subtracting the average value from each hologram. In fig. 6.20, no high peak is obtained at the origin. Figures 6.18, 6.19, 6.20 are very similar except for the region close to the origin. The cuts through the reconstructions of experimental holograms agree reasonably well with the cuts of fig. 3.10 obtained from reconstructions of calculated holograms. The main difference lies in the distance between the emitter and its next-nearest neighbors which is smaller for the reconstructions of experimental holograms. The peak heights depend upon the heights obtained at the single energies and their relative weights. Due to the high number of counts in the hologram measured at 9.9 keV, the peaks obtained in this reconstruction are especially high (table 6.2) and are dominant in the energy-added reconstruction. For the calculated holograms, comparable peak heights are obtained at the different single energy reconstructions (table 3.2). As an example of different relative weights, the holograms can be divided by their total number of counts and multiplied by the number of counts obtained at 9.9 keV. This corresponds to using the single-energy reconstruction at 9.9 keV with a weight of 1, and using the other single-energy reconstructions with heigher weights. Fig. 6.21 shows the same cuts as fig. 6.20 but using these weights. The relative peak heights differ from each other in the two figures. For example, the peaks close to the third-nearest neighbor positions are higher in fig. 6.21 (b) than in fig. 6.20 (b).

Table 6.2 gives peak heights m_m, positions d_m, and widths r_m obtained from single energy reconstructions and from the energy-added reconstruction. The accuracy is about ± 0.2 Å for peak positions and widths. In a few cuts that were used to determine the peak-widths (figs. 6.19, D.6, D.7, D.8), the highest peaks are not close to atom positions. In these cases, the table lists the parameters of peaks that are close to atom positions.

An estimate of statistical noise in the holograms can be made in the following way: The total number of counts at the Fe K_α line varied between 10^9 and 5×10^9 at the single energies and was 1.6×10^{10} for all energies together (table C.3). According to section 2.3.1 and under simplifying assumptions, about $8r_j/\lambda$ steps need to be measured in 360°. For a distance $r_j \approx 4$ Å, $8r_j/\lambda \approx 25$ at 9.5 keV. For a distance $r_j \approx 5$ Å, $8r_j/\lambda \approx 36$ at 11.1 keV. If 10^9 counts are distributed on a hemisphere of $(32 \times 8) = 256$ relevant sampling bins in $(\varphi_s \times \theta)$ then the average number of counts per angular bin is $N \approx 10^9/256 \approx 3.9 \times 10^6$. The statistical noise at each bin is on the order of $\sqrt{N} \approx 2000$. The holographic signal at each bin is on the order of $10^{-4}N \approx 400$ or smaller which is smaller than the statistical noise. In order to fulfil the requirement $10^{-4}N \approx \sqrt{N}$ at each of 256 bins, about $256 \times 10^8 = 2.56 \times 10^{10}$ total counts need to be recorded. This is a lower limit to the necessary number of counts since a hologram contains values smaller than $10^{-4}N$ so that the requirement $10^{-4}N \approx \sqrt{N}$ may not be sufficient. The total number of counts in all holograms was 1.6×10^{10} which is smaller than the estimate. Therefore many peaks in the reconstructions are caused by statistical noise in the holograms. The holograms were symmetrized along φ_s before extending them to 4π. The symmetrization was performed in the following way: The holograms were added to themselves after shifting them by 90°, 180°, and 270°. The resulting

nn	9.5 keV			9.9 keV			10.3 keV		
	m_m	d_m	r_m	m_m	d_m	r_m	m_m	d_m	r_m
1^{st}	-	-	-	60000	2.5	0.5	7300	2.5	0.5
2^{nd}	6900	2.4	0.9	4000	3.2	0.7	4000	2.9	0.5
3^{rd}	4100	4.3	0.7	7500	3.8	0.4	3300	4.2	0.5
5^{th}	1000	5.5	0.5	18000	5.5	0.5	1700	5.2	0.5

nn	10.7 keV			11.1 keV			(9.5, ...11.1) keV			d_k
	m_m	d_m	r_m	m_m	d_m	r_m	m_m	d_m	r_m	
1^{st}	4300	2.3	0.4	5300	2.3	0.4	160000	2.4	0.5	2.49
2^{nd}	1200	3.2	0.5	2200	2.7	0.4	12000	3.4	0.7	2.87
3^{rd}	5500	3.7	0.8	3800	3.2	0.7	23000	4.3	0.5	4.06
5^{th}	7100	4.4	0.4	5300	5.2	0.7	42000	5.4	0.6	4.97

Table 6.2: Distances d_m from the detector atom to its 1^{st}, next- (2^{nd}), third- (3^{rd}) and fifth- (5^{th}) nearest neighbors (nn), determined from three-dimensional reconstructed images $|\psi_k(\mathbf{r})|^2$ of holograms measured at the energies 9.5 keV, 9.9 keV, ...11.1 keV, and from the energy-added reconstructed image $|\psi(\mathbf{r})|^2$ using these energies. The full widths at half maximum r_m and the maximum values m_m are also given. d_m and r_m have an accuracy of ± 0.2 Å. The values d_k are obtained from the tabulated lattice constant $a_0 = 2.87$ Å of bcc Fe.

holograms were added to themselves after reflecting them at $\varphi_s = 180°$. This way, 8 holograms were summed in the symmetrization procedure, increasing the effective number of counts by a factor of 8. The effective number of counts summed over all holograms is $8 \times 1.6 \times 10^{10} \approx 13 \times 10^{10}$ which is larger than the estimate for the necessary number of counts.

In order to understand the experimental results, table 6.2 can be compared to table 3.2 obtained from reconstructions of calculated holograms. Deviations between the results from calculated and experimental holograms can partly be attributed to the assumptions made in the hologram calculations: XSW line patterns are visible in experimental but not in calculated holograms since the holograms were calculated for a cluster but the experimental holograms were measured on a crystal. Future hologram calculations for crystals can be used to study the dependence of reconstructions on structure size theoretically. The coherence of the incident radiation in MEXH experiments can be reduced in order to study this dependence experimentally. Polarization effects were not taken into account in the calculations (section 3.1). In MEXH, polarization effects are more dominant than in XFH (section 2.3) so that deviations between experiment and calculation may be larger in MEXH than in XFH. For reconstructions of calculated and experimental holograms, high peaks occur not only at atom positions as can be seen in the one-dimensional cuts. Peaks that are close to atom positions in bcc Fe can be compared for experiment and calculation.

Under simple assumptions, the heighest peaks occur at correct atom *positions* $\mathbf{r}_j$ or at positions $-\mathbf{r}_j$. Peak *heights* $|\psi(\mathbf{r})|^2 \propto 1/(Rr_j)^2$ are expected for simple cases at single energies, where R is the distance from the fluorescence atom to the detector. Twin image effects and effects due to many atoms in a structure will usually lead to deviations from this (section 2.6.3). Many peaks heights in the reconstructions of experimental holograms are proportional to the corresponding peak heights in reconstructions of calculated holograms with a proportionality factor of about 100. Peak heights in reconstructions of experimental and calculated holograms are expected to be proportional to each other since the absolute heights are proportional to $1/R^2$ and since R was different for experiment and calculation. The proportionality factor is also different for this MEXH experiment and the XFH experiment of October 1998 because the distance R to the detector was smaller in this MEXH experiment than in the XFH experiment. Deviations from the proportionality are caused by statistical noise in experimental holograms or by systematic deviations between experiment and calculations: errors may occur in the extension of the experimental holograms to 4π, many-atom effects are more dominant in the experiment than in the calculations, and polarization and near-field effects were neglected in the calculations.

An agreement within accuracy is found between the reconstructions of experimental and calculated holograms at 9.5 keV for the *positions* of the third- and fifth-nearest neighbors of the detector atom, at 9.9 keV, 10.3 keV and 10.7 keV for its nearest, next- and fifth-nearest neighbors, at 11.1 keV for its next-, third- and fifth-nearest neighbors, and in the energy-added reconstruction for its nearest and fifth-nearest neighbors.

The peak *widths* in reconstructions of experimental MEXH holograms (table 6.2) vary between (0.4 ± 0.2) Å and (0.8 ± 0.2) Å. They agree with the widths in the corresponding reconstructions of calculated holograms (table 3.2) within the accuracy. Peak widths of 0.7Å at 9.5 keV and of 0.6Å at 11.1 keV would be expected from the simple estimate of eq. 2.93 so that the peak widths in reconstructions of experimental holograms agree reasonably well with this estimate.

6.3 Comparison of XFH and MEXH

A theoretical comparison of XFH and MEXH in the framework of classical electrodynamics is given in section 2.3. The reference wave in XFH is given by fluorescence radiation while it is given by an external x-ray source in MEXH. This allows different experimental setups for the methods, including different kinds of incident radiation, different detection systems and different angular and energy resolutions. Additionally, the phases of the exponentials in XFH and MEXH and the effective scattering factors that depend on polarization and near-field effects are different.

The interference energies in XFH and MEXH are different if the same fluorescence line is used for detection, so that different holograms are measured in XFH and MEXH and a direct comparison of the holograms is not useful. Instead, the reconstructions obtained in XFH and MEXH can be compared. The reconstructions depend upon hologram energy and angular range, on the reconstruction algorithm and the image function chosen. Reconstructions of holograms taken at multiple energies depend also upon the relative weights of the single-energy contributions. The Barton reconstruction algorithm used in this text is similar to a Fourier transform but with different relative weights and phases of the single-energy contributions. At a single energy or at few energies, twin image effects can lead to peaks at positions where no atoms are and, depending on hologram energy, to the cancellation of peaks at atom positions in the reconstructions. If effects due to many atoms are taken into account, peaks can also be shifted away from their ideal positions. This can lead to different peak position at different energies and therefore to different positions in XFH and MEXH. This makes the use of holograms at multiple interference energies desirable, where misleading effects that occur at single energies can cancel each other. The spatial resolution in the reconstructions depends upon energy and angular range of the holograms. The highest and most isotropic spatial resolution is obtained for 4π holograms and is given for $|\psi_k(\mathbf{r})|^2$ of the Barton algorithm (eq. 2.67) by about half the interference wavelength (section 2.6.3). This allows a higher spatial resolution in MEXH than in XFH since higher interference energies are available in MEXH than in XFH.

Holograms were calculated numerically for a bcc Fe cluster and reconstructed numerically. These calculations provide results for an ideal theoretical case (chapter 3). The hologram energies and angular ranges correspond to those available in XFH and MEXH experiments. The only systematic difference between XFH and MEXH in these hologram calculations lies in different energies and possibly angular ranges. The reconstructions of calculated 4π holograms deviate, depending on the hologram energy, from the bcc Fe structure. The peaks in reconstructions of 4π holograms were evaluated in a volume of $(7\ \text{Å})^3$ centered at the emitter atom. The volume contains the emitter and its nearest, next-, third- and fifth-nearest neighbors. Peak heights, widths and distances to the emitter atom are summarized in table 3.1 for the energies available in XFH, and in table 3.2 for energies available in MEXH. The accuracy of peak widths and distances given in the tables is about ± 0.2 Å. The widths can roughly be described by the simple theoretical estimate $\lambda/2$. In accordance with this, the peak widths obtained at 6.400 keV and 7.058 keV

are larger than the widths at energies above 9.5 keV. Energy-dependent position shifts of nearly 1 Å were observed at single energies. As an example, the following distances from the emitter to its nearest neighbors were obtained at various energies: (2.2 ± 0.2) Å, (2.4 ± 0.2) Å, (2.5 ± 0.2) Å, and (2.8 ± 0.2) Å. The distance between emitter and its nearest neighbors in bcc Fe is 2.49 Å. Many distances obtained at the single-energy reconstructions agree with each other and with the correct distance within ± 0.2 Å while others deviate from them.

In the energy-added reconstruction of holograms calculated at the energies 6.400 keV and 7.058 keV, the distances from the emitter to its next- and fifth-nearest neighbors are consistent with the distances in bcc Fe. If the energies from 7.9 keV to 11.3 keV are used in steps of 0.2 keV, the distances from the emitter to its nearest, next-, and fifth-nearest neighbors agree within the accuracy with those in bcc Fe. In spite of this already large energy range, the peak at the third-nearest neighbor position is lower than another peak at a smaller distance to the emitter so that this range is not quite sufficient for an unambiguous structure determination. The reconstructions of holograms calculated at energies differing by 0.2 keV can differ significantly from each other, showing that it is essential for an unambiguous determination of an unknown structure to measure holograms for many energies in small energy steps which is usually only possible in MEXH. A simple estimate for optimized hologram step sizes and ranges in angle and energy is given in section 2.3.1.

XFH and MEXH experiments usually have different absorption geometries and the holograms are measured at different angular resolutions. Differences between experiment and calculations can also arise from assumptions made in the calculations that do not correspond to the experimental situation: Multiple scattering and the large structure size that contributes to experimental holograms, polarization and near field effects, statistical noise in experimental holograms, and errors in background removal were neglected in the cluster calculations. Errors in background removal can lead to systematic errors in experimental holograms, especially in symmetrized holograms and in holograms that are extended to 4π. XFH and MEXH holograms were measured for a bcc Fe single crystal. Every atom in bcc Fe has the same atomic neighborhood which simplifies the interpretation of the results. The present experimental situation and recommendations for future experiments are discussed in chapters 4, 5. An optimized measurement procedure is described in section 5.5.

Statistical noise in experimental holograms causes in the reconstructions peaks that do not correspond to the structure and that cannot be separated a priori from peaks that are caused by the structure. Reconstructions from holograms measured individually under the same experimental conditions must be similar. Therefore, full holograms should be repeated and their reconstructions should be compared to ensure that the results are reliable and not caused by statistical noise. For example, experimental XFH holograms of bcc Fe measured at the Fe K_α line required about 4×10^9 total counts in order to obtain similar reconstructions from holograms measured by different detectors. Even at $\approx 10^{10}$ total counts the full symmetry of the structure was not obtained in the holograms or in the reconstructions because of statistical noise. A simple estimate for the necessary number of counts is given in section 5.5.

Reconstructions that were symmetrized in real space or taken from 4π extended holograms were analyzed in a volume of (7 Å)^3 centered at the emitter atom in XFH and at the detector atom in MEXH. Peak heights, widths and distances to the emitter atom are summarized in table 6.1 for XFH and in table 6.2 for MEXH. The accuracy of peak widths and distances is about ± 0.2 Å. The peak *widths* obtained in XFH at the Fe K_α and K_β lines are larger than the widths obtained in MEXH at energies above 9.5 keV and can be approximated by $\lambda/2$. The widths agree within the accuracy with the widths in the corresponding reconstructions of calculated holograms. A higher spatial resolution can be achieved in MEXH than in XFH. The *distances* in reconstructions at single energies between 6.4 keV and 11.1 keV can differ significantly from each other, just as for the reconstructions of calculated holograms. For example, distances from the emitter to its nearest neighbors of (2.3 ± 0.2) Å, (2.4 ± 0.2) Å, (2.5 ± 0.2) Å, (2.6 ± 0.2) Å, and (3.0 ± 0.2) Å were determined from various single-energy reconstructions. Not all peak positions in reconstrcutions of experimental holograms agree with the corresponding peak positions in reconstrcutions of calculated holograms. Differences can be attributed to the reasons given above.

For a single energy and an unknown structure, it cannot be determined a priori if a reconstruction will be more successful at an energy available in XFH or at a different energy available in MEXH. Calculations show that holograms should be measured at many energies and in small energy steps in order to obtain unambiguous results. This is usually only possible in MEXH. XFH can provide at least a starting point for a refined structure analysis. The results obtained at few energies can be refined by theoretical calculations or by combining the atomic resolution holography results with results obtained from other methods of structure determination.

In spite of present practical limitations, especially high statistical noise, some preliminary structural information can already be *directly* obtained from both methods of atomic resolution x-ray holography. Symmetries available from Kossel or XSW lines in the holograms can be used to extend holograms to 4π and to obtain three-dimensional images of nearly isotropic spatial resolution of $\approx \lambda/2$, where λ is the interference wavelength. If holograms are measured in the future nearly on a hemisphere and with a large number of counts, a spatial resolution of $\approx \lambda$ can be obtained in three dimensions without symmetrizing holograms and without extending them to 4π.

Chapter 7

Conclusion and Future Perspectives

XFH and MEXH are two new, closely-related methods for structure determination at an early stage of development. In these holographic methods, holograms are measured in **k**-space and then reconstructed, i.e. transformed into real space, with the goal to solve an unknown structure directly in three dimensions. In order to reach this goal, XFH and MEXH are systematically investigated in this work both in theory and experiment. The key questions are the following: How should holograms be measured? How should the data be evaluated? What qualitative and quantitative results are to be expected for a given experiment and a given data evaluation procedure? What are the differences and similarities of XFH and MEXH? The answers to these questions are summarized below.

XFH and MEXH may use different kinds of incident radiation and different detection systems. If both incident x rays and fluorescence radiation are used, then the same processes occur inside the sample for XFH and MEXH so that a mixing of XFH and MEXH contributions to holographic intensities can occur. If this is the case then the XFH and MEXH contributions to the interference signal have to be separated during the data evaluation. Methods to separate mixed signals were developed but it was shown that a complete separation is not always possible. Therefore experiments should be performed in such a way that either the XFH signal or the MEXH signal is recorded. Such pure XFH and MEXH experiments were for the first time realized in the context of this work. They allow a straightforward data evaluation.

In order to record the holographic interference pattern, angular and energy ranges and sampling must be sufficient. The following estimates were derived under simple assumptions: At least $8r_j/\lambda$ angular bins should be measured in 360°, where r_j is the distance from the fluorescence atom to the scattering neighbor atom, and λ is the interference wavelength. Kossel or XSW line patterns are visible if holograms of crystals are measured in angular bins of $\lesssim 1°$. Detailed Kossel or XSW line shapes can be measured simultaneously with a hologram and provide additional structural information. A large angular range has to be measured in order to detect the angular variation in the hologram for arbitrary atom positions of an unknown

structure, and a large angular range is also necessary for a high spatial resolution. The energy bin size must not exceed $hc/(4r_j)$, where h is Planck's constant and c is the speed of light, and a large energy range is necessary to average over effects that occur at single energies. The energy range should cover at least $hc/(2r_j)$. In practice, angular and energy sampling are usually different in XFH and MEXH. Different interference energies are available, and higher energies are available in MEXH than in XFH. Only the x-ray emission lines of atoms incorporated in the structure under investigation are available in XFH, while in MEXH the energy can be chosen freely above an electron binding energy. MEXH experiments were performed at multiple energies.

The holographic signal is on the order of $\lesssim 10^{-4}N$ and must not be dominated by the statistical noise that is on the order of $\sqrt{N}$, where N is the number of photons recorded. This requires to record at least 10^8 counts per angular and energy bin. If holograms are dominated by statistical noise then the noise causes peaks in the reconstructions that cannot be separated a priori from the peaks caused by the structure. Hologram measurements should be repeated to increase the statistics and to determine the influence of statistical noise.

The incident intensity should be constant for a full hologram recording so that typical recording times should not exceed a few hours. Continuous scans integrate over one angular coordinate. They ensure a sufficient sampling and allow a large duty cycle.

The data should be treated in a very straightforward way in order to allow a direct interpretation of the results. The two necessary steps are the background removal and the transformation of the holograms into real space. For a straightforward background removal, it is most important that experiments are performed in such a way that the recorded intensities contain either the XFH or the MEXH signal. It was also shown that the reference wave can and should be determined from experimental holograms by fitting angular-dependent absorption corrections but not by a filtering procedure: Removing reference wave and absorption effects or Kossel or XSW lines through a convolution with a Gaussian from the holograms is not advisable for unknown structures since, under simple assumptions, a high pass filter suppresses in the reconstruction short distances from the fluorescence atom and a low pass filter suppresses large distances.

A careful background removal is necessary since since systematic errors in the background removal lead to errors in the reconstructions. A constant offset in the holograms leads to high peaks in the reconstructions at the position of the fluorescence atom. If the background is removed from individual angular scans then the average information along the other angular coordinate is lost in the hologram so that information is also lost in the reconstructions. This can be avoided in fast experiments. Kossel or XSW lines can be used to extend holograms of crystals to the full 4π angular range in order to allow a high spatial resolution but a better approach is to measure directly in a large angular range.

The Barton algorithm used here for reconstruction is similar to a Fourier transform but with different weights and phases at single energies. Therefore the energy-added reconstructions differ for the Barton algorithm and a Fourier transform. An isotropic spatial resolution of about $\lambda/2$ is expected for holograms known on a full 4π sphere. A resolution of at least $\approx \lambda$ is expected for holograms known on a hemisphere where λ is the interference wavelength. A higher spatial resolution can be obtained in MEXH than in XFH due to higher available interference energies. At a single energy or at few energies, twin images can lead to peaks at positions where no atoms are. Also, the image of an atom and the twin image of its centrosymmetric counterpart can cancel each other, depending on the interference energy. Peaks due to different atoms can influence each other so that peak positions can be shifted away from atom positions at single or few energies. Shifts up to 1 Å were observed in reconstructions of calculated and experimental holograms. Under simple assumptions, peaks appear at the correct positions and with heights $(2r_e f_0)^2/(R^2 r_j)^2$, where r_e is the classical electron radius, R is the distance from the fluorescence atom to the detector, and r_j is the distance from the fluorescence atom to the neighboring atom which has a real and constant scattering factor f_0. Deviations from this are caused by twin-image and multiple-atom effects. Improved reconstructions are expected at multiple energies.

Reconstructions of holograms measured on a bcc Fe single crystal were compared to the corresponding reconstructions of holograms calculated for a bcc Fe cluster. The peak widths in reconstructions of numerically calculated holograms agree within the accuracy of ± 0.2 Å with the widths in reconstructions of experimental holograms. Most peak distances and heights agree for calculation and experiment. Deviations can be explained by statistical noise and systematic errors.

The optimization of the experiments and of the data evaluation made it possible to obtain preliminary structural information directly at a single energy or at few energies in both XFH and MEXH. Such information can be used as a starting point for a refined structure analysis, either using theoretical calculations or other methods of structure determination. A structural refinement will usually be necessary in XFH where only few interference energies are available but may not be necessary in MEXH at multiple energies.

Future Perspectives

A rigorous theory of atomic-resolution x-ray holography is still under development. Special reconstruction algorithms need to be found to remove or use the influence of many-atom effects in crystalline objects and to obtain additional information on the long-range order from Kossel or XSW lines. A rigorous reconstruction algorithm will not assume isotropic scattering but take into account atomic scattering factors, polarization and near field effects. A rigorous algorithm will reconstruct the electron density and give direct meaning to peak heights. This will require that holograms are measured in an optimized way as described above.

Faster energy-resolving detectors will help to improve the experimental statistics.

Current developments of multi-element silicon drift detectors can improve the statistics or reduce the data acquisition time at least by a factor of 100. Another promising way is the application of wavelength dispersive optics based on curved analyzer crystals. MEXH allows detection in a wide angular range which can be used to increase the experimental statistics. In order to follow this approach, an electron yield detector with a large detection angle was developed and used for recording MEXH holograms.

A special characteristic of MEXH in the experimental schemes is the extremely high resolution in **k**-space. This feature becomes a disadvantage when high sampling rates are not required, which is for example the case when only the nearest coordination shells of the detector atom are of interest. However, the plane wave like geometry of the incident wave can be relaxed experimentally. The energy bandwidth can be increased by using multilayer or mosaic crystal monochromators or even further by using a direct undulator beam or a pink beam from a total reflecting mirror system. The angular collimation can be widened by inserting a focusing x-ray lens or an x-ray total reflecting capillary into the beam to generate a convergent monochromatic incident beam.

For crystalline samples, present radiation sources provide scattered fluorescence intensities which can hardly be handled with state-of-the-art detectors but higher source brilliances will be necessary to study diluted structures, e.g. surfaces, interfaces, impurities, or defects. Higher source brilliances can in the future be supplied by x-ray free-electron-lasers using the excitation principle of self-amplified spontaneous emission. With such a source and new detectors it will become possible to generate a full XFH hologram with one pulse of 100 fs duration, providing an extreme time resolution.

The holographic approach does not depend on long-range translational order which provides a unique opportunity to study new classes of objects. Atomic resolution x-ray holography is highly tolerant to misorientation and sensitive to the local environment of definite sorts of atoms independent of their concentration. This makes the holographic methods applicable to atomic structures which can hardly be studied by traditional methods, for example active sites in biological materials of low crystalline quality or crystals with very low dopant concentrations.

XFH and MEXH have the potential to become effective tools for direct investigations of atom arrangements in clusters and solid matter.

Appendix A

Calculation of XFH Intensity

Consider just two atoms, a fluorescence atom at the origin $(0,0,0) = \mathbf{0}$ of a coordinate system, and another atom at position $\mathbf{r}_j$. The local intensity

$$I_i(\mathbf{0}) = \langle |\mathbf{E}_i(\mathbf{0},t)|^2 \rangle \tag{A.1}$$

excites the atom at the origin to fluorescence if the energy of the incident wave lies over an absorption edge of the sample. The incident wave has an electric field $\mathbf{E}_i$ and a wave vector $\mathbf{k}_i$ with absolute value $k_i = \omega_i/c$. Here, $\langle x \rangle$ denotes the time average of x over an interval large compared with the period $T = 2\pi/\omega_i$. A fraction of the incident intensity is converted to fluorescence radiation. In the electric dipole approximation, fluorescence radiation can be described by

$$\mathbf{E}_d(\mathbf{r},t) = -\frac{k^2}{r}\left[(\mathbf{u}(\mathbf{up}) - \mathbf{p}) - (3\mathbf{u}(\mathbf{up}) - \mathbf{p})\left(\frac{1}{k^2r^2} - \frac{i}{kr}\right)\right], \tag{A.2}$$

where $\mathbf{r}$ is the vector from the electric dipole $\mathbf{p}$ to the observation point, $\mathbf{u} = \mathbf{r}/r$, $\mathbf{k} = \mathbf{k}_f$ is the wavevector of the fluorescence radiation, $k_f = \omega_f/c < k_i$. For a source of dimension $d \ll \lambda = 2\pi c/\omega = 2\pi/k$, there are three spatial regions defined: the near (static) zone $d \ll r \ll \lambda$, the intermediate (induction) zone $d \ll r \sim \lambda$, and the far (radiation) zone $d \ll \lambda \ll r$. For large enough energies or atomic distances r, the scattering atom is in the far field of the fluorescence atom. In the far field, the second term of eq. A.2 may be neglected [Jackson75]. The dipole moment of a fluorescence atom at the origin can be expressed as

$$\mathbf{p}_f(\mathbf{r},t) = \mathbf{p}_0 e^{i(k_f r - \omega_f t)}. \tag{A.3}$$

p_0^2 is proportional to $\langle |\mathbf{E}_i(\mathbf{0})|^2 \rangle$, so that the fluorescence intensity is proportional to $I_i(\mathbf{0})$. At a distance $\mathbf{r}$ from the origin, the electric field is

$$\mathbf{E}_f(\mathbf{r},t) = \mathbf{E}_d(\mathbf{r},t) + \mathbf{E}_s(\mathbf{r},t), \tag{A.4}$$

where $\mathbf{E}_d(\mathbf{r},t)$ is the field radiated by the fluorescence atom,

$$\mathbf{E}_d(\mathbf{r},t) \;=\; -\frac{k_f^2}{r} e^{i(k_f r - \omega_f t)} \mathbf{p}_r \tag{A.5}$$

$$\mathbf{p}_r = \frac{\mathbf{r}}{r}\left(\frac{\mathbf{r}}{r}\mathbf{p}_0\right) - \mathbf{p}_0 - \left(3\frac{\mathbf{r}}{r}\left(\frac{\mathbf{r}}{r}\mathbf{p}_0\right) - \mathbf{p}_0\right)\left(\frac{1}{k_f^2 r^2} - \frac{i}{k_f r}\right) \quad (A.6)$$

$$\equiv C_r \frac{\mathbf{r}}{r}\left(\frac{\mathbf{r}}{r}\mathbf{p}_0\right) - D_r\mathbf{p}_0 \quad (A.7)$$

$$\mathbf{p}_r = \frac{\mathbf{r}}{r}\left(\frac{\mathbf{r}}{r}\mathbf{p}_0\right) - \mathbf{p}_0 \qquad \text{if } r \gg \lambda_f. \quad (A.8)$$

$\mathbf{E}_s(\mathbf{r},t)$ is the same field scattered from the atom at $\mathbf{r}_j$ at the retarded time $\tau = t - |\mathbf{r}-\mathbf{r}_j|/c$. Let $\mathbf{r}'_j = \mathbf{r} - \mathbf{r}_j$. Far from any absorption edges of the scattering atom, $\mathbf{E}_s(\mathbf{r},t)$ may be described by the Thomson scattering amplitude,

$$\mathbf{E}_s(\mathbf{r},t) = -\frac{k_f^2}{r'_j}\mathbf{p}'_{sj} \quad (A.9)$$

$$\mathbf{p}'_{sj} \equiv \frac{\mathbf{r}'_j}{r'_j}\left(\frac{\mathbf{r}'_j}{r'_j}\mathbf{p}_d\right) - \mathbf{p}_d - \left(3\frac{\mathbf{r}'_j}{r'_j}\left(\frac{\mathbf{r}'_j}{r'_j}\mathbf{p}_d\right) - \mathbf{p}_d\right)\left(\frac{1}{k_f^2 r'^2_j} - \frac{i}{k_f^2 r'_j}\right) \quad (A.10)$$

$$\mathbf{p}'_{sj} = \frac{\mathbf{r}'_j}{r'_j}\left(\frac{\mathbf{r}'_j}{r'_j}\mathbf{p}_d\right) - \mathbf{p}_d = \frac{\mathbf{r}}{r}\left(\frac{\mathbf{r}}{r}\mathbf{p}_d\right) - \mathbf{p}_d \qquad \text{if } r'_j \approx r \gg \lambda_f. \quad (A.11)$$

$$\mathbf{p}_d = \mathbf{p}_d(\mathbf{r}_j,\tau) \quad (A.12)$$

The electric dipole moment $\mathbf{p}_d$ is induced at the position of the scattering atom $\mathbf{r}_j$ by the incident $\mathbf{E}_d(\mathbf{r}_j,\tau)$. Let $\mathbf{x}$ be the elongation of the point charge q from its origin, caused by the Lorentz force

$$\mathbf{F}(\mathbf{r},t) = md^2\mathbf{x}(\mathbf{r},t)/dt^2 = q\mathbf{E}_d(\mathbf{r},t).$$

$$\mathbf{p}_d(\mathbf{r},t) = q\mathbf{x}(\mathbf{r},t) = -\frac{q^2}{m\omega_f^2}\mathbf{E}_d(\mathbf{r},t) = -\frac{q^2}{mc^2k_f^2}\mathbf{E}_d(\mathbf{r},t)$$

$$= -\frac{r_e f(\mathbf{r}_j,\mathbf{k}_f)}{k_f^2}\mathbf{E}_d(\mathbf{r},t), \quad (A.13)$$

where the last equality holds for a point like atom with atomic form factor $f(\mathbf{r}_j,\mathbf{k}_f)$ for scattering from the direction $\mathbf{r}_j$ to $\mathbf{k}_f$. The atomic form factor is defined for the scattering of plane waves so that its use implies an approximation. In this case q^2 is replaced by $e^2 f(\mathbf{r}_j,\mathbf{k}_f)$, where $-e$ is the electron charge. The classical electron radius is $r_e = e^2/mc^2 = 2.818 \cdot 10^{-5}$ Å.

$$\mathbf{p}_d(\mathbf{r}_j,\tau) = \frac{r_e f(\mathbf{r}_j,\mathbf{k}_f)}{r_j} e^{i(k_f r_j + k_f r'_j - \omega_f t)}\mathbf{p}_j \quad (A.14)$$

$$\mathbf{p}_j \equiv \frac{\mathbf{r}_j}{r_j}\left(\frac{\mathbf{r}_j}{r_j}\mathbf{p}_0\right) - \mathbf{p}_0 - \left(3\frac{\mathbf{r}_j}{r_j}\left(\frac{\mathbf{r}_j}{r_j}\mathbf{p}_0\right) - \mathbf{p}_0\right)\left(\frac{1}{k_f^2 r_j^2} - \frac{i}{k_f r_j}\right) \quad (A.15)$$

$$\equiv C_j\frac{\mathbf{r}_j}{r_j}\left(\frac{\mathbf{r}_j}{r_j}\mathbf{p}_0\right) - D_j\mathbf{p}_0 \quad (A.16)$$

$$\mathbf{p}_j = \frac{\mathbf{r}_j}{r_j}\left(\frac{\mathbf{r}_j}{r_j}\mathbf{p}_0\right) - \mathbf{p}_0 \qquad \text{if } r_j \gg \lambda_f. \quad (A.17)$$

Using this,

$$\mathbf{p}'_{sj} = \frac{r_e f(\mathbf{r}_j, \mathbf{k}_f)}{r_j} e^{i(k_f r_j + k_f r'_j - \omega_f t)} \mathbf{p}'_j \tag{A.18}$$

$$\mathbf{p}'_j \equiv \left(C'_j \frac{\mathbf{r}'_j}{r'_j} \left(\frac{\mathbf{r}'_j}{r'_j} \mathbf{p}_j \right) - D'_j \mathbf{p}_j \right). \tag{A.19}$$

Now, inserting eqns. A.5, A.9, A.18 into eq. A.4 gives

$$\mathbf{E}_f(\mathbf{r}, t) = -\frac{k_f^2}{r} e^{i(k_f r - \omega_f t)} \mathbf{p}_r - \frac{k_f^2}{r'_j} \frac{r_e f(\mathbf{r}_j, \mathbf{k}_f)}{r_j} e^{i(k_f r_j + k_f r'_j - \omega_f t)} \mathbf{p}'_j. \tag{A.20}$$

The second term in eq. A.20 is the scattering term corresponding to the holographic object wave. Compared with the first term which describes the reference wave, it is typically of the order of or smaller than $r_e f(\mathbf{r}_j, \mathbf{k}_f)/r_j \approx 10^{-4}$. The interference intensity for XFH is given by

$$I_f(\mathbf{r}) = \langle |\mathbf{E}_f(\mathbf{r}, t)|^2 \rangle. \tag{A.21}$$

Summation over n scattering neighbors of the fluorescence atom yields

$$\begin{aligned} I_f(\mathbf{r}) &= \left| -\frac{k_f^2}{r} e^{ik_f r} \mathbf{p}_r - \sum_{j=1}^{n} \frac{k_f^2}{r'_j} \frac{r_e f(\mathbf{r}_j, \mathbf{k}_f)}{r_j} e^{ik_f (r_j + r'_j)} \mathbf{p}'_j \right|^2 \\ &= \frac{k_f^4 p_r^2}{r^2} \left\{ 1 + 2 r_e \mathrm{Re} \sum_{j=1}^{n} \frac{r f(\mathbf{r}_j, \mathbf{k}_f)}{r'_j r_j} e^{ik_f (r_j + r'_j - r)} \frac{\mathbf{p}_r^* \mathbf{p}'_j}{p_r^2} \right. \\ &\quad \left. + r_e^2 \sum_{j=1}^{n} \sum_{m \neq j} \frac{r^2 f(\mathbf{r}_j, \mathbf{k}_f) f^*(\mathbf{r}_m, \mathbf{k}_f)}{r'_j r_j r'_m r_m} e^{ik_f (r_j + r'_j - r_m - r'_m)} \frac{\mathbf{p}'_j \mathbf{p}'^*_m}{p_r^2} \right\}. \end{aligned} \tag{A.22}$$

For small clusters and far away from Bragg angles, multiple scattering is very weak so that the last term in A.22 may be neglected. Since scattering is much stronger for electrons than for X-rays, this simplification is more valid for X-rays [Len94]. For spontaneous emission of fluorescence radiation, $\mathbf{E}_f(\mathbf{r}, t)$ has to be averaged over all directions of the polarization $\mathbf{p}_0$. Without making the far field approximation, one obtains

$$\begin{aligned} \mathbf{p}_r^* \mathbf{p}'_j = {} & C_r^* C'_j C_j \frac{(\mathbf{r}\mathbf{r}'_j)(\mathbf{r}'_j \mathbf{r}_j)(\mathbf{r}_j \mathbf{p}_0)(\mathbf{p}_0 \mathbf{r})}{r^2 r'^2_j r_j^2} - C_r^* C'_j D_j \frac{(\mathbf{r}\mathbf{r}'_j)(\mathbf{r}'_j \mathbf{p}_0)(\mathbf{p}_0 \mathbf{r})}{r^2 r'^2_j} \\ & - C_r^* D'_j C_j \frac{(\mathbf{r}\mathbf{r}_j)(\mathbf{r}_j \mathbf{p}_0)(\mathbf{p}_0 \mathbf{r})}{r^2 r_j^2} + C_r^* D'_j D_j \frac{(\mathbf{r}\mathbf{p}_0)^2}{r^2} \\ & - D_r^* C'_j C_j \frac{(\mathbf{r}'_j \mathbf{r}_j)(\mathbf{r}_j \mathbf{p}_0)(\mathbf{p}_0 \mathbf{r}'_j)}{r_j^2 r'^2_j} + D_r^* C'_j D_j \frac{(\mathbf{r}'_j \mathbf{p}_0)^2}{r'^2_j} \end{aligned}$$

$$+D_r^* D_j' C_j \frac{(\mathbf{r}_j \mathbf{p}_0)^2}{r_j^2} - D_r^* D_j' D_j p_0^2 \tag{A.23}$$

$$\overline{(\mathbf{r}\mathbf{p}_0)^2} = \frac{r^2 p_0^2}{4\pi} \int_0^{2\pi} d\varphi \int_0^{\pi} \sin\theta d\theta \cos^2\theta = \frac{r^2 p_0^2}{3} \tag{A.24}$$

$$\overline{(\mathbf{r}_j \mathbf{p}_0)(\mathbf{p}_0 \mathbf{r})} = \frac{(\mathbf{r}\mathbf{r}_j) p_0^2}{3} \tag{A.25}$$

$$\begin{aligned}\overline{\mathbf{p}_r^* \mathbf{p}_j'} = \frac{p_0^2}{3} \Bigg[& C_r^* C_j' C_j \frac{(\mathbf{r}\mathbf{r}_j')(\mathbf{r}_j'\mathbf{r}_j)(\mathbf{r}_j\mathbf{r})}{r^2 r_j'^2 r_j^2} - C_r^* C_j' D_j \frac{(\mathbf{r}\mathbf{r}_j')^2}{r^2 r_j'^2} \\ & - C_r^* D_j' C_j \frac{(\mathbf{r}\mathbf{r}_j)^2}{r^2 r_j^2} + C_r^* D_j' D_j - D_r^* C_j' C_j \frac{(\mathbf{r}_j'\mathbf{r}_j)^2}{r_j^2 r_j'^2} \\ & + D_r^* C_j' D_j + D_r^* D_j' C_j - 3 D_r^* D_j' D_j \Bigg]\end{aligned} \tag{A.26}$$

$$\overline{p_r^2} = \overline{(\mathbf{p}_r^* \mathbf{p}_r)} = \frac{2p_0^2}{3} \left(1 + \frac{1}{k_f^2 r^2} + \frac{3}{k_f^4 r^4} \right). \tag{A.27}$$

In the far field $\mathbf{r}_j' \approx \mathbf{r} \gg \lambda_f$, $C_r^* \approx 1$, $D_r^* \approx 1$, $C_j' \approx 1$, $D_j' \approx 1$, so that

$$\begin{aligned}\overline{\mathbf{p}_r^* \mathbf{p}_j'} &= \frac{p_0^2}{3} \left[C_j - 2D_j - \frac{C_j (\mathbf{r}\mathbf{r}_j)^2}{r^2 r_j^2} \right] \\ &= -\frac{p_0^2}{3} \left[1 + \frac{1}{k_f^2 r_j^2} - \frac{i}{k_f r_j} + \left(1 - \frac{3}{k_f^2 r_j^2} + \frac{3i}{k_f r_j} \right) \frac{(\mathbf{r}\mathbf{r}_j)^2}{r^2 r_j^2} \right] \\ &= -\frac{p_0^2}{3} \left[1 + \frac{(\mathbf{r}\mathbf{r}_j)^2}{r^2 r_j^2} + \left(\frac{1}{k_f^2 r_j^2} - \frac{i}{k_f r_j} \right) \left(1 - \frac{3(\mathbf{r}\mathbf{r}_j)^2}{r^2 r_j^2} \right) \right]\end{aligned} \tag{A.28}$$

$$\overline{p_r^2} = \frac{2p_0^2}{3}. \tag{A.29}$$

(If also $r_j \gg \lambda_f$, then $C_j \approx 1$, $D_j \approx 1$.) If $\mathbf{r}_j' \approx \mathbf{r} \gg \mathbf{r}_j$, then $1/\mathbf{r}_j' \approx 1/r$ and $\exp(ik_f r_j') \approx \exp(ik_f r - i\mathbf{k}\mathbf{r}_j)$, so that $\mathbf{k}_f = k_f \mathbf{r}/r$, and

$$\begin{aligned}I_f(\mathbf{r}) &= \frac{2p_0^2 k_f^4}{3r^2} \Bigg\{ 1 - r_e \mathrm{Re} \sum_{j=0}^{n} \frac{f(\mathbf{r}_j, \mathbf{k}_f)}{r_j} e^{i(k_f r_j - \mathbf{k}_f \mathbf{r}_j)} \\ &\qquad \left[1 + \frac{(\mathbf{r}\mathbf{r}_j)^2}{r^2 r_j^2} + \left(\frac{1}{k_f^2 r_j^2} - \frac{i}{k_f r_j} \right) \left(1 - \frac{3(\mathbf{r}\mathbf{r}_j)^2}{r^2 r_j^2} \right) \right] \Bigg\}\end{aligned} \tag{A.30}$$

$$\equiv \frac{2p_0^2 k_f^4}{3r^2} \left\{ 1 - 2r_e \mathrm{Re} \sum_{j=0}^{n} \frac{f'(\mathbf{r}_j, \mathbf{k}_f)}{r_j} e^{i(k_f r_j - \mathbf{k}_f \mathbf{r}_j)} \right\}. \tag{A.31}$$

$f'(\mathbf{r}_j, \mathbf{k}_f)$ is an effective scattering factor.

Appendix B

Reconstructions of Calculated Holograms

This appendix shows additional numerical reconstructions of calculated holograms. Intensities were calculated for a bcc Fe cluster as in chapter 3. The φ_d rotation axis was parallel to the [001] direction in the calculations. The holograms are obtained by subtracting the constant background of intensity $I = I_0$ from the calculated intensities if no other information on background subtraction is given. The reconstructions were performed according to eqns. 2.67, 2.70 where the integrations were replaced by summations as in chapter 3. At single energies, $|\psi_k(\mathbf{r})|^2$ is displayed and at multiple energies, $|\psi_k(\mathbf{r})|^2$ is displayed. Each image is displayed without any cutoff in a linear greyscale where black corresponds to maximum peak intensity and white to minimum intensity.

- Fig. B.1: The image plane is parallel to the (001) lattice planes and passes through the emitter atom. Reconstructions $|\psi_k(\mathbf{r})|^2$ of holograms calculated at the energies $E_1 = 6.400$ keV, $E_2 = 7.058$ keV, and the energy-added reconstruction $|\psi_k(\mathbf{r})|^2$ are shown for the angular ranges $\Delta\theta_1 = 0°...59°$, $\Delta\theta_2 = 24°...83°$, and a full 4π sphere.

- Fig. B.2: The image plane is parallel to the (001) lattice planes and passes through the emitter atom. Reconstructions of holograms calculated at energies from 7.9 keV to 11.1 keV, and energy-added reconstructions are shown for the angular range $\Delta\theta_1 = 19°...90°$.

- Fig. B.3: As fig. B.2 but here the average value was subtracted from each φ scan of the calculated intensities.

- Fig. B.4: The image plane is parallel to the (010) lattice planes and passes through the emitter atom. Reconstructions of holograms calculated at energies from 7.9 keV to 11.1 keV, and energy-added reconstructions are shown for the angular range $\Delta\theta_1 = 19°...90°$.

- Fig. B.5: As fig. B.4 but here the average value was subtracted from each φ scan of the calculated intensities.

- Fig. B.6: Different image planes through the three-dimensional energy-added reconstruction. The energies 9.5 keV, 9.9 keV, ...11.1 keV were used for the hologram calculations.
- Fig. B.7: Different image planes through the three-dimensional energy-added reconstruction. The energies 7.9 keV, 8.1 keV, ...11.3 keV were used for the hologram calculations.

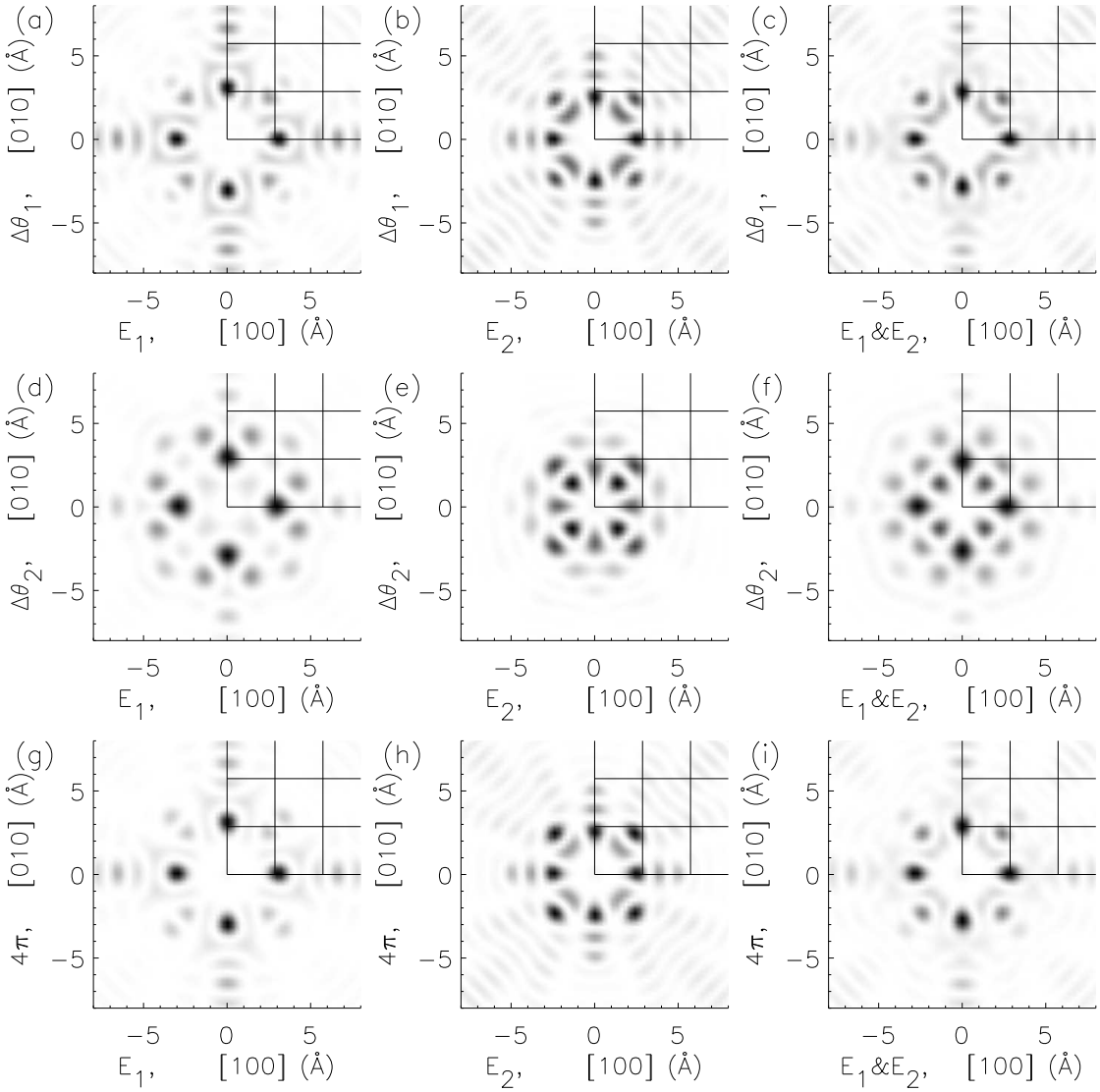

Figure B.1: The same reconstructions are shown as in fig. 3.4, but in a larger area: Reconstructions of calculated holograms in a plane parallel to the (001) lattice planes and passing through the emitter atom. The hologram range $\Delta\theta_1 = 0°...59°$ was reconstructed in (a)-(c), the range $\Delta\theta_2 = 24°...83°$ in (d)-(f), and a full 4π sphere in (g)-(i). In all cases, $\varphi = 0°...359°$ was used. The hologram energies are $E_1 = 6.400$ keV in (a), (d), (g), $E_2 = 7.058$ keV in (b), (e), (h), and both energies were added according to eq. 2.103 in (c), (f), (i). The low spatial resolution perpendicular to the image planes is obvious for the angular range $\Delta\theta_2$ from (d) and (f). There, peaks occur due to atoms from planes half a lattice constant above or below the image plane.

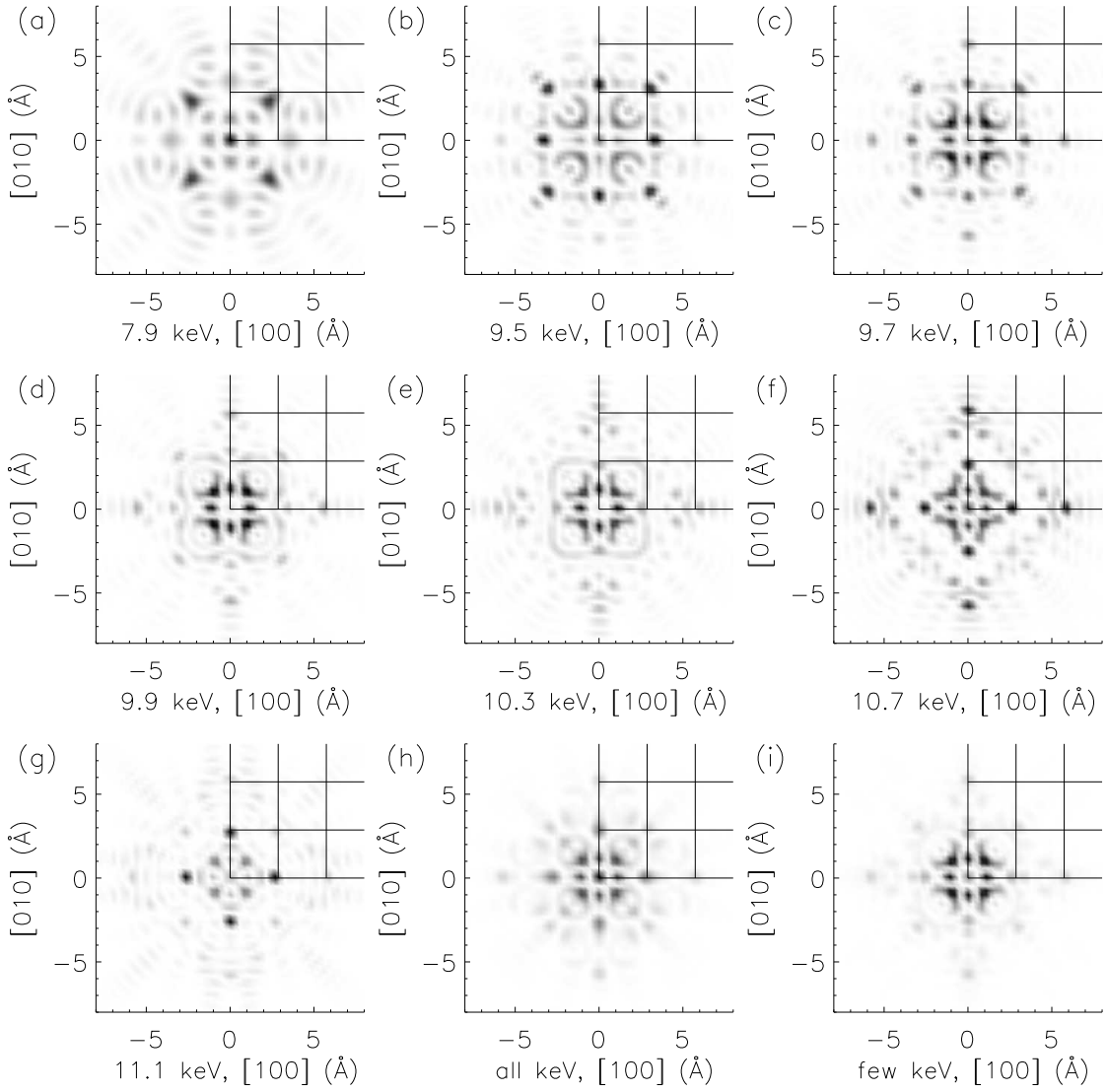

Figure B.2: Reconstructions of calculated holograms in a plane parallel to the (001) lattice planes and passing through the emitter atom. The hologram range $\Delta\theta_1 = 19°...90°$ was reconstructed for the energies from 7.9 keV to 11.1 keV in steps of 0.2 keV. (a)-(g) show single-energy reconstructions. (h) shows the energy-added reconstruction of the holograms calculated at the energies from 7.9 keV to 11.3 keV in steps of 0.2 keV. (i) shows the energy-added reconstruction of the holograms calculated at the energies from 9.5 keV to 11.1 keV in steps of 0.4 keV. The constant reference wave of intensity $I = I_0$ was subtracted from each calculated hologram before the reconstruction.

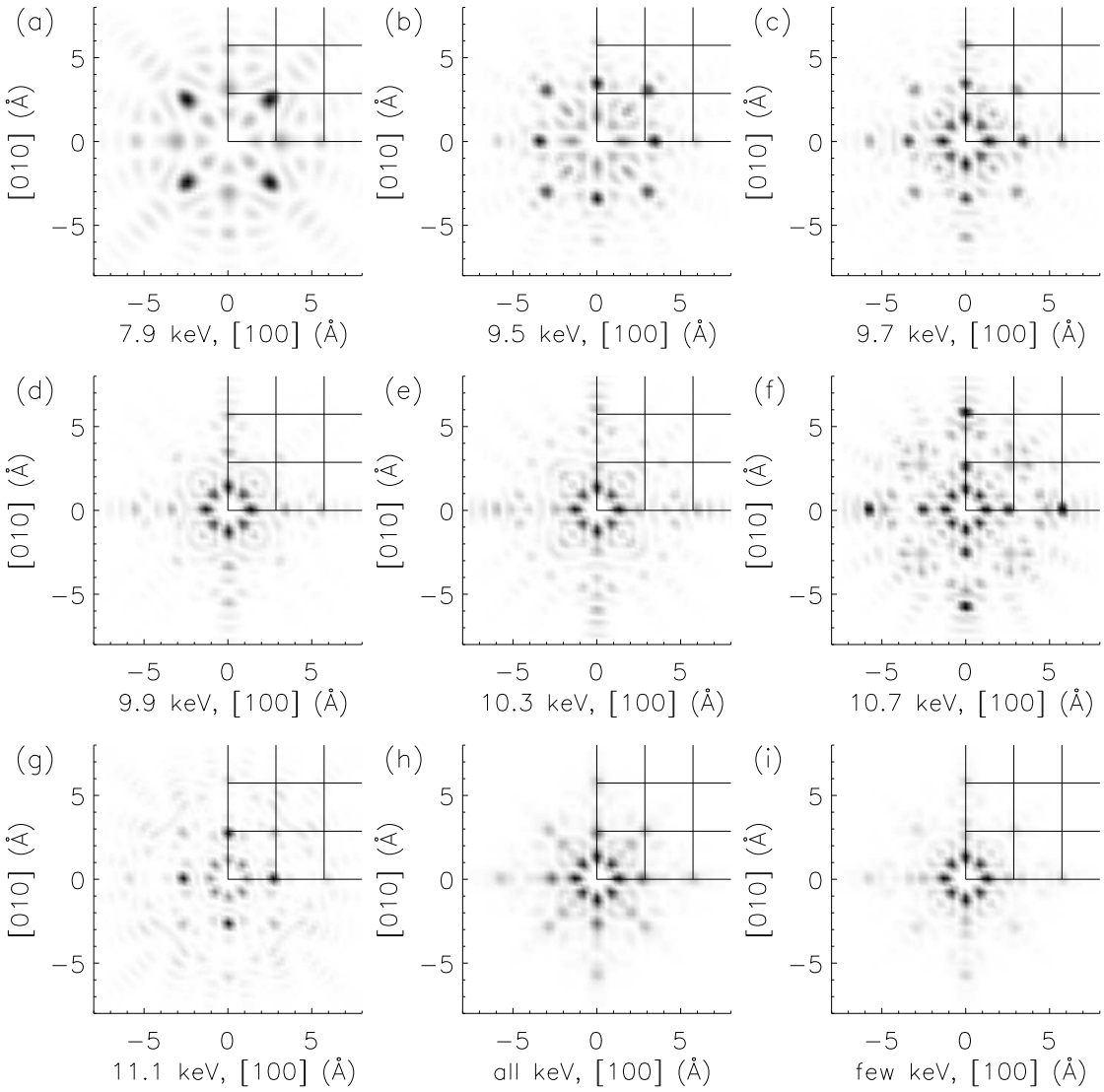

Figure B.3: The same holograms were reconstructed as in fig. B.2 but here the average value was subtracted from each φ scan of the calculated intensities.

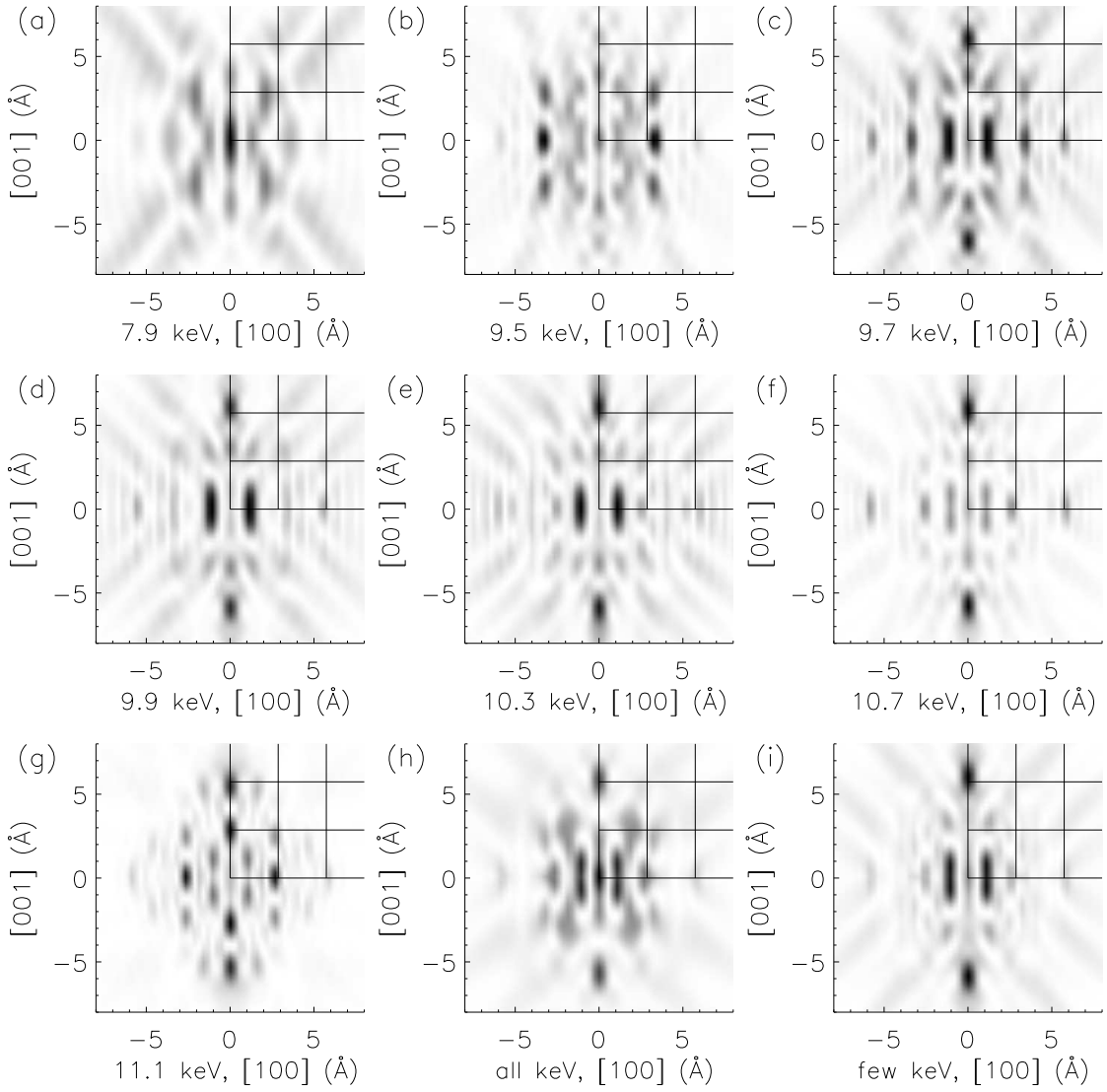

Figure B.4: Reconstructions of calculated holograms in a plane parallel to the (010) lattice planes and passing through the emitter atom. The hologram range $\Delta\theta_1 = 19°...90°$ was reconstructed for the energies from 7.9 keV to 11.1 keV in steps of 0.2 keV. (a)-(g) show single-energy reconstructions. (h) shows the energy-added reconstruction of the holograms calculated at the energies from 7.9 keV to 11.3 keV in steps of 0.2 keV. (i) shows the energy-added reconstruction of the holograms calculated at the energies from 9.5 keV to 11.1 keV in steps of 0.4 keV. The constant reference wave of intensity $I = I_0$ was subtracted from each calculated hologram before the reconstruction.

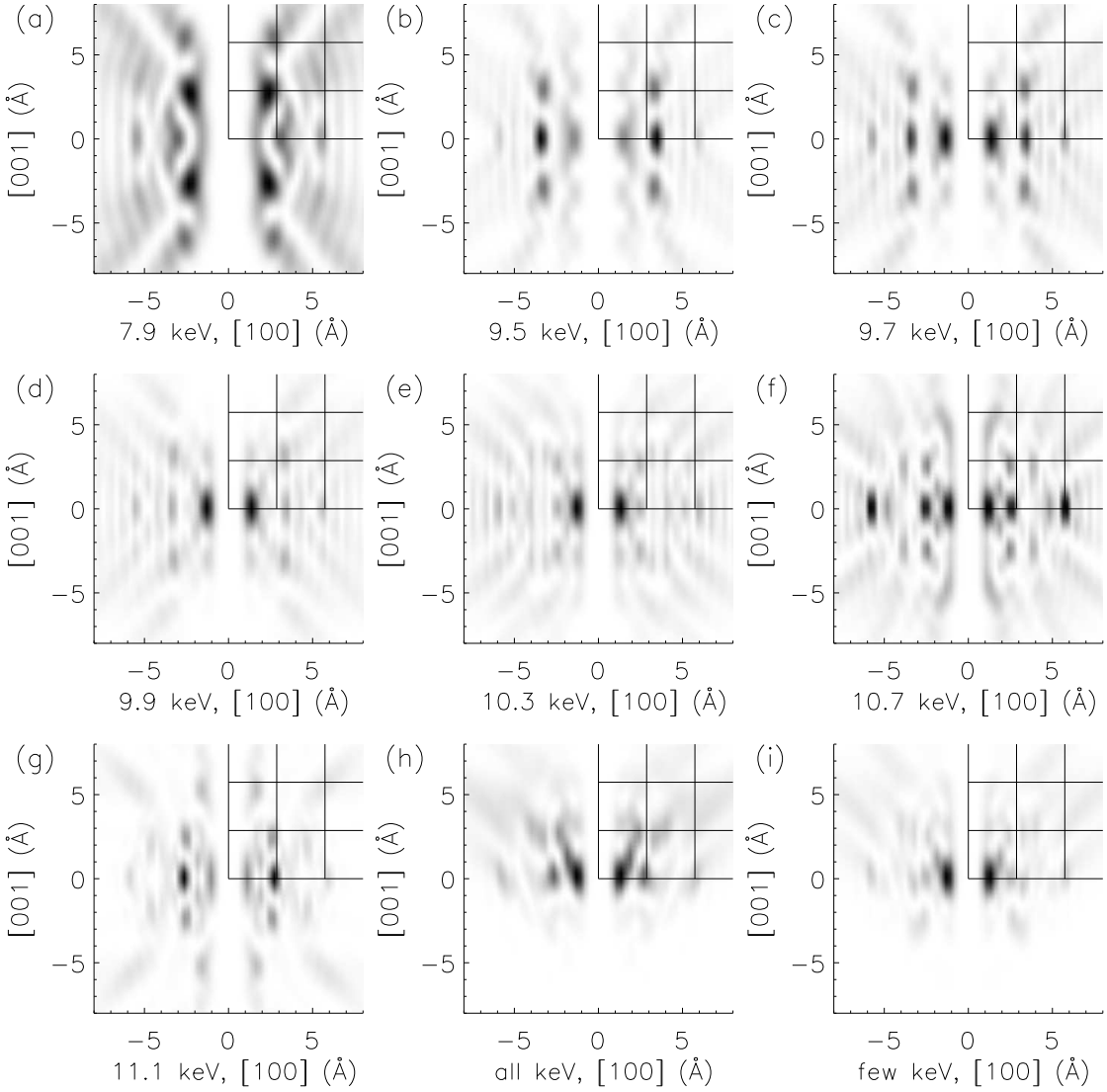

Figure B.5: The same holograms were reconstructed as in fig. B.4 but here the average value was subtracted from each φ scan of the calculated intensities.

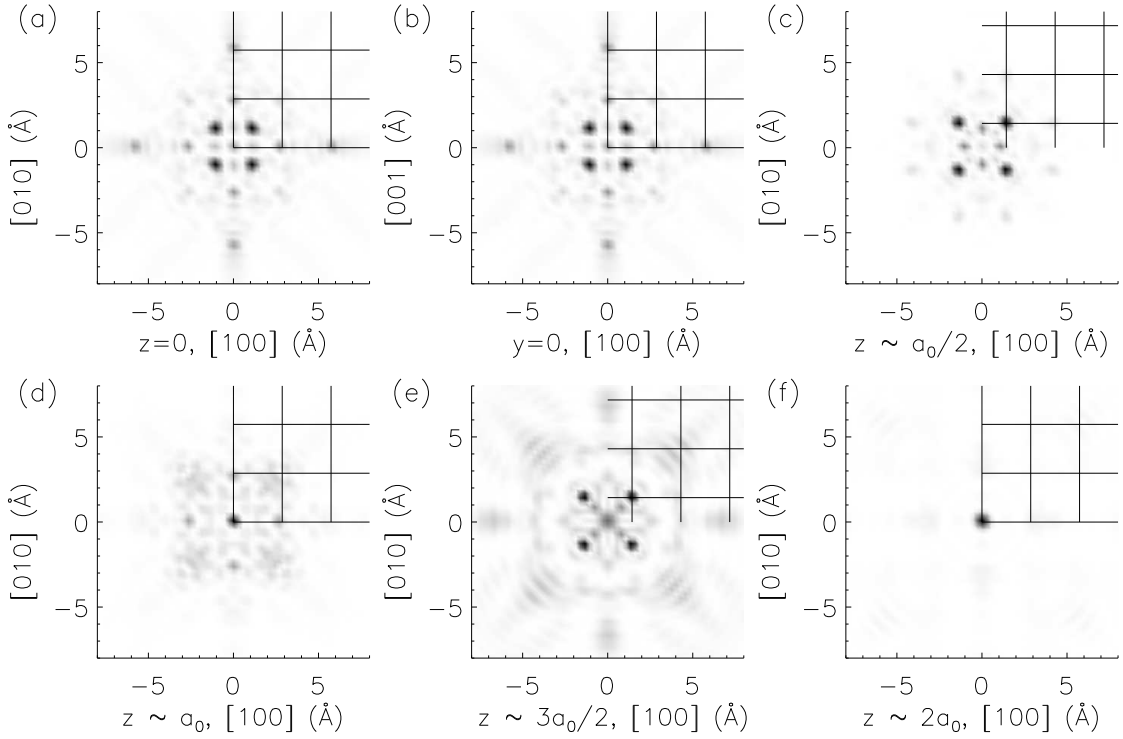

Figure B.6: Images of the energy-added reconstruction of calculated 4π holograms in different planes, using the energies 9.5 keV, 9.9 keV, ...11.1 keV. (a) The plane passes through the emitter atom parallel to the (001) lattice planes. (b) The plane passes through the emitter atom perpendicular to the (001) lattice planes. (c)-(f) The planes are parallel to the (001) lattice planes at a distance z from the emitter. (c) $z = 1.3$ Å $\approx a_0/2 = 1.44$ Å, (d) $z = 2.6$ Å $\approx a_0 = 2.87$ Å, (e) $z = 4.3$ Å $\approx 3a_0/2 = 4.31$ Å, (f) $z = 5.8$ Å $\approx 2a_0 = 5.74$ Å.

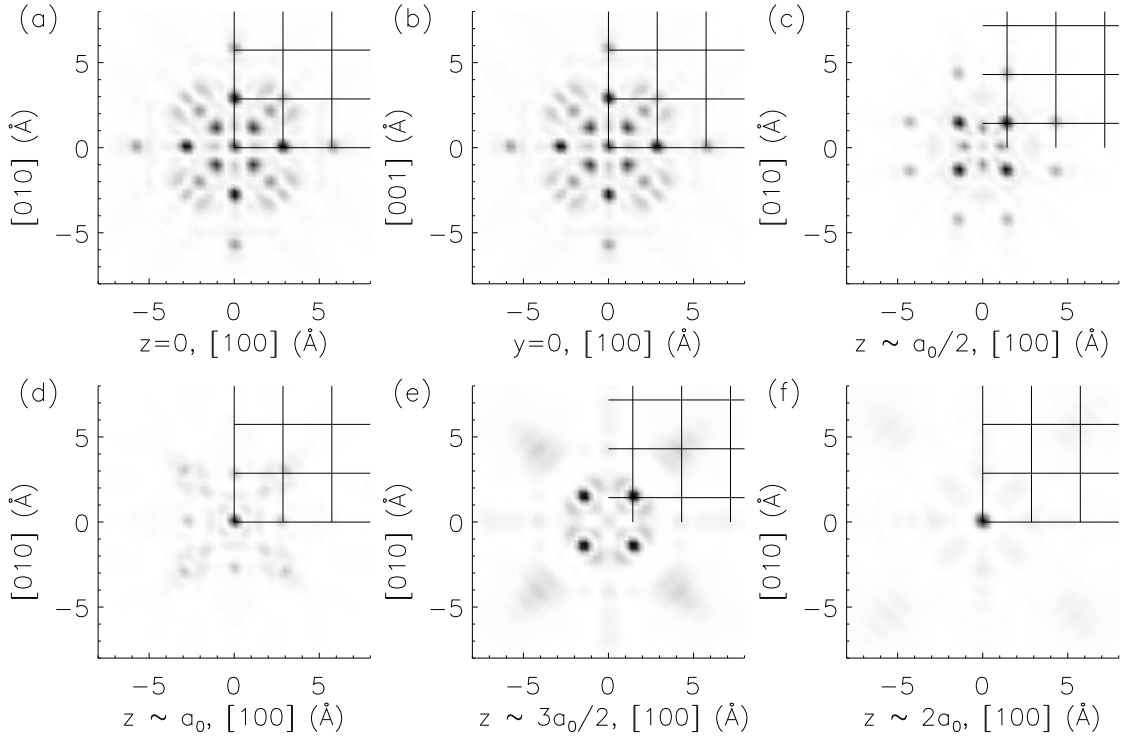

Figure B.7: Images of the energy-added reconstruction of calculated 4π holograms in different planes, using the energies 7.9 keV, 8.1 keV, ...11.3 keV. (a) The plane passes through the emitter atom parallel to the (001) lattice planes. (b) The plane passes through the emitter atom perpendicular to the (001) lattice planes. (c)-(f) The planes are parallel to the (001) lattice planes at a distance z from the emitter. (c) $z = 1.3$ Å $\approx a_0/2 = 1.44$ Å, (d) $z = 2.6$ Å $\approx a_0 = 2.87$ Å, (e) $z = 4.3$ Å $\approx 3a_0/2 = 4.31$ Å, (f) $z = 5.8$ Å $\approx 2a_0 = 5.74$ Å.

Appendix C

Parameters of XFH and MEXH Experiments

C.1 bcc Fe XFH Experiment of October 1998

XFH in 10/1998	undulator beamline BW1
DORIS	4.44 GeV positron energy
5 bunch mode	current decreased from 140 mA to 80 mA
	during one run
beamline	2 focusing mirrors, one before and one after the
	2 symmetric Si (111) monochromator crystals
incident energy	9.0 keV
slit size	$(1.0\ \mathrm{mm})^2$ in front of the ionisation chamber
incident photons	$\approx 5 \times 10^{10}$ photons/s/mm^2
	stabilized within ≈ 0.5 % for single φ_d scans
sample	bcc Fe single crystal
θ, φ_s	$\theta = 90°$, $\varphi_s = const$
angular resolution	$\approx 1°$
angular range	sdd1, sdd2: $\varphi_d = 0°, 1°, ...360°$,
	sdd1: $\Delta\alpha_1 = 0.4°, 1.4°, ...59.4°$
	sdd2: $\Delta\alpha_2 = 24°, 25°, ...83°$
SCA settings	Fe K_α line, Fe K_β line are recorded
measuring time	2 s per angular point
recording time	12 days total, yielding about 10 holograms
count rate	$\approx 10^4$ counts/s/detector
counts	4×10^4 average number of counts
	per angular element and per data set
	10^9 total counts in each of 10 data sets
	10^{10} total counts, 7×10^9 at Fe K_α, 3×10^9 at Fe K_β

Table C.1: Parameters of the bcc Fe XFH experiment at BW1 in October 1998.

C.2 bcc Fe MEXH Experiments of July 1998 and March 1999

MEXH in 07/1998	bending magnet beamline CEMO
DORIS	4.44 GeV positron energy
5 bunch mode	current decreased from 140 mA to 60 mA
beamline	1 Au coated mirror, before the
	2 symmetric Si (111) monochromator crystals
incident energies	7.9 keV, 8.1 keV, ... 11.3 keV
slit size	0.6 mm (width) ×0.4 mm (height)
	in front of the ionisation chamber
sample	bcc Fe single crystal
angular resolution	vertical $\approx 0.003°$, horizontal $\approx 0.02°$
angular range	sdd1, sdd2: $\varphi_d = 0°, 1°, ...150°$,
	$\theta = 90°, 89°, ...20°$
α, φ_d	$\alpha = const$, $\varphi_d = const$
acceptance angles	$\approx 1°$ for sdd1, sdd2
SCA settings	total over both Fe K lines and the elastic line,
	and total over both Fe K lines recorded
measuring time	on average 3 s per angular point
recording time	16 days total for 18 holograms
counts	4.3×10^{10} total counts at Fe K total

total counts at Fe K total:

energy (keV)	7.9	8.1	8.3 8.5	8.7	8.9	9.1	9.3	9.5	
counts (10^9)	4	3	4	3	3	4	3	4	2
energy (keV)	9.7	9.9	10.1	10.3	10.5	10.7	10.9	11.1	11.3
counts (10^9)	1	1	2	2	3	1	2	1	1

Table C.2: Parameters of the first bcc Fe MEXH experiment at CEMO in July 1998.

MEXH in 03/1999	bending magnet beamline CEMO
DORIS	4.44 GeV positron energy
5 bunch mode	current decreased from 140 mA to 60 mA
2 bunch mode	current decreased from 100 mA to 50 mA
beamline	1 Au coated mirror, before the
	2 symmetric Si (111) monochromator crystals
incident energies	9.5 keV, 9.9 keV, 10.3 keV, 10.7 keV, 11.1 keV
slit size	$(0.4\ \mathrm{mm})^2$ in front of the ionisation chamber
incident photons	$\approx 2 \times 10^{10}$ photons/s/$(0.4\ \mathrm{mm})^2$ at 9.5 keV,
	$\approx 4 \times 10^{9}$ photons/s/$(0.4\ \mathrm{mm})^2$ otherwise
	stabilized within ≈ 0.5 % for single φ_s scans
sample	bcc Fe single crystal
angular resolution	vertical $\approx 0.003°$, horizontal $\approx 0.02°$
angular range	sdd1, sdd2: $\varphi_d = 0°, 1°, ...360°$,
	while $\theta = 90°, 89°, ...44°$
	and $\varphi_d = 85°, 86°, ...180°$,
	while $\theta = 43°, 42°, ...1°$
α, φ_d	$\alpha = const$, $\varphi_d = const$
acceptance angles	$\approx 1°$ for sdd1, sdd2
SCA settings	Fe K_α line, total over both Fe K lines recorded
measuring time	3 s per angular point
recording time	10 days total, yielding 8 holograms
	(2 at 9.5 keV, 3 at 9.9 keV,
	1 at 10.3 keV, 10.7 keV, 11.1 keV each)
counts	average number of counts
	per angular element per energy
	9×10^4 at Fe K_α, 1.2×10^5 at Fe K total
total counts	1.6×10^{10} at Fe K_α
	2.1×10^{10} at Fe K total

	total counts at Fe K_α:					total counts at Fe K total:				
energy (keV)	9.5	9.9	10.3	10.7	11.1	9.5	9.9	10.3	10.7	11.1
counts (10^9)	1	5	3	3	3	2	7	4	4	4

Table C.3: Parameters of the second bcc Fe MEXH experiment at CEMO in March 1999.

Appendix D

Reconstructions of Experimental Holograms

This appendix shows additional reconstructions of experimental holograms. The φ_d rotation axis in XFH and the φ_s rotation axis in MEXH was parallel to the [001] direction in the experiments. At a single energy, the reconstruction $|\psi_k(\mathbf{r})|^2$ according to eq. 2.67 is shown and at multiple energies, $|\psi(\mathbf{r})|^2$ according to eq. 2.70 is shown. The integrations in eqns. 2.67, 2.70 were replaced by summations. Each image is displayed without any cutoff in a linear greyscale where black corresponds to maximum peak intensity and white to minimum intensity.

D.1 Reconstructions of bcc Fe XFH Holograms

This appendix shows reconstructions of experimental XFH holograms measured at BW1 in October 1998.

- Fig. D.1: The reconstructions of unsymmetrized holograms were symmetrized in real space according to the symmetry of bcc Fe. The image plane is parallel to the $\{001\}$ lattice planes and passes through the emitter atom. Reconstructions of holograms measured at the energies of the Fe K_α and K_β lines and the energy-added reconstruction are shown. The angular ranges of the holograms were $\Delta\theta_1 = 0°...59°$ and $\Delta\theta_2 = 24°...83°$.

- Fig. D.2: Reconstructions of holograms are shown that are comparable to the reconstructions of fig. D.1. Here, the holograms were extended to 4π and the reconstructions were not symmetrized. The image plane is parallel to the (001) lattice planes and passes through the emitter atom.

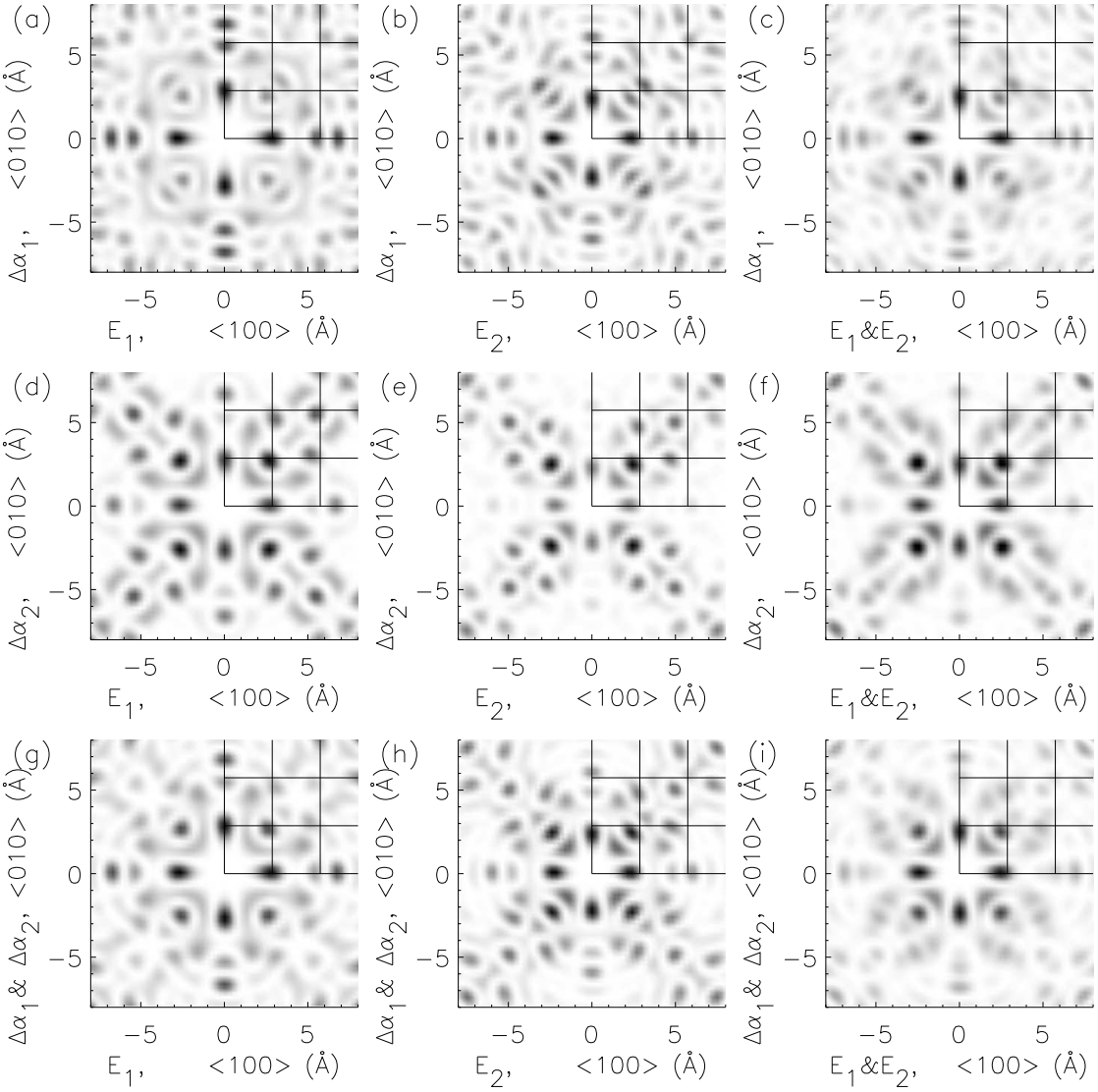

Figure D.1: These reconstructions from unsymmetrized holograms were symmetrized in real space according to the symmetry of bcc Fe. The reconstructions of holograms measured at the energies (a), (d), (g) of the Fe K_α line, (b), (e), (h) of the Fe K_β line, and (c), (f), (i) energy-added reconstructions. The angular range of the holograms was $\varphi = 0°, ...359°$, and (a)-(c) $\Delta\alpha_1 = 0°, ...59°$, (d)-(f) $\Delta\alpha_2 = 24°, ...83°$. (g), (h), (i) show the summations over the reconstructions (a) with (d), (b) with (e), and (c) with (f), respectively. The reconstructions pass through the emitter atom in a plane parallel to the {001} lattice planes.

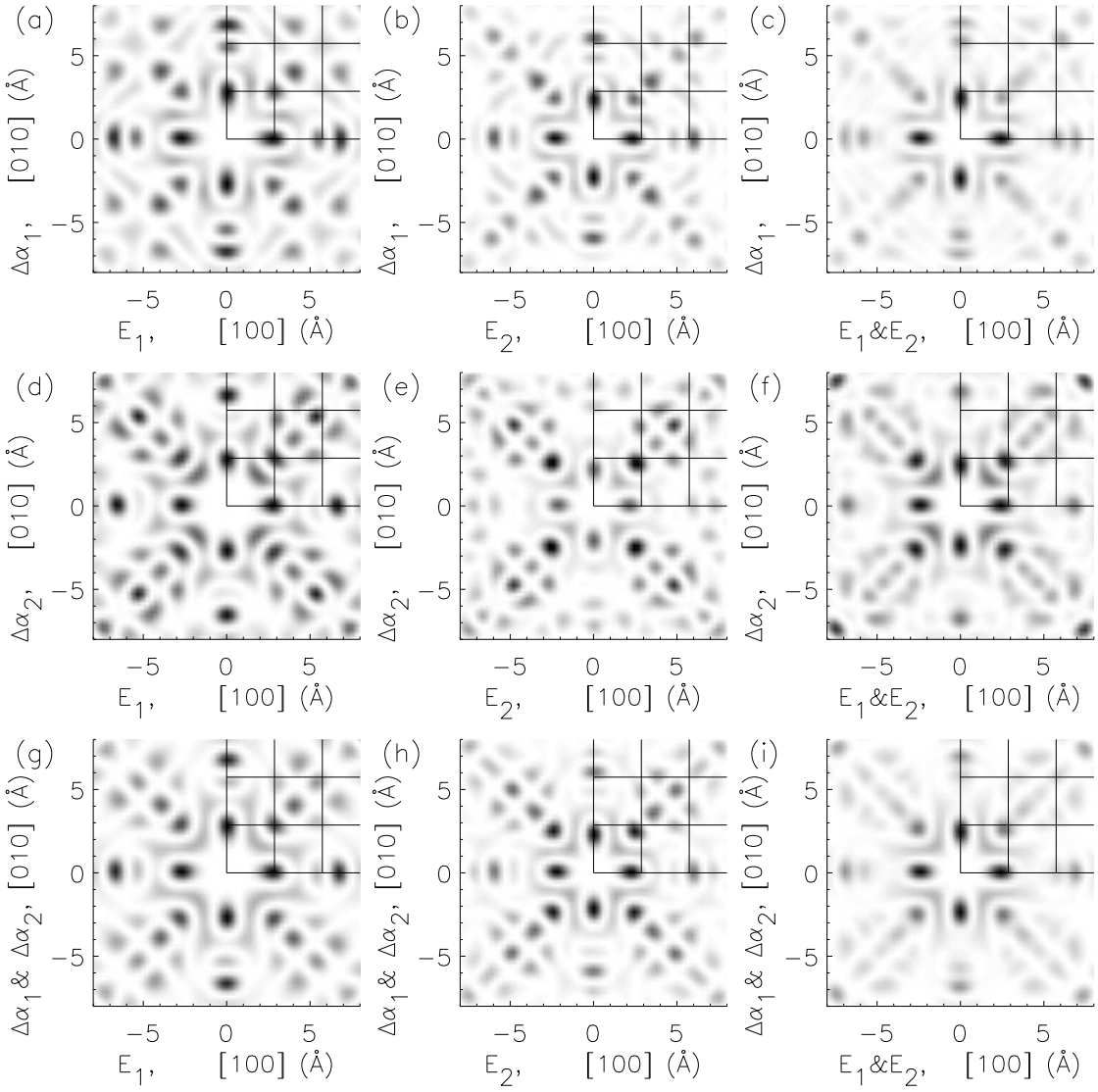

Figure D.2: Reconstructions of holograms that were measured at the energies (a), (d), (g) of the Fe K_α line, (b), (e), (h) of the Fe K_β line, and extended to 4π. (c), (f), (i) show energy-added reconstructions. The angular range of the original holograms was $\varphi = 0°, ...359°$, and (a)-(c) $\Delta\alpha_1 = 0°, ...59°$, (d)-(f) $\Delta\alpha_2 = 24°, ...83°$, but the full 4π angular range was reconstructed. (g), (h), (i) show the summations over the reconstructions (a) with (d), (b) with (e), and (c) with (f). The image (d) is obtained from the hologram of fig. 6.2 (e). The reconstructions pass through the emitter atom in a plane parallel to the (001) lattice planes. The φ_d rotation axis was parallel to the [001] direction.

D.2 Reconstructions of bcc Fe MEXH Holograms

This appendix shows additional reconstructions of experimental MEXH holograms measured at CEMO in March 1999. The MEXH holograms were measured at the energies 9.5 keV, 9.9 keV, ... 11.1 keV. They were extended to 4π and reconstructed in three dimensions.

- Fig. D.3: Images at the 5 single energies and the energy-added image in a plane parallel to the (001) lattice planes, at a distance 2.6 Å $\approx a_0 = 2.87$ Å above the detector atom.
- Fig. D.4: Images at the 5 single energies and the energy-added image in a plane parallel to the (001) lattice planes, at a distance 4.5 Å $\approx 3a_0/2 = 4.31$ Å above the detector atom.
- Fig. D.5: Images at the 5 single energies and the energy-added image in a plane parallel to the (001) lattice planes, at a distance 5.8 Å $\approx 2a_0 = 5.74$ Å above the detector atom.
- Fig. D.6: One-dimensional cuts through the second-nearest neighbors of the detector atom at the 5 single energies and the energy-added image. The central $(0.8\ \text{Å})^3$ of the reconstructions are set to zero.
- Fig. D.7: One-dimensional cuts through the third-nearest neighbors of the detector atom at the 5 single energies and the energy-added image. The central $(0.8\ \text{Å})^3$ of the reconstructions are set to zero.
- Fig. D.8: One-dimensional cuts through the nearest and fifth-nearest neighbors of the detector atom at the 5 single energies and the energy-added image. The central $(0.8\ \text{Å})^3$ of the reconstructions are set to zero.

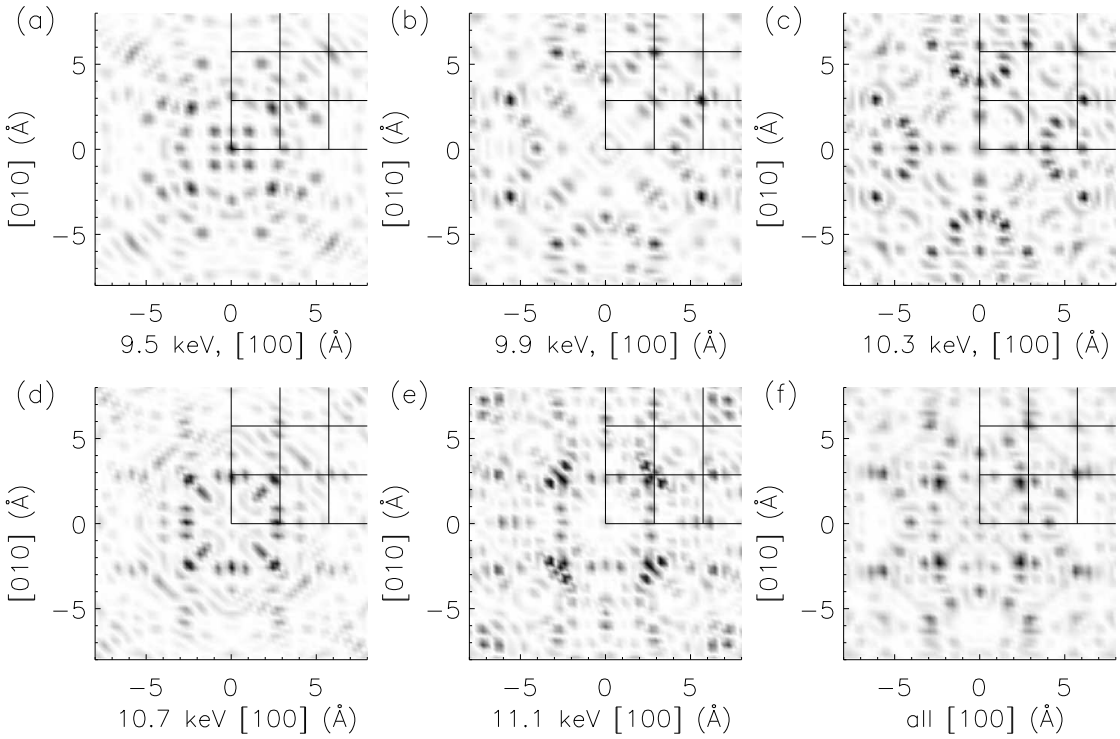

Figure D.3: Reconstructions of holograms measured at the energies (a) 9.5 keV, (b) 9.9 keV, (c) 10.3 keV, (d) 10.7 keV, (e) 11.1 keV, that were extended to 4π. (f) shows the energy-added image. The reconstructions are taken in a plane parallel to the (001) lattice planes, at a distance 2.6 Å $\approx a_0 = 2.87$ Å above the detector atom.

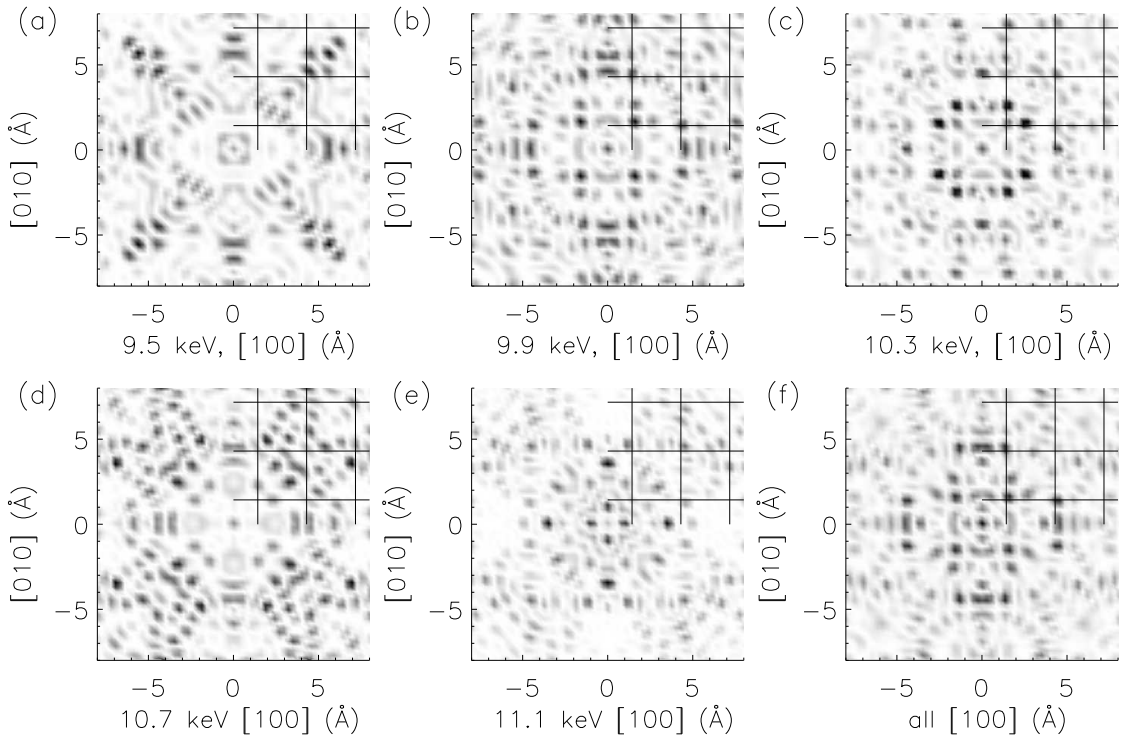

Figure D.4: Reconstructions of holograms measured at the energies (a) 9.5 keV, (b) 9.9 keV, (c) 10.3 keV, (d) 10.7 keV, (e) 11.1 keV, that were extended to 4π. (f) shows the energy-added image. The reconstructions are taken in a plane parallel to the (001) lattice planes, at a distance 4.5 Å $\approx 3a_0/2 = 4.31$ Å above the detector atom.

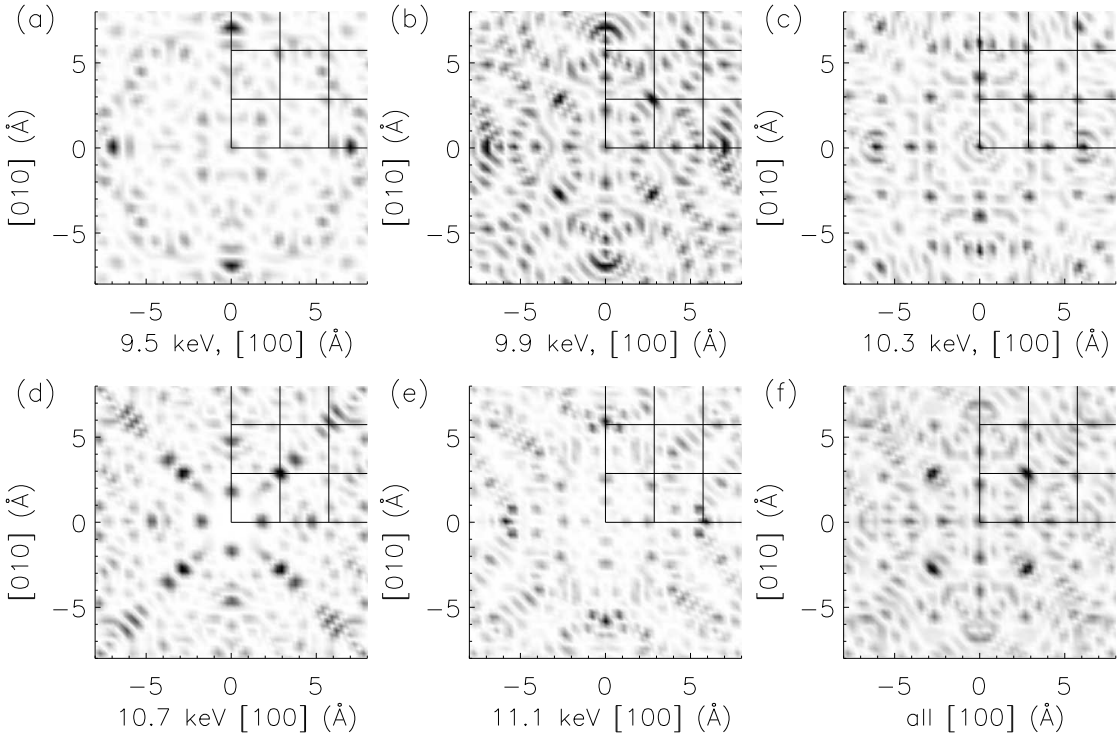

Figure D.5: Reconstructions of holograms measured at the energies (a) 9.5 keV, (b) 9.9 keV, (c) 10.3 keV, (d) 10.7 keV, (e) 11.1 keV, that were extended to 4π. (f) shows the energy-added image. The reconstructions are taken in a plane parallel to the (001) lattice planes, at a distance 5.8 Å $\approx 2a_0 = 5.74$ Å above the detector atom.

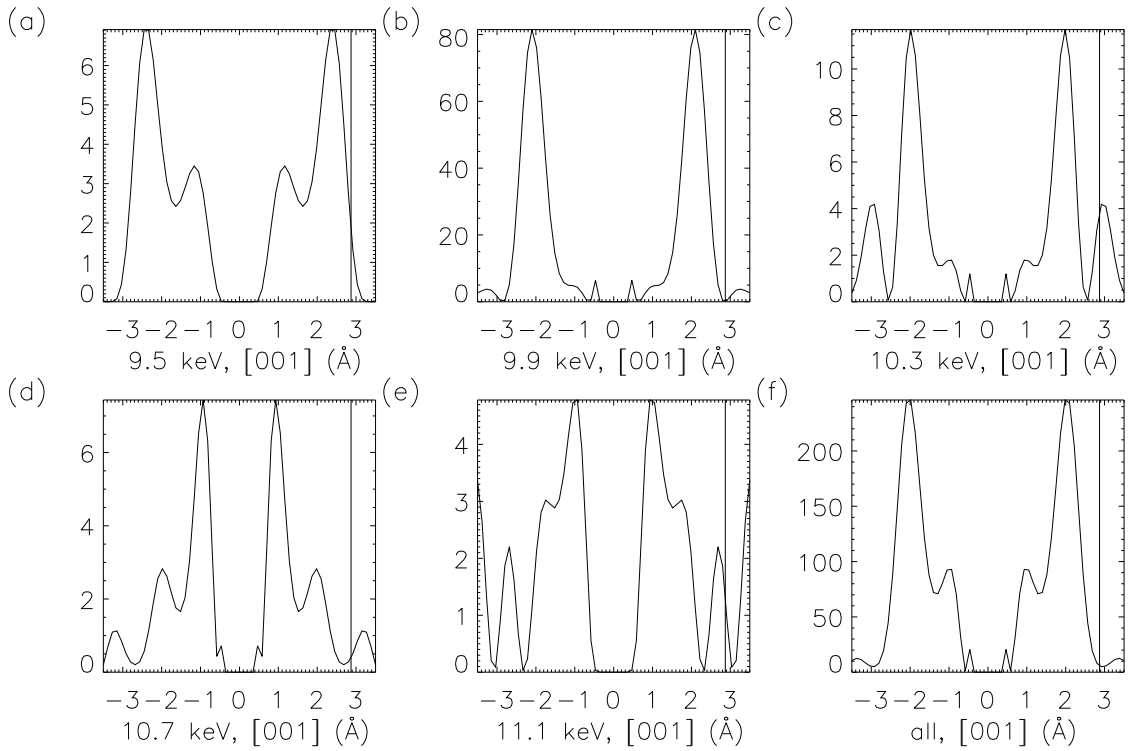

Figure D.6: One-dimensional radial cuts through the three-dimensional reconstructions of 4π extended holograms. The holograms were measured at the energies (a) 9.5 keV, (b) 9.9 keV, (c) 10.3 keV, (d) 10.7 keV, (e) 11.1 keV. (f) shows the cut through the energy-added reconstruction. The detector atom is in the center (0) of the cuts which pass parallel to the [001] direction through its next-nearest neighbors. The central (0.8 Å)^3 of the reconstruction were set to zero. The cuts were divided by 1000.

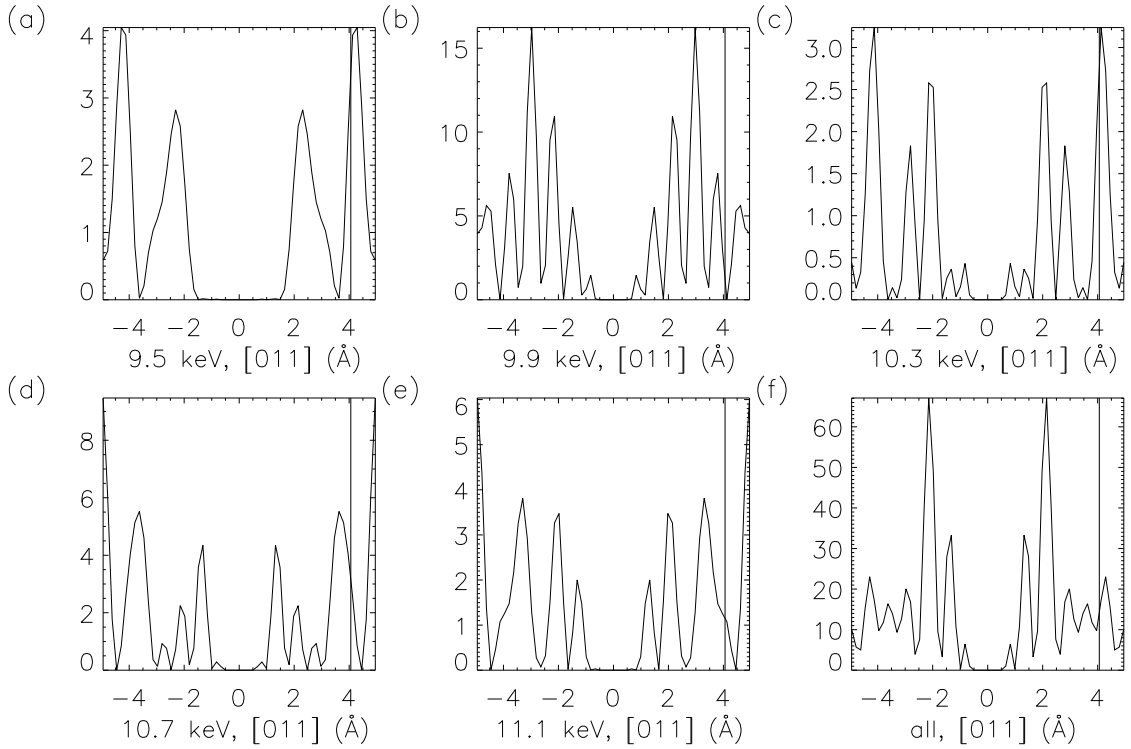

Figure D.7: One-dimensional radial cuts through the three-dimensional reconstructions of 4π extended holograms. The holograms were measured at the energies (a) 9.5 keV, (b) 9.9 keV, (c) 10.3 keV, (d) 10.7 keV, (e) 11.1 keV. (f) shows the cut through the energy-added reconstruction. The detector atom is in the center (0) of the cuts which pass parallel to the [011] direction through its third-nearest neighbors. The central $(0.8\ \text{Å})^3$ of the reconstruction were set to zero. The cuts were divided by 1000.

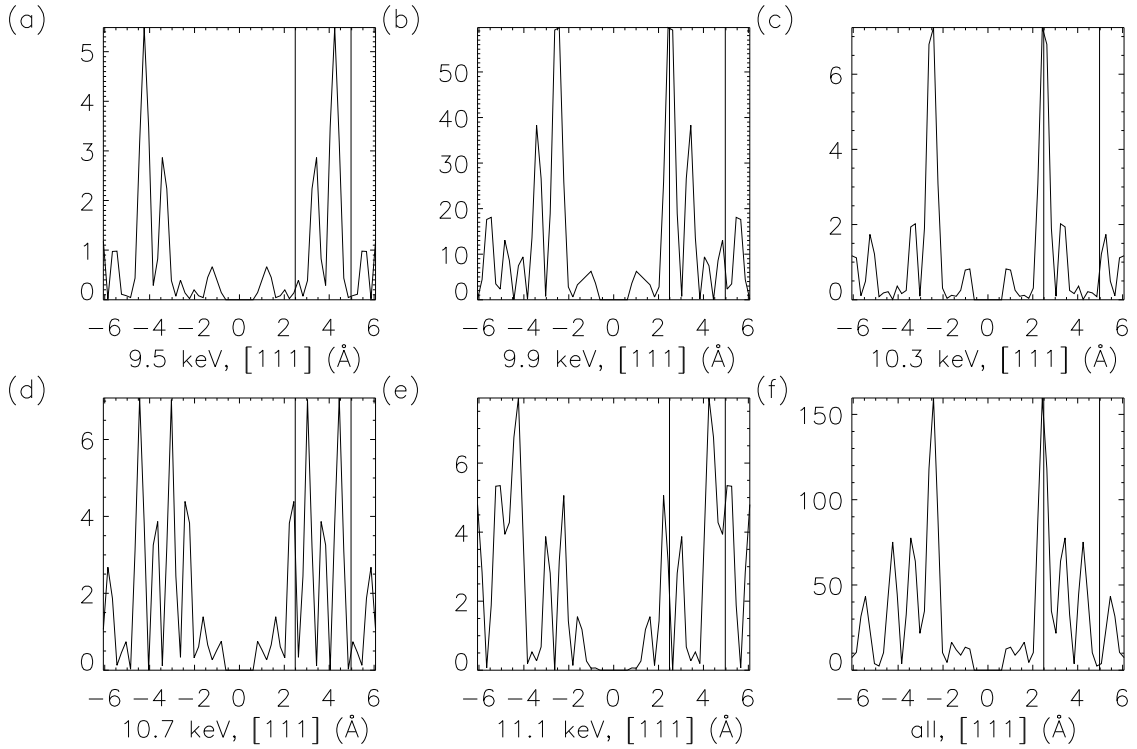

Figure D.8: One-dimensional radial cuts through the three-dimensional reconstructions of 4π extended holograms. The holograms were measured at the energies (a) 9.5 keV, (b) 9.9 keV, (c) 10.3 keV, (d) 10.7 keV, (e) 11.1 keV. (f) shows the cut through the energy-added reconstruction. The detector atom is in the center (0) of the cuts which pass parallel to the [111] direction through its nearest and fifth-nearest neighbors. The central $(0.8\ \text{Å})^3$ of the reconstruction were set to zero. The cuts were divided by 1000.

Bibliography

[Adams95] B. Adams, Ordnungskinetik in Cu_3Au an einer (001)-Oberfläche, Dissertation, Fakultät für Physik der Ludwigs-Maximilians-Universität München (1995)

[Adams98] B. Adams, D. V. Novikov, T. Hiort, and G. Materlik, E. Kossel, Atomic Holography with X-Rays, Phys. Rev. B **57**, 7526 (1998)

[Adams99] B. Adams, T. Hiort, E. Kossel, G. Materlik, Y. Nishino, D. V. Novikov, X-Ray Fluorescence Holography in Theory and Experiment, phys. stat. sol. (b) **215**, 757 (1999)

[Adams00a] B. Adams, T. Hiort, G. Materlik, Y. Nishino, D. V. Novikov, Atom-Resolving X-Ray Holography, in *X-Ray and Inner-Shell Processes*, edited by R. W. Dunford et al., AIP Conference Proceedings No. 506, page 549 (American Institute of Physics, New York, 2000)

[Adams00b] B. Adams, G. Materlik, Y. Nishino, D. V. Novikov, A Novel Experimental Technique for X-Ray Holography, to be published

[Aoki72] S. Aoki, Y. Ichihara, S. Kikuta, X-Ray Hologram Obtained by Using Synchrotron Radiation, Japan. J. Appl. Phys. **11**, 1857 (1972)

[Arthur95] J. Arthur, G. Materlik, R. Tatchyn, and H. Winick, The LCLS: A Fourth Generation Light Source Using the SLAC Linac, Rev. Sci. Instrum. **66**, 1987 (1995)

[Barton88] J. J. Barton, Photoelectron Holography, Phys. Rev. Lett. **61**, 1356 (1988)

[Barton90] J. J. Barton, Photoelectron Holography = Holography + Photoelectron Diffraction, J. Electron Spectroscopy Relat. Phenom. **51**, 37 (1990)

[Barton91] J. J. Barton, Removing Multiple Scattering and Twin Images from Holographic Images, Phys. Rev. Lett. **67**, 3106 (1991)

[Beckhoff94] B. Beckhoff, B. Kanngießer, J. Scheer, W. Swoboda, Toroidally Shaped HOPG Crystals as Strongly Focusing Bragg Reflectors of Characteristic X-Ray Tube Radiation for EDXRF Analysis, Advances in X-Ray Analysis **37**, 523 (1994)

[Beckhoff97] B. Beckhoff, B. Kanngießer, Improvement of the Detection Sensitivity of EDXRF Trace Element Analysis by Means of Efficient X-Ray Focusing Based on Strongly Curved HOPG Crystals, Advances in X-Ray Analysis **39**, 109 (1997)

[Bedzyk85a] M. J. Bedzyk and G. Materlik, Two-Beam Dynamical Diffraction Solution of the Phase-Problem: A Determination with X-Ray Standing-Wave Fields, Phys. Rev. B **32**, 6456 (1985)

[Bedzyk85b] M. J. Bedzyk and G. Materlik, Electron-Energy-Loss X-Ray-Absorption Spectroscopy: A Nondestructive Structural-Depth Microprobe, Phys. Rev. B **32**, 4228 (1985)

[Bompadre99] S. G. Bompadre, T. W. Petersen, and L. B. Sorensen, Tabletop Bremsstrahlung X-Ray Holography: Making Multiwavelength X-Ray Holograms, Phys. Rev. Lett. **83**, 2741 (1999)

[Bonifacio84] R. Bonifacio, C. Pellegrini and I. M. Narducci, Collective Instabilities and High-Gain Regime in a Free Electron Laser, Opt. Commun. **50**, 373 (1984)

[Born97] M. Born and E. Wolf, Principles of Optics: Electromagnetic Theory of Propagation, Interference and Diffraction of Light, sixth edition 1980 (with corrections), reissued by Cambridge University Press, Cambridge (1997)

[Bragg42] W. L. Bragg, The X-Ray Microscope, Nature **149**, 470 (1942)

[Brinkmann97] R. Brinkmann, G. Materlik, J. Rossbach, J. R. Schneider, B.-H. Wiik, An X-Ray FEL Laboratory as Part of a Linear Collider Design, Nucl. Instrum. Meth. A **393**, 86 (1997)

[Bronstein91] I. N. Bronstein, K. A. Semendjajew, Taschenbuch der Mathematik, 25., durchgesehene Auflage, B. G. Teubner Verlagsgesellschaft, Stuttgart, Leipzig, und Verlag Nauka, Moskau (1991)

[Chukhovskii98] F. N. Chukhovskii, D. V. Novikov, T. C. Hiort, E. Kossel, G. Materlik, Electron Charge Density Imaging with X-Ray Holography, unpublished

[Dolbnya95a] I. P. Dolbnya, K. V. Zolotarev, M. A. Sheromov, A. A. Antonov, I. G. Grigoryeva, Focusing Parabolic Pyrolytic Graphite X-Ray Monochromator, Nucl. Instrum. Meth. A **359**, 141 (1995)

[Dolbnya95b] I. P. Dolbnya, K. V. Zolotarev, M. A. Sheromov, A. A. Antonov, I. G. Grigoryeva, Comment on "Focusing Parabolic Pyrolytic Graphite X-Ray Monochromator ", Nucl. Instrum. Meth. A **370**, 646 (1996)

[Eichler93] J. Eichler and G. Ackermann, Holographie, Springer-Verlag Berlin Heidelberg New York (1993)

[Fadley93] C. S. Fadley, Diffraction and Holography with Photoelectrons and Auger Electrons: Some New Directions, Surface Science Reports **19**, 231 (1993)

[Faigel99] G. Faigel and M. Tegze, X-Ray Holography, Rep. Prog. Phys. **62**, 355 (1999)

[Fonda97] L. Fonda, Evaluation of a Scattered Radiation Field in a Cluster Relevant for Multiple-Energy X-Ray Holography, phys. stat. sol. (b) **201**, 329 (1997)

[Frahm95] R. Frahm, J. Weigelt, G. Meyer, and G. Materlik, X-Ray Undulator Beamline BW1 at DORIS III, Rev. Sci. Instrum. **66**, 1677 (1995)

[Gabor48] D. Gabor, A New Microscopic Principle, Nature **161**, 777 (1948).

[Gatti84a] E. Gatti and P. Rehak, Semiconductor Drift Chamber - An Application of a Novel Charge Transport Scheme, Nucl. Instrum. Meth. **225**, 608, (1984)

[Gatti84b] E. Gatti, P. Rehak, J. T. Walton, Silicon Drift Chambers - First Results and Optimum Processing of Signals, Nucl. Instrum. Meth. **226**, 129, (1984)

[Gauthier96] Ch. Gauthier et al, A High Resolution, 6 Channels, Silicon Drift Detector Array with Integrated JFET's Designed for XAFS Spectroscopy: First X-Ray Fluorescence Excitation Spectra Recorded at the ESRF, Nucl. Instrum. Meth. A **382**, 524 (1996)

[Gog95] T. Gog, D. Bahr, and G. Materlik, Kossel Diffraction in Perfect Crystals: X-Ray Standing Waves in Reverse, Phys. Rev. B **51**, 6761 (1995)

[Gog96a] T. Gog, P. M. Len, G. Materlik, D. Bahr, C. S. Fadley, and C. Sanchez-Hanke, Multiple-Energy X-ray Holography: Atomic Images of Hematite (Fe_2O_3), Phys. Rev. Lett. **76**, 3132 (1996)

[Gog96b] T. Gog, R. H. Menk, F. Arfelli, P. M. Len, C. S. Fadley, G. Materlik, X-ray Holography with Atomic Resolution: Trying to Make It Work, Synchrotron Radiation News **9**, 30 (1996)

[Gog98] T. Gog, R. A. Eisenhower, R. H. Menk, M. Tegze, G. LeDuc, Multiple-Energy X-Ray Holography with Atomic Resolution, J. Electron Spectroscopy and Related Phenomena **92**, 123 (1998)

[Grigoryeva90] I. G. Grigoryeva, A. A. Antonov, V. B. Baryshev, Tunable Band-Pass X-Ray Optic Elements from Shaped Pyrolytic Graphite, Synchrotron Radiation News **3**, 15 (1990)

[Harp90] G. R. Harp, D. K. Saldin, and B. P. Tonner, Atomic-Resolution Electron Holography in Solids with Localized Sources, Phys. Rev. Lett. **65**, 1012 (1990)

[HASYLAB97] Experimental Stations at HASYLAB, Hamburger Synchrotronstrahlungslabor HASYLAB at Deutsches Elektronen-Synchrotron DESY (1997)

[HASYLAB99] HASYLAB Annual Report (I), 17 (1999)

[Hayashi98] K. Hayashi, T. Yamamoto, J. Kawai, M. Suzuki, S. Goto, S. Hayakawa, K. Sakurai, and Y. Gohshi, Atomic-Resolution X-Ray Fluorescence Holography of Zn (0.02 wt%) in a GaAs Wafer, Analytical Sciences **14**, 987 (1998)

[Hiort97] T. C. Hiort, D. V. Novikov, B. Adams, G. Materlik, H. Graafsma, A. Kvick, Experimental Results with Multiple Energy X-Ray Holography, 5. Jahrestagung der Deutschen Gesellschaft für Kristallographie 1997, Zeitschrift für Kristallographie, Supplement Issue No. 12, Referate, R. Oldenbourg Verlag, München

[Hiort98] T. C. Hiort, D. V. Novikov, E. Kossel, B. Adams und G. Materlik, Atomarauflösende Röntgenholographie von Cu_3Au, Verhandl. DPG (VI) **33**, 886 (1998)

[Hiort99a] T. C. Hiort, D. V. Novikov, E. Kossel, B. Adams, Y. Nishino, G. Materlik, Vergleich von direkter und reziproker atomarauflösender Röntgenfluoreszenzholographie, Verhandl. DPG (VI) **34**, 938 (1999)

[Hiort99b] T. Hiort, D. V. Novikov, B. Adams, Y. Nishino, and G. Materlik, Imaging of Fe Crystal Structure Using Multiple Energy X-Ray Holography, HASYLAB Annual Report (I), 899 (1999)

[Hiort00] T. Hiort, D. V. Novikov, E. Kossel, and G. Materlik, Quantitative Assessment of X-Ray Fluorescence Holography for bcc Fe as a Test Case, Phys. Rev. B **61**, R830 (2000)

[Howells87] M. Howells, C. Jacobsen, J. Kirz, R. Feder, K. Mc Quaid, S. Rothman, X-ray Holograms at Improved Resolution: A Study of Zymogen Granules, Science **238**, 514 (1987)

[Howells90] M. R. Howells, C. J. Jacobsen, X-ray Holography, Synchrotron Radiation News **3**, No. 4, 23 (1990)

[IUC85] International Tables for X-Ray Crystallography, Volume III, Physical and Chemical Tables, edited by C. H. Macgillavry and G. D. Rieck, general editor K. Lonsdale, second reprinted edition, D. Reidel Publishing Company, Dordrecht (1985)

[IUC93] International Tables for X-Ray Crystallography, Volume B, Reciprocal Space, edited by U. Shmueli, Kluwer Academic Publishers, Dordrecht Boston London (1993)

[IUC92] International Tables for X-Ray Crystallography, Volume C, Mathematical, Physical and Chemical Tables, edited by A. J. C. Wilson, Kluwer Academic Publishers, Dordrecht Boston London (1992)

[Jackson75] J. D. Jackson, Classical Electrodynamics, second edition, John Wiley & Sons, Inc., New York, Chichester, Brisbane, Toronto, Singapore (1975)

[Kawai98] J. Kawai, K. Hayashi, T. Yamamoto, S. Hayakawa, and Y. Gohshi, X-Ray Fluorescence Holography of $SrTiO_3$ Compared with X-Ray Photoelectron Holography, Analytical Sciences **14**, 903 (1998)

[KETEK] MPI Halbleiterlabor & KETEK GmbH, Otto-Hahn-Ring 6, D-81739 München, Germany

[Kondratenko80] A. M. Kondratenko and E. L. Saldin, Generation of Coherent Radiation by a Relativistic Electron Beam in an Ondulator, Part. Accel. **10**, 207 (1980)

[Kordesch84] M. E. Kordesch and R. W. Hoffman, Electron-Yield Extended X-Ray Absorption Fine Structure with the Use of a Gas-Flow Electron Detector, Phys. Rev. B **29**, 491 (1984)

[Korecki97] P. Korecki, J. Korecki, and T. Slezak, Atomic Resolution γ-ray Holography Using the Mössbauer Effect, Phys. Rev. Lett. **79**, 3518 (1997)

[Korecki99] P. Korecki, J. Korecki, and W. Karas, Holography with γ-Rays - Simulations Versus Experiment for $\alpha-^{57}$Fe, Phys. Rev. B **59**, 6139 (1999)

[Kossel35] W. Kossel, H. Loeck, H. Voges, Die Richtungsverteilung der in einem Kristall entstandenen charakteristischen Röntgenstrahlung, Z. Physik **94**, 139 (1935)

[Kossel98] E. Kossel, Untersuchung der Wellenlängenabhängigkeit der reziproken Röntgenfluoreszenzholographie, Diplomarbeit des Fachbereichs Physik der Universität Hamburg (1998), DESY-THESIS-1999-014, May 1999, Deutsches Elektronen-Synchrotron

[Krolzig84] A. Krolzig, G. Materlik, M. Swars and J. Zegenhagen, A Feedback Control System from Synchrotron Radiation Double Crystal Instruments, Nucl. Instrum. Meth. A **219**, 430 (1984)

[Laue60] M. von Laue, Röntgenstrahlinterferenzen, Akademische Verlagsgesellschaft Frankfurt am Main, dritte, neubearbeitete und erweiterte Auflage (1960)

[Lauterborn93] W. Lauterborn, T. Kurz, M. Wiesenfeldt, Kohärente Optik: Grundlagen für Physiker und Ingenieure, Springer-Verlag Berlin Heidelberg New York (1993)

[Lechner95] P. Lechner, L. Strüder, Ionisation Statistics in Silicon X-Ray Detectors - New Experimental Results, Nucl. Instrum. Meth. A **354**, 464 (1995)

[Lechner96] P. Lechner et al, Silicon Drift Detectors for High Resolution Room Temperature X-Ray Spectroscopy, Nucl. Instrum. Meth. A **377**, 346 (1996)

[Len94] P. M. Len, S. Thevuthasan, and C. S. Fadley, A. P. Kaduwela and M. A. Van Hove, Atomic Imaging by X-Ray-Fluorescence Holography and Electron-Emission Holography: A Comparative Study, Phys. Rev. B **50**, 275 (1994)

[Len96] P. M. Len, S. Thevuthasan, A. P. Kaduwela, M. A. Van Hove, C. S. Fadley, Optimization of **k**-Space Sampling in Atomic Imaging by Electron Emission Holography, Surf. Sci. **365**, 535 (1996)

[Len97a] P. M. Len, T. Gog, C. S. Fadley, G. Materlik, X-Ray Fluorescence Holography and Multiple Energy X-Ray Holography: A Critical Comparison of Atomic Images, Phys. Rev. B Rapid Comm. **55**, 3323 (1997)

[Len97b] P. M. Len, T. Gog, D. Novikov, R. A. Eisenhower, G. Materlik, and C. S. Fadley, Multiple Energy X-Ray Holography: Incident-Radiation Polarization Effects, Phys. Rev. B **56**, 1529 (1997)

[Len97c] P. M. Len, F. Zhang, S. Thevuthasan, A. P. Kaduwela, C. S. Fadley, M. A. Van Hove, Optimal Atomic Imaging by Photoelectron Holography, J. Electron Spectroscopy and Related Phenomena **85**, 145 (1997)

[Len97d] P. M. Len, C. S. Fadley, G. Materlik, Atomic Holography with Electrons and X-Rays, in *X-Ray and Inner Shell Processes*, edited by R. L. Johnson, H. Schmidt-Bocking, B. F. Sonntag, AIP Conference Proceedings No. 389, page 295 (American Institue of Physics, Woodbury, New York, 1997)

[Leo94] W. R. Leo, Techniques for Nuclear and Particle Physics Experiments: A How-to Approach, second Revised Edition, Springer-Verlag New York Berlin Heidelberg (1994)

[Lindaas96] S. Lindaas, M. Howells, C. Jacobsen, A. Kalinovsky, X-Ray Holographic Microscopy by Means of Photoresist Recording and Atomic Force Microscope Readout, J. Opt. Soc. Am. A **13**, 1788 (1996)

[Lueth98] H. Lüth, Surfaces and Interfaces of Solid Materials, Third Edition 1995, Springer-Verlag Berlin Heidelberg New York, Third Corrected Printing (1998)

[Mendez92] M. A. Mendez, C. Glück, and K. Heinz, Holography with Conventional LEED, J. Phys.: Condens. Matter **4**, 999 (1992)

[Mendez93] M. A. Mendez, C. Glück, M. Wagner, U. Löffler, R. Döll, and K. Heinz, Sampling of Diffuse LEED Intensity Distributions by Conventional Spot Intensities, Surf. Sci. **290**, 45 (1993)

[Miller97] G. A. Miller and L. B. Sorensen, Quantum Electrodynamics of the Internal Source X-Ray Holographies: Bremsstrahlung, Fluorescence, and Multiple-Energy X-Ray Holography, Phys. Rev. B **56**, 2399 (1997)

[Nishino99] Y. Nishino and G. Materlik, Holographies and EXAFS in Quantum Electrodynamics, Phys. Rev. B **60**, 15074 (1999)

[Novikov97] D. Novikov, B. Adams, T. Hiort, E. Kossel, and G. Materlik, X-Ray Holography with Atomic Resolution at Multiple Wavelengths, HASYLAB Annual Report (I), 899 (1997)

[Novikov98] D. V. Novikov, B. Adams, T. Hiort, E. Kossel, G. Materlik, R. Menk, and A. Walenta, X-ray Holography for Structural Imaging, J. Synchrotron Rad. **5**, 315 (1998)

[Pinotti93] E. Pinotti et al, The pn-CCD on-Chip Electronics, Nucl. Instrum. Meth. A **326**, 85 (1993)

[Rehak85] P. Rehak, E. Gatti and A. Longoni, J. Kemmer, P. Holl, R. Klanner, G. Lutz and A. Wylie, Semiconductor Drift Chambers for Position and Energy Measurements, Nucl. Instrum. Meth. A **235**, 224, (1985)

[Rehak90] P. Rehak et al, Feedback Charge Amplifier Integrated on the Detector Wafer, Nucl. Instrum. Meth. A **288**, 168, (1990)

[Reuter97] K. Reuter, J. Bernhardt, H. Wedler, J. Schardt, U. Starke, and K. Heinz, Holographic Image Reconstruction from Electron Diffraction Intensities of Ordered Superstructures, Phys. Rev. Lett. **79**, 4818 (1997)

[ROENTEC96] RÖNTEC Röntgenanalyse-Technik GmbH, Rudower Chaussee 6, D-12489 Berlin, Instruction Manual (1996), detectors V3-0068 and B8-0069

[Saldin90] D. K. Saldin, P. L. de Andres, Holographic LEED, Phys. Rev. Lett. **64**, 1270 (1990)

[Saldin91] D. K. Saldin, G. R. Harp, B. L. Chen, and B. P. Tonner, Theoretical Principles of Holographic Crystallography, Phys. Rev. B **44**, 2480 (1991)

[Saldin92] D. K. Saldin, G. R. Harp, and B. P. Tonner, Effect of the Reference Wave in Auger-Electron Holography, Phys. Rev. B **45**, 9629 (1992)

[Saldin95] D. K. Saldin, X. Chen, Three-Dimensional Reconstruction by Holographic LEED: Proper Identification of the Reference Wave, Phys. Rev. B **52**, 2941 (1995)

[Saldin97] D. K. Saldin, Holographic Crystallography for Surface Studies: A Review of the Basic Principles, Surface Review and Letters **4**, 441 (1997)

[Shevchik79] N. J. Shevchik and D. A. Fischer, High Pass Photocathode X-Ray Ionisation Chamber for Surface EXAFS, Rev. Sci. Instrum. **50**, 577 (1979)

[Soltau96] H. Soltau et al, Performance of the pn-CCD X-Ray Detector System Designed for the XMM Sattelite Mission, Nucl. Instrum. Meth. A **377**, 340 (1996)

[Stoehr84] J. Stöhr, C. Noguera, and T. Kendelewicz, Auger and Photoelectron Contributions to the Electron-Yield Surface Extended X-Ray Absorption Fine-Structure Signal, Phys. Rev. B **30**, 5571 (1984)

[Strueder90] L. Strüder et al, The MPI / AIT X-Ray Imager (MAXI) - High Speed pn CCDs for X-Ray Detection, Nucl. Instrum. Meth. A **288**, 227 (1990)

[Strueder95] L. Strüder and H. Soltau, High Resolution Silicon Detectors for Photons and Particles, Radiation Protection Dosimetry **61**, 39 (1995)

[Strueder96] L. Strüder and J. Kemmer, Neuartige Röntgendetektoren für die Astrophysik, Physikalische Blätter **52**, 21 (1996)

[Strueder97] L. Strüder et al, High Resolution, High Speed Detectors with Integrated JFET Electronics, Journal de Physique IV France **7** (1997), Colloque C2, Supplement au Journal de Physique III, C2-21 (1997)

[Strueder98] L. Strüder et al, High-Resolution, High-Count-Rate X-ray Spectroscopy with State-of-the-Art Silicon Detectors, J. Synchrotron Rad. **5**, 268 (1998)

[Szoeke86] A. Szöke, X-Ray and Electron Holography Using a Local Reference Beam, in *Short Wavelength Coherent Radiation: Generation and Applications*, edited by D. T. Attwood and J. Boker, AIP Conference Proceedings No. 147 , page 361 (American Institute of Physics, New York, 1986)

[Szoeke93] A. Szöke, Electron-Diffraction Spectroscopy and the Holographic Inverse Problem, Phys. Rev. B **47**, 14044 (1993)

[Szoeke97a] A. Szöke, H. Szöke, and J. R. Somoza, Holographic Methods in X-ray Crystallography. V. Multiple Isomorphous Replacement, Multiple Anomalous Dispersion and Non-crystallographic Symmetry, Acta Cryst. A **53**, 291 (1997)

[Szoeke97b] A. Szöke, Holographic Microscopy with a Complicated Reference, Journal of Imaging Science and Technology **41**, 332 (1997)

[Tegze91] M. Tegze and G. Faigel, Atomic-Resolution X-Ray Holography, Europhys. Lett. **16**, 41 (1991)

[Tegze96] M. Tegze, G. Faigel, X-Ray Holography with Atomic Resolution, Nature **380**, 49 (1996)

[Tegze99] M. Tegze, G. Faigel, S. Marchesini, M. Belakhovsky, A. I. Chumakov, Three Dimensional Imaging of Atoms with Isotropic 0.5Å Resolution, Phys. Rev. Lett. **82**, 4847 (1999)

[Terminello93] L. J. Terminello, Holographic Imaging of Atoms Using Multiple-Wave-Number Electron Angular Distribution Patterns, Phys. Rev. Lett. **70**, 599 (1993)

[Thevuthasan91] S. Thevuthasan, G. S. Herman, A. P. Kaduwela, R. S. Saiki, Y. J. Kim, W. Niemezura, M. Burger, and C. S. Fadley, Electron Emission Holography at keV Energies: Estimates of Accuracy and Limitations, Phys. Rev. Lett. **67**, 469 (1991)

[Thevuthasan93] S. Thevuthasan, R. X. Ynzunza, E. D. Tober, and C. S. Fadley, High Energy Photoelectron Holography for an Adsorbate Test System: $c(2 \times 2)$S on Ni(001), Phys. Rev. Lett. **70**, 595 (1993)

[Tong91] S. Y. Tong, Hua Li, and H. Huang, Energy Extension in Three-Dimensional Atomic Imaging by Electron-Emission Holography, Phys. Rev. Lett. **67**, 3102 (1991)

[Tonner91] B. P. Tonner, Zhi-Lan Han, G. R. Harp, and D. K. Saldin, Scattered-Wave Integral-Transform Method of Holographic-Image Reconstruction from Forward-Scattering Diffraction Patterns, Phys. Rev. B **43**, 14423 (1991)

[Tonomura90] A. Tonomura, Electron Holography: A New View of the Microscopic, Physics Today, p. 22, April (1990)

[Tonomura92] A. Tonomura, Electron-Holographic Interference Microscopy, Advances in Physics **41**, 59 (1992)

[Treusch95] R. Treusch, Untersuchung dünner magnetischer Filme mit Röntgenstrahlung: Gd/Fe(100), Dissertation, Fachbereich Physik der Universität Hamburg (1995)

[Wille96] K. Wille, *Physik der Teilchenbeschleuniger und Synchrotronstrahlungsquellen*, 2nd, revised and extended edition, B. G. Teubner, Stuttgart (1996)

[Wyckoff63] R. W. G. Wyckoff, *Crystal Structures*, 2nd ed., Interscience, New York (1963), Reprint Edition, Robert E. Krieger Publishing Company Inc., Malabar (1982)

[Xraydata86] Center for X-Ray Optics: X-Ray Data Booklet, edited by D. Vaughan, Lawrence Berkeley Laboratory, University of California, Berkeley, California 94720, Second printing, with corrections (1986)

[Zegenhagen93] J. Zegenhagen, Surface Structure Determination with X-Ray Standing Waves, Surf. Sci. Reports **18**, 199 (1993)

[Zharnikov95] M. Zharnikov, M. Weinelt, P. Zebisch, M. Stichler, H.-P. Steinrück, Holography of Clean and Sulphur-Covered Ni(111) using Multiple Wave Number Photoelectron Diffraction Patterns, Surf. Sci. **334**, 114 (1995)

Danksagung

Mein Dank gilt allen, die zum Gelingen dieser Arbeit beigetragen haben. Insbesondere danke ich

Prof. Dr. G. Materlik, der mich für die atomarauflösende Röntgenholographie begeistert hat, für seine Betreuung und sein großes Interesse an der Arbeit,

Dr. D. V. Novikov für die hervorragende Zusammenarbeit während der gesamten Zeit der Arbeit und bei den Experimenten, sowie allen an der Röntgenholographie Beteiligten für die sehr gute und freundschaftliche Zusammenarbeit und konstruktive Gespräche: ganz besonders E. Kossel, Dr. B. Adams auch dafür, daß ich sein Programm zur Berechnung von Hologrammen benutzen konnte, Dr. P. Korecki, Dr. Y. Nishino, A. Schley,

den übrigen heutigen und ehemaligen Mitgliedern der Arbeitsgruppe für viele Diskussionen und die außergewöhnlich gute Arbeitsatmosphäre. Stellvertretend genannt seien hier K. Anduleit, Dr. F. Beckmann, T. Eickhoff, Dr. R. Eisenhower auch für ihre Hilfe bezüglich der englischen Sprache, J. I. Flege, P. Kappen, Dr. C. Sánchez-Hanke, Dr. T. Schmidt, Dr. H. Schulte-Schrepping, Dr. R. Treusch,

den Mitarbeitern des HASYLAB und des DESY in allen Bereichen für ihre Hilfsbereitschaft und die gute Zusammenarbeit,

Dr. P. Lechner von der KETEC GmbH sowie Dr. K. Hansen und Dr. C. Reckleben von DESY FEC für die Zusammenarbeit beim Testen der Silizium-Driftdetektoren,

der mechanischen Werkstatt des II. Instituts für Experimentalphysik der Universität Hamburg unter der Leitung von J. Weber für die Herstellung des Elektronendetektors,

meinen Freunden, besonders Jutta, Tish, Jung-Chen, Vidya, Alex, Jan,
Johannes, Malte, meinen Eltern,

Karsten Roland.